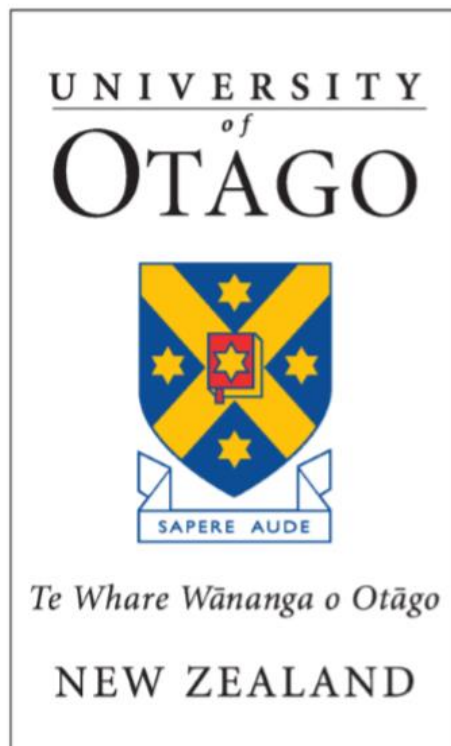


# A Modern Reinvestigation of the 1987 Moutere Depression Seismic Survey

Justin Chen Lo



*A thesis submitted for the degree of*

Master of Science

*At the University of Otago, Dunedin, New Zealand.*

# Table of Contents

Abstract.....	iv
Acknowledgements.....	vi
1.0 Introduction .....	1
1.1 Project Aim.....	1
1.2 Geological Background .....	2
1.2.1 Moutere Depression .....	2
1.2.2 Moutere Gravels & Glen Hope Formation.....	2
1.2.3 Western Province.....	3
1.2.4 Eastern Province .....	3
1.2.5 South of Nelson.....	4
1.3 Seismic Hazard Considerations .....	5
1.4 Data Processing: 1980 to Present .....	8
1.5 Original Seismic Data .....	10
2.0 Seismic Theory .....	12
2.1 Seismic Waves, Wave Propagation and Simple Seismic Models .....	12
2.2 Attenuation .....	16
2.3 Elastic deformation .....	19
2.4 Elastic Constants .....	20
2.5 Body waves .....	24
2.5.1 P-waves .....	25
2.5.2 S-waves .....	26
2.6 Surface Waves.....	27
2.7 Huygen’s principle.....	28
2.8 Snell’s Law .....	29
2.9 Zoeppritz Equations .....	31
2.10 Partition coefficients.....	32
3.0 Seismic Method .....	33
3.1 Seismic Reflection Method .....	33
3.2 Seismic Resolution: The Fresnel zone .....	36
3.3 Velocities.....	39
3.4 Common Mid-Point Method (CMP).....	39
3.5 Fourier Transforms.....	42
3.5.1 Fast Fourier Transform (FFT).....	46
3.6 Vibroseis.....	46

4.0 Processing Sequence (1987) .....	49
4.1 Initial Processing .....	49
4.2 Crooked Line Analysis .....	50
4.3 Common Depth Point Gathers.....	53
4.4 Deconvolution.....	54
4.5 Elevation static correction .....	57
4.6 Normal Move-Out Dynamic Corrections .....	58
4.7 Pre-Stack Mute.....	60
4.8 Amplitude Modulation.....	60
4.9 Refraction Static Corrections .....	61
4.10 CDP Trim and Stack .....	61
4.11 Time Variant Bandpass Filtering and Time Variant Scaling.....	62
4.12 Migration.....	62
4.13 Adaptive K-F Filtering.....	64
5.0 New Processing Flow and Line 01 Results .....	67
5.1 Line 01- initial notes.....	69
5.2 Adding Geometry.....	69
5.3 Floating Datum Application .....	73
5.4 Pre-stack processing Trace Removal.....	74
5.5 Brute stacking .....	81
5.6 First Breaks.....	84
5.7 AREAL Module.....	87
5.8 Refraction Statics .....	90
5.9 Gain .....	97
5.10 Initial refraction mute .....	103
5.11 Noise Suppression Testing .....	106
5.12 Comparisons .....	114
5.13 Deconvolution Parameter Testing .....	120
5.14 Bandpass Filter Parameter Testing .....	127
5.15 Compilation.....	135
5.19 Velocity Analysis.....	139
5.20 Residual Static Analysis .....	143
5.20a Stack Power Residual Static .....	143
5.20b Residual Static Module .....	146
5.21 Second Pass Velocity Analysis.....	147
5.22 Post-Stack Deconvolution .....	151

5.23 Migration.....	153
6.0 Processing Results (Line 02 – 08).....	156
6.1 Resolution Considerations .....	156
6.2 Processing Summary .....	157
6.3 Line 02.....	160
6.4 Line 03.....	169
6.4 Line 05.....	175
6.5 Line 05.....	181
6.6 Line 06.....	183
6.7 Line 07.....	185
6.9 Line 08.....	189
6.10 3D modelling.....	194
6.11 Processing Results Summary .....	202
7.0 Interpretations.....	203
7.1 Faults.....	203
7.2 Stratigraphy.....	206
8.0 Conclusions .....	213
8.1 Moutere Depression .....	213
8.2 Data and technical limitations .....	214
8.3 Future work.....	215
Appendix .....	217
References .....	219



## Abstract

The quality of seismic processing and interpretation in the past has always been shackled to the limitations of the acquisition equipment and analysis systems used. The variability of seismic processing between different projects has been due to the geophysicists own personal subjective preferences and interpretations. With the rapid development in computer processing power and technology, this project aims to refine the data processing of a regional data set collected in 1987 with modern methods, in a bid to better the geological understanding of the area and present it in a novel way.

The original 1987 Vibroseis seismic survey involved eight seismic lines encompassing the entire Moutere Depression in Nelson, New Zealand. The target area is an elongated, NNE trending sedimentary basin that is infilled with primarily mid-Miocene to Pleistocene sediments. The age and depositional environment is similar to that of the neighbouring, hydrocarbon bearing Taranaki Basin in the north; it was this similarity that prompted the initial study.

The data processing in this thesis was performed using the Globe Claritas™ software package with the ultimate outputs being post-stack time migration. The project followed standard seismic practices and used conventional noise reduction methods such as frequency domain (FDFILT) and frequency-offset deconvolution (FXDECON) filters. New frequency-wavenumber and deconvolution filters native to Claritas such as QFK were also tested. Despite a range of filters being trialled, only one type of migration and gain compensator was applied, these were the Finite-Difference Migration and Automatic Gain Control respectively. After processing, the data was then imported into IHS Kingdom™ to produce a 3D model of the basin. The six seismic horizons captured during interpretation were defined by their seismic facies. The upper layers were difficult to image due to ground roll and narrow frequency bandwidth sweeps. However, the lower horizons positioned between 500 ms – 2500 ms time depths were interpreted with higher confidence. The strongest reflection occurred with horizon three. The modelling showed a heavily folded and fractured formation with extensive reverse faulting and their corresponding antithetic splays, indicative of a compressive stress environment.

The seismic processing goals of the project was moderately successful. Minor improvements in noise reduction were made using a combination of post- and pre- migration noise filtering. However, due to the poor resolution in the data itself blended with a lack of borehole data in the area, it was difficult to constrain the horizons and interpret the shallow sections accurately. This was a similar issue experienced in the two previous studies of the area. Regardless, my project was able to successfully recreate a 3D interpolated model of the Moutere Depression capturing its significant geological structures such as the Ruby Bay-Moutere and Waimea-Flaxmore faults and as a result, provide a unique perspective of the basin.

## Acknowledgements

Firstly, I would like to say a special thanks to my supervisor Andrew Gorman for taking me on as his student and providing me with a project that I am obsessing over the more I progress.

Thank you to Hamish Bowman and Jasper Hoffman for helping me with IHS Kingdom and ArcGIS.

A special thanks to Kayleigh for transcribe manually the seismic data into a text file while simultaneously carrying out quality control on the raw values for her GEOL302 project, you did a marvellous job and made my life easier.

Thank you to the team at Starbucks for providing me with the necessary caffeine to make it through this process, there have been many long days and nights. I would also like to thank Will, Taki and Aleasha, who sat with me at Starbucks and took the time to help proofread my thesis. You are all such huge life savers, and arguably better than Grammarly.

Thank you to the entire Barkers family and my adopted mum Christine Hope-Lowe, Isaac Lee, Samuel Marmion, Bartholomew Lind, Nathan Soloman and especially my best friends Sarah Sarang Han and Lennox Kelway-Pope. Words cannot express my gratitude and love for you all, I would not have been able to finish this journey without you.

Thank you to my family, friends and especially my mum for all endless support and love throughout this project. I love you.



## 1.0 Introduction

---

### 1.1 Project Aim

The aim of this project is to improve the images created from the Moutere Depression Vibroseis seismic survey carried out in 1987, officially titled MD87. The seismic data spans across the Moutere Depression in Nelson, New Zealand and was collected along public and private roads giving the lines a nonlinear and highly irregular shape. The positions of such seismic lines are shown in red in Figure 1.1.

With the exponential increase in computer processing power and technology since the 1980s, this project aims to take advantage of the available resources to enhance the seismic imaging and identify characteristics that were previously missed. As a result of this data reprocessing, the goal is to ultimately achieve a better understanding of the geological structure of the Moutere Depression.

Although the seismic data is two dimensional in character, by using Globe Claritas and IHS Kingdom software packages, the data can be interpolated and evaluated in three dimensions. These programs will allow a more detailed and intricate analysis of the underlying geology of the basin. The novelty of this project is the three-dimensional perspective it is able to provide, the technique of which was still in its infancy and considered very costly back in the 1980s. The following chapters will elaborate further on essential seismic theory, locality information and processing modules needed to meet the objectives.

---

---

## 1.2 Geological Background

---

### 1.2.1 Moutere Depression

The Moutere Depression is a basin that underlies the region southwest of the city of Nelson, located on the northern tip of the South Island, New Zealand. The north-northeast stretching basin dips to the east and is made up of sedimentary sequences ranging from Paleogene to Quaternary in age (Rainey & Waghorn, 1989). It stretches approximately 25 km wide and is bound between the Richmond Range in the east and the Arthur Range to the west and reaches elevations of roughly 600 m inland to sea-level in Tasman Bay (Walrond, 2010).

The sedimentary basin is, on average, 1 km thick and based on previous borehole data collected in the Richmond Ranges to the East, can reach depths of up to 2.5 km (Lihou, 1992). The depression was formed during the uplift and faulting of the Tasman mountains (Lihou, 1992). Together with many rivers and tributaries such as the Waimea and Motueka, flowing from the Spenser Mountains that began approximately 0.5 to 2.8 Ma, this fluvial movement created the recognisable hilly topography (Stewart et al, 2004).

The Moutere Depression is the southernmost on-land extent of the hydrocarbon bearing Taranaki Basin, thus prompting early seismic surveys by the oil and gas industry. Small seams of coal can be found in both sides of the basin (Rattenbury et al, 1998). The basin separates two varying geologies in the west and in the east while overlying the Median Tectonic Zone (Rattenbury et al, 1998).

---

### 1.2.2 Moutere Gravels & Glen Hope Formation

The two Neogene sedimentary packages, the Moutere Gravels and Glenhope Formation which are both part of the Tadmor Group, can reach up to 300 m thick and overlie the older carbonaceous sedimentary Westhaven Group (Rainey & Waghorn, 1989). These deposits overlie the Median Batholith which is comprised of a mixture of Eastern and Western Province terranes depending on location. As such the basement is made up of the late

Triassic Rotoroa Complex originating in the east, which consists of altered biotite granite, granodiorite, hornblende-biotite diorite and early Cretaceous Separation Point Granitoids in the west (Rattenbury et al, 1998).

The youngest of the two formations, Moutere Gravels, is composed of deeply weathered, poorly-to-moderately sorted gravels of late Pliocene – early Pleistocene age (Basher & Jackson, 2002). These gravels cover over 10,000 ha of Nelson and has a distinctive yellow-brown colour due to the accumulation of clay (Basher & Jackson, 2002). The gravels are made up of well-rounded quartzofeldspathic clasts and clay (Shulmeister & Campbell, 2008). The clasts are derived from greywacke, while the kaolinitic clays are from deeply weathered Torlesse sandstone and semi-schist (Stewart et al, 2004). The Glenhope Formation however, is made up of granitic pebbles that are sourced from the neighbouring Median Batholith (Johnston, 1971).

---

### 1.2.3 Western Province

West Nelson is dominated by northeast trending granite and lower Palaeozoic sedimentary and metamorphic rocks. The contact between the Moutere Depression and the 115 km long granitic belt of western Nelson is defined by the Moutere Fault (McIntock, 1966). The granite in this area is massive and is the source of sand for many beaches in the surrounding coasts such as Tasman Bay and Kaiteriteri. Small seams of coal can be found along the western flank of the depression (Johnston, 1971).

---

### 1.2.4 Eastern Province

East Nelson consists of northeast trending belts of upper Palaeozoic Sedimentary, volcanic and ultramafic rocks. The NE belts include marine volcanic rocks part of the NZ geosyncline called the Brook Street Volcanics (McLintock, 1966), where Triassic sandstone and conglomerates are the youngest basement rocks found in this syncline. The Triassic sedimentary rocks are part of the Murihiku Terrane can be found exposed in the Wairoa

Gorge north of the Moutere Depression. The depression is constrained in this area by the Waimea-Flaxmore Fault System (Rattenbury et al, 1998). The Waimea-Flaxmore system extends further north off-shore connecting with the Manaia and Taranaki faults (Bull et al. 2015).

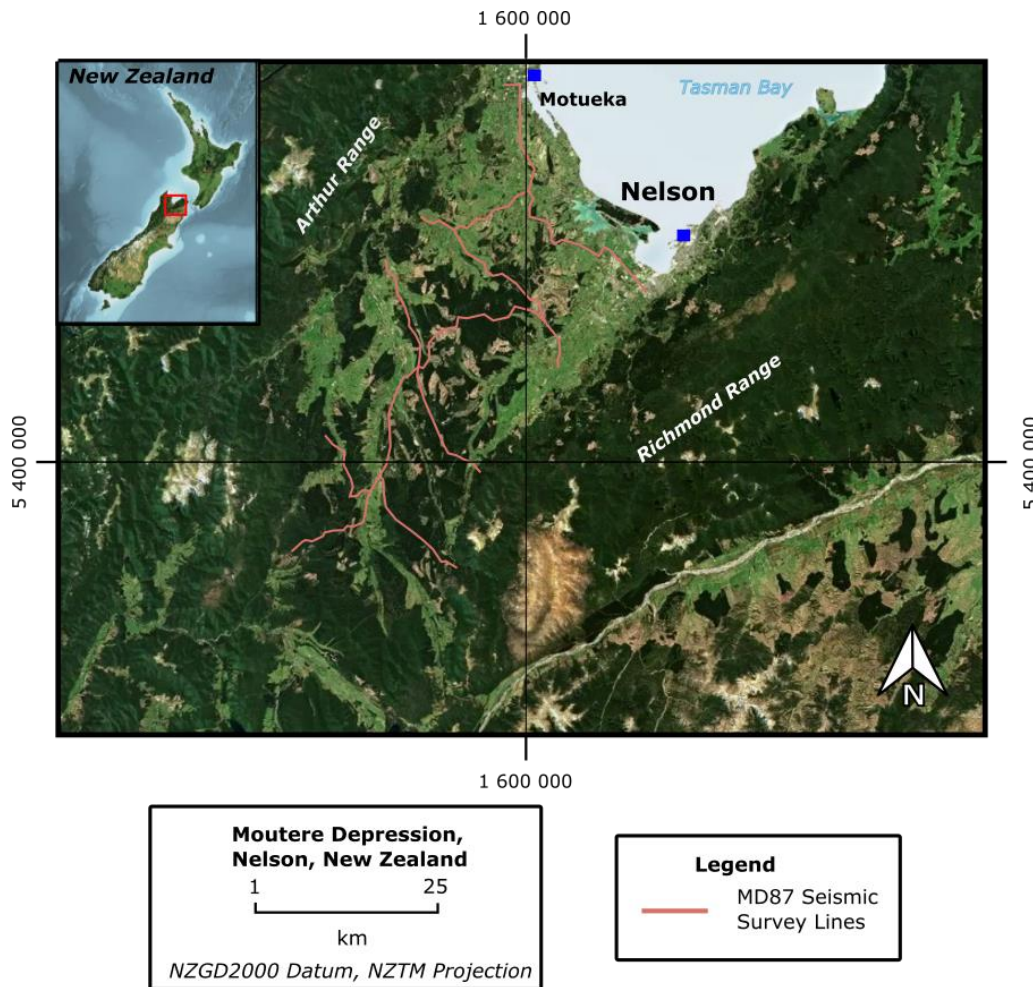
---

#### 1.2.5 South of Nelson

South of the depression, the gravel formation is overlain by the Porika Formation. The formation is the oldest Quaternary glacial deposit in New Zealand and is responsible for the herringbone topography of the Moutere Hills in the late Pleistocene (Walrond, 2010). The region is prone to landslides and erosion due to absent vegetation and poor soil which was frequent in the Late Otiran period. Evidence of such slope failures was shown by fossils that originated from higher elevations were found in scree deposits in lower altitude areas (Lihou, 1992; Shulmeister & Campbell, 2008).

A geological map of the Moutere Depression can be found in the Appendix (i).





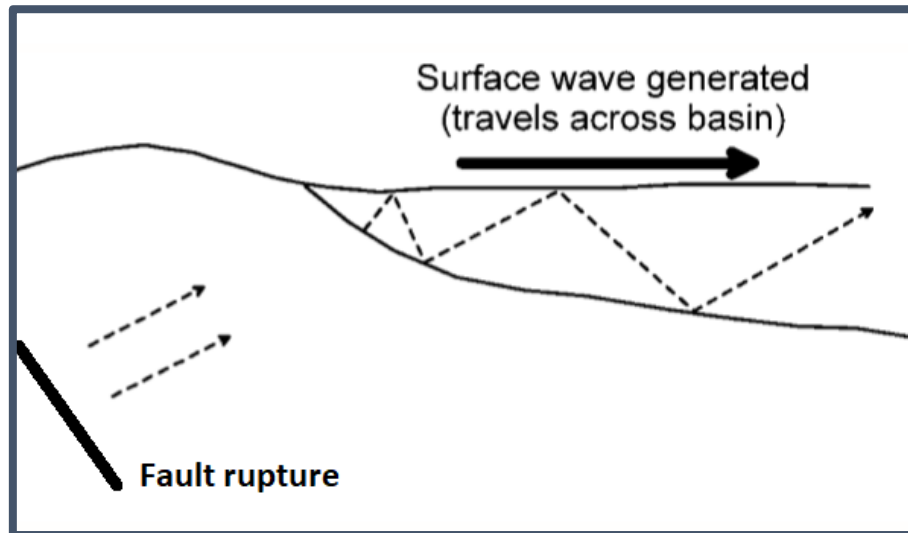
*Figure 1.1 Map showing the Moutere Depression in Nelson. The red lines are the seismic lines from the Vibroseis survey in 1987. The basin can be defined by these seismic lines.*

### 1.3 Seismic Hazard Considerations

The awareness of seismic hazard has risen substantially in the general public following the 2011 Christchurch earthquake, prompting an increase of seismic hazard analysis reports to be carried out across many regions of New Zealand. The Moutere Depression, similar to Christchurch, is also a sedimentary basin bound by many faults. Faults of significance include the Waimea-Flaxmore fault system to the east and the Moutere and Matariki faults to the west. The movement of the Alpine fault just south of the depression averages 38mm/yr (Kaiser et al. 2011).

As a sedimentary basin, the Moutere Depression will experience basin effects from earthquakes. If a rupture occurs outside the basin, the waves will enter the basin and

become trapped (Figure 1.2). These trapped waves are then reflected within the basin and amplified when they are combined with each other, forming stronger and longer earthquakes (Choi et al., 2005).



*Figure 1.2 Illustration of a rupture occurring outside the basin where the waves enter the basin. These waves become trapped if they hit the surface at critical angles. These waves are surface waves. (Adapted from Choi et al. 2005).*

Earthquake liquefaction is a major concern for many coastal areas as well as areas positioned over fluvial sedimentary layers, and the Nelson region is no exception. Due to the unique nature of the Moutere Gravels, many aquifers can be found in the Moutere Basin (Stewart et al. 2004).

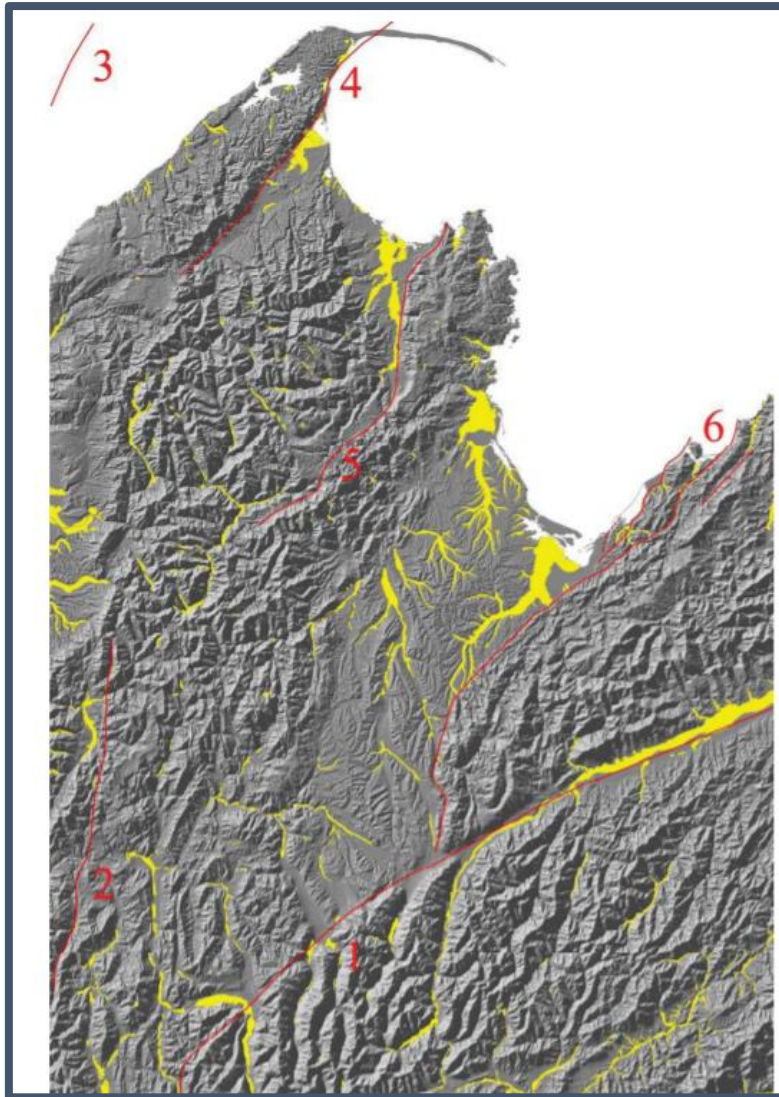
Johnston (2013) produced a preliminary assessment of the liquefaction and identified several general factors that contribute to liquefaction occurrences:

- Unconsolidated sediments.
- Water saturated soil.
- Source magnitude of greater than 7 on the Modified Mercalli Scale.

The study concluded that there are indeed potentially liquefiable sediments currently present in the Moutere Basin (Figure 1.3). The only concern Johnston has, is the unpredictability of the occurrence of an earthquake that could generate enough ground shaking required for

liquefaction. The Waimea-Flaxmore Fault system was the only fault deemed to have the strength required to induce liquefaction.

Further work on the basin would include extended analysis of the subsurface features including both known and unknown faults which would prove invaluable for seismic hazard assessment.



*Figure 1.3 A schematic map of liquefaction risk in the Tasman Region. Yellow areas are locations with liquefaction potential while grey areas are not. Red lines in are known major faults. 1) Alpine fault, 2) White Creek Fault, 3) Cape Foulwind Fault zone, 4) Wakamarama Fault, 5) Karamea-Pikikiruna Fault, 6) Waimea-Flaxmore Fault System. (After Johnston, 2013)*

---

#### 1.4 Data Processing: 1980 to Present

Seismic reflection surveys are relatively mature in terms of their scientific method. They were first developed by Maud Field in 1927 and used for geophysical exploration by the start of 1930 (Roden, 2005). However, the heavily used Common Depth Point (CDP) method was only

developed in 1955 (by Harry Mayne). For the sake of relevancy, I shall only discuss differences between the decade of seismic acquisition (the 1980s) and to present.

Focusing on the period of the 1980s where colour images had only recently been introduced, enabling colour combinations in raster and variable intensity displays. Although initially considered insignificant, development of colour images became one of the major advances of seismic interpretation (Roden, 2005). The variable colour combinations enabled distinguishing the seismic waveforms within seismic profiles. During this decade, 3D surveys were still in their infancy. Despite being highly valued, they were rarely undertaken for geophysical exploration due to their high cost. Post-stack migration during this period was common, in contrast to the 1990's where the use of pre-stack time and migration algorithms became popular and allowed better interpretations. This change was simply due to the growth in computer processing power. The pre-stack migration method is still in use today, where pre-stack time and depth migrated data are used for frequently for seismic interpretations. However, there are circumstances where pre-stack migration does not outshine post-stack migration but rather creates a noisier output. This is common in surveys that contain uneven Common Depth Point (CDP) fold distribution which limits the ability to produce accurate scaling functions for which pre-stack migration is heavily dependent on (Wu, 2001). Such uneven CDP fold distribution is prevalent throughout the MD87 seismic survey as it followed local road networks making pre-stack migration an unnecessary approach for this project.

For target areas with shallow layers such as the Moutere Depression, pre-stack migration may not be better than post-stack migration and if anything, is noisier. This is because CDP folds is distributed unevenly in shallow layers, making it difficult to produce proper scaling functions for migration.

As processing power has increased, so has the number of processing techniques. For example, presently there are different inversion programs for acoustic and elastic impedance, correlation with geostatistical parameters as well as modelling solutions such as ray tracing and Amplitude Versus Offset analysis (AVO) (Roden, 2005).

---

## 1.5 Original Seismic Data

The seismic data acquired for reprocessing is from a seismic land reflection survey carried out over a period of 30 days in June - July 1987 by Seismograph Service Ltd for Petrocorp NZ. This project was licenced by the government to further assess the hydrocarbon potential in the Nelson area, and a report of the findings was published in the Petroleum Report Series (PR1488). The processing aspect for the project was then undertaken by GECO NZ Ltd. This was the very first large scale Vibroseis seismic reflection study in the area. The field crew undertook noise analysis and comparison tests.

A standard walk-away noise analysis was performed to determine the amount of noise in the area. The result was inconclusive because there were no significant noise waves visible on the seismogram. There are two types of walkaway tests: a Fixed Receiver Walk-away (FRW) and a Fixed-Source Walk-away (FSW) test. Both types of tests are used to determine near-surface seismic phase velocities for coherent waves such as surface, shallow and direct refracted waves which may conceal low-amplitude reflections (Vincent et al, 2006). This then allows the determination of the optimum measurement parameters such as receiver spacing and sampling rate without obtaining noisy data (Knapp & Steeples, 1986). FRW tests are preferred for laterally homogeneous velocity fields with horizontal reflectors because it can provide information for lateral changes of wave properties. Meanwhile FSW provides stacking velocities and frequency content for successive waves, as they can monitor the continuous change in wavefield based off the change in source-to receiver offset and thus more suitable for dipping beds (Vincent et al, 2006). The aforementioned original survey they performed a FRW test with source positions at 300 m intervals.

The acquisition team surveyed eight seismic lines, which extended over a total of 213 km and over 8,500 shot points. The seismic reflection survey was carried out with three Vibroseis trucks. The survey primarily followed highways as well as forestry roads, explaining the haphazardness of the seismic lines on the map (Figure 1.1). The trucks were positioned in a line where at least one truck and a series of geophones were recording whilst the other one was operating to increase efficiency; this is also known as the roll-over or roll-along method. The sweep range that was generated was 16-66 Hz over 10 s but was changed to 14-64 Hz

mid-way through the project to determine if the penetration might improve. According to the survey there was no improvement.

The survey team used a Sercel SN 348 telemetry system with 120 channels and a Sercel CS 2502 correlator stacker for the seismic survey. The pressure-sensitive geophone first logged the physical movements caused by vibrations as voltages with respect to time. Subsequently, a multiplexor was used to break the recordings apart into separate variables (time and voltage). This was because the telemetry system was unable to wirelessly transmit the two measurements as one and therefore, must be transmitted as two individual data sets. The impulses were received and then the correlator stacker combined the two to reproduce the data. The vibrator truck had had its own 240 V single phase generator and a 3 Lambda 12 V power supply. The geophones used were 10 Hz SM4 digital reflection geophones, which are able to record vertical and horizontal motion. However, GECO only recorded vertical movements for their survey. The survey was conducted with a centred shot (i.e. a split spread) survey. Geophones were deployed as arrays with strings of 12 geophones evenly spaced with a group interval of 25 m centred on a shot station with 120 groups per shot. A linear array was implemented to reduce ground roll (Wiederhold, 2018). The positions of each point were surveyed, giving an Easting and Northing as well as elevation in reference to New Zealand Map Grid (NZMG) and Mean Sea Level (MSL).

As per the norm in 1987, seismic data were recorded originally in the field format SEG-B. The format is stored for digital tape storage in binary for multiple channels of one-dimensional data. SEG-B files are multiplexed data, meaning the data were simultaneously recorded from multiple channels and were able to incorporate the time of acquisition (Fortner, 2012). These were subsequently demultiplexed into single channel records for analysis (SEG-Y).

---

## 2.0 Seismic Theory

The theory of seismic waves is a broad and intricate topic. Despite its extensive nature, the current study considered it necessary to cover the topic in detail as it is central to seismic reflection surveys. Utilisation of concepts such as wave fronts and rays permit geophysicists to visualise and understand the propagation of seismic waves. Factors that determine the energy and movement of such waves when they proliferate through a medium is often restricted to the material's own elastic properties. These theories are in turn, applied to simple one-dimensional earth models to further recognize the movement of waves as they progress deeper through the subsurface.

The different types of seismic waves as well as the concepts, described in the previous paragraph will be elaborated in a concise as possible manner in the following sections of this chapter.

---

### 2.1 Seismic Waves, Wave Propagation and Simple Seismic Models

Seismic waves are generated by an impulse usually from some form of explosive source such as an earthquake or for this specific project, a Vibroseis truck (Yilmaz, 2015).

#### **Seismic Waves**

Seismic waves overall are classified as "elastic waves". "Elastic" refers to a situation where a deformed particle will return to normal once the induced stress or energy has been transferred from that particle to another (Yilmaz, 2015). While "wave" on the other hand, simply is defined as a disturbance moving through a medium (Gerken, 1989). As such, seismic waves follow the general wave theory, which allows geophysicists to apply the rudiments of optical laws. These include concepts such as frequency, wave front and wavelength that ultimately permit the examination of events such as refractions and reflections.



On a microscopic scale, seismic waves can be defined as the internal response of rocks to small elastic deformation to vibrations. These deformations are caused by the complex relationship between stress and strain in a rock where the mathematical relationship can be established based on the theory of elasticity (Keary, 2002).

The elastic movement of a particle within a seismic wave mimics that of a spring or an oscillator. As such, you can solve the velocity or energy of the particle by using simple harmonic wave equations (Lays, 1995). The equation of simple harmonic motion is:

$$x = A \sin\left(\sqrt{\frac{k}{m}} t\right)$$

where  $x$ ,  $A$ ,  $k$ ,  $m$  and  $t$  are the displacement, amplitude, elastic constant, mass and time respectively. The second derivative of such an equation with respect to time would give the velocity,  $v$ . The new equation would now be:

$$v = \omega A \cos(\omega t)$$

where  $\omega$  is the angular frequency. By viewing seismic waves as harmonic waves, computations are made easier for seismic processing further down the line. This is because the waves can be broken down into individual components such as displacement and time by using the Fourier transform/integral (Gerken, 1989).

The seismic wave equation is more complex than the simple harmonic wave equation and involves the Lamé parameters ( $\lambda$  and  $\mu$ , the elastic and shear modulus respectively). The equation for seismic motion is shown by:

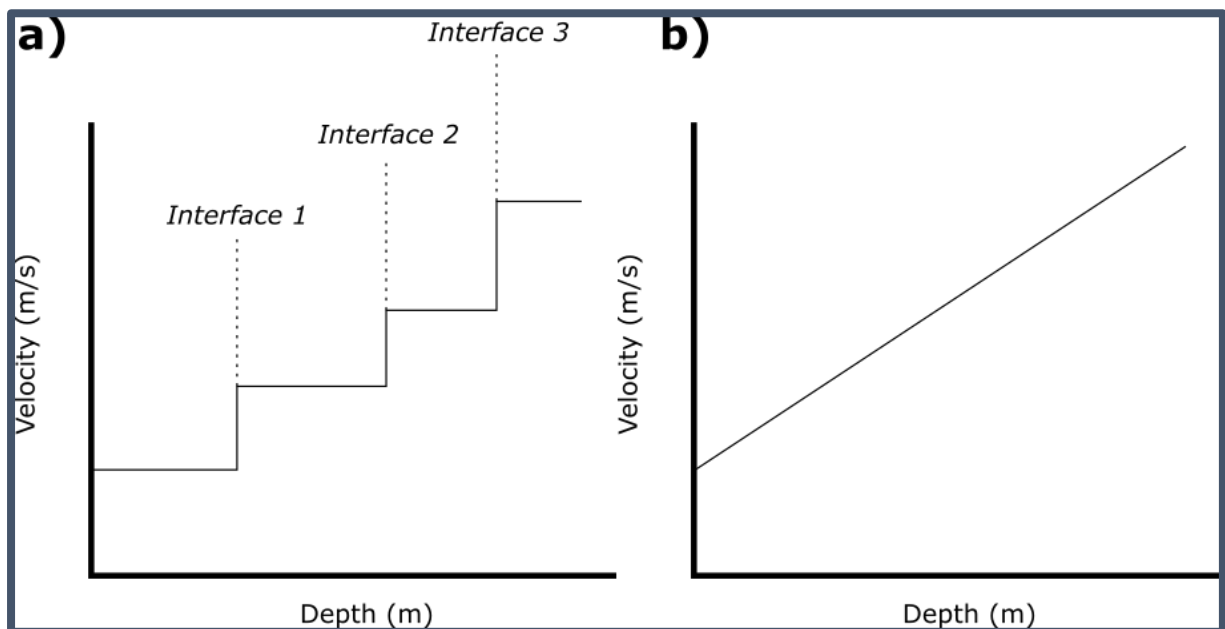
$$\rho \ddot{\mathbf{u}} = (\lambda + 2\mu) \nabla \nabla \cdot \mathbf{u} - \mu \nabla \times \nabla \times \mathbf{u}$$

with  $\mathbf{u}$  being the displacement vector and  $\ddot{\mathbf{u}}$  being acceleration.

For the sake of simplicity, many seismic models ignore some of these terms. The following sections summarises the two most frequently used approaches.

### Approach 1

The first approach revolves around the variability of velocity with depth. In this scenario the supposed medium is composed of a series of homogenous layers. Because the layers are homogenous and the Lamé parameters describe the amount of change within a layer, the Lamé parameters will go to zero. The overall model will ultimately produce a “staircase shaped model” where the only change in velocity that occurs will be at the interface between each layer. As the number of layers increase, the gradient will smooth out and converge, producing a single line. This is the most simplistic approach and is used in one dimensional earth models (Yilmaz, 2015)



*Figure 2.1 A graphic illustration of the “staircase model”. Figure a) shows that for this model, the only change in velocity at depth occurs at the interfaces between layers. In this particular figure, there are only four different layers. When the number of layers increase, sudden changes in velocity become more subtle. The overall graph smooths out, illustrating a seemingly linear relationship between velocity and depth as shown in Figure b). This model does not assume other factors such as compaction that would influence velocity increase.*

## Approach 2

The second approach utilises the relationship between the gradient and time, such that time is inversely proportional to the angular frequency of the wave since

$$t = \frac{1}{2\pi f}$$

As such, based on the equation above for high-frequency waves, the gradient will approach zero. This method falls under the ray-theoretical method. Both methods are used for homogenous media and for linear, isotropic earth models. These approximation methods also neglect gradients induced by gravity and velocity.

The maximum deviation of the wave, known as the amplitude of the wave, is calculated by a series of equations where the wave spreads out from the point source (Gerken, 1989). The amplitude can also be defined as the maximum displacement the particle moves during wave propagation (Burger, 1996). Based on the dispersion of energy, as the wave disperses away from the source the amplitude would decrease as well, since elastic energy transferred from particle to particle will be lost and converted to other forms such as heat and sound. For spherical waves, the generalised wave function is:

$$\frac{1}{r} f(r - Vt)$$

where  $r$ ,  $V$ , and  $t$ , are the distance from the source, velocity and travel time, respectively. The phase of the wave is represented by the function  $f(r - Vt)$  and shows the amount of “disturbances” that occurs at that point. The function generally will never equal zero due to a multitude of reasons including the real inelastic effects of the medium (Yilmaz, 2015).

## Wave fronts and Rays

Although difficult to visualise, a wave front can be viewed as a plane, or surface. The plane of a seismic wave front is the instantaneous point where all the points of the plane are in phase and have the same amplitude (Gerken, 1989).

Another notion that is used frequently in seismology and unison with wave fronts is the idea of rays. Rays are part of a mathematical concept that is normal to the wave front and aids geophysicists with visualising the movement of seismic waves in the subsurface. In homogeneous media, these rays are depicted as straight while in inhomogeneous media they are curved (Parasinis, 1996).

The speed of which the wave front travel is dependent on the elastic properties of the medium. Refraction and reflection occur when the travelling wave encounters a change in elastic moduli (Gerken, 1989), this generally happens at the interface between two different rocks.

## 2.2 Attenuation

Briefly mentioned previously, the amplitude of a wave decreases with the distance travelled. The three main factors that influence this are: spherical divergence, partial transmission and reflection, and attenuation of energy (Parasinis, 1997)

### Spherical Divergence

Spherical divergence, also known as geometrical spreading, is simply the inverse proportionality relation of amplitude with distance ( $r$ ) and is represented by the equation:

$$Q \propto 1/r^2$$

where  $Q$  and  $r$  are energy and the radius, respectively. The equation describes that the greater the distance travelled, the smaller the amplitude of the propagating wave will become. The total energy of the wave, however, is not lost but rather dispersed over a larger area.

Dispersion of a seismic wave is defined as the alteration of a seismic pulse due to the relation of phase velocity,  $V$  and wavelength,  $\lambda$ . This pulse is a combination of superimposed sinusoidal waves, where each wave they will possess different wavelengths and frequencies. The velocity at which the pulse travels is called the group velocity,  $U$ . The relationship between  $V$  and  $U$  is given by the equation (Parasinis, 1996)

$$U = V - \lambda \frac{dV}{d\lambda},$$

and

$$V = \frac{\omega}{\lambda}, \quad \omega \text{ is the angular frequency}$$

Initially at the time of the event, all the waves are superimposed, and it is difficult to distinguish the difference between velocities. As time progresses, the harmonic waves end up separating where phase and group velocity become easier to see due to energy attenuation.

### **Partial Transmission and Reflection**

Partial transmission and reflection is when a seismic wave progresses through media of differing bulk densities and velocities, a portion of the amplitude is partitioned. Segments of the wave would be reflected and some of would be transmitted. This reduction of amplitude continues to occur on the receiving end of the journey as the reflected wave comes back to the surface. These concepts will be further in Section 2.10.

### **Attenuation of Energy**

The attenuation of energy is a large factor for the decrease amplitude of a wave. It differs from spherical divergence in the fact that it is energy loss rather than energy dispersion (Parasinis, 1997).

The dissipation of strain energy (which is the opposing energy to stress) causes the overall energy loss when the wave passes through an anelastic medium (Mashinskii, 2008). Where anelasticity is defined as the property where there is no relation between stress and strain.

Through practical observation and using the equation of a damped harmonic oscillator, the following equation describes the average wave attenuation through the Earth:

$$A(x) = A_0 \exp\left(-\frac{f \pi x}{Qv}\right)$$

Variables  $A$ ,  $F$ ,  $x$ ,  $Q$  and  $v$  are the amplitude, frequency, displacement, attenuation parameter and phase velocity, respectively. Where  $Q$  for the earth is generally  $\pi/\delta$  and  $\delta$  is the logarithmic decrement approximately 0.02 (Parasinis, 1997) and can be viewed as the amount of energy loss per cycle. Based on the above equations, the increase frequency also increases the degree of amplitude attenuation. In other words, this means that higher frequency waves would not penetrate as deeply as low frequency waves because it loses energy at a faster rate.

The loss of energy,  $Q$ , can be further subdivided into intrinsic attenuation and multiple scattering. Intrinsic attenuation, also known as absorption (Shapiro et al. 1993), is the irreversible exchange of potential and kinetic energy of particles. This trade of energy converts potential energy into heat from processes such as shearing at grain boundaries and anelastic losses from fluid movement (Dvorkin et al 1993). This means  $Q$  values would be generally higher for P-waves than S-waves since S-waves are unable to travel through liquid.

Multiple scattering in a way mimics intrinsic attenuation (Reine et al. 2009). The energy reduction of multiple scattering is caused by the dispersion of a wave into different phases due to changes in the physical environmental that occur at areas such as medium interfaces. This form of attenuation is dependent on the degree of variation between rock parameters. Such small-scale heterogeneities in energy were first investigated by Aki and Chouet in 1975, where they loosely defined it as an incoherent signal in a medium that varies not only with depth and but also with the medium's extremely variable heterogeneity. In practice, scattering attenuation is calculated through an ensemble of statistical analysis assuming the medium is ergodic. Depending on what type of wave function and statistical analysis is used, this form of attenuation would have varying final estimates (Shapiro et al 1993).

---

## 2.3 Elastic deformation

Despite seismic waves being deemed as “elastic waves”, seismology classifies wave propagation into two classes: acoustic and elastic. Both classes are still based on the theory of elasticity but used in various areas in geology.

Acoustic wave propagation is a theory that is applied in geophysical exploration because it simplifies data processing algorithms (Parasinis, 1996). This theory provides good approximations where it assumes that P-waves are the dominant wave within the medium and its shear effects are negligible. However, out of the two, elastic wave propagation is a more pragmatic approach. This type of motion includes rocks with a non-zero shear strength and shear waves (Nazarchuk et al. 2017).

When waves propagate through a rock, they induce deformation that can then be further categorised into elastic or inelastic. The amount of distortion that a medium undergoes is dictated by its following three variables: the bulk modulus, Poisson’s ratio, and shear modulus (Gerken, 1989). These values will be further explained in Section 2.4.

Elastic deformation, as previously defined, is the alteration of the shape or volume of a medium due to an applied force. When this force is removed, the subject returns to its original form. If the applied force exceeds a certain value however, permanent warping will occur. This specific value is known as the elastic limit of a material and is defined by Hooke’s Law (Gerken, 1989). This law is a constitutive law that is generally expressed as

$$F \propto x$$

where  $F$  is the applied force and  $x$  is the displacement. Hooke’s Law essentially states that the stress applied to a material is proportional to its strain. This law is not 100% true for many materials but generally is applicable for most geological situations (Parasinis, 1999).

The degree of deformation that a rock undergoes can then be further characterized by its vector fields  $\mathbf{u}$ . Within geophysics, mathematical operators like divergence and curl, are used to describe and assess such fields. The divergence describes the amount in which the vectors vary from one another while the curl describes the degree in which the vectors are rotating or “twisting” (Taylor, 2004; Schroeder, 1999). A positive divergence value illustrates an

environment which the vectors spread out from each other while a negative value demonstrates a vector field that converges into one source (Taylor, 2004; Schroeder, 1999). The divergence and curl are defined by the dirac delta function as shown below:

$$\textit{Divergence} = \nabla \cdot \mathbf{u}$$

$$\textit{Curl} = \nabla \times \mathbf{u}$$

## 2.4 Elastic Constants

The principles of seismic methods rely on the theory of elasticity. The variables mentioned previously (e.g. elastic modulus) specifically describe a materials relationship with stress and strain.

### Stress

Stress is defined as the force applied to the area of a material and thus, the unit of measurement would be N/m<sup>2</sup> or equivalently Pa. There are two type of stress, compressive (normal) stress and shear stress. Compressive stress is when the stress applied acts normal to the target area while shear stress acts parallel. Similar to shear waves and compressive waves, the same rules apply to these stresses. Compressive waves change the volume of the material while a shear wave maintains the same volume but distorts the shape (Parasnis, 1997). Strain on the other hand, is the opposite of stress. The strain that acts on a body is known as a restorative force opposing the corresponding stress.

First, considering P-waves (compressive waves), the velocity of a material is dependent on the stiffness of the rock. This can be constrained by the longitudinal modulus, bulk modulus and the shear modulus. The moduli can be represented by the following equations:

*Longitudinal Modulus:*

$$\psi = \frac{\textit{Longitudinal stress}}{\textit{Longitudinal strain}}$$



$\psi$  is used to describe the stiffness of the rock. The modulus expresses the necessary force per unit area required to stretch the material a certain unit distance. Longitudinal modulus is also known as the axial modulus in the case where the material is deformed uniaxially.

*Bulk modulus:*

$$K = \frac{\text{Volume stress, } P}{\text{Volume strain, } \Delta V/V}$$

*Shear modulus:*

$$\mu = \frac{\text{shear stress, } \sigma}{\text{shear strain, } \tan\theta}$$

The bulk and shear modulus are required for general calculations because the deformation that occurs when the wave propagates through the medium involves both compressing and shearing components.

It is inferred that the larger the longitudinal modulus, the greater the velocity through the medium, as shown by the equation:

$$v = \sqrt{\frac{\psi}{\rho}}$$

where  $\rho$  is the density of the medium.

The three moduli have a relation:

$$\psi = K + 4/3 \mu$$

Combining the relationship between all the moduli, the P-wave velocity through a material would then be expressed as:

$$v_p = \left[ \frac{K + 4/3 \mu}{\rho} \right]^{1/2}$$

While S-wave velocity,  $V_s$  can be represented as:

$$v_s = \left[ \frac{\mu}{\rho} \right]^{1/2}$$

The three main moduli that directly affect the elasticity of medium are the Bulk, Shear, and Young's moduli. These three moduli are often represented by a 3x3 strain and stress matrix where the nine stress components fully define the state of stress of the medium (Lowrie, 2007).

$$\begin{bmatrix} \sigma_{xx} & \sigma_{xy} & \sigma_{xz} \\ \sigma_{yx} & \sigma_{yy} & \sigma_{yz} \\ \sigma_{zx} & \sigma_{zy} & \sigma_{zz} \end{bmatrix}$$

The normal stress value  $\sigma_{xx}$  represents the normal force acting on the x-axis of the area  $A_x$ , while  $\sigma_{yx}$  and  $\sigma_{zx}$  represents components of the force acting along the y- and z-axis on area  $A_x$ , these stresses are shear stresses. If this matrix was symmetrical, the shear stresses would equal one another, resulting in no rotation of the body (Lowrie, 2007). Longitudinal and shear strains are can also be represented by such a matrix

$$\begin{bmatrix} \epsilon_{xx} & \epsilon_{xy} & \epsilon_{xz} \\ \epsilon_{yx} & \epsilon_{yy} & \epsilon_{yz} \\ \epsilon_{zx} & \epsilon_{zy} & \epsilon_{zz} \end{bmatrix}$$

Longitudinal strain is represented by  $\epsilon_{xx}$ ,  $\epsilon_{yy}$  and  $\epsilon_{zz}$  and the rest represent the shear strain. Each longitudinal strain value for the x-axis is  $\epsilon_{xx} = du/dx$  where  $u$  is some displacement value. The first order derivative on the x-axis represents the infinitesimally small change in length of  $u$  with each change of  $x$ . Different values are assigned to different axis strains, for example  $\epsilon_{yy}$  would have some value  $w$  on their corresponding axis since  $u$  is used for  $\epsilon_{xx}$ . Although it may be easy to think strain values are independent of each other when in actuality they are not. For example, when the body in question gets stretched along the x-axis, it will consequently become thinner along the y-axis and z-axis (Lowrie, 2007). So

$$\epsilon_{yy} = \epsilon_{zz} = -\nu\epsilon_{xx}$$

where the constant of proportionality ( $\nu$ ) is known as the Poisson Ratio. The Zoeppritz equations, which will be discussed later, are also dependent on the Poisson ratio of material. Where the ratio is defined as:

$$\nu = \frac{\text{Lateral strain}}{\text{Longitudinal strain}} = -\frac{\Delta y/y}{\Delta x/x} = -\frac{\epsilon_{yy}}{\epsilon_{xx}}$$

Essentially, the ratio expresses the material's resistance to deformation. Most natural materials have a positive Poisson ratio, with some exceptions such as cork. The Poisson ratio, named after the French Mathematician Simeon Poisson, expresses the compressibility of material perpendicular to the applied stress and varies with mineral composition and fluid content (Bagaini et al, 2012). For hard rocks such as granite  $\nu$  is about 0.45, while for soft sediments it is about 0.05 (Lowrie, 2007). The equation that relates the Poisson's ratio to Bulk modulus and Young's modulus is shown:

$$K = \frac{E}{3(1 - 2\nu)}$$

Bulk modulus ( $K$ ), also known as the incompressibility of a medium, is reflective of the materials resistance to volume change. This provides a ratio of hydrostatic pressure to the induced compression (Lowrie, 2007) and is measured in the SI unit in Pa. The higher this value is the more readily the wave will be transmitted through.

The Young's modulus ( $E$ ) describes the longitudinal strain when a uniaxial normal stress is applied to a material (Lowrie, 2007). The longitudinal strain components are proportional their relevant stress components shown by the equation below.

$$\sigma_{xx} = E \varepsilon_{xx}, \sigma_{yy} = E \varepsilon_{yy}, \sigma_{zz} = E \varepsilon_{zz}$$

Young's modulus is used to describe the amount of stress required for a certain amount of deformation for the material. It is frequently used for boreholes in hydrocarbon projects where the modulus of a medium directly effects its closure stress (Rajput et al, 2016). Where the closure stress of a rock is the amount pressure required to cause fracturing (Crain et al, 2002). The higher the closure stress, the more force needed to break a rock. So, anisotropic rocks such as poorly consolidated clay, would have a higher closure stress (Rajput et al, 2016).

The Shear modulus ( $\mu$ ) of a material is the property which describes the materials resistance to shearing deformation. Often called the rigidity modulus of a material, it illustrates the ratio of shear stress to shear strain (Lowrie, 2007) shown by

$$\mu = \frac{\sigma}{\varepsilon} = \frac{\text{Force}}{\text{Area} \times \theta}$$

where stress ( $\sigma$ ) is an applied force that is not directly measurable but can be calculated from different formulas for loading, whereas  $\Theta$  is the displacement angle. The strain ( $\varepsilon$ ) value of the above equation, is the ratio of length change to original length which can also be defined as:

$$\varepsilon = \frac{\Delta L}{L_0}$$

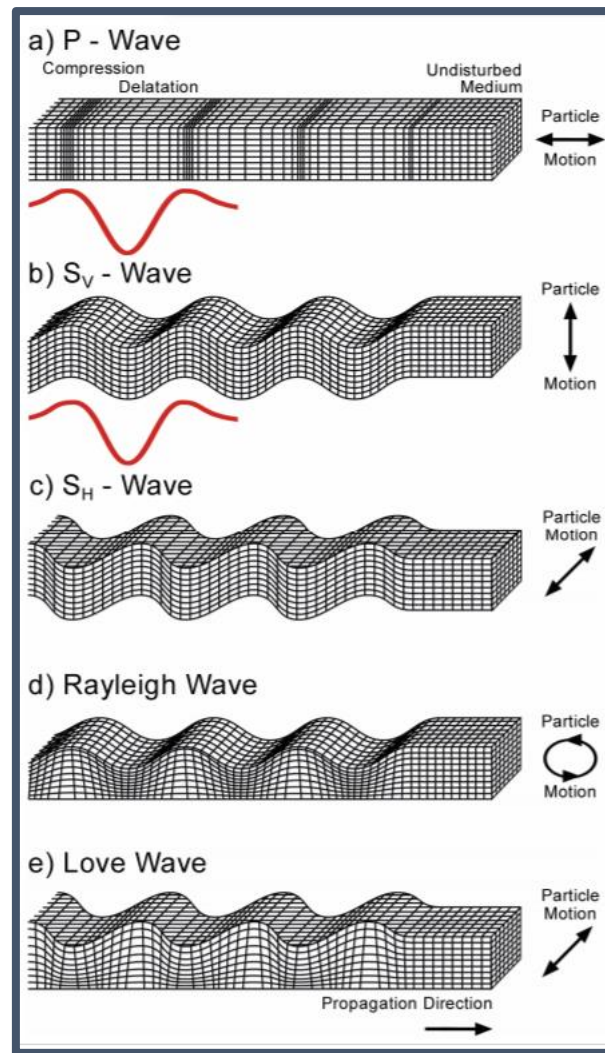
If the modulus of the material is high, this means that it is resistant to shearing and will hence transmit shear energy readily (Rajput et al, 2016). Although it should be noted, however, that the amount shear in a medium is generally lower in lab measurements than real-life seismic measurements since they are made under low-strain conditions (Rajput et al. 2016). The relation of the modulus and shear wave velocity and density is expressed as:

$$\mu = \rho V_s^2$$

## 2.5 Body waves

In physics, waves are grouped into standing and progressive waves. Standing seismic waves occur in strong earthquakes and refer to the vibrations of the Earth as a whole. Meanwhile, progressive waves are defined as waves that travel away from the source (Novotney, 1999), meaning that they are the only waves applicable to seismic surveys. These progressive seismic waves, however, can be broken down further into two types of waves, compressional waves (P-waves) and shear waves (S-waves) (Yilmaz, 2015). Compressional waves involve volume change while shear waves only involve shear deformation.

The majority of the energy of a seismic wave is transmitted as a body wave, the rest of the energy is released on the surface as surface waves (Lowrie, 2007). As a result, body waves have the property of being non-dispersive, this means that the velocities at which they travel are independent of the frequencies of the wave. The velocities are only influenced by the elastic constants and densities of the medium (Kearey et al 2004).



*Figure 2.2 An illustration showing the propagation direction and overall particle movement of a surface wave and body wave (after Steeples, 2005).*

### 2.5.1 P-waves

As the primary wave, the P-wave is the fastest elastic wave from the seismic source. It is a longitudinal, compressional body wave whose velocity through a material is given by the equation:

$$v_p = \left[ \frac{K + 4/3 \mu}{\rho} \right]^{1/2}$$

where  $\rho$  is the density of the material. This longitudinal wave is able to travel through gases and liquids as well. There is no shear component for these fluid states so the P-wave velocity in these media then becomes:

$$v_p = \left[ \frac{K}{\rho} \right]^{1/2}$$

The P-wave represents a series of dilatations and compressions, where the movement is rather one dimensional and occurs in only one direction. i.e. the x-direction. Dilatation,  $\theta$ , is known as the fractional change of the volume when its surface area is reduced zero (Lowrie, 2007). Such a change from displacement is the sum of the shear stress:

$$\theta = \varepsilon_{xx} + \varepsilon_{yy} + \varepsilon_{zz}$$

### 2.5.2 S-waves

Shear waves are a secondary wave that arrive after P-waves on a seismogram. Its transverse motion is due to the particles moving perpendicular to the direction of the wave propagation (Parasnis, 1997). The velocity of the S-wave is given by the equation.

$$V_s = (\mu/\rho)^{1/2}$$

When transverse waves propagate long distances, they become plane polarised where the particles oscillate in a manner that is normal to the direction of wave propagation. When the motion of the particle is solely on the vertical plane, they are called SV (Shear Vertical) waves and intuitively if the motion is solely on the horizontal plane they are called SH (Shear Horizontal) waves (Gerken, 1989, Sheriff, 2004). These polarised waves are usually attenuated more rapidly than P-waves (Ricker, 1976).

Unlike P-waves, S-waves cannot travel through liquids and gases since these media have no shear strength. Despite this, shear wave velocities are still valuable and are often used to provide information on sediments and other media. This is because they are independent of the bulk modulus and therefore more sensitive to lithological variations and less so by fluid content (Ayres & Theilen 1999).

Historically, S-waves are not commonly utilised in seismic surveying because the geophones in the past were only sensitive to one direction of motion.

---

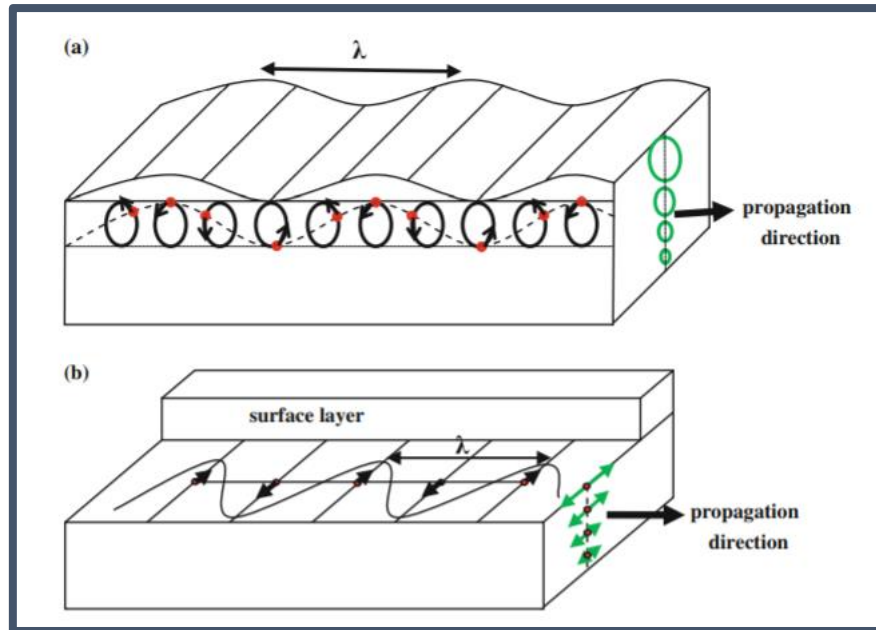
## 2.6 Surface Waves

Surface waves, a form of category of guided waves, occur in a medium that has a free surface. A free surface is defined as the surface of a medium that is subject to zero shear stress. These waves have a significantly lower frequency than that of body waves, with a frequency of less than 15 Hz (Parasinis, 1997), this makes these waves easily identifiable on a seismogram. Common surface waves include Rayleigh waves, Stonely waves, Scholte waves and Love waves.

In Rayleigh waves, commonly known as ground roll, the particles move in an elliptical manner in the vertical plane along the direction of wave propagation (Figure 2.3). Near the surface, with reference to the wave direction, the particles' movement is retrograde (Parasinis, 1997) meaning the rotational movement of the particle is in the opposite direction to the wave. The elliptical motion is caused by the coupling of P-waves and SV-waves that are trapped within the surface layer. Rayleigh waves are slightly slower than shear waves, with a velocity of approximately  $0.9 V_s$  (Parasinis, 1997).

Similar to Rayleigh waves, which occur at the solid-air interface, are Stonely waves and Scholte waves. These waves are surface waves as well but occur on solid-solid and solid-liquid interfaces, respectively (Kugler et al 2006). Both of these waves are slower than Rayleigh waves for shorter wavelengths but become almost synchronous once the wavelengths are increased. The significance of these waves is that by combining their velocities it is possible to calculate the Poisson ratio of the interface. This can therefore provide an insight to the porosity of the material at such a location (Gaiser, 1996).

The final type of surface wave is the Love wave. This type of wave is the fastest surface wave and its movement is purely in the horizontal plane parallel to the surface, moving side to side like a snake. Love waves are essentially horizontally polarised shear waves, whereas for short wavelengths in the upper layer and long wavelengths in substrata, the Love wave velocities are equal to  $V_s$  (Parasinis, 1996).



*Figure 2.3 An illustration showing the surface waves a) Rayleigh waves, b) Love waves. Note how for both waves the degree of motion decreases with depth (after Al-Sadi 2017).*

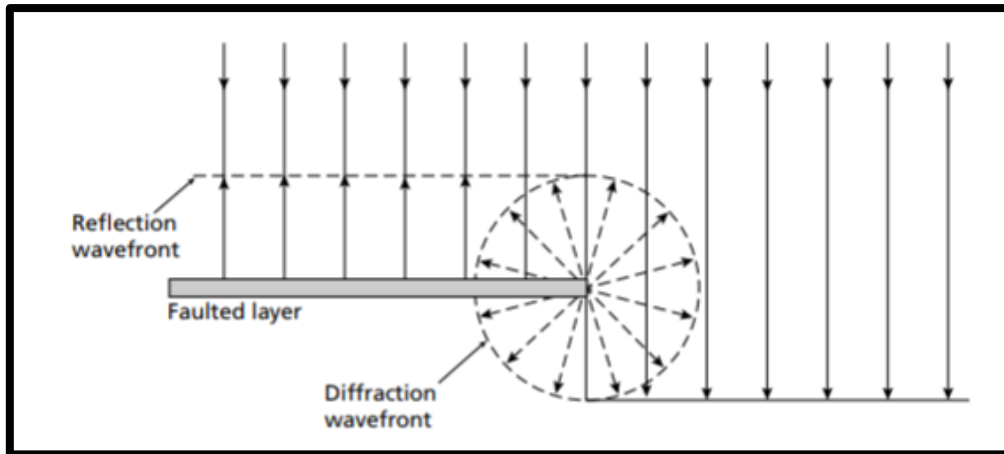
---

## 2.7 Huygen's principle

Huygen's Principle, based on the work of Dutch physicist Christiaan Huygens in 1678, is a model that was initially used to describe the movement of electromagnetic waves (light). The principle states that each point on a wave front acts as a source of secondary wavelets that disperses from that point (Parasinis, 1996). Combined with Fresnel's principle of interference, it explains the constructive and destructive addition of secondary sources when their respective wavelets coincide with each other. The envelope that forms from these secondary sources represent the wave front at some point later in time.

This principle applies to seismic waves and helps to explain the effects of diffraction, where the wave hits the end of the surface such as faults and the signal radiates outwards. This divides up the seismic waves and their energy to further smaller wavelets.





*Figure 2.4 Illustration showing Huygen's principle. Where each point on the surface acts as a secondary source. When the wave hits a break, or end of a surface it diffracts radially (after Keary et al, 2002).*

---

## 2.8 Snell's Law

When a wave travels through one medium to another, it generally either refracts or reflects. Snell's Law describes the degree of refraction and reflection that occurs. Also known as the law of refraction, it was named after Dutch mathematician Willebroed Snell in 1621. Although this law was developed to explain the movement of light, it is also applicable to seismic waves.

When seismic rays hit an interface of two differing media, they will either be refracted or reflected. The amount of refraction that occurs is dependent on the refractive index of the specific media. The basic equation of Snell's Law is given by:

$$n_1 \sin \phi_1 = n_2 \sin \phi_2$$

where  $n_1$  and  $n_2$  are the refractive index of the respective media. In general, these waves are reflected at the same angle as the angle of incidence since the wave will remain within the same medium with the same refractive index.

When a seismic ray travels from one medium to another where the first medium has a significantly larger refractive index, the ray gets trapped within the first medium; this is called total internal reflection. The critical angle is the first angle at which the total internal

reflection occurs. Another way to explain this is that the critical angle is the angle of incidence that causes the secondary reflected angle to be  $90^\circ$ . When the ray is travelling along the boundary between two mediums, it will travel at a velocity faster than that of the seismic velocity of the upper layer. This causes a shockwave throughout the projection of the wave along the interface. These perturbations are called head waves and subsequently pass through the upper layer up to the surface at the critical angle (Keary, 2002).

At the boundary between two mediums, mode conversion can occur, and the incident P-wave gets converted into four waves: reflected P-wave, reflected S-wave, refracted P-wave and refracted S-wave. Despite these additional classifications, the waves still follow the velocity ratios and bulk modulus of their respective media. The relationship between the waves can be shown by the equation:

$$\frac{\sin\theta_{ip}}{V_{p1}} = \frac{\sin\theta_p}{V_{p1}} = \frac{\sin\alpha_p}{V_{p2}} = \frac{\sin\theta_s}{V_{s1}} = \frac{\sin\alpha_s}{V_{s2}} = p$$

where  $p$  is a ray parameter. The ray parameter is defined as the reciprocal of the apparent velocity and is used to specify a ray path (Sheriff, 2004).

It is useful to note that a  $0^\circ$  incidence P-wave does not produce an S-wave while a  $0^\circ$  incidence S-wave will produce a P-wave (Parasinis, 1996).

Snell's Law can be derived from another law known as the Fermat's Principle. This is another optics law involving second order derivative trigonometric functions that describes how light travels the path of least time,

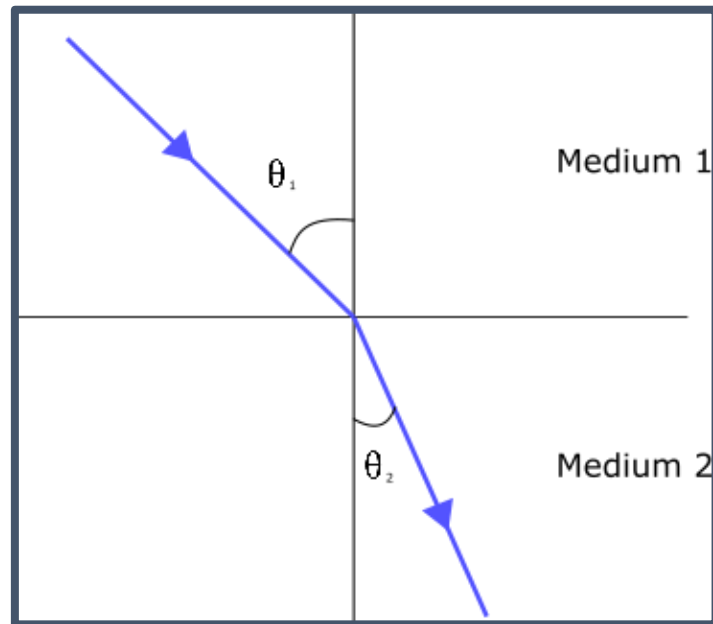
$$t = \frac{\sqrt{x^2 + h_1^2}}{v_1} + \frac{\sqrt{(d-x)^2 + h_2^2}}{v_2}$$

where  $t$  is time,  $d$  is the combined thickness of the two mediums,  $x$  is the thickness of medium 1,  $h_1$  and  $h_2$  are the horizontal positions of the entry and exit points of the ray paths respectively, while  $v_1$  and  $v_2$  are the respective velocities in the two media.

To find the absolute minimum values, the derivative of the above equation is set to zero which eventually shapes into Snell's Law,

$$\frac{dt}{dx} = \frac{x}{v_1\sqrt{x^2 + h_1^2}} - \frac{(d-x)}{v_2\sqrt{(d-x)^2 + h_2^2}} = 0$$

$$= \frac{\sin\theta_1}{v_1} = \frac{\sin\theta_2}{v_2}$$



*Figure 2.5 The above illustration shows the effect of Snell's Law graphically. The difference in impedance causes the incoming wave to refract. For this example, the steeper angle of the outgoing wave suggests that Medium 2 has a lower acoustic impedance.*

## 2.9 Zoeppritz Equations

Zoeppritz equations have become a vital part of reflection seismology. These equations created by German seismologist Karl Bernhard Zoeppritz (1881 - 1908) are used to describe the behaviour of seismic waves at the interface of two media (Shuey, 1995). In such cases, an incident P-wave on an interface will produce four subsequent waves: reflected S-waves, reflected P-waves, transmitted P-waves and transmitted S-waves. It determines how energy is partitioned or divided between the resultant waves. These equations have become very useful in assessing the variability of reflections with offset or incidence angle, which in turn can be used to assess particular lithologies or pore fluid characteristics within a layer rock unit.

## 2.10 Partition coefficients

The strength of a reflection is dependent on the angle of incidence as well as the acoustic impedance (Shuey, 1995). Acoustic impedance is the product of the bulk density ( $\rho$ ) of the medium and the P-wave velocity. Where velocity is dependent on the medium's fluid and rock properties. The acoustic impedance is represented by the following equation:

$$Z = \rho \times V_p$$

It should be noted that the greater the contrast of impedance between two materials the greater the seismic reflection amplitude. The equation for the reflectivity ( $R$ ) between two media is determined by the fraction:

$$R = \frac{Z_2 - Z_1}{Z_2 + Z_1} = \frac{I_2}{I_1}$$

where  $I_1, I_2$  is the intensities of rays and  $Z_1, Z_2$  are the acoustic impedance of the primary and secondary layers, respectively. The remaining value that was not reflected would be the amount proportion of energy that was successfully transmitted into the second medium. As such, the displacement amplitude of the transmitted wave can be shown by:

$$T = 1 - R = \frac{I_2 + I_1}{I_2 + I_1} - \frac{I_2 - I_1}{I_2 + I_1} = \frac{2 I_1}{I_2 + I_1}$$

The variables  $T$  and  $R$  are known as the transmission and reflection coefficients. These variables are dependent on other factors and rock properties such as porosity, incident angle, fluid content, and degree of lithification (Parisinis, 1996, Zoeppritz, 1919).

As an example, in sedimentary beds, the velocity of a seismic wave travelling through a layered system generally increases with depth due to compaction. This causes the acoustic impedance of various media to become similar to one another. This ultimately results in a lower  $R$  coefficient, meaning that the media boundaries become less reflective with depth. Reduction of the displacement amplitude will occur as well and is inevitable, especially in addition with other attenuation factors such as geometrical divergence and absorption (Parisinis, 1996).

## 3.0 Seismic Method

The two main forms of data procurement in seismology are based around the seismic refraction and reflection method. Both methods can be applied to a single seismic source since reflections and refractions will occur in a regular solid-state medium. This chapter focuses on the seismic reflection method since this was the technique used for the 1987 Moutere Depression project. The Vibroseis seismic source employed by Petrocorp NZ was the first of its kind in the Nelson area, its working principles will be touched upon together with the Fourier transform and its essential role in geophysical data processing.

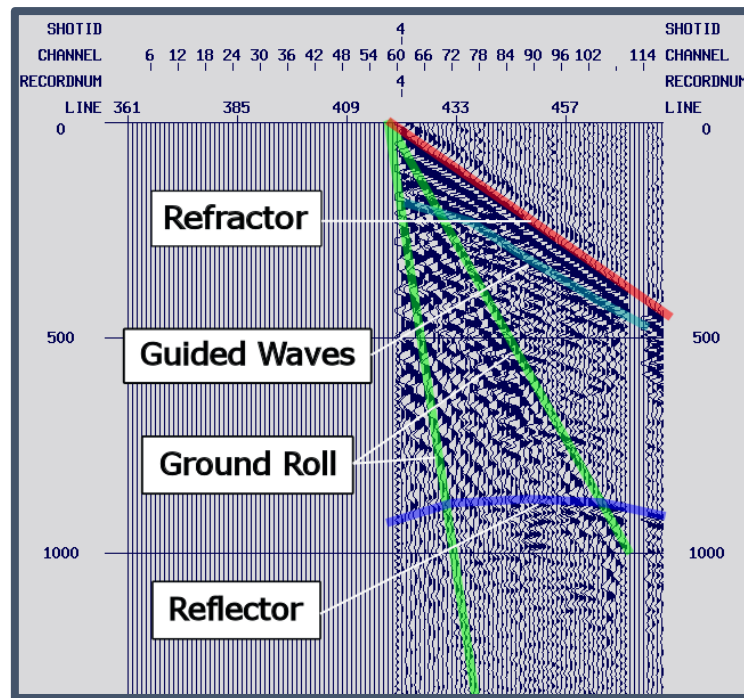
---

### 3.1 Seismic Reflection Method

When a seismic wave encounters a new medium with a different impedance, part of the wave is reflected. By measuring the time taken and the strength of the reflected wave, it is possible to determine the depth at which this reflection occurs and interpret the underlying geological structures (Wiederhold, 2002). The basis of the seismic reflection method relies largely on this principle.

P-waves are used more frequently for this method because they are the dominant body wave in artificial seismic sources i.e., explosives (Roy, 2007). That said, reflected waves generally arrive on a seismogram much later than the first refracted waves, so processing is required to separate them out.

When a seismic survey is made, the reflected waves are recorded as digitised waveforms at a particular geophone or seismometer. These recordings are commonly displayed as time sections or as shot gathers (Figure 3.1). In time sections, the x-axis represents the offset from the shot point while the y-axis represents time taken (ms). Similarly, in shot-gathers, the x-axis also represents the displacement but instead it depicts the channels/receiver position relative to the source, whereas the y-axis continues to represent time.



*Figure 3.1 A raw shot-gather of shot 4, MD87 line 04 illustrating the four main features of a shot-gather.*

Four distinct features are present in a land-based, seismic shot gather: ground roll, guided waves, refracted waves, and reflected waves. Ground roll occurs near the surface and the source. They are a form of coherent noise that approach detectors slowly and as a result give a straight, steep slope on the shot-gather as seen by the green lines in Figure 3.1.

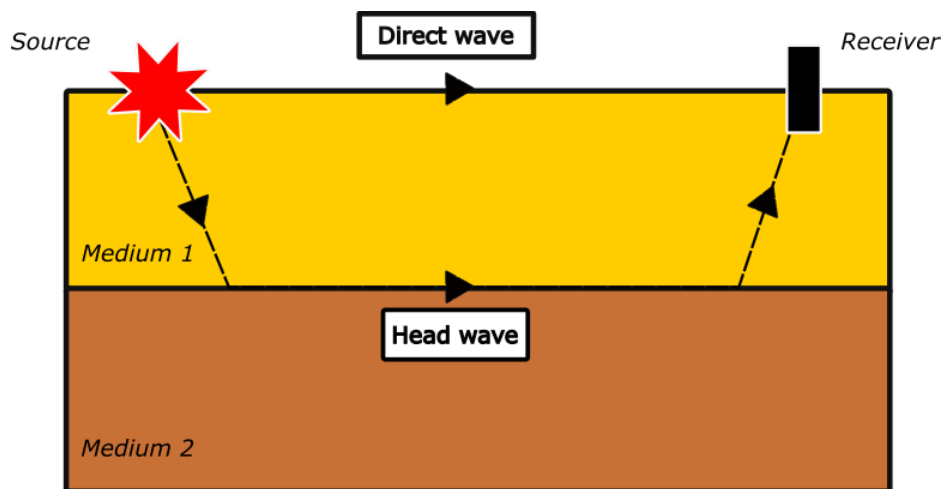
Guided waves are another form of coherent noise that is prevalent in land as marine records. These are generally faster waves that compose some of the early arrivals following the primary refracted waves (red line in Figure 3.1) in the near surface layer. When there is a large velocity difference between mediums, the strength of the guided waves will become more significant since there is more energy trapped within that layer (Yilmaz, 2001).

When a seismic wave propagates through a medium and encounters an interface, some of the energy is reflected up to the surface while the rest of it is transmitted through to the deeper layers. If the seismic wave hits the interface at the critical angle, the wave will travel along the interface boundary becoming a head wave (Figure 3.2). The displacement from the source,  $x_c$ , which the critical angle would occur can be calculated by the equation:

$$x_c = 2htan(\phi_c)$$

where  $h$  is the thickness of the layer and  $\phi_c$  is the critical angle.

After a certain distance, interestingly, the head waves end up travelling faster than direct waves and end up reaching the surface geophones first (Schrott et al, 2013). This is because velocities in lower layers are faster due to factors such as increased pressure. P-waves are mainly used for the seismic reflection method because they are the dominant wave type in artificial sources i.e. Vibroseis (Roy, 2007), because of this head waves are often taken to be the first arrivals (seen in red in Figure 3.1).



*Figure 3.2 An illustration showing the movement between a direct wave and a head wave. The direct wave travels along the surface of the source straight to the geophone while the head wave is a refracted wave that moves along the first interface. The point at which the head wave begins to travel faster and reach the receiver first is known as the cross-over distance.*

The final and most important feature in a seismic gather is the primary reflections (indicated by the blue line in Figure 3.1). This coherent signal offers beneficial information required by geophysicists to interpret the geological features in the subsurface. In particular, the two-way (TWT) time taken for the wave to reach back to the surface is invaluable because it allows the calculation of the reflector depth. This can be done by rearranging the hyperbolic equation:

$$t = \frac{2}{V} \sqrt{h^2 + (x^2/4)}$$

or

$$t^2 = \frac{x^2}{V^2} + t_0^2$$

where  $t_0$  is the direct two-way time, in other words  $t_0 = 2h/V$ .

The above equations, however, only apply to single interface scenarios. For situations where there is more than one interface (which is all the time), the equations become more complicated. With more than one medium, the velocity is no longer constant. The equation is then altered depending on number of layers present and instead the root-mean-squared (RMS) velocity is used.

The RMS velocity of a layer can be calculated by the equation (Sheriff & Geldart, 1982):

$$V_{rms} = \sqrt{\left( \frac{\sum_{i=1}^n V_i^2 \Delta t_i}{\sum_{i=1}^n \Delta t_i} \right)}$$

where  $i$  is the layer number,  $n$  the total number of layers, and  $\Delta t_i$  is the travel time in the respective layer. The above equation can be adjusted to suit the necessary number of horizons.

### 3.2 Seismic Resolution: The Fresnel zone

The resolution of a seismic image is dictated by its horizontal and vertical dimensions and describes how well two events can be separated from one another. The greater the resolution, the more clearly seismic events can be seen.

The vertical resolution of a seismic image is invaluable for calculating bed thickness and the resolution can be calculated by the equation:

$$r = \frac{\lambda}{4}$$

Where  $r$  is the minimum resolvable size and  $\lambda$  is the wavelength (Sheriff, 2001). This equation implies that within a seismic section, only reflectors with a vertical separation greater than  $\lambda/4$  can be separated and observed (Brown, 1999). The equation is notably more simplified



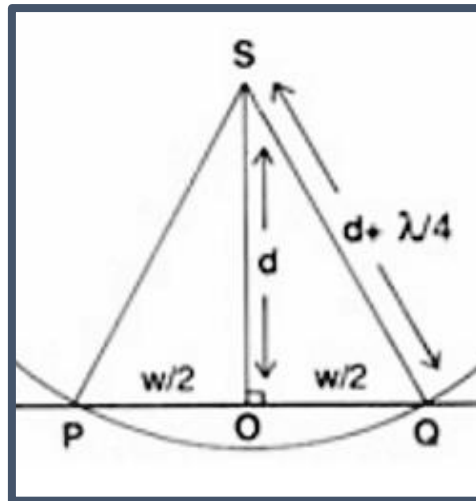
than the horizontal dimension because the vertical component is concerned with the zeros, maxima and minima of the waveform.

The horizontal resolution is more complex than the vertical resolution as the reflected energy does not come from a singular point but rather an area of points. This area is impacted heavily by phase difference and as a result also effected by the constructive and destructive effects of multiple waveforms. This area of concern, known as the Fresnel zone, determines the minimum resolution in the horizontal dimension. The radius of the Fresnel zone can be calculated by the equation:

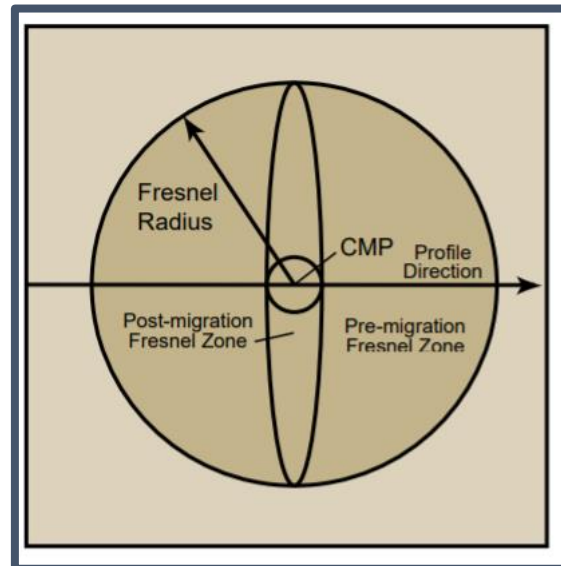
$$r = \sqrt{\frac{h \lambda}{2}} = 0.5 V \sqrt{\frac{T_0}{f}}$$

where  $r$  being the radius of the Fresnel zone,  $h$  depth of reflector,  $V$  velocity,  $T_0$  two-way travel time and  $f$  being the frequency (Wiederhold, 2002).

The Fresnel zone can be further defined as the area on the reflective interface where the ray path from source to receiver differs no more than  $\lambda/2$  (Parasinis, 1996). In this area, reflected waves are in phase with incident waves and become constructive resulting in stronger signals. Beyond this zone, any wave interference will occur in an alternating constructive and destructive fashion (Figure 3.3). Because of this, signals from the Fresnel zone are significantly more pronounced than signals outside this area (Sheriff, 2001). However, due to strength of the signal in the area, if two scattering features are located within the radius of the Fresnel zone, the reflected signals blend together to make the features almost indistinguishable from each other. The implication of this is that the Fresnel zone can lead to the misrepresentation of small events in the subsurface and incorrectly display the velocity variations caused by a reflector, ultimately leading to an erroneous velocity model (Thore & Juliard, 1999).



*Figure 3.3* Illustration detailing the area of the first Fresnel zone (referred to as just the Fresnel zone). The first Fresnel zone is an area where the first wave of constructive interference occurs. All waves reflected from the area within the space P-Q will give anomalously strong amplitude results. Any constructive interference that occurs after the first zone has less impact since it is offset by the corresponding destructive waves (after Keary et al, 2002).



*Figure 3.4* The following illustration is a bird's eye view of the Fresnel zone. This shows that it is not two-dimensional but rather operates in three-dimensional space. With 2D migration it is possible to compress the area laterally into an ellipse to reduce the effect of the Fresnel zone. With 3D migration the area can be reduced into a smaller circle by changing the dimensions (after Sheriff, 2004).

---

### 3.3 Velocities

There are a variety of seismic velocity systems that need to be considered for seismic processing. Using borehole data, such as sonic log and vertical seismic profiling, can provide an accurate view of seismic velocities within a layered geological setting that can be used in conjunction with velocities determined from or imposed on seismic data. Depending on the stage of the processing, certain types of velocities may be used over others (Sheriff, 2002):

$V_{int}$  → An interval velocity is a constant seismic velocity found within a single layer.  $V_{int}$  can be calculated from the inverse of the  $V_{rms}$  equation.

$V_{nmo}$  → The Normal Moveout (NMO) velocity is the velocity required for the best NMO correction for a given reflection in the seismic data. It assumes hyperbolic moveout meaning that corresponds to a single average velocity between the surface and the reflector.

$V_{stack}$  → The stacking velocity is the best velocity used for NMO when stacking.  $V_{stack}$  is generally equivalent to  $V_{nmo}$ .

$V_{rms}$  → The Root Mean Square velocity is calculated by stacking velocities from a set of input interval velocities (or vice versa). This assumes multiple flat layers with varying, but internally constant, interval velocities and assumes that the offset is small compared to depth. This velocity is useful for time-to-depth conversions.

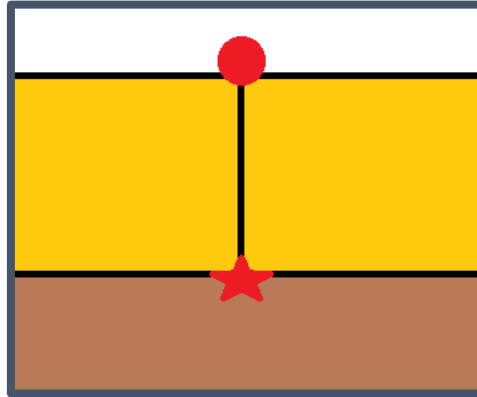
$V_{mig}$  → Migration velocity is the velocity that is best suited for migrating the data.

---

### 3.4 Common Mid-Point Method (CMP)

The aim of the seismic reflection method is to use multichannel seismic recordings to obtain a zero-offset seismic trace equivalent to source and receiver being in the same location on the surface (Figure 3.5). To simply position just a source and receiver together in one location can work, but is however, less accurate than it could be where the measurements would be subject to the undulating surface conditions. Addition of multiple receivers for each source,

permits the full use of the power of stacking and increase the reliability of the seismic data. This is where the Common Mid-Point method is used to full effect.



*Figure 3.5 Shows a zero offset seismic trace. The circle represents the source and the receiver, as they are found in the same position while the star is the reflecting surface.*

The Common Mid-Point Method, also known as the Common Depth-Point (CDP) method, is a procedure used for seismic reflection surveys to improve the reliability of the measurements by generating a multi-fold zero-offset seismic section. The source emits a wave in a radial fashion which then reflects off subsurface horizons and is reflected to an array of evenly spaced geophones/receivers. This results in each receiver picking up a different reflection point from the same source. In horizontally stratified media, the position of each reflection point is normally the mid-point between the source and the receiver (Yilmaz, 2001). Since shot points and receivers are always evenly spaced in a survey, each CMP can be easily derived by half the cable length by the shot point and geophone spacing.

The position of the seismic source and the geophones is then moved along the line by one increment. This iterative process is repeated all the way along the targeted project field. Each reflector is then represented by a series of traces, known as a gather, recorded from different offsets from source to receiver. The number of traces collected for a given subsurface position is known as the fold (Sheriff, 1999). As the number of movements along the line increases, so does the fold and imaging accuracy. The traces from each CMP are then summed up (stacked), combining the coherent signals resulting in an improved signal-to-

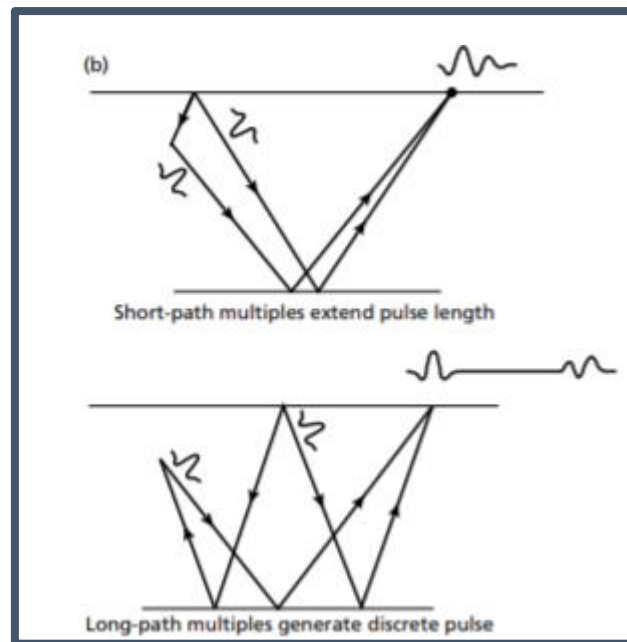
noise ratio (s/n). The improved s/n is due to the effects of incoherent signals, such as noise, being reduced from stacking (Keary et al. 2002). The signal-to-noise ratio is proportional to  $\sqrt{n}$  where n is the number of traces (Yilmaz, 1989). In other words, the larger the number of traces the more reliable an image becomes.

When the number of traces increase in a CMP gather, so does the fold of the stack. These two terms are often used synonymously for a seismic survey, i.e. a six-fold stack contains six traces in each CMP. The fold of a survey can be determined by the equation (Parasinis, 1999):

$$Fold = \frac{1/2(Channelspacing \times No. of Channels)}{Shot spacing}$$

It should be noted that the fold, however, can also be expressed as a percentage to describe the coverage of profile (Keary et al, 2002). For example, a single-fold profile is 100% coverage, while a seven-fold profile is considered to have 700% coverage.

Long path multiples (Figure 3.6) are reverberations of rays that reflect at more than one interface. These rays may have high amplitudes comparable to those of primary reflections; however, they arrive later in time because of their longer path lengths and therefore can be easily observed as distinct events (Figure 3.6) (Keary et al. 2002).



*Figure 3.6 The schematic diagram illustrates different kinds of multiples and their impact on the final recorded pulse. Long path multiples produce separate distinct events while short path multiples extend the actual primary reflected pulses (after Keary et al, 2002).*

---

### 3.5 Fourier Transforms

The Fourier transform (between frequency and time domain) is prevalent in most areas of physics. This is due to the attribute that most systems are composed of a primary source that is sinusoidal in nature, such as electrical circuits and seismic signals. This makes Fourier Transforms useful for seismic processing since seismic data is recorded in the time domain. Using the Fourier transform it is possible to shift data from the time domain to the frequency domain. This makes it possible to separate and determine the different frequencies that compose the seismic signal. By splitting the frequencies, it makes it easier to identify and remove coherent noise such as ground roll.

French Scientist Jean Baptiste Fourier (1768 - 1830) observed that all movements that are periodic can be constructed from the summation of a series of constant-amplitude sinusoidal waves (Taylor, 2005).

Such functions of time,  $f(t)$ , could then be expressed as:

$$f(t) = \frac{a_0}{2} + \sum_{n=1}^{\infty} [a_n \cos(n\omega t) + b_n \sin(n\omega t)]$$

where  $a_n, b_n$  are coefficients of the  $n^{\text{th}}$  sample also known as the Fourier coefficients and  $\omega$  is the angular frequency. With:

$$\omega = \frac{2\pi}{T} = 2\pi f$$

where  $T$  and  $f$  represent period and frequency respectively.

To analyse the coefficients  $a_n, b_n$ , the continuous Fourier series/transform is applied to the function:

$$X(f) = \int_{-\infty}^{\infty} f(t) e^{-i\omega t} dt$$

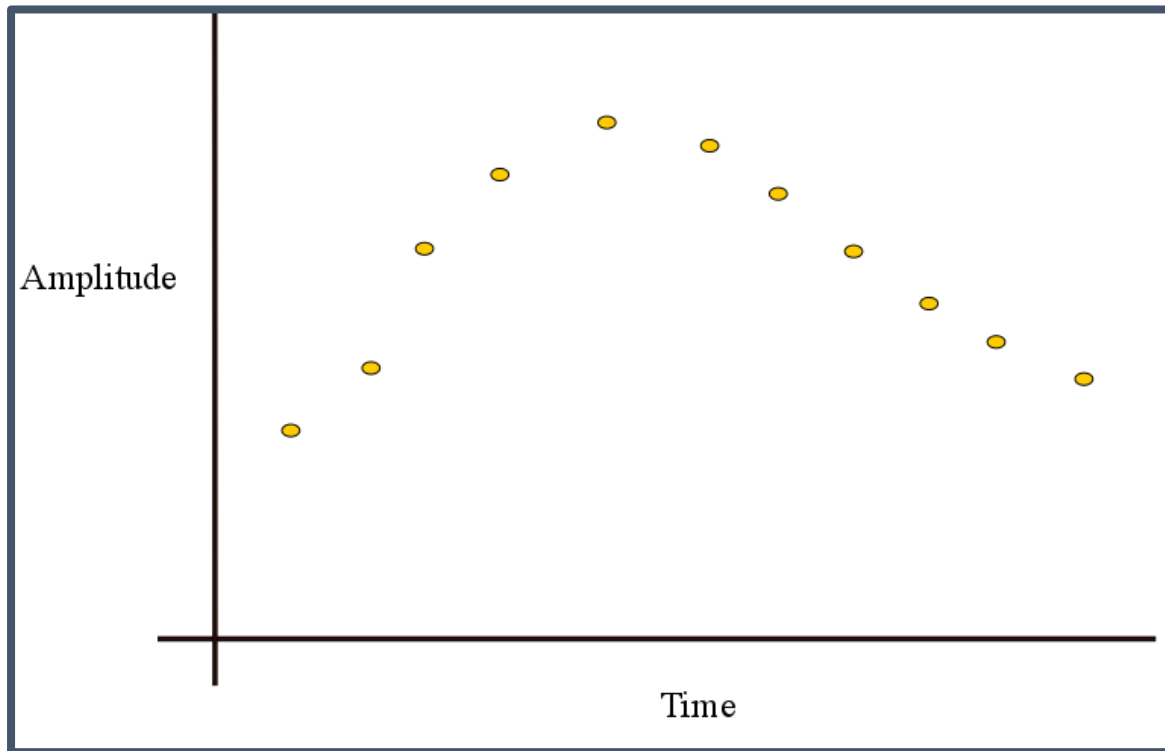
The analysing function is a sinusoidal function that is multiplied together with the function. The bigger the difference, the larger the coefficient will be and vice versa. The imaginary number “ $i$ ”, indicates that the coefficient is a complex number. It is possible to overcome this and obtain two real numbers as opposed to one complex number by using the orthogonality of sine and cosine functions (Taylor, 2005). When this orthogonal principle is applied to the function, we can then write:

$$a_n = \int_{-\infty}^{\infty} x(t) \cos(n\omega t) dt$$

$$b_n = \int_{-\infty}^{\infty} x(t) \sin(n\omega t) dt$$

However, this requires the calculations of two additional equations.

Instead of using a continuous Fourier Transform, for computer based seismic processing the Discrete Fourier Transform is used instead. This is because the analogue to digital converter that is used for seismic acquisition cannot continuously sample the data, as a result we get a series of discrete data over a given time period at a predetermined sampling interval (Yilmaz, 2001).



*Figure 3.7 Example of a discrete data set. Autocorrelation would create a line which connects the data set.*

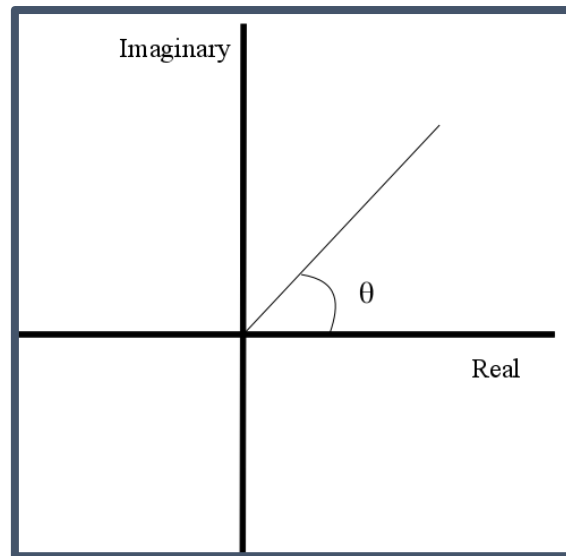
The Discrete Fourier Transform is then given by:

$$X_k = \sum_{n=0}^{N-1} x_n \cdot e^{\frac{-i 2 \pi k n}{N}}$$

where  $k$  is the frequency bin,  $n$  is the  $n^{\text{th}}$  sample and  $N$  is the total number of samples. The use of the Euler's formula then allows the computation of the phase and amplitude. Euler's formula is given by:

$$e^{ix} = \cos(x) + i\sin(x)$$





*Figure 3.8* Imaginary and real numbers of a wave can be separated as y- and x-axis variables, respectively. Much like a grid reference, the phase of the wave would be the angle  $\theta$ .

The imaginary and real components of each coefficient can then be used to find the amplitude and phase of the wave using the Pythagorean theorem.

With regard to seismic data, the Fourier Transform will convert spatial variables ( $t, x, y, z$ ) to their Fourier counterparts ( $\omega, k_x, k_y, k_z$ ) with  $k$  representing the wavenumber. The wavenumber would be calculated by the number of peaks within a certain interval in a specific axis (Yilmaz, 2005) and is then mapped against the temporal frequency. So, the Frequency- Wavenumber plane that is produced by a 2D FT is representative of the amplitude spectrum in the T-X domain.

The terms “Fourier series” and “Fourier transform” are used ubiquitously in geophysics but the distinction between the two is important. The Fourier series represents a discrete periodic function while the Fourier Transform is used as a general representation for non-periodic continuous functions (Taylor, 2005). In other words, the Fourier transform is the Fourier series of a function for which the period approaches infinity.

---

### 3.5.1 Fast Fourier Transform (FFT)

The Fast Fourier Transform (FFT) operates on the same inputs and produces equivalent outputs as the regular Discrete Fourier Transform (DFT). This adaptation of the Fourier Transform is implemented by modern-day noise removal techniques such as f-x deconvolution and f-k filtering. As the name suggests, the FFT reduces the time required for computation. This is carried out by splitting the data into smaller subsets with an exponent of 2 and then combining them in the end to achieve the same result as the DFT.

The FFT is an approach based on the regular DFT by Cooley and Tukey (1965). They expressed the DFT in a matrix-vector product format where given a waveform with  $N$  samples, the number of multiplication calculations would be  $N^2$  while the corresponding FFT format would require only  $2N\log_2 N$  calculations.

For example:

#### Number of Multiplications

Number of Samples	Regular FT	FFT
500	$2.5 \times 10^5$	$2.7 \times 10^3$
3375	$1.1 \times 10^7$	$2.4 \times 10^4$

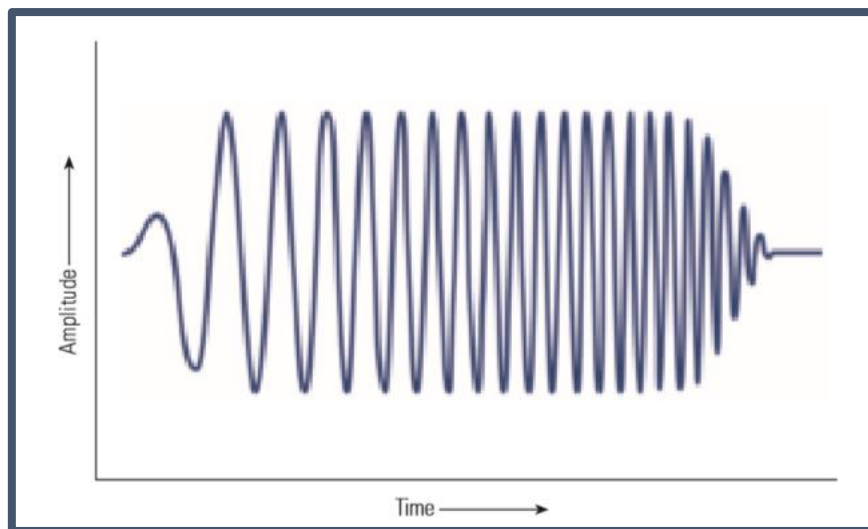
It can be seen that the use of FFT significantly reduces the number of multiplications and hence processing time.

---

### 3.6 Vibroseis

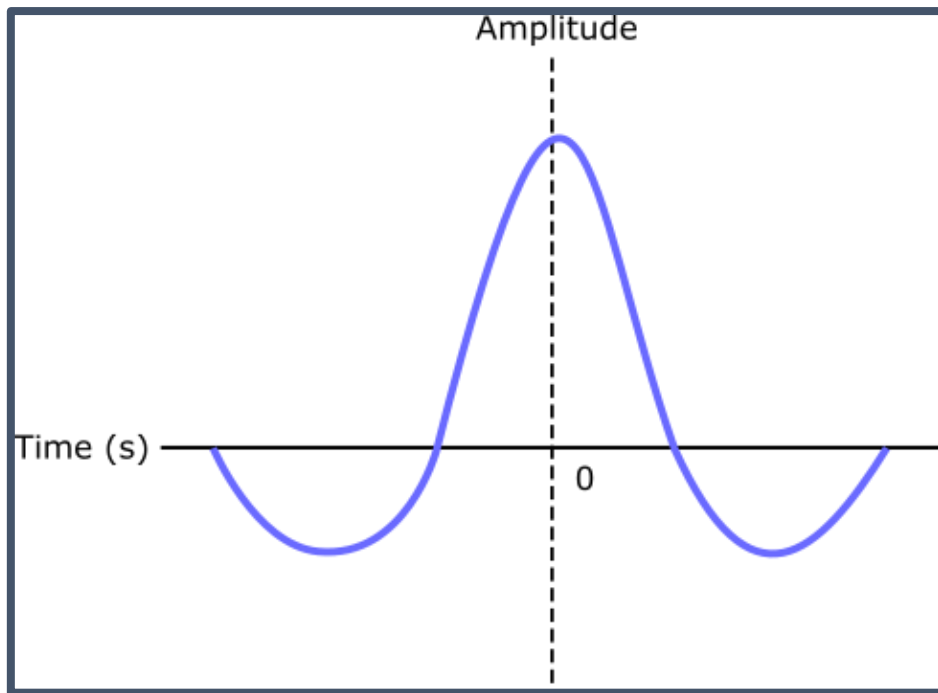
Vibroseis was first developed and patented by Conoco (now ConocoPhillips) in 1952. It is a truck-mounted system which utilises an oscillating mass. This mass allows for the controlled input of a range of low amplitude frequencies into the subsurface to produce a seismic source referred to as a sweep signal (Keary et al, 2002). The vibrating motion creates an

undulating movement usually starting from no motion, to some low frequency and then slowly increasing to a higher frequency. This envelope of waves is known as an upsweep, while vice versa, it can go from high to low and is then called a downsweep (Bagaini et al, 2010). For land surveys, artificial sources such as explosives and Vibroseis are commonly used. For the sake of safety, repeatability, efficiency and its non-destructive nature, the Vibroseis method is often most preferred (Redshaw, 2012).



*Figure 3.9 An illustration of an upsweep envelope from a Vibroseis source (after Onajite, 2014).*

The typical bandwidth produced by Vibroseis generally varies between 8 and 105 Hz with each sweep being approximately up to 20 s long (Keary et al. 2002). Because the recorded values are carried out as a sweep as opposed to an impulse, the seismogram is cross correlated with the known sweep signal to convert signals into short sharp wavelets to recover the impulse response. The wavelets generated by this correlation process are zero-phase wavelets, meaning that the maximum amplitude of these symmetrical wavelets is centred at  $t=0$  (Onajite, 2014). The benefit of a zero-phase wavelet is that it provides greater accuracy for seismic interpretation since the peaks of a wavelet will correspond directly with the position of a reflector (Henry, 1997).



*Figure 3.10 An illustration of a simple zero-phase wavelet. This particular even form is known as a Klauder Wavelet.*

Baigani et al, 2012 explained the basic operation of a vibrator source in detail by describing how a vibrating truck operates primarily on the driving of the base plate onto the ground. The base plate is a rectangular pad that is in contact with the surface that is positioned in the middle of the vehicle. Above this base plate is a reaction mass where its vertical movement is driven by a hydraulic piston.

## 4.0 Processing Sequence (1987)

To determine whether modern-day seismic processing techniques are more effective on the seismic data, the original processing procedures and sequences implemented in 1987 on the Moutere Depression data need to be reviewed. By recognizing the effects of each stage of processing, it makes it easier to draw comparisons and conclusions between the currently obtained final seismic images and those produced by GECO Ltd in 1987. In this chapter, the subsections are laid out in chronological order following the processing methodology used by GECO Ltd and their processing sequence is presented in the Appendix (ii).

---

### 4.1 Initial Processing

The seismic data was initially processed and edited in the field to check that the correct results have been produced. This process included the use of multiplexors, correlator-stackers and field computers, which in turn provided effective recording, transmission, and editing.

The initial seismic data in 1987 was recorded using geophones and transmitted through a single cable using a multiplexer. The multiplexer device is particularly effective for multichannel systems, where it samples the signals for multiple channels at the same time (Parasinis, 1997). The sampled signals are then compiled and delivered as a single output data stream through copper cables. By using a multiplexer, the field operators are able to save running costs by avoiding the use of multiple transmission lines.

The geophone receives the seismic signal in a multiplexed format. The seismic data are then demultiplexed or “demuxed”, into separate components and rearranged into sample-sequential order (i.e. Channel 1, sample 1; Channel 1, sample 2...; Channel 2, sample 1; Channel 2, sample 2...). Reordering the data as such permits the correlator-stacker to reduce ambient noise via stacking. The correlator-stacker is a device specifically designed for land Vibroseis surveys and is used in conjunction with one or more Vibroseis trucks. It is able to cross-correlate the pilot sweep and raw seismic data, cancelling out noise in the process (Gadallah and Fisher, 2004).

During the field stage, the signals obtained are weakened by energy loss during transmission. To increase this lost signal, gain recovery is added systematically. Gain recovery will additionally be reapplied a second time at the “spherical divergence” stage where it corrects for the amplitude loss using a scaling function representative of the wave spreading out in a radial manner (Yilmaz, 2001). Initial preliminary trace editing will also occur at this stage, where noisy traces and dead traces will be removed or muted. This can be accomplished by killing the individual trace or setting the amplitudes to zero (Parasisnis, 1997).

---

## 4.2 Crooked Line Analysis

Crooked acquisition lines are a reality of large-scale seismic surveys. In rugged, topographically challenging terrains and unfavourable conditions, truck-mounted seismic sources are limited to the more accessible routes found along highways or roads. As such, the acquisition line that develops has a non-linear form and would consequently impact the accuracy of the seismic profile. Since most CMP processing techniques are based on the premise of a straight survey line (Wu, 1996), modifications are needed to enable the processing of lines along crooked profiles.

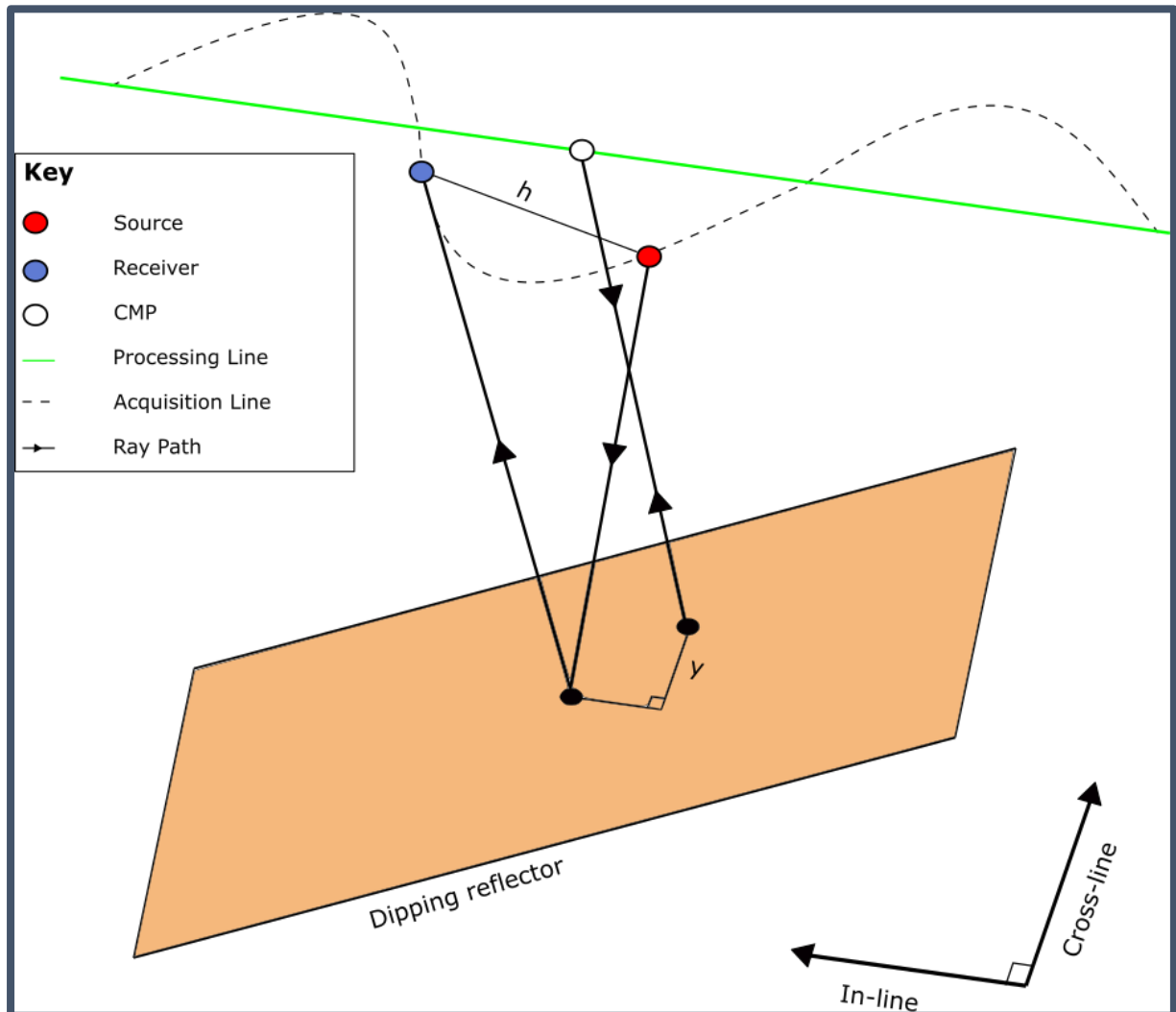
The majority of seismic lines of the Moutere Depression seismic survey possess a highly irregular shape and are rarely linear due to the hilly topography of the region. These haphazardly shaped acquisition lines cause potential problems for seismic profiles. One of the significant issues surrounding crooked acquisition lines is that the midpoints between traces possess an offset component which is perpendicular to the actual profile direction, known as the cross-line offset (Beckel and Juhlin, 2019). For straight line surveys, the CMP travel-time equation is:

$$t^2(x, h) = t_0^2(x) + p_x^2 h^2$$

where  $t(x, h)$  is the source-receiver travel-time,  $t_0(x)$  is the zero-offset reflection travel-time,  $x$  is the CMP position,  $p_x$  is the medium’s slowness factor in the x-direction and  $h$  is the source receiver offset. But because of the cross-line offset component ( $p_y$ ) present in crooked line CMP’s, the generalised CMP travel-time equation now becomes:

$$t^2(x, y, h) = (t_0(x) + p_y y)^2 + p_x^2 h^2$$

where  $p_y$  is the slowness in the y-direction and  $y$  is the offset distance between the CMP position and the processing line (Figure 4.1).



*Figure 4.1 An illustrative example of a crooked-line survey depicting the actual ray path from source to receiver of the survey line and the ray path of the CMP of the processing line. As the example shows, there is a difference between the positions of the two reflection events. The difference is the cross-line offset that is perpendicular to the seismic processing line and is represented by “ $y$ ” where “ $y$ ” can be calculated using “ $h$ ”, the total distance between source and receiver, and the slowness values,  $p$ , in  $x$ - and  $y$ - directions. This extra factor increases the real travel time shown by the equation:  $t^2(x, y, h) = (t_0(x) + p_y y)^2 + p_x^2 h^2$  (after Nedimovic and West, 2003).*

In other words, the previous equation shows that if a reflector has a cross-line offset component, the depth to reflector would vary for each individual trace and therefore, create CMP alignment problems (Nedimovic and West, 2003).

To overcome this obstacle, time shifts are applied to the data. If the dataset is uncorrected, the stacked seismic image would present focussing issues on seismic reflections where inappropriate offset values could contaminate the overall energy distribution (Beckel and Juhlin, 2019). The basic equation defined by Lerner et al. (1979) is used to correct for the cross-line offset time shift. In this equation, ( $\Delta t_{cross}$ ) is given by:

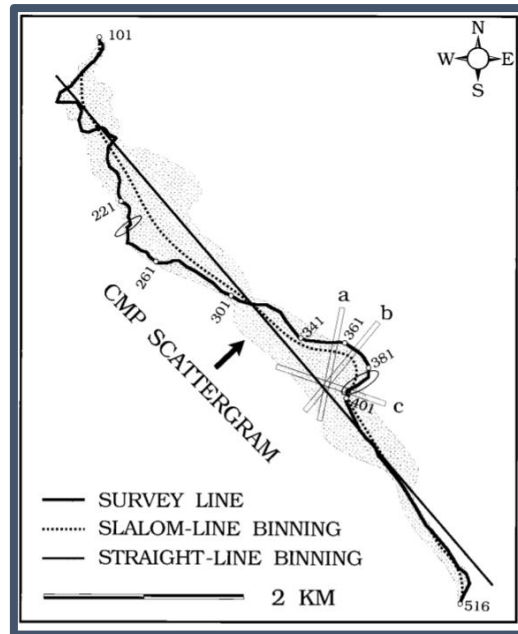
$$\Delta t_{cross} = \frac{2\sin(\phi)}{v} y$$

where  $\phi$  is the cross-line dip angle,  $v$  is the medium velocity and  $y$  is the cross-line offset.

However, as part of the crooked line analysis and prior to time corrections, the seismic data is first divided into 2D segments, or bins that are centred on the midpoint. For extremely crooked survey lines, many of the CDPs have high fold densities where the data obtained could be comparable to 3D swaths (Nedimovic and West, 2003). By grouping the dataset into bins and defining the source-receiver offsets, the data density is better regulated thus saving processing time.

When the CDP binning profile is defined for the crooked line survey, it should incorporate as much necessary seismic information as possible. Optimally, this will produce a smooth synthetic slalom line through the survey (Wu, 1996). If the newly formed line has sharp turns or curves and neglects a few CDP values, that specific section would be broken down further into smaller CDP bins where the software would automatically place the traces to the nearest bin. An example of CMP binning for a crooked line Vibroseis seismic survey is shown in Figure 4.2.





*Figure 4.2 As an example of a crooked line survey, this is a map from a Vibroseis survey in Sudbury, Canada from Wu (1995). Numbers are the stations, while a, b and c are the CMP bins that are found along a tight curve of the survey line. Ellipses are areas of coherent noise while the rectangles are just exaggerations to show the intersecting properties of the three bins. Straight line binning is another method where essentially a straight line-of-best-fit is produced for a straight seismic profile.*

---

### 4.3 Common Depth Point Gatherers

After the crooked line analysis, traces are sorted based on the same Common Depth Point (CDP), or also known as the Common Mid-Point (CMP), ultimately forming a gather (Parasinis, 1997). This is a major step in seismic reflection processing that ultimately enables the signal-to-noise ratio enhancement through stacking (Boyce, 1986). This practice is known as the CMP method. Further information regarding this subject can be found in section 3.4.

GECO Ltd processed the data with the parameters defined by the field reports. The 1987 data had average CDP folds of 30 with 120 channels per shot and trace spacing of 25 m. The current data processing aimed to follow the same parameters applied by GECO Ltd as much as possible to enable controlled comparisons.

---

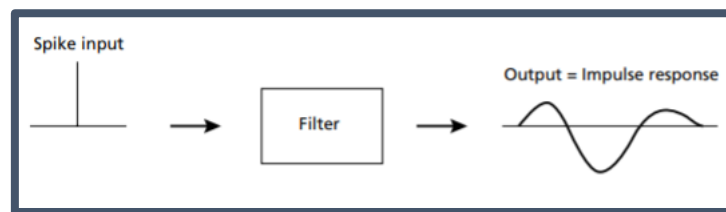
---

#### 4.4 Deconvolution

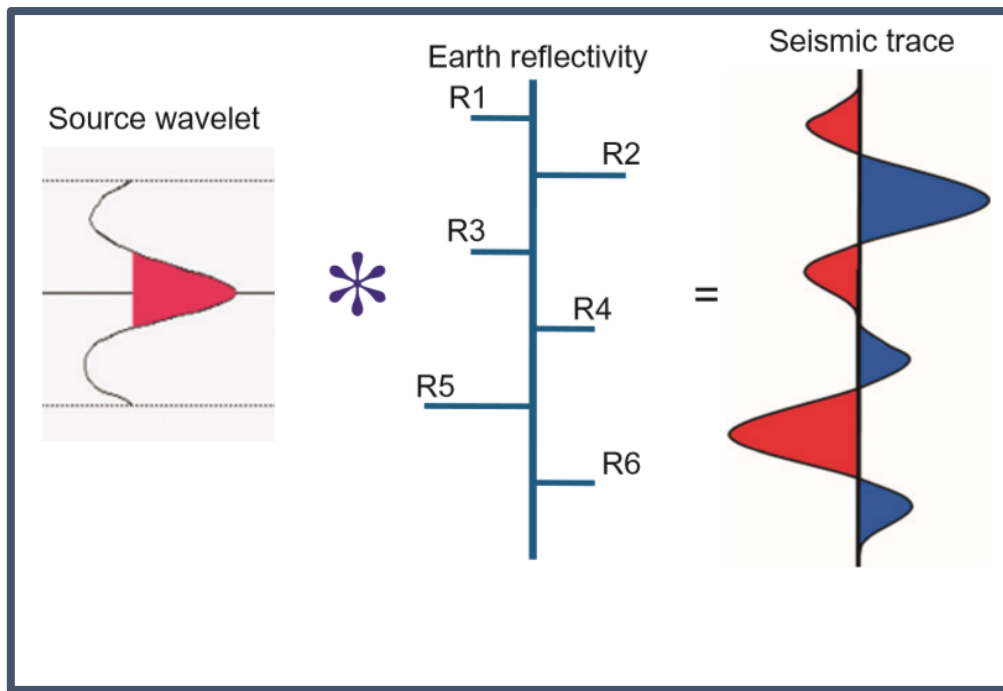
Deconvolution is the process of removing the effect of signal modifications from previous acquisition operations and to recover high frequencies that were lost due to signal transmission through the subsurface (Onajite, 2014). The output seismic response, or trace ( $x$ ), that is recorded in a survey is the convolution of the reflection coefficient ( $r$ ) and source wavelet ( $w$ ) with reference to time (Redshaw, 2005):

$$x = r * w * N$$

In practice, the output seismic response will always include some form of noise ( $N$ ). Figures 4.3 and 4.4 help to illustrate the concept of convolution.



*Figure 4.3 Mathematically, convolution is the operation defining the change in shape of a wave through the application of a filter, producing an output wave. The spike input is often the measure of the amplitude of the wave. The spike input is a way of assessing the acoustic impedance contrast and reflectivity coefficient of a given horizon where a negative amplitude shows a negative change in reflectivity at the layer boundary (Yilmaz, 1987) (after Keary et al., 2002).*



*Figure 4.4 Illustration showing the basic function of convolution. The asterisk represents the convolution process (after Onajite, 2014).*

The aim of the deconvolution process is to deconvolve the seismic signal by compressing the source wavelet (ultimately to mimic the reflectivity coefficients) producing a spike-like function. This allows the interpreter to better define the subsurface horizons by their reflection coefficients.

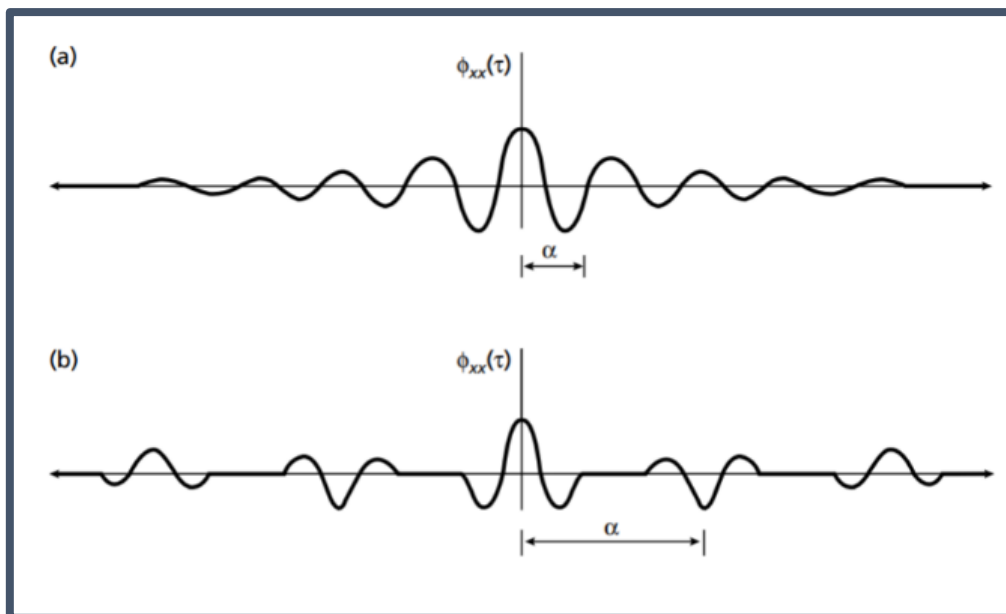
Inadvertently, the deconvolution process can also aid in the removal of  *multiples*. Multiples are a source of lower amplitude secondary waves and are preferentially removed because they can often be misinterpreted as primary reflections (Yilmaz, 1987). Examples of other inverse filters used to remove multiples include dereverberations and deghosting. All of which, involve shortening the pulse length and improving vertical resolution (Keary et al, 2002).

Dereverberations involve filtering out repeating secondary reflective waves that are found at the boundary of water layers while deghosting focuses on the removal of short path reflective waves that are trapped at boundary layers (Sheriff, 2002).

Variations of deconvolution includes spiking deconvolution, time-variant deconvolution and predictive deconvolution. *Spiking deconvolution* reduces the source wavelet into a spike using a Wiener filter (Parasinis, 1997). *Time-variant* deconvolution has the deconvolution

parameter act in a way such that it varies with time in response to changes in frequency spectrum with reflection depth.

Finally, *predictive deconvolution*, as utilised in the 1987 study by GECO Ltd, uses the arrival times of primary reflections to predict the arrival times of multiples. Determining the arrival times as such allows these artefacts to be removed (Keary et al. 2002). Autocorrelation and cross-correlation serves as the basis for predictive deconvolution. A cross-correlation function detects the time phase differences between two waveforms which is optimal if the source pulse and the recorded waveform are known (as is the case with Vibroseis data). If the source pulse is unknown, the autocorrelation function is used instead. This function compares the signal with itself which is efficient in the detection of lag times between peaks. The autocorrelations of seismic waves results zero-phase wavelets. Figure 4.5 below displays the effects of traces with noise that underwent the autocorrelation function.



*Figure 4.5 A) shows a function with short wave path multiples with a decaying function. B) shows the function with long wavelength reverberations, indicative of long side "lobes" which are areas where primary reflections coincide with multiples cancelling out (after Keary et al. 2002).*

The deconvolution control parameters used in the GECO Ltd. processing are the filter length, gap length and the design window. Filter length defines the time length for the inverse filter to be carried out. The length must of sufficient length to encompass at least two bounces from short path multiples; however, too long could distort the image (Onajite, 2014). Gap length refers to the sampling time; short sampling is used for spiking deconvolution and longer values are for predictive deconvolution. While the design window is used to establish the deconvolution parameters, the process should be applied to the entire dataset. Therefore the design window is usually set for an interval with good signal.

For GECO Ltd's predictive deconvolution, they used an operator length of 200 ms, gap of 12 ms, and a design window of 2000 ms. White noise was also not added.

#### 4.5 Elevation static correction

Land surveys are conducted on surfaces where sources and receivers are located at different elevations and in variable near-surface layers. The elevation static correction is used to account for the elevation difference between receivers and sources and to reference the processed seismic data onto a common datum. An elevation that is lower than the lowest receiver on a given profile is commonly used (Figure 4.6).

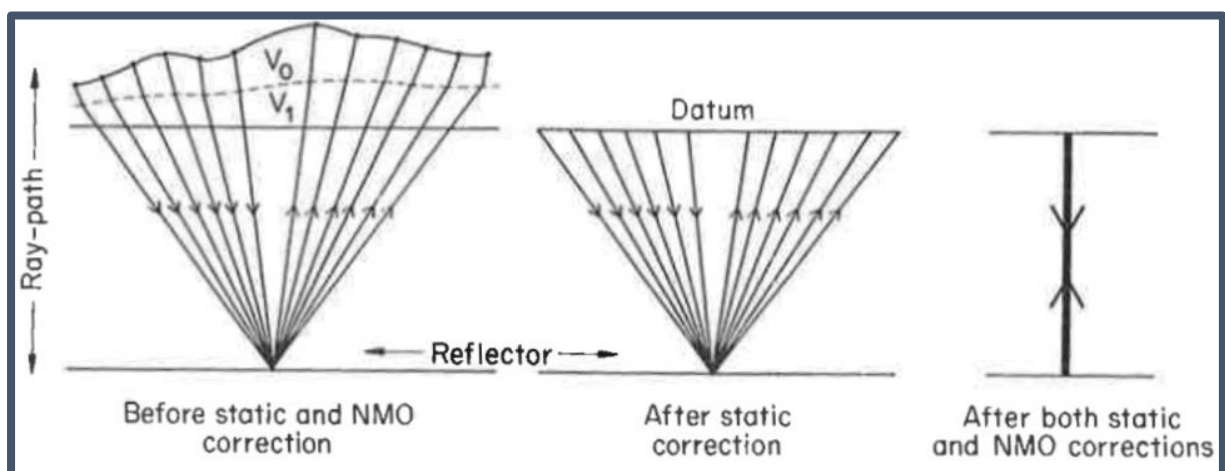


Figure 4.6 An illustration of the effects of Normal Move-Out (NMO) and static correction (after Alsadi, 2017).

In the original processing, GECO Ltd utilised the aforementioned technique and then adjusted the elevations to MSL. The replacement velocity ( $V_R$ ) used for static vertical shifts was 2500 m/s. The velocity was used to calculate time shift ( $T_c$ ) that was applied to corresponding seismic traces (Bancroft, 1999).

Although it is not explicitly stated in the original report, I have inferred that GECO Ltd used wave equation datuming. This was because surveys with large elevation changes required all recorded values converted to a single datum (Bancroft, 1999). This form of datuming can be further incorporated into poststack migration, which was also carried out by GECO Ltd. The elevation static correction ( $T_c$ ) is given by:

$$T_c = \frac{(E_s - E_D) + (E_R - E_D)}{V_R}$$

where  $E_s$  is the elevation at the shot location,  $E_R$  is the elevation at the receiver location, and  $E_D$  is the datum elevation. Normally there are additional variables for the depth of the receiver and depth of the source; however, because for Vibroseis acquisition they are positioned at the surface, these values are zero.

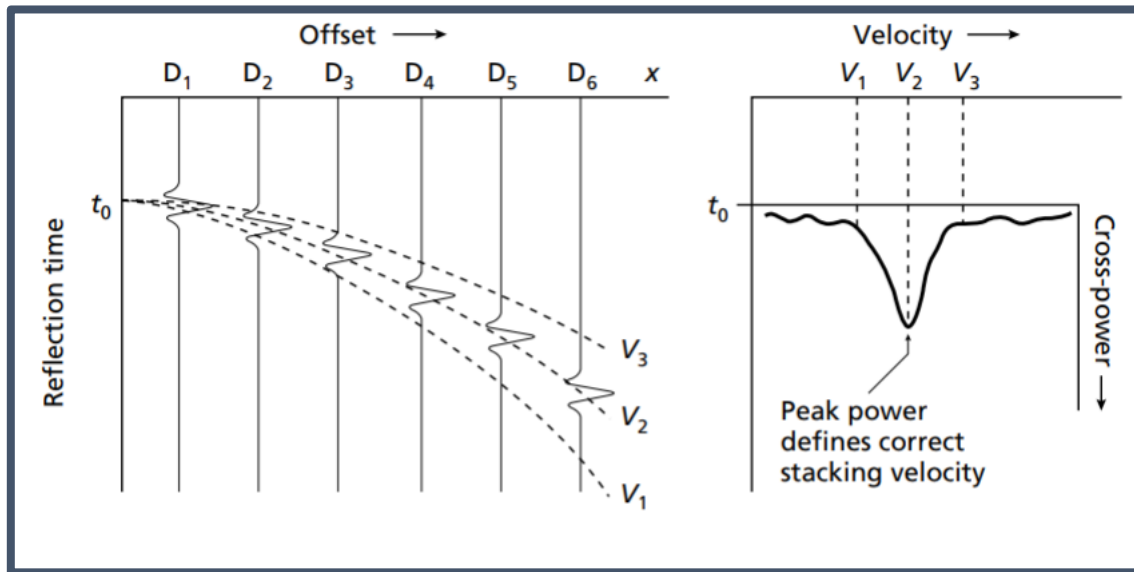
#### 4.6 Normal Move-Out Dynamic Corrections

Normal Move-Out (NMO) is defined as the effect that increasing the distance between the seismic source and the receiver has on the travel time of a reflected seismic wave. When the distance between the receiver and the source increases, the time it takes for the wave to reach the receiver also increases. "Moveout" is defined as the additional time from the apex of the hyperbola to the point of interest (Rehmer, 1997)

This effect is what causes the hyperbolic shape of the wave in CDP and shot records (Figure 4.7). The travel-time curve of the reflections for different offsets between source and receiver for a simple geological setting is defined by the following hyperbolic equation:

$$t^2 = t_0^2 + \frac{x^2}{v_{stack}^2}$$

where  $t_0$  is the travel-time for a reflected ray at zero-offset distance,  $x$  is the distance from the source to the receiver. The difference between  $t$  and  $t_0$  is the NMO ( $\Delta t$ ). Based off the variables, it is evident that the normal move-out is dependent on the offset and velocity. It is useful to note however, that along a trace, the correction/velocity can change. Due to this characteristic the NMO-correction is known as dynamic correction (Yilmaz, 1987).



*Figure 4.7 T-X offset hyperbolae for a 1-D example. After stacking along the hyperbolic curves, the velocity/hyperbola that provides the highest amplitude is used as the stacking velocity for the reflector (after Taner and Koehler 1969).*

NMO can be approximated by the equation (Parasinis, 1997):

$$\Delta t \approx \frac{x^2}{2t_0V^2}$$

During the assessment of stacking velocities, caution must be made to be as accurate as possible. If the velocity used is too low, the resulting reflection would be over-corrected, and the reflection would curve upwards and vice versa for velocities being too high.

The analysis method GECO used for velocity determination at the Moutere Depression was the Constant Velocity Stacking (CVS) method. This is where the data are repeatedly corrected at a range of NMO velocities and summed by stacking. The final stacking velocity is then chosen by producing a V-T function with a range of velocities and times where the highest amplitude produced is the stacking velocity (Yilmaz, 2001).

---

#### 4.7 Pre-Stack Mute

Similar to the description of the earlier trace editing process, muting is the technical term used for removing an unwanted section of a trace and setting the amplitude to zero (Sheriff, 2001). During this phase, signals such as direct waves and refracted waves are muted as these signals would result in artefacts on the stacked seismic profile. This step requires extra cautions as seismic data are sensitive to adjustments with regards to time and excessive muting can therefore, cause major image distortion (Parasinis, 1997).

---

#### 4.8 Amplitude Modulation

GECO Ltd applied amplitude modulation to the data to compensate for the absorption of seismic energy. Absorption preferentially affects high frequencies in the seismic data (Telford et al, 1990; Henry 1997). In contrast, deconvolution methods such as whitening (spiking deconvolution), tend to accentuate low frequency signals and noise while masking stronger primary signals. Therefore, the true seismic signal is permanently altered (Henry, 1997).

The amplitudes of seismic waves are time dependent; however, phase and frequency are often considered as constant (Oopong and Danour, 2014). Amplitude variation of a wave while keeping frequency and phase constant is called Amplitude Modulation. The amount of modulation is determined by the modulation index ( $m$ ) where its equation is given by:

$$m = \frac{\Delta a_r}{a_m}$$

where  $\Delta a_r$  and  $a_m$ , are the change in amplitude at the receiver and amplitude at the source respectively (Gupta, 2009).

---



---

#### 4.9 Refraction Static Corrections

This is another form of static correction which attempts to remove the effects of near surface variability in the seismic data. Sources and receivers are often positioned on a weathered near-surface layer. This layer creates heterogeneities and alter the arrival times of reflected waves (Parasinis, 1997). This correction to the seismic trace effectively repositions the source and the receiver below this near surface layer (often referred to as the Low Velocity Layer, LVL) on a constant datum (Sheriff, 2001). The key difference between refraction statics and elevation statics is that residual statics are centered on travel times of refracted raypaths in shallow units as opposed to strictly the elevations of the shots and geophones.

Long-wavelength corrections are used in this process, instead of using short-wavelength components, because of the relative ease of recovering long wavelength components (Dziewonski,2004). This form of correction additionally assumes the presence long-wavelength anomalies. These anomalies are often caused by gradual changes in the near surface (Cox, 1999; Yilmaz, 2001). However, this form of static correction is more sensitive to noise on the input data hence why the prestack muting and stack was carried out beforehand (Cox, 1999). The final result for this method is generally more unstable than short-wavelength techniques unless it is combined in unison with uphole surveys (Cox, 1999)

---

#### 4.10 CDP Trim and Stack

Stacking in seismic reflection surveys combines (adds or averages) traces from different shot records with a CDP (Sheriff, 1991). It is the summation of traces to produce a single, more defined result. The process of stacking increases the signal-to-noise ratio because when traces are added together, noise is diminished by destructive interference, while true reflections in the trace are combined in with constructive interference resulting in a stronger signal (Keary et al 2002).

A CDP trim static is applied to traces within each CDP before stacking. Trim is the application of secondary statics based on aligning shallow reflections on the CDP to improve the quality of the stack and improve the fine-scale alignment of events prior to stacking (Sheriff, 2001).

---

#### 4.11 Time Variant Bandpass Filtering and Time Variant Scaling

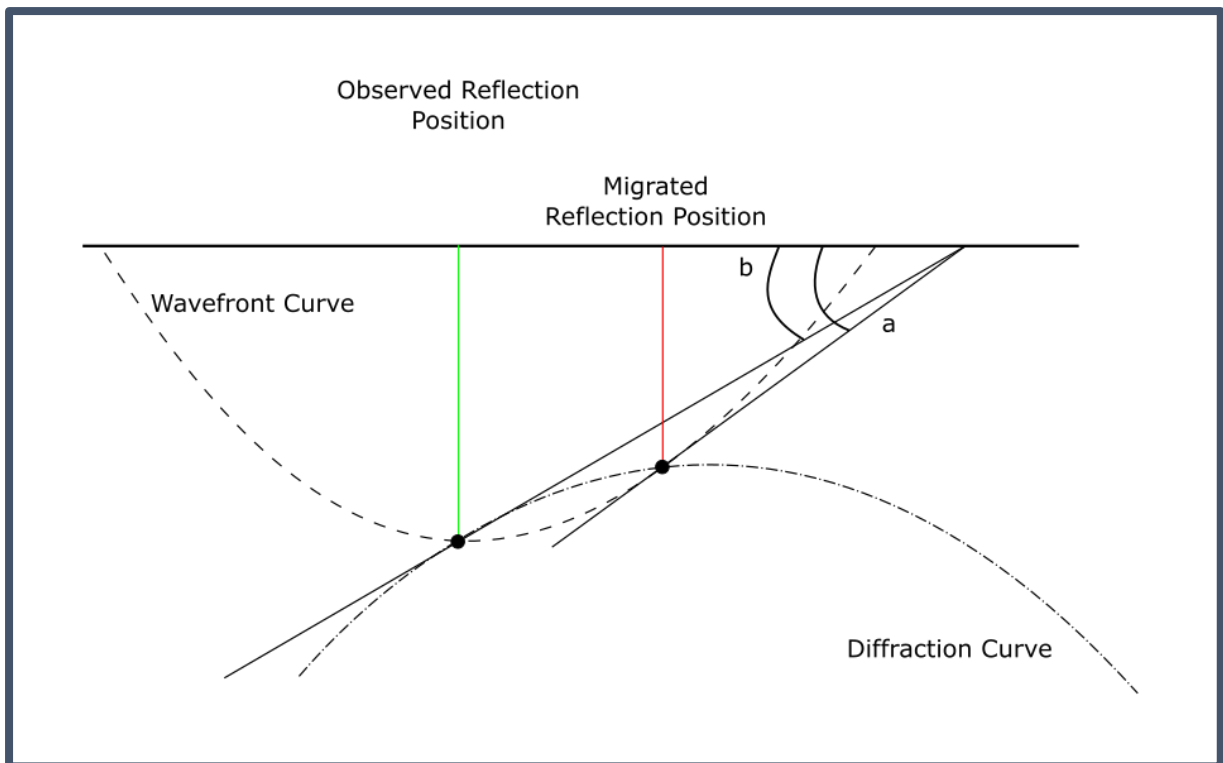
Seismic signals decrease in frequency as time progresses due to the frequency damping effect of wave frequency as it propagates through the Earth (Parasini et al, 1997). The normal protocol in such instances, is to apply a deconvolution technique to recover this systematic loss of frequency and remove low-frequency noise. Despite its efficacy, this method also tends to enhance high-frequency noise at later time intervals which clouds the overall coherency of reflections. A Time-Variant Bandpass Filter (TVBF) was thus introduced to provide cut off frequencies for such accentuated noise (Scheuer and Oldenburg, 1988).

An additional gain function was applied to the seismic data at this stage. It was introduced to the data to bring up weak signals as an attempt to mitigate the effects of the TVBF that may have diminished real seismic signals (Yilmaz, 2001). The gain function used was a Time-Variant Scaling function (TVS). GECO Ltd used a gain window of 500 ms for the TVS.

---

#### 4.12 Migration

CMP stacks usually assume that reflections originate on a horizontal layer, which realistically is rarely the case. A dip component is typically encompassed in traces, either due to the reflector itself not being horizontal or the receiver placement on an irregular dipping surface causing it to be not level (Keary et al. 2002; Yilmaz, 2001). The goal of migration is to reconstruct the seismic section to adjust the reflections and diffractions to their true geometric positions (Figure 4.8) (Keary et al, 2002). To achieve this, migration methods collapse or sum the amplitudes of multiple diffraction hyperbolas into a single point (Yilmaz, 2001).



*Figure 4.8* Illustration of migration. The goal of migration is to shift the observed reflection point to the actual reflection point (line in red). The observed reflection point is migrated to a position of intersection between the wavefront curve and the approximate convex maxima of the diffraction curve. The apparent dip,  $b$ , of the observed reflection point and the actual dip,  $a$ , has a relation given by  $\sin(a) = \tan(b)$  (after Sheriff, 2002).

There are many different forms of migration such as diffraction, Kirchhoff, and wave equation migration. Within the wave equation sub-category there are a multitude of other methods. These include, for example the split-step Fourier approach by Stoffa et al. (1990) and the high-order Fourier transform based method by de Hoop et al. (2000). Most migration methods are based on the Fourier transform due to its ability to change seismic data from a time domain into a frequency domain and back again (Keary et al. 2002). These Fourier transform based methods are more favoured as they reduce artificial numerical dispersion effects that are common in finite-difference based methods (Huang and Fehler, 2001a).

The specific type of migration used by GECO Ltd was not defined in the original report, but it is likely to have been Kirchhoff migration as it was considered the most advanced form of migration in the 1980s.

---

### 4.13 Adaptive K-F Filtering

When a seismic wave travels through a medium, it moves in a sinusoidal fashion. As such, it is associated with a frequency,  $f$ , and wavenumber,  $k$ , component. The relation between these two components is given by the equation (Keary et al, 2002):

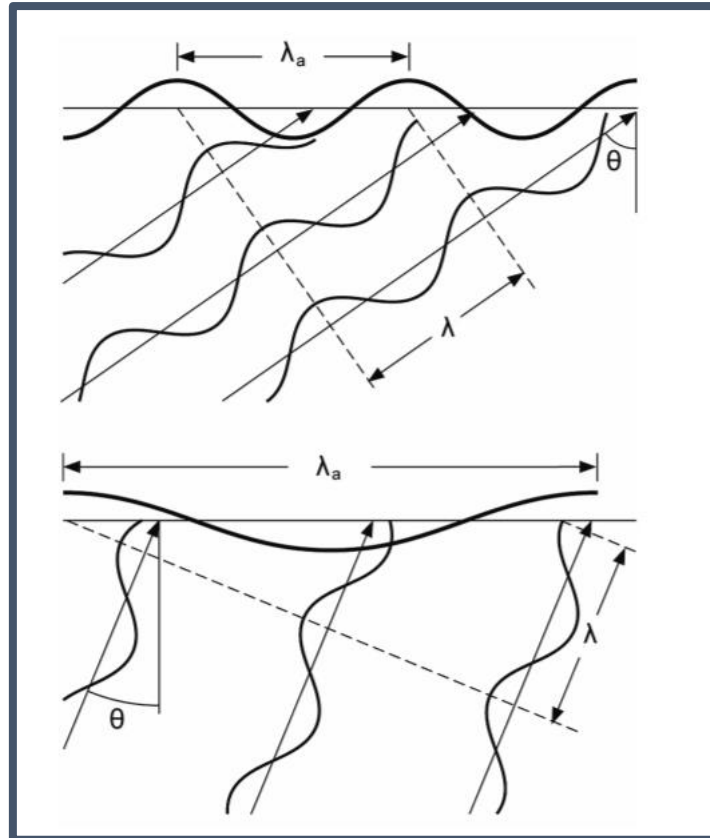
$$f = v_a k$$

where  $v_a$  is the apparent velocity which is subsequently given by:

$$v_a = \frac{v}{\sin\theta}$$

where  $v$  is the real propagation velocity and  $\theta$  is the angle of incidence on the receiver. The following Figure 4.9 illustrates the effect of various incidence angles on apparent wavelength,  $\lambda_a$ . Conversion from wavelength to wavenumber can be done using the equation:

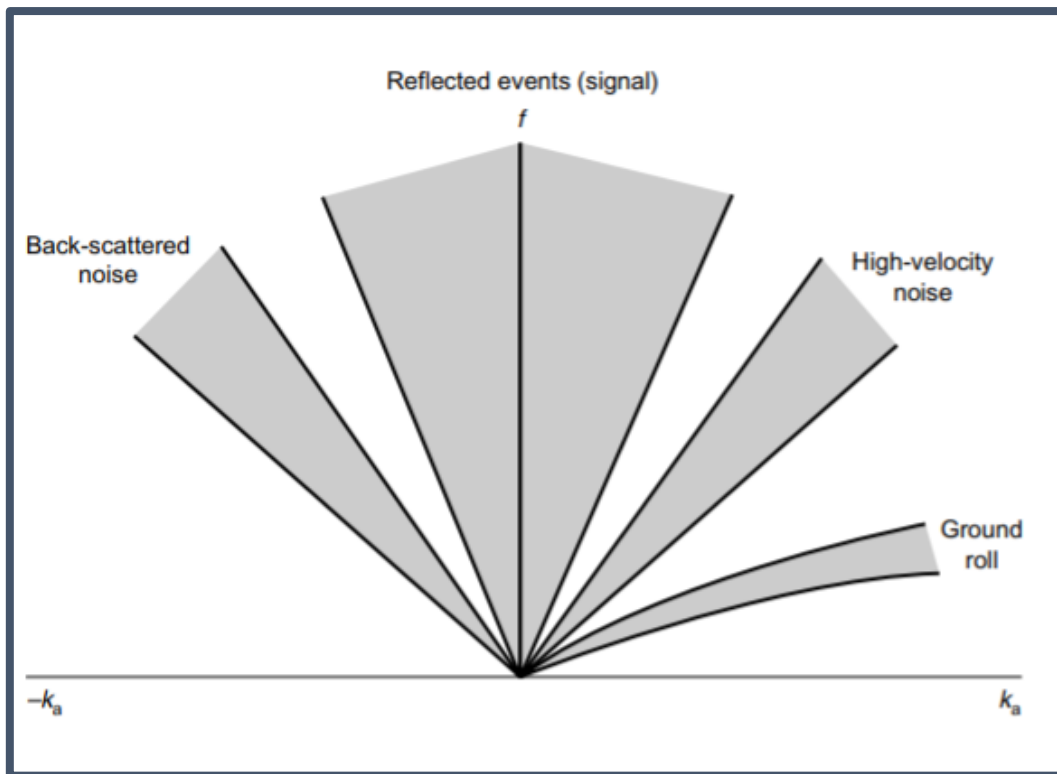
$$\lambda_a = \frac{1}{k}$$



*Figure 4.9 An illustration showing the relation of the angle of incidence of propagating waves on their apparent wavelengths,  $\lambda_a$ . Older geophones were only able record the apparent characteristics of the waves (2D components). By rearranging the above equations to find the real velocity and wavelength values of the incidence waves, the geophysicist is able to correctly assess and remove these coherent noise using f-k filtering (after Wiederhold, 2018).*

K-F filtering, or f-k filtering, uses the frequency and apparent wavelength characteristics mentioned previously of the incoming waves to distinguish and remove the coherent noise from real signals. As each type of coherent noise possess its own general unique frequency and wavenumber attributes (Figure 4.10), it makes it significantly easier to form a broad f-k filter targeting specific types of coherent noise.

For the 1987 Moutere Depression seismic data, GECO Ltd used an adaptive f-k filter. This was used as an additional post-migration filter that aimed at removing noise that may have been amplified during migration. The descriptive term “adaptive” refers to the time-variant element that has incorporated this filter.



*Figure 4.10 F-K spectrum showing the general frequency and wavenumber attributes of different forms of coherent noise (after Keary et al, 2002).*

## 5.0 New Processing Flow and Line 01 Results

The 2D seismic reflection processing flow and initial processing results for this project are outlined within this chapter. The general type of seismic processing flow used is one that leads to a post-stack migration sequence (Figure 5.1). The sequence follows the general method used by petroleum industry geophysicists, and follows the techniques outlined in the Globe Claritas Land Tutorial (2013), with adjustments made to suit the 1987 Moutere Depression seismic data. Each major process is outlined with its own heading, for example Residual Statics. Unless stated otherwise, processing of every seismic line of the MD87 survey will follow the same processing sequence. In light of this, chapter 5 is written in reference to line 01 with occasional figures from other lines to emphasise specific points. Results as well as notes for other lines will be shown in the ensuing Section 6.

Within this chapter, Globe Claritas modules and processors will frequently be referred to and made distinguishable by the capitalised font, e.g. DATUM\_FLT, FXDECON, AGC. The functions of these modules will be explained further in the text.

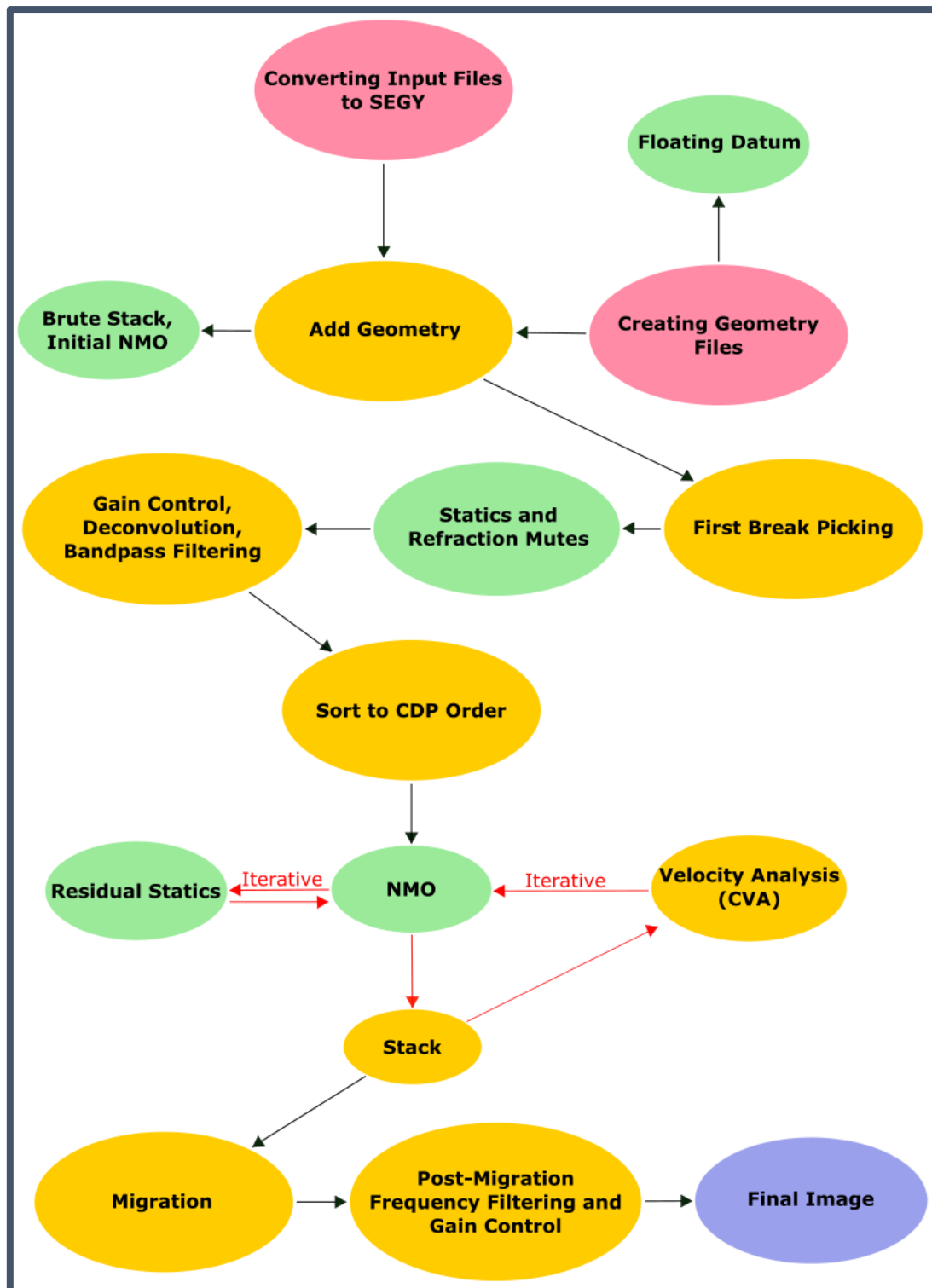


Figure 5.1 The overall 2D processing flow used for this project. Primary files involving and/or created by the raw data are in pink. While secondary files that are produced by major actions (yellow) are in green, these are either used as references or are combined back into the main file.



---

## 5.1 Line 01- initial notes

Line 01 posed a series of problems. Based off the observer's log, it seems that the crew were new to and were probably still being trained in the Vibroseis method. The first 300 or so shots appear to have been considered untrustworthy and so the whole survey was repeated. Numerous noise-control test shots labelled 900 - 999, were found and present throughout all the lines.

In addition to this, several geophones in the raw shot files were inactive. Erroneous peg numbering was recorded in the observer's log where the positions of shots did not correspond to the positions in the geometry file. Manual adjustments to the digital data were made to correct this problem.

Various shots had more than the designated 120 traces that were described in the initial survey parameters. A module was thus formed to remove these extra traces by using a series of IF-loops. These loops were also used to remove the first 300 flawed shots and the test shots (labelled 900 - 999).

A geometry file was then produced with manual picking of hit points used to define the trajectory of the binned seismic line. The resulting line had angles that were too sharp in places and it was unable to be processed as a smoothed wiggly line; instead, it was treated as a series of linear line gathers. The bin size parameters were made sizable enough to incorporate all traces.

---

## 5.2 Adding Geometry

The original position data were recorded in a United Kingdom Offshore Operators Association (UKOOA) format, which is the general format for land seismic surveys. The data were initially edited as a text file and then converted into a format which was merged into the headers of the seismic field data in SEG-Y format, or the Claritas-specific version CSG-Y.

The Claritas geometry application was used to create a rudimentary geometry base for this project. This application can be used for not just land surveys but also small complex marine

surveys too. The geometry was created using surveyor input (\*.sur) and observer logs (\*.obl) text file (where the asterisk refers to the name of the file). The prescribed format of these files also allows the geophysicist to produce a floating datum for static corrections required due to undulating topographies. The geometry file can also be created using a processor module "MAKEGEOM" within Claritas directly from the SEG-Y files, but this method is primarily for when there are no raw survey files available.

The MD87 study mainly utilised the \*.obl and \*.sur formats which are native to Claritas. The \*.obl observer logs provide information such as shot peg numbers, channel, source, receiver and records. Meanwhile, \*.sur logs compile the peg/geophone positions and elevation. Such surveying data additionally provide complementary information regarding specific traces and shots such as auxiliary and preliminary acquisition tests, while also detailing missing traces to help determine whether interpolation is required to make up for missing data.

A wiggly-line gather was then created, with hit-points selected via either the manual or automatic picking method depending on the line structure. While straighter lines such as line 02 permitted time saving via the automatic picking functions; however, both types of picking functions were tested on line 01. The more "wiggly" or "crooked" lines such as lines 04 and 08, required additional attention and utilised the manual picking function in order to bin and incorporate as much data as possible. The automatic picking feature of the program selects a certain number of hit-points at the geophysicist's discretion (generally around 40). These hit-points then connect, forming a processing line along which common mid-points must lie. Bin-size parameters were adjusted to include as many traces as possible without smearing the data during processing. Previously, the bin sizes were made so that some traces could be omitted to reduce overall processing time. However, the required processing time has exponentially decreased since the 1980s, making this a non-issue.

Selection for "extreme curvature" was included for certain seismic lines such as line 08. When this option is chosen, the program within Globe Claritas makes more calculations to compensate for the extreme changes in direction along crooked lines. The selection of this option results in a slightly more extended processing time.

Figure 5.2 (line 01) presents an example of the capability of the geometry function in Claritas. It can be seen that this line has a degree of extreme curvature in particular areas. The varying

colours shown in this image signify the change in elevation while the red circles with crosses represent the hit-points selected by the “auto-pick” function. The image additionally shows a cluster of yellow points that represent the traces lost from the common mid-point bins while creating the gather. These lost traces can arise from a number of reasons such as: the traces failing to fall into the capture area of the bin, or the maximum fold of the bin being reached. The latter of which, is more frequently the reason in wiggly lines. In the case of the image below (Figure 5.2), the maximum fold of 120 traces per bin was exceeded.

The maximum fold of a survey can be expressed by the following equation:

$$F_{max} = \frac{C_n \times C}{2 \times S}$$

where  $F_{max}$ ,  $C_n$ ,  $C$  and  $S$  are the maximum fold, the number of channels, channel spacing and shot spacing respectively.

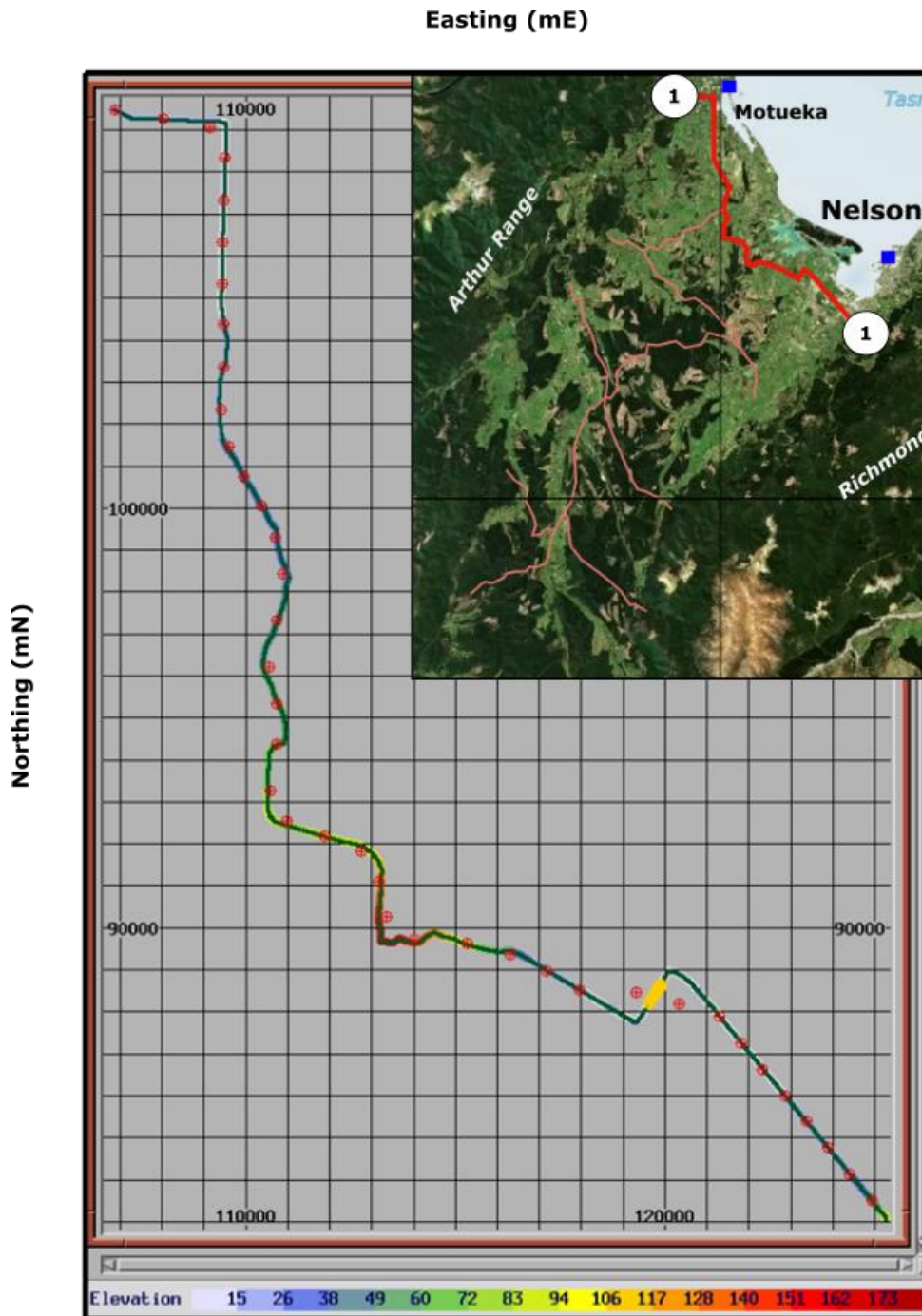


Figure 5.2 The geometry for line 01 in Claritas. The red circles represent the hit-points for CDP binning while the yellow highlighted area is the location of lost traces. A cropped topographical map of Figure 1.1 has been added to provide a reference to the rest of the survey. Grid scales of the geometry are northings and eastings (mN, mE) in the NZMG coordinate system. Elevation is metres above MSL (m).

### 5.3 Floating Datum Application

A floating datum file (\*.shf) was created at the same time as assigning geometry for the seismic line (Figure 5.3). The purpose of this file is to correct for time delays caused by topographical changes on the ground surface. Thus, a series of time shifts are produced and applied prior to NMO and stacking to combat these time distortions, potentially effecting NMO hyperbolas.

The floating datum calculations are dependent on three main variables: the fixed datum ( $D_f$ ), the replacement velocity ( $V_r$ ) and the smoothed time shifts for each CDP ( $t_{smooth}$ ). The equation of which is given by:

$$\text{Floating Datum} = D_f + \left( V_r \times \frac{t_{smooth}}{2000} \right)$$

The fixed datum is an arbitrary elevation that can be any value but is usually picked to be slightly higher than the source/receiver elevations to minimise the total of time shift required for each CDP. The replacement velocity variable in the equation is the sub-weathering rock velocity. For this project,  $V_r$  was estimated and was replaced at a later stage when first breaks were picked. The smoothed time shift values were determined by the elevation static corrections for each trace. The traces were then grouped into CDPs, averaged and heavily smoothed using a sizable running mix. By smoothing the values at the end of the geometry process, it reduces the effects of any discontinuities which may disrupt seismic horizons.

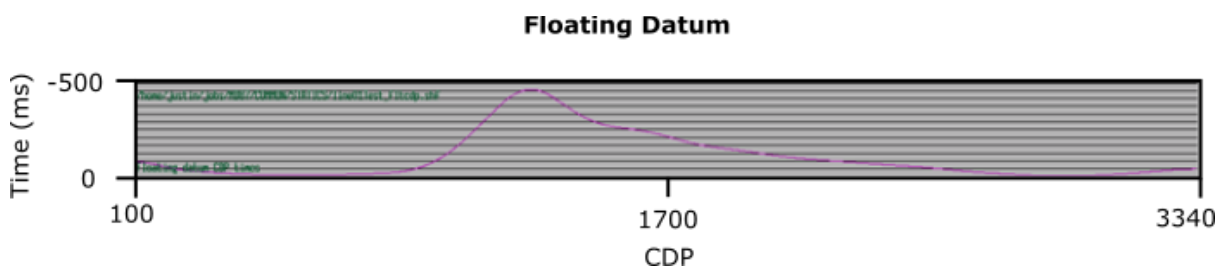


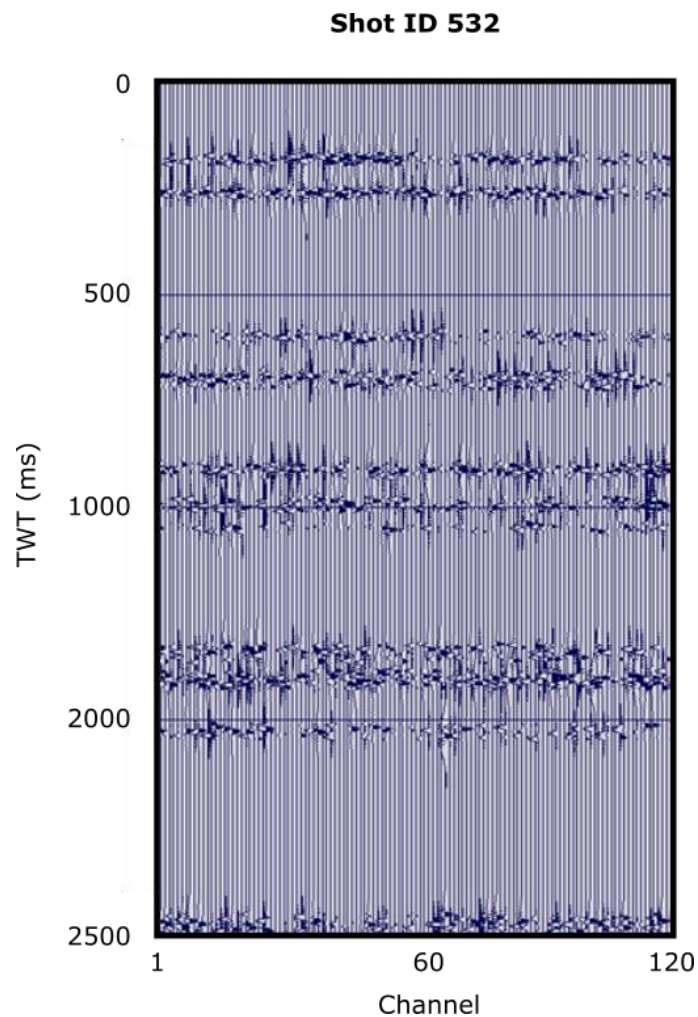
Figure 5.3 A graphical representation of the floating datum time shifts established for line 01.

---

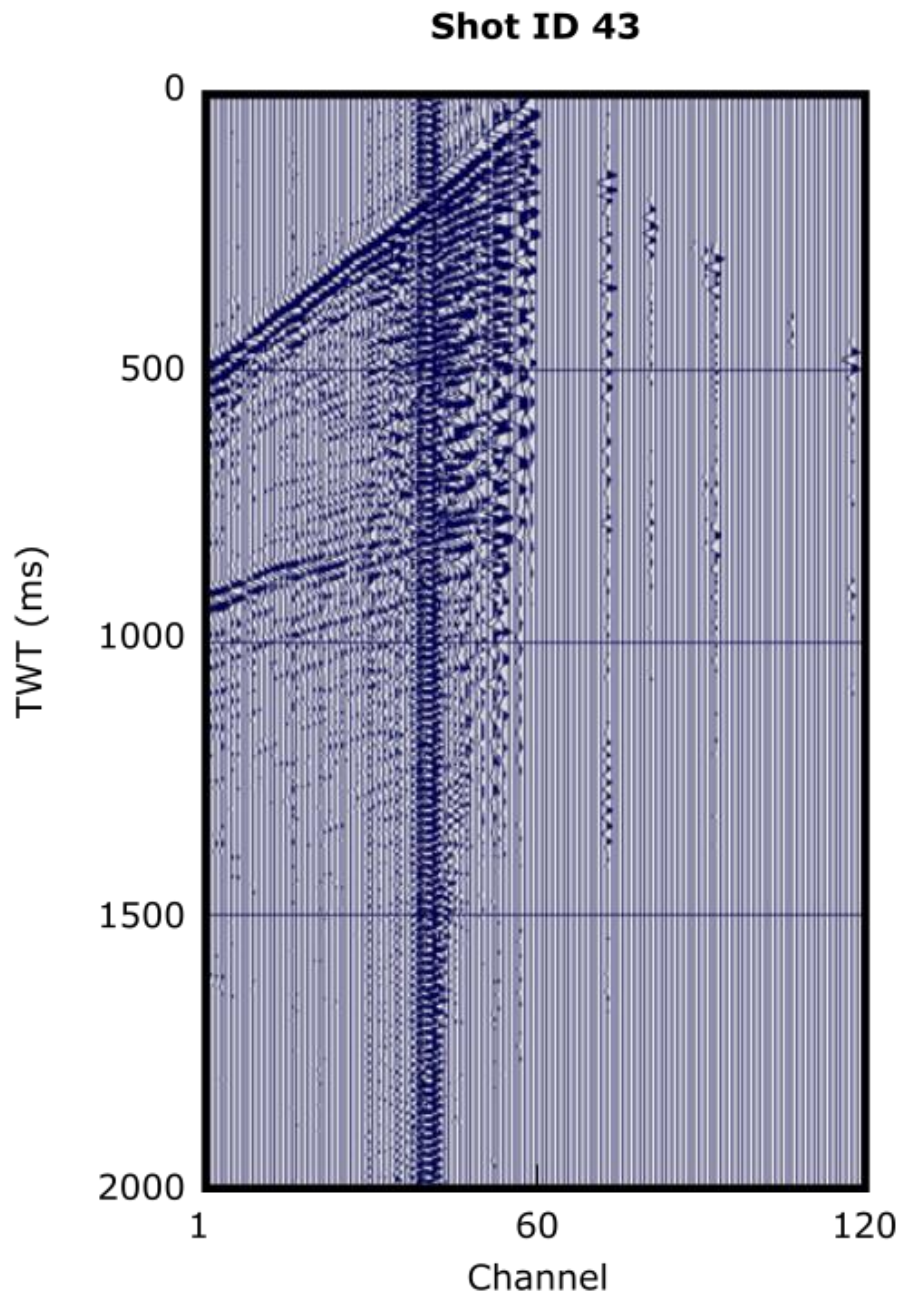
## 5.4 Pre-stack processing Trace Removal

At this stage, poor shots and noisy traces were investigated and either muted or killed. Faulty geophones, extreme electrical noise (Figure 5.4a) and noisy traces (Figure 5.4b) were present throughout all eight seismic lines. However, the frequencies of their occurrence vary from line to line.

For line 01 in particular, there were several shot records that were short and contained no signal after a certain travel time,  $t_0$  (e.g. Figure 5.5b). However, these were a non-issue as they did not have a major impact on the overall seismic image. A regular shot with no peculiarities is shown in Figure 5.5a for comparison.

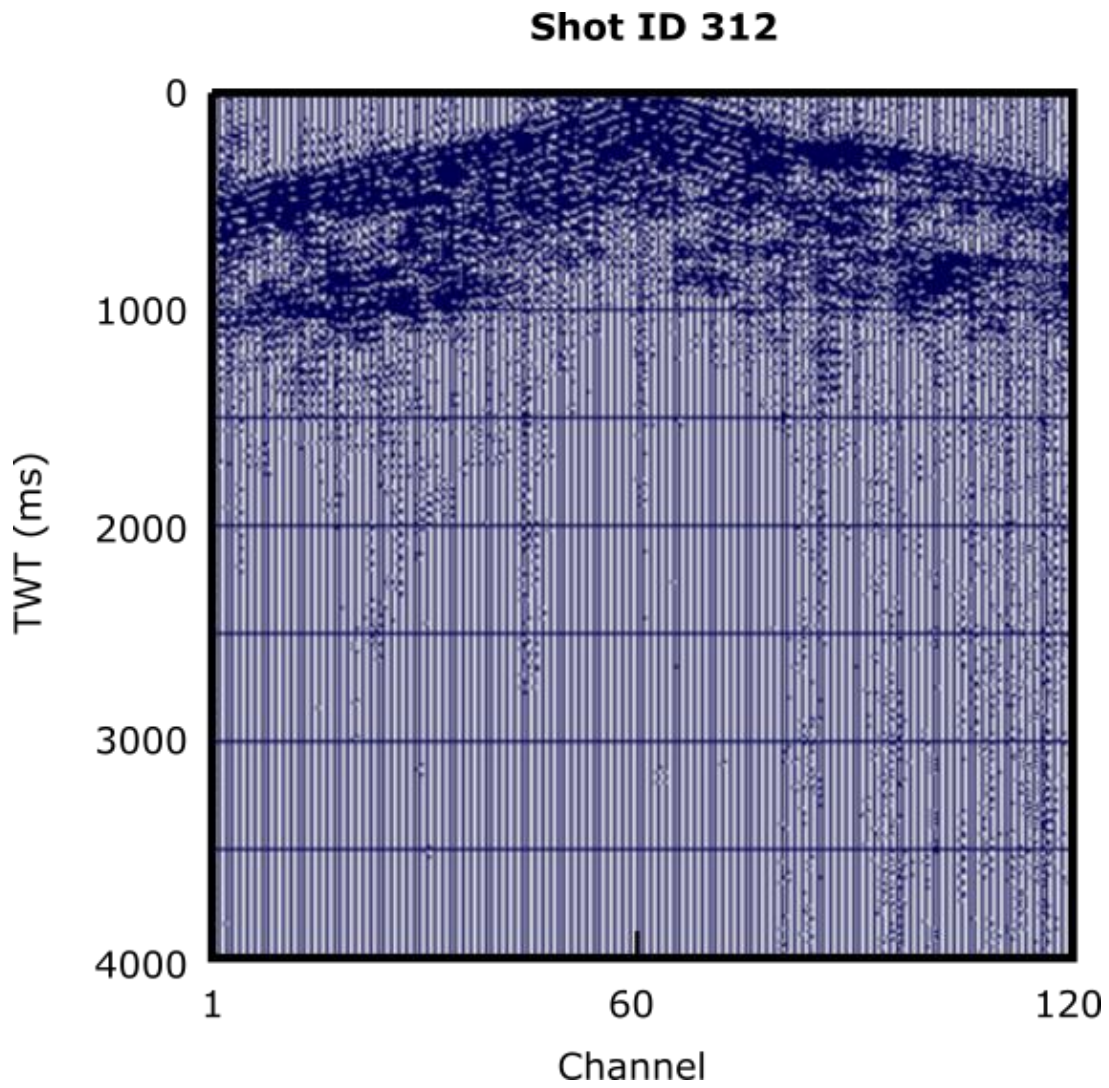


*Figure 5.4a* Shot gather 532 of line 01. Electrical noise can be easily identified based on how ubiquitous, instantaneous and similar in shape it is throughout the shot gather.



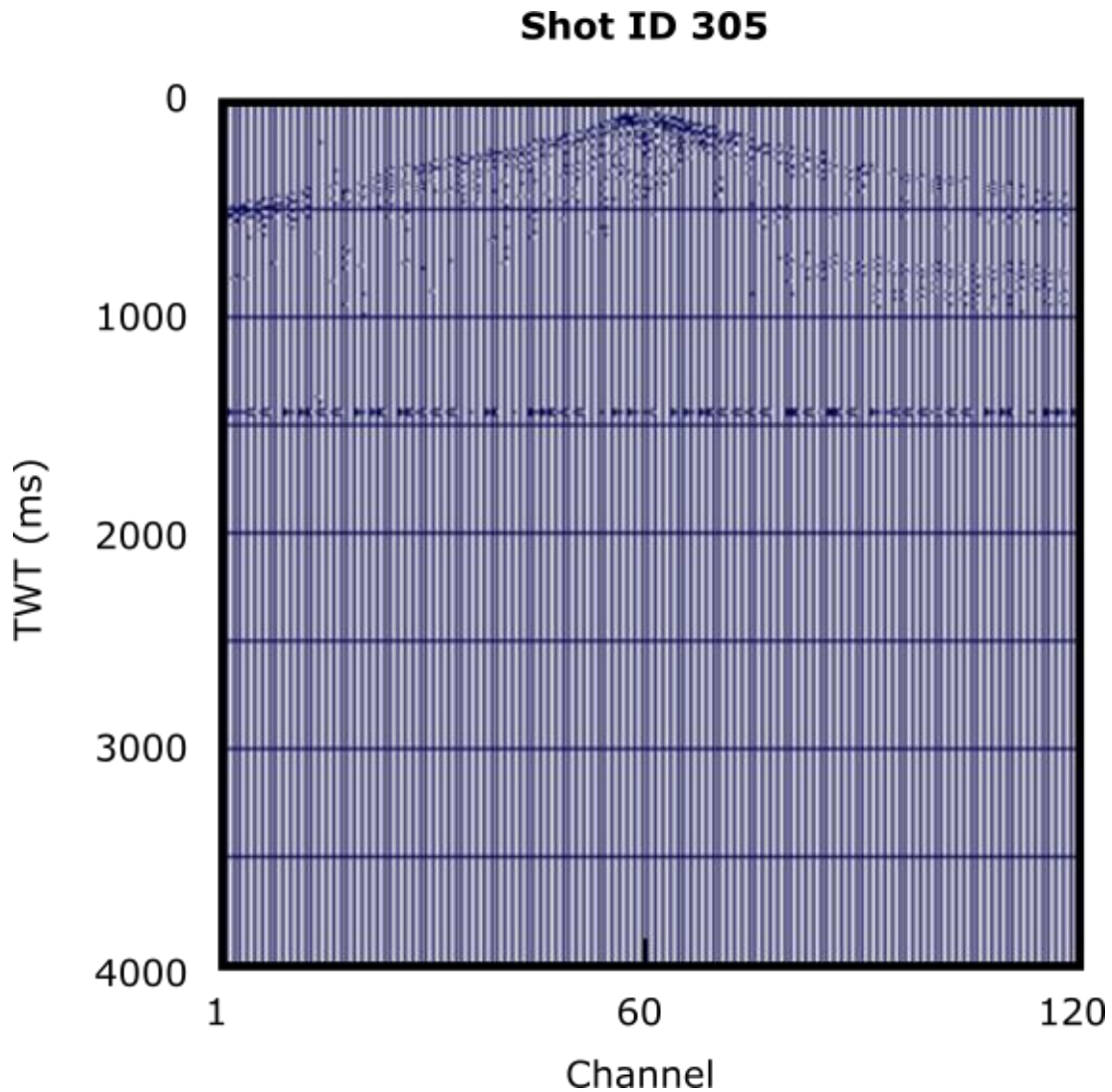
*Figure 5.4b* Raw shot gather 43 of line 01 with evidence of noisy channels about channel 40.





*Figure 5.5a* Shot 312 of line 01. A regular shot gather with signal present throughout the whole image. A “balance” amplitude enhancement has been used to improve the image for viewing purposes.

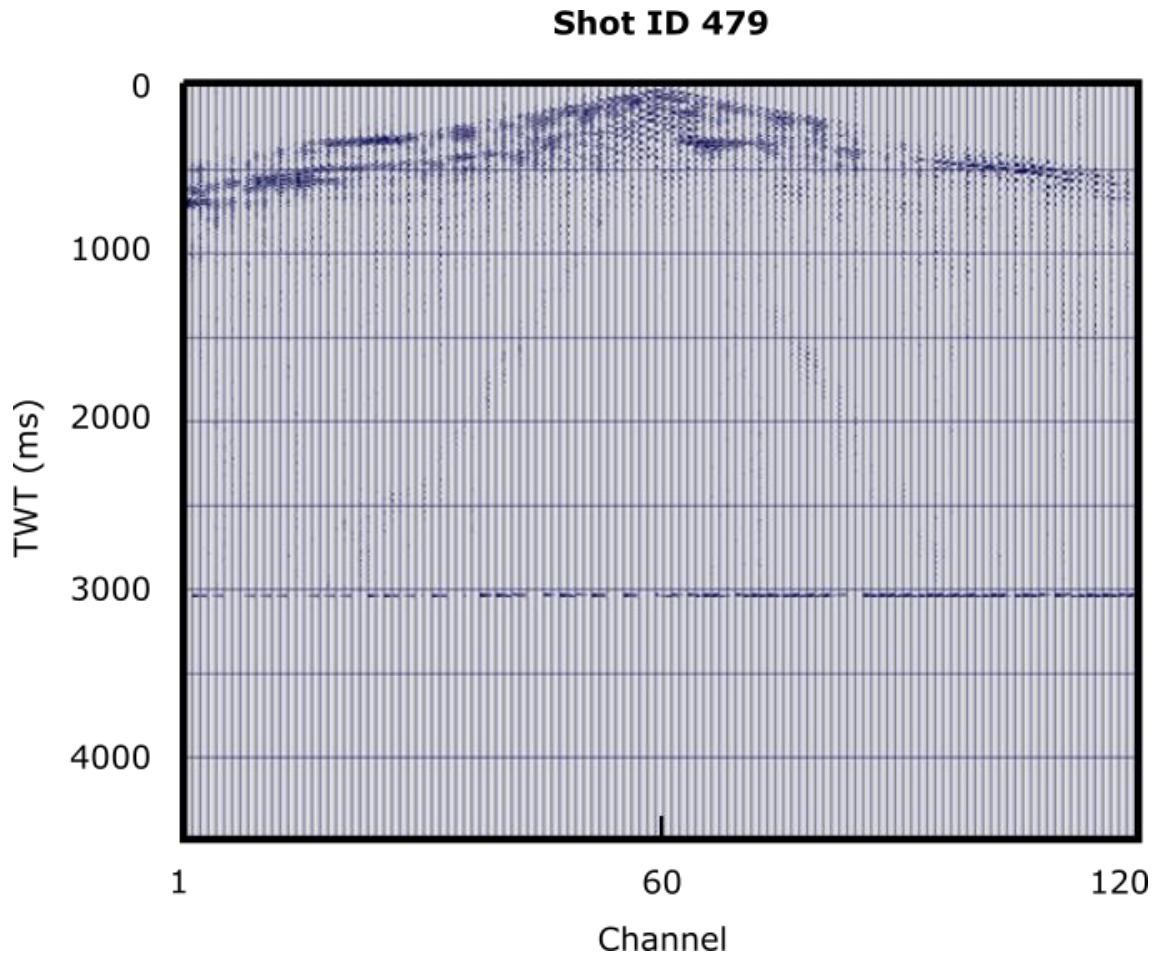




*Figure 5.5b* Example of a short shot (shot 305) to compare to a regular length shot (Figure 5.5a). In shot 305, the signal ends at just before 1500 ms. Note the obvious electrical noise present in shot 305. A BALANCE amplitude enhancement has been applied to the image for viewing purposes.

Some shots presented a series of distinguishable, uniform spikes in amplitude that were carried over across all the channels. An example of this would be shot 479 shown in the figure below (Figure 5.6) and the previous image (Figure 5.5b). The uniform spikes in amplitude are deemed to be electrical noise due to their consistent and ubiquitous nature across the traces. To combat this problem, DESPIKEV and DESPIKEH Claritas muting modules were trialed. These proved much more efficient than the initial method of manually

removing the individual traces for each shot. The two muting modules were placed within the ADDGEOM job flow.



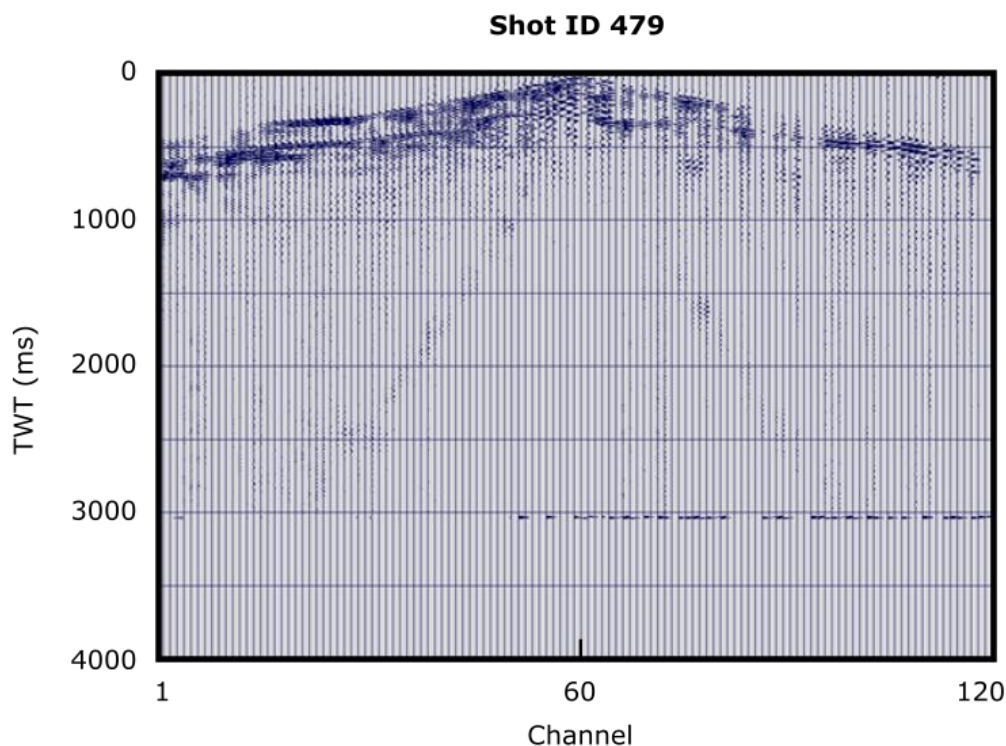
*Figure 5.6 Raw shot gather of shot 479 of line 01. A distinguishable series of spikes can be seen in the horizontal direction of the image at 3000 ms where recording truncated early. No form of amplitude enhancement has been applied to the image.*

## DESPIKEH

The DESPIKEH process module in Claritas removes incoherent data from the traces in the horizontal direction. The module operates on the average absolute amplitude of a trace within a specified window length. If a spike exceeds the specified high amplitude envelope, the module compares the amplitudes with the traces that are immediately adjacent to it. If the amplitude spike does not occur on both sides, the spike is flagged and then muted.

The module determines the average amplitude for a predetermined window length within the trace. Therefore, the average amplitude is dependent on the chosen window length. As a result, if a longer window length is chosen, it would trigger less readily because there would be a wider range of amplitudes.

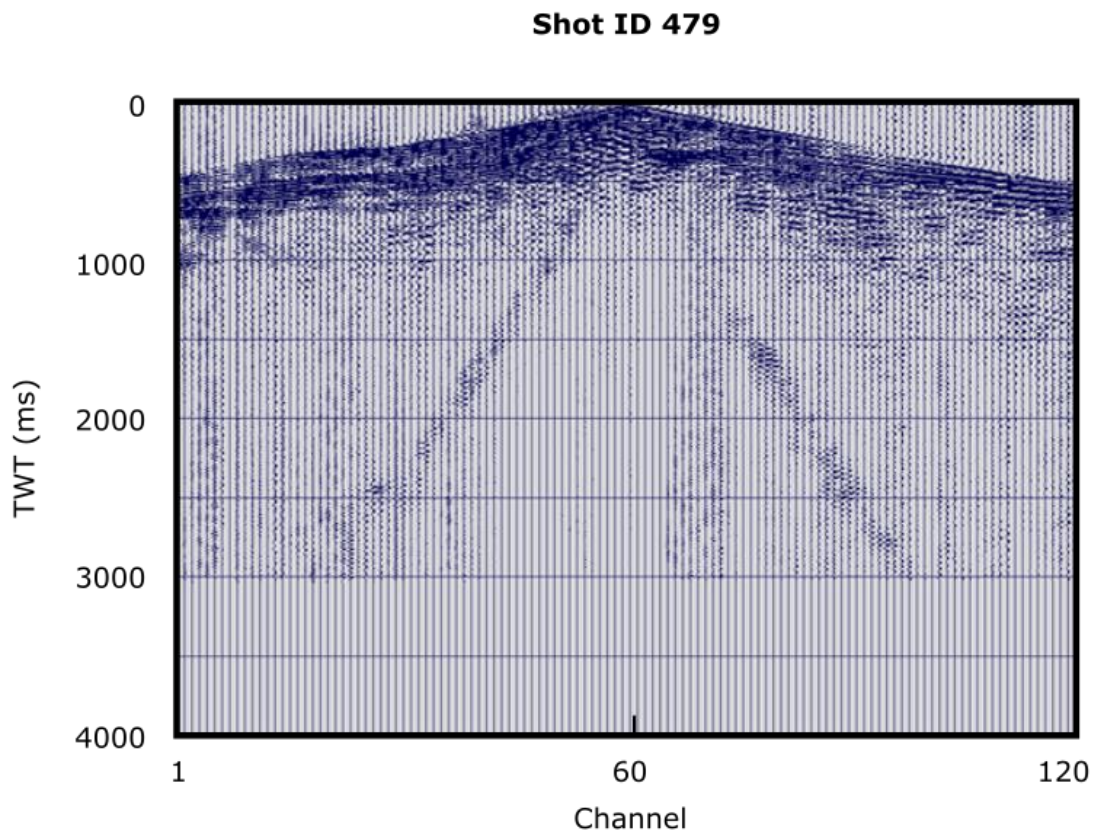
Because of the nature of the spikes occurring horizontally in line 01, DESPIKEH would only partially remove the spikes, since both sides of the neighbouring traces would contain this noise and the algorithm would not recognise them as an anomaly (Figure 5.7).



*Figure 5.7 The DESPIKEH process module was applied to shot 479 of line 01. The module produced a partial removal of the amplitude spikes. No other AGC or equivalent process has been applied to this image.*

## DESPIKEV

The DESPIKEV module was more successful in muting the electrical noises in line 01 (Figure 5.8). It operates with the same parameters as DEPSIKEH except it compares the average amplitudes of the same trace as opposed to neighbouring traces. The DESPIKEV performs a long running average (LRA) together with a short running average (SRA). If the SRA exceeds the LRA, the spike is removed. Naturally, the time window of the SRA and the LRA can be adjusted.



*Figure 5.8 The application of DESPIKEV on shot 479 of line 01. A full successful removal the spikes along 3000 ms compared to Figure 5.7.*

## FILLHOLES

The FILLHOLES module may be applied later in the sequence to fill in zeros in the traces arising from DESPIKEV. Using the TREDIT module, noisy and poor traces from poorly connected geophones or environmental noise are removed. This module also removes non-live traces. The final geometry job flow is thus formed and shown in the table below (Table 5.1).

*Table 5.1 A general job flow used to add geometry to the shot file. Modules can be toggled on or off or added in depending on the requirements of each individual line.*

Geometry Job Flow		
Order	Claritas Module	Purpose
1	DISCREAD	Reads input *.csgy shot file
2	TREMOVE	Removes non-live traces
3	IF	Creates first <i>if-endif</i> loop
4	TREMOVE	Removes extra channels 121-150
5	ENDIF	End of first loop
6	IF	Creates second <i>if-endif</i> loop
7	TREMOVE	Removes test shots 900 - 999
8	ENDIF	End of second loop
9	TREDIT	Mutes specific traces via *.tre file
10	ADDGEOM	Incorporates geomtery file
11	AREAL	Identification of noisy shots
12	DESPIKEV/DESPIKEH	Incoherent spiking noise removal
13	FILLHOLES	Fills empty gaps in traces
14	BALANCE	Gain balancing for traces
15	DISCWRITE	Writes new output file

---

## 5.5 Brute stacking

Brute stacking allows for an initial understanding of the data and additionally helps identify the problems which may arise during data processing. This form of stacking uses raw data with minimal or no processing, or velocity analysis which consequently gives it its other name, "raw stacking". The job flow created for brute stacking is outlined in Table 5.2 and the final stacked product is shown in Figure 5.9.

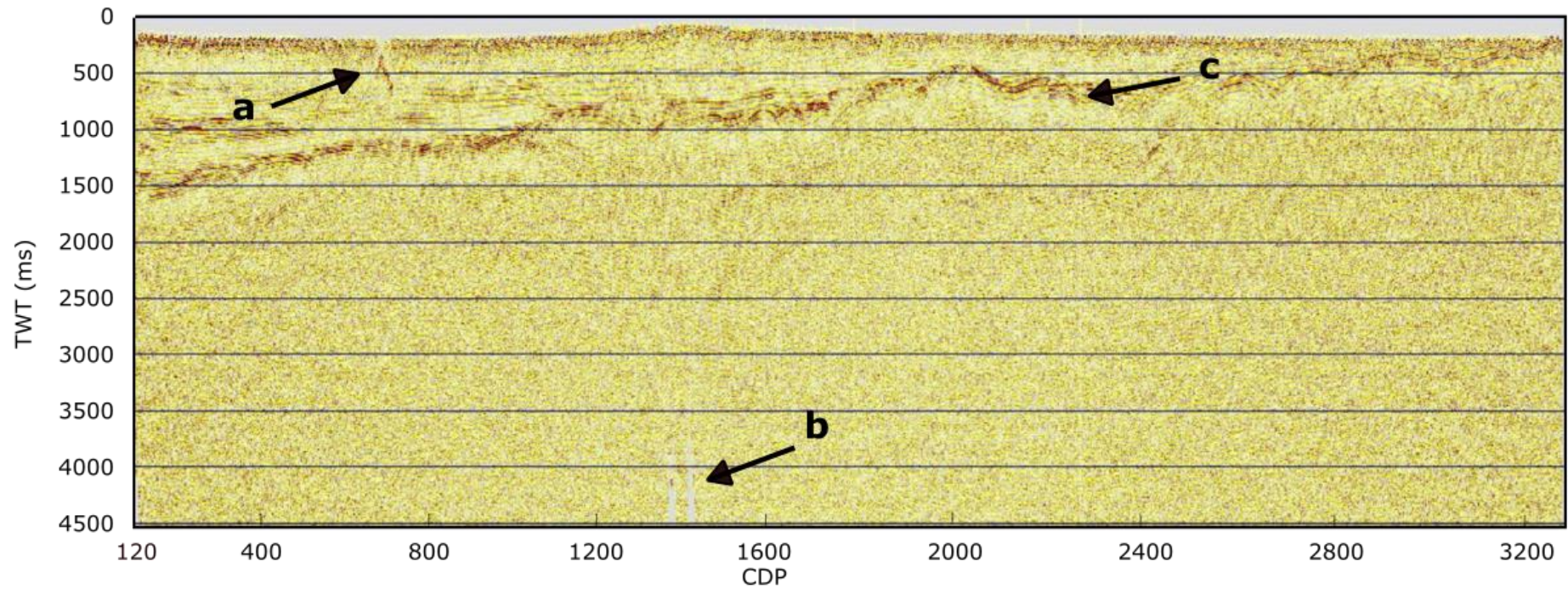
The brute stacking process first begins by rearranging the primary and secondary key headers to prepare the file for stacking. Shots and channels are sorted to CDP and CDPTRACE respectively since stacking is performed in CMP or CDP format as explained in Chapter 4.9. The data was corrected to the floating datum via the DATUM\_FLT module using the \*.shf file created during the geometry stage.

Following sorting to CMP's, a frequency filter (FDFILT) removes the excessive noise and a basic or predetermined normal move out (NMO) correction is applied to adjust for time-offset delays. In terms of the stretch mute and automatic gain control parameters, an automatic value of a window length 500 ms and stretch mute of 70% have been picked. Further testing of gain control will be explored in Section 5.9.

*Table 5.2 Job flow for brute stacking. Static and stretch mutes can be applied if necessary but was not applied to raw stack of line 01.*

<b>Brute Stacking Job Flow</b>		
<b>Order</b>	<b>Claritas Module</b>	<b>Purpose</b>
<b>1</b>	DISCREAD	Reads in CDP ordered*.csgy file with geometry file applied
<b>2</b>	FDFILT	Applies a frequency filter
<b>3</b>	STATIC	Applies static corrections
<b>4</b>	SMUTE	Surgical mutes on specific traces
<b>5</b>	NMO	Applies *.nmo file to correct travel times
<b>6</b>	STACK	Normal stacks the seismic data
<b>7</b>	DATUM_SRD	Corrects floating datum to seismic reference datum
<b>8</b>	AGC	Gain control for viewing purposes
<b>9</b>	DISCWRITE	Writes out stacked output file





*Figure 5.9* Raw stack of line 01 with a 500 ms AGC applied for viewing. Arrow **a** points to an area with an artefact possibly caused by some form of near surface noise. Arrow **b** shows an area where the short shots occurred. Arrow **c** indicates a yellow straight line, that was created by the agc, to fill the empty traces/shots that were removed because they were either dead or too noisy.

---

## 5.6 First Breaks

First breaks were then picked in the shot records to detect the refracted signals at the contact between the initial weathering layer (with a velocity of  $V_0$ ) and the sub-weathering layer. The breaks are selected using the Seismic Viewer (SV) utility in Claritas which allows further inspection of each shot (Figure 5.10 - 11). The program has multiple methods to determine the first breaks. There are automatic picking options in Claritas as well as manual options, the former of which was preferred for this project. While the latter was used as a refinement procedure for several lines.

The automatic picking option was divided into three different segments: primary, secondary and tertiary. The primary pick was based around Linear Move-Out (LMO) to calculate the estimates of the first breaks.

The LMO calculations followed the equation:

$$T_{pick} = T_{LMO} + 1000.0 \times \frac{Offset}{V_{LMO}}$$

where  $T_{pick}$  is the expected time,  $T_{LMO}$  is the starting time and  $V_{LMO}$  is the selected LMO velocity for first breaks. The 1000.0 value is a constant used for conversion between seconds (SI unit) and milliseconds. This equation will be used once more for the estimation of arrival times in the “Areal Noise Analysis Module” in Section 5.7.

The next parameter required for picking for first breaks was the secondary pick, also known as the main pick. For this segment, an envelope threshold was required. First break values that were previously determined in the first segment were scrutinised. If the numbers exceed the geophysicist’s envelope threshold, then the estimate was rejected. The rejection value used for line 01 was 0.539. The algorithm used for this type of picking is based on the Hilbert transform which calculates the instantaneous seismic amplitude. The transform itself can be considered as a filter which shifts the phase of all frequency components of the input signal by  $-\pi/2$ . The equation is defined as:



$$h(t) = \frac{1}{\pi} \int_{-\infty}^{\infty} \frac{f(\tau)}{t - \tau} d\tau$$

where  $h(t)$  is the Hilbert transform of some signal  $f(\tau)$ .

For convolution purposes the above equation can be rewritten as:

$$h(t) = \frac{1}{\pi} * f(\tau)$$

The beauty of the Hilbert transform is that it allows the construction of a complex analytic signal of a real input signal. i.e. the seismic signal.

$$Y(t) = y(t) + ih(t)$$

where:

- $Y(t)$  = the complex analytic signal.
- $y(t)$  = the real input signal.
- $h(t)$  = the Hilbert transform of the input signal.
- $i$  = the imaginary component of the complex equation.

With the construction of a complex equation, it can then be converted to its exponential notation.

$$Y(t) = A(t) \exp[i\Psi(t)]$$

where:

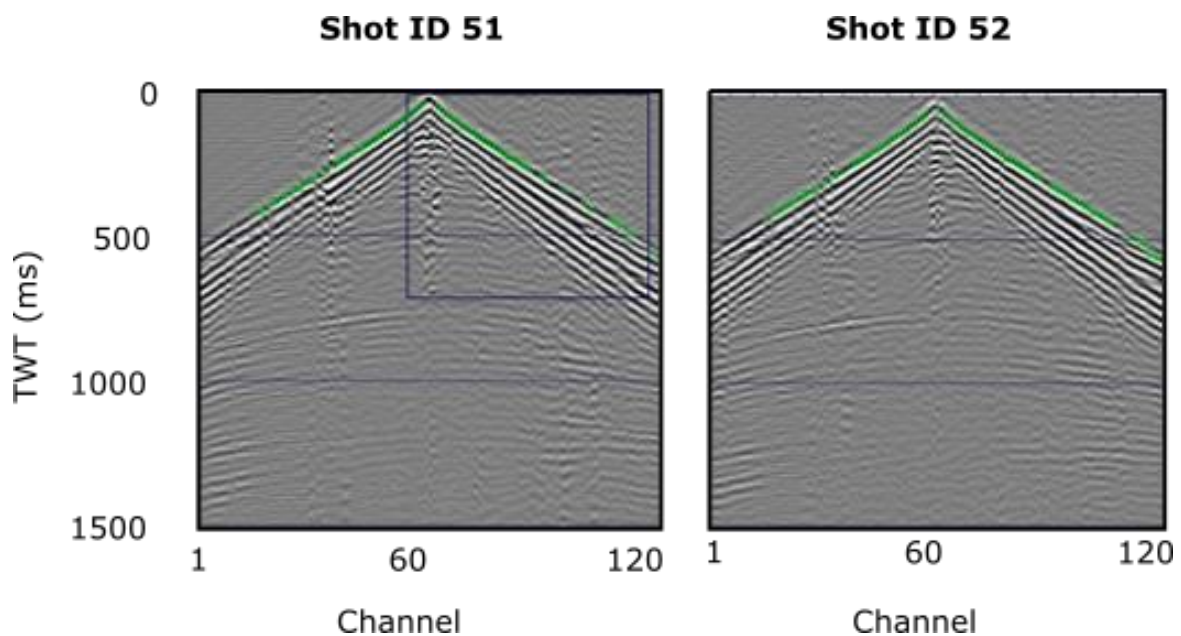
- $A(t)$  = envelope of the analytic signal also known as the instantaneous amplitude.
- $\Psi(t)$  = the instantaneous phase of the signal.

The  $A(t)$  value is particularly helpful to find the envelope of simple harmonic signals such as the impulse response. If we calculate the derivative of the instantaneous phase, we will achieve the instantaneous frequency.

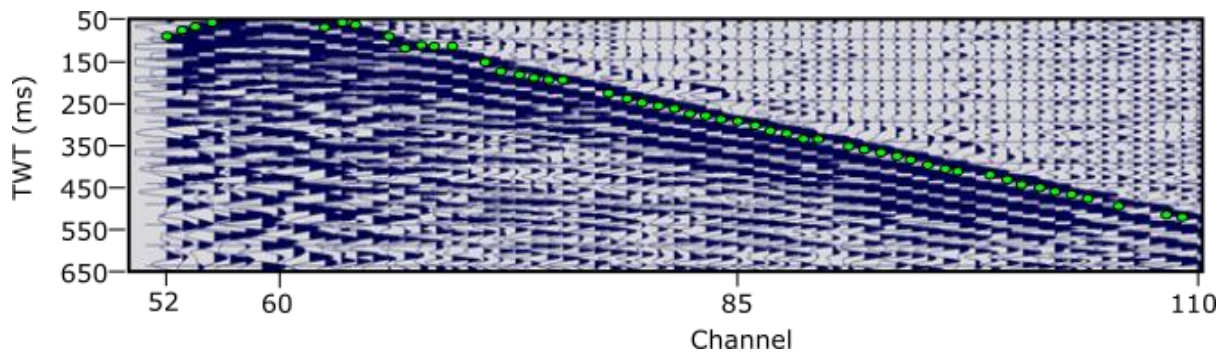
$$f(t) = \frac{1}{2\pi} \frac{d\Psi}{dt}(t)$$

The instantaneous frequency is used for deducing the sweeping signals (Vibroseis seismic signals). This method is used heavily in medical imaging, array processing for direction of arrivals and sampling of narrow band signals.

The third stage of the Claritas picking process is refinement of picks which further adjusts the picks to closer waveform peaks. During this stage the program will reject picks that exceed certain envelope values. The rejection parameters calculated uses the RMS amplitude (RMS1) down the trace before a certain time window and the RMS (RMS2) amplitude after. Whether or not the pick is deemed acceptable depends on the ratio of RMS1 to RMS2. The higher this ratio is, the noisier the trace will be.



*Figure 5.10 First break picking using the SV application in Claritas for shot 51, line 01. Selected first breaks are shown by the green dots. The program interprets the pick parameters carried out on a particular shot and applies them to the other shots intuitively. Manual picks can be used as well to improve the calculated picks done by Claritas.*



*Figure 5.11 An enlarged image of the square in Figure 5.10 of shot 51. The Variable Area Wiggly-trace Gather (VAWG) makes it easier to identify the maxima and minima of the refracted wavelets.*

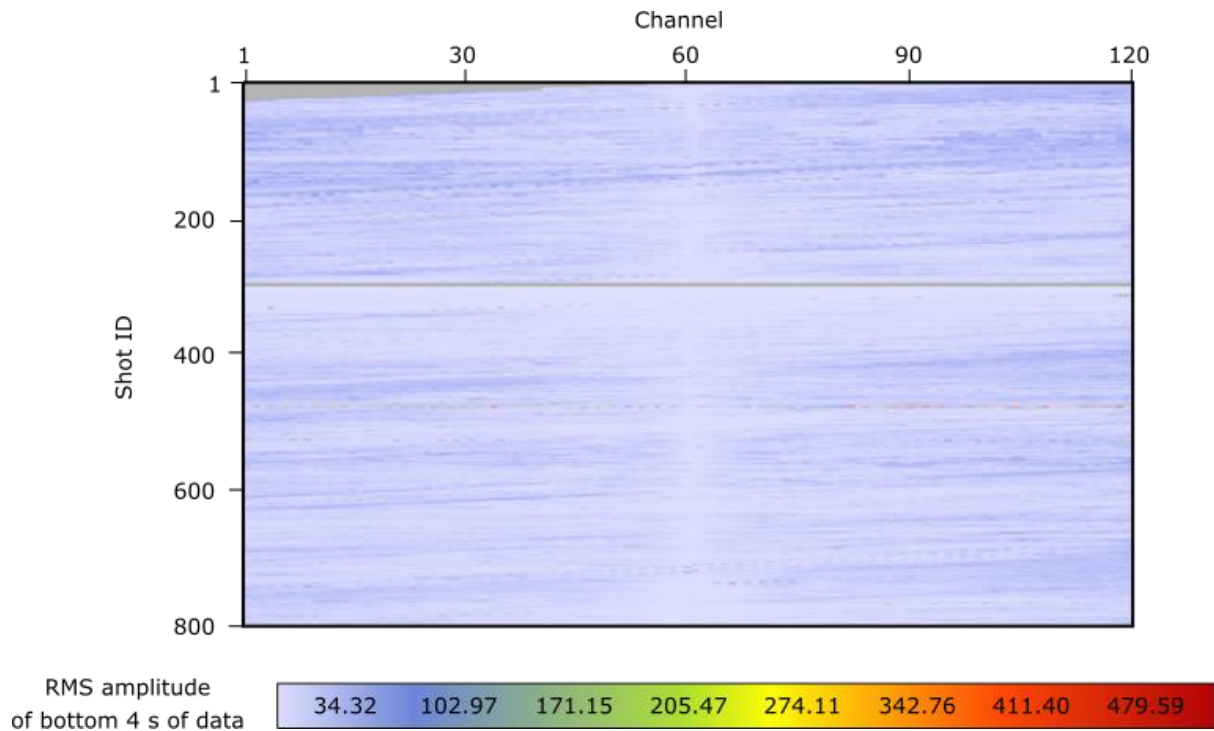
---

## 5.7 AREAL Module

This module identifies regions in the data of ambient and/or environmental noise that is prevalent in land surveys. These sources can be caused by many factors such as: wind, rain or vibrations from industrial machinery. Such noises are generally sedentary and do not alter much down the trace and therefore, can be stacked out.

AREAL extracts information from seismic traces and/or headers and compiles it into a text file for use in the AREAL application. The AREAL application is a graphical process where it can plot displays with regards to the seismic data time-slice, trace amplitudes, shot/receiver statics, RMS amplitude on plots and 3D fold plots.

Prior to data extraction, a job flow consisting of the DATUM\_FLT, STATIC and AGC modules was applied. This was laid out to correct for the elevation, refraction statics and spherical divergence amplitude decay. Three AREAL modules were included in the job flow to target different areas of the seismic data. The first AREAL module was used to extract the RMS amplitudes of the last 5 s of the seismic data (1 to 6 s) as the most valuable part of the data located in this section (Figure 5.12).



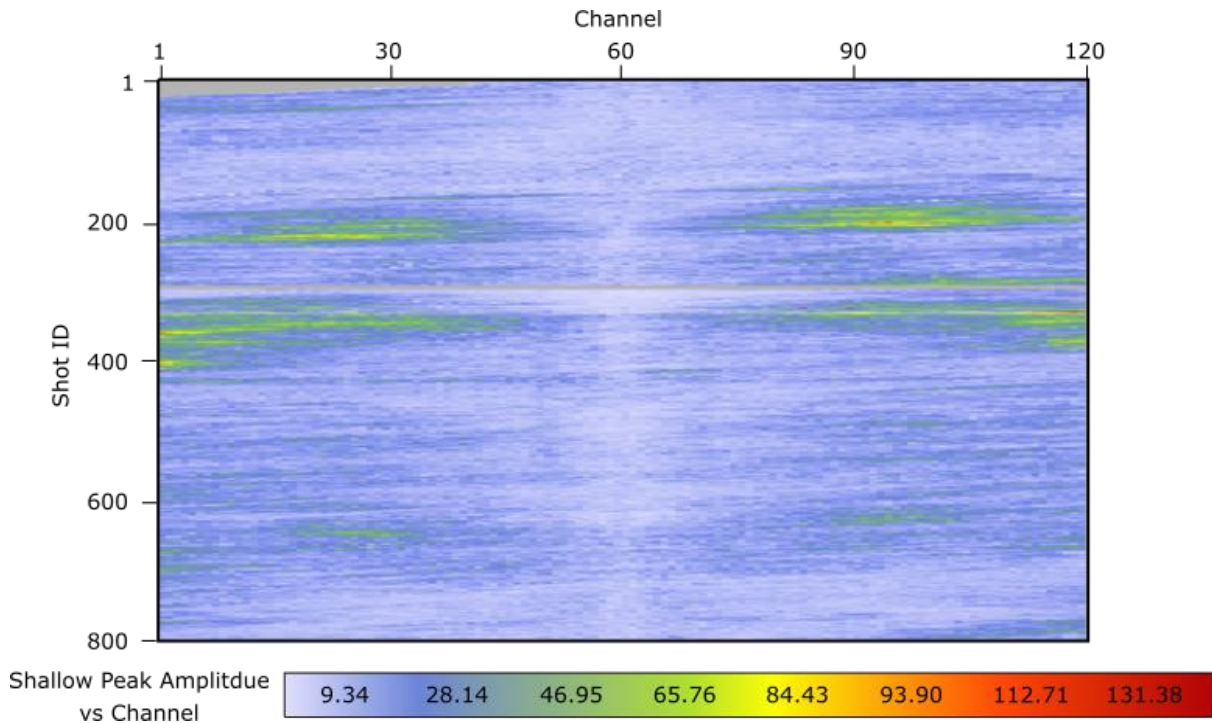
*Figure 5.12 An AREAL image showing the RMS amplitudes of the bottom 5 s of the seismic data of line 01. There is little environmental noise present in this image.*

The line is mostly devoid of environmental noise as seen in Figure 5.12. The gap in data in the middle of the image is from an absence of data in seismic line 01, where the surveyors skipped shots 296 - 303 because of building obstructions.

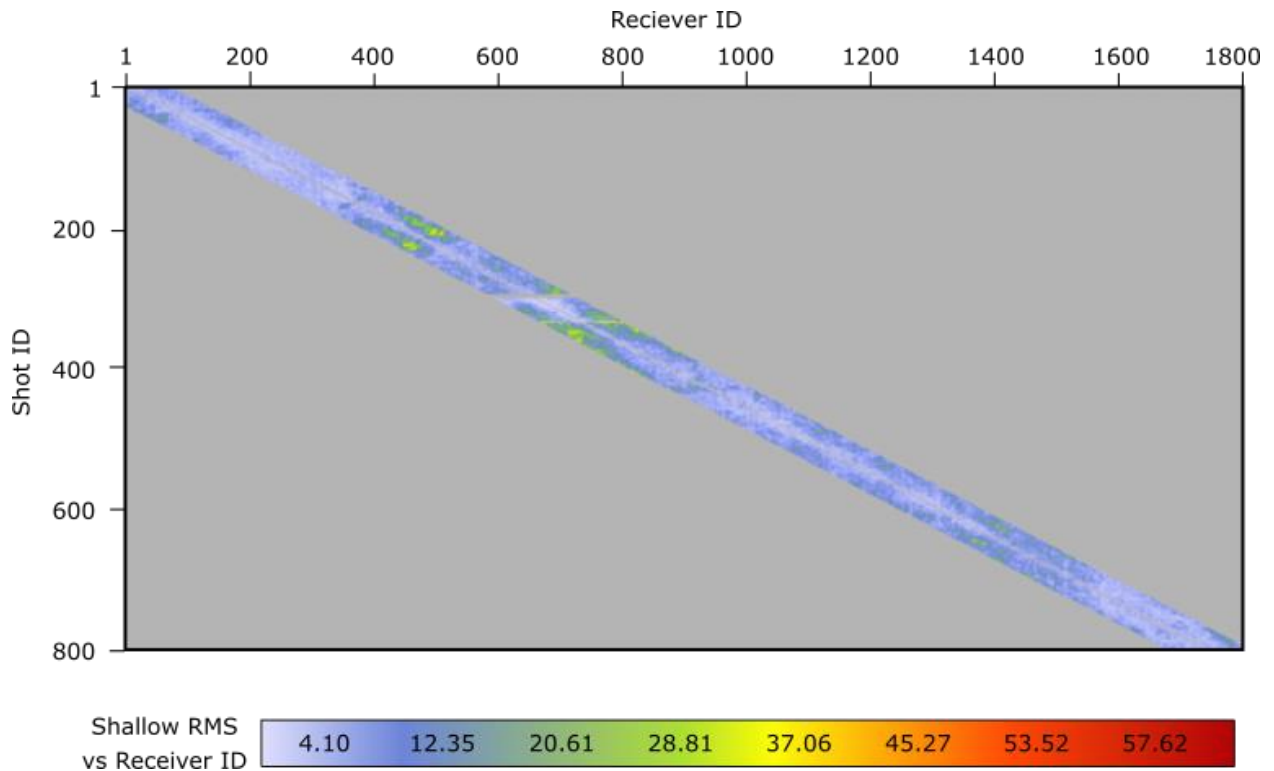
Two additional AREAL modules that were inserted were used to measure the peak and RMS amplitudes in the shallow parts of the sections. The second AREAL module had an x-axis for channels (Figure 5.13), while the third module had one for receiver pegs with both modules having a y-axis of shot ID (Figure 5.14). The purpose of these two modules was to measure the background amplitude of the data before the first arrival. Because the estimated arrival time has not been calculated yet, we created an additional dynamic trace header with the formula:

$$T_{est. arrival} = 1000 \times \frac{|x_{offset}|}{V_{LMO}}$$

It can be seen that the value that the formula produced is very similar to that found in the “First Breaks” section, where  $T_{\text{est. arrival}}$  is equivalent to  $T_{\text{pick}} - T_{\text{LMO}}$ . The 10.0 division of the offset is for conversion into decimetres.



*Figure 5.13 AREAL file showing the shallow peak amplitudes of line 01, with shot ID plotted against channels. It can be seen that the channels are slightly noisier than the deeper sections with a couple of spikes found at shots 355 and 410. The miniscule number of high amplitude values makes this a non-issue when it comes to affecting the seismic image. However, we ended up selecting a value of 45.45 for flagging which only removed approximately 1% of total traces.*



*Figure 5.14 The shallow RMS amplitude values relative to the receiver pgs. There are a couple of high amplitude receivers present in this image. Amplitudes of 18.13 and greater were for flagged and edited out, thereby removing approximately 3% of traces.*

All three images show that environmental noise is largely absent. Once an appropriate amplitude threshold has been selected, higher amplitude values are flagged and the data is extracted as a text file which can then be used by the TREDIT process module to be removed.

---

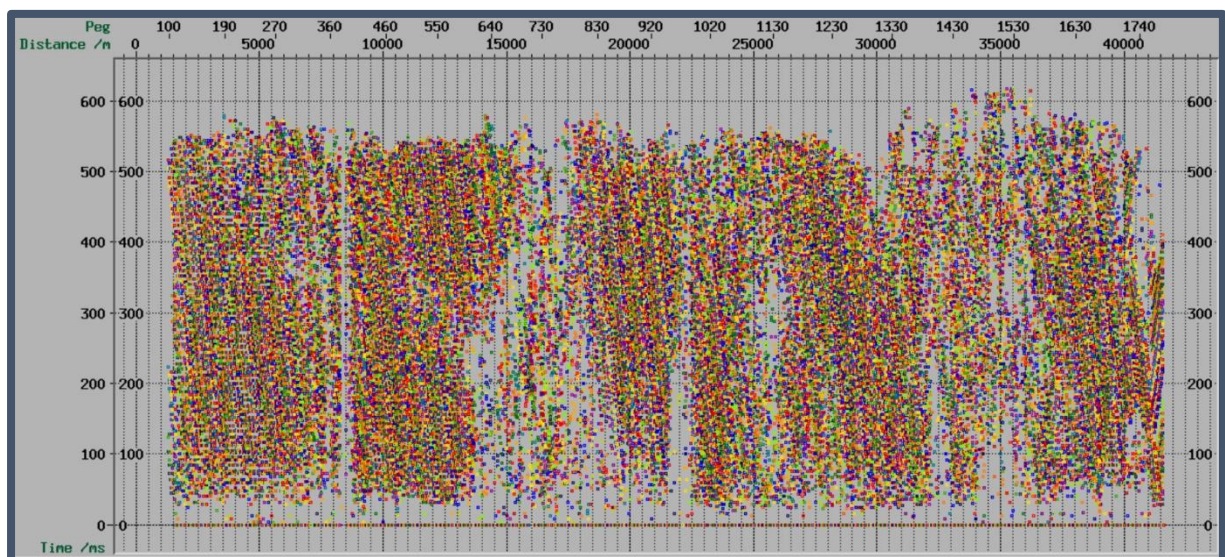
## 5.8 Refraction Statics

Correcting for near-surface variability that affects travel times will significantly improve data quality. The refraction statics account for lagging travel times which are caused by uneven topography and irregularities in the surface weathering layer. As such, refraction statics are used regularly in land data and rarely in marine data except in shallow environments (Yilmaz, 2001). Velocities that have been picked and not had refraction statics applied are thus considered raw. This current project uses the Refraction Inversion Method (RIM), which



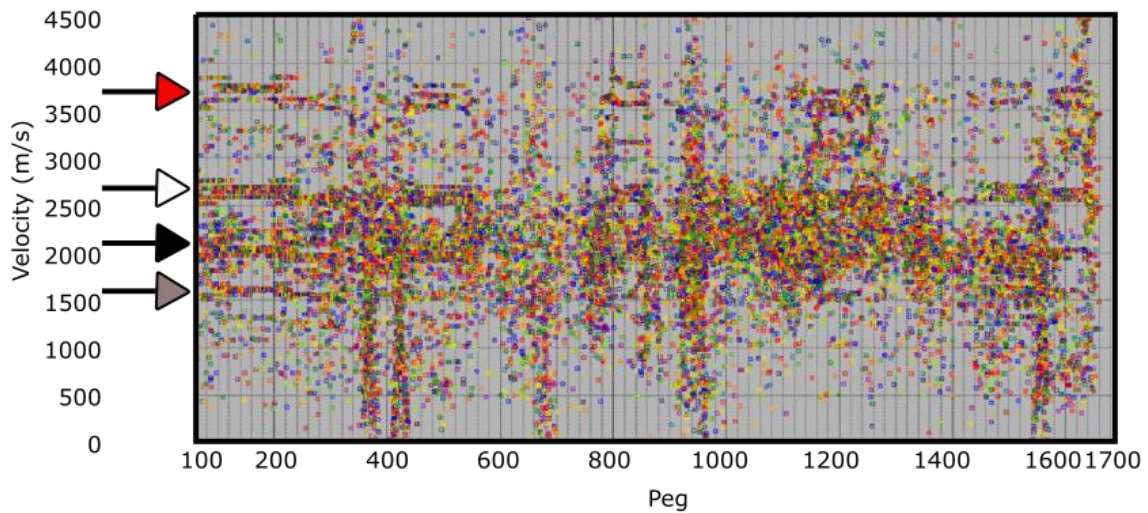
utilises a simple layer-based velocity model. This results only two near surface layers, the weathered layer with  $V_0$  and the sub-weathered layer with  $V_1$ . More layers can be added if the near surface is more complex. Corrections were assessed with the 2D-refstat application in Claritas.

The picked travel times is displayed below (Figure 5.15). Each colour represents a particular shot, showing first-break picks as well as its corresponding offset positions and the modelled travel times of the refracted wave. This forms an overall V shape for each shot. This was the preferred method due to the more stable nature of the calculations in Claritas' inversion programming towards the sub-weathering layer and interface depth parameters (Globe Claritas, 2010).



*Figure (5.15) Picked travel times of line 01.*

Due to the lack of borehole and outcrop data, the “Apparent Vels” tab was used to estimate the weathered layer velocities of  $V_0$ . Selecting a time period of “0 ms to 300 ms” where the first breaks were predicted to occur, will cause Claritas to create a window for the enlarged image of the velocity scattergram (Figure 5.16).

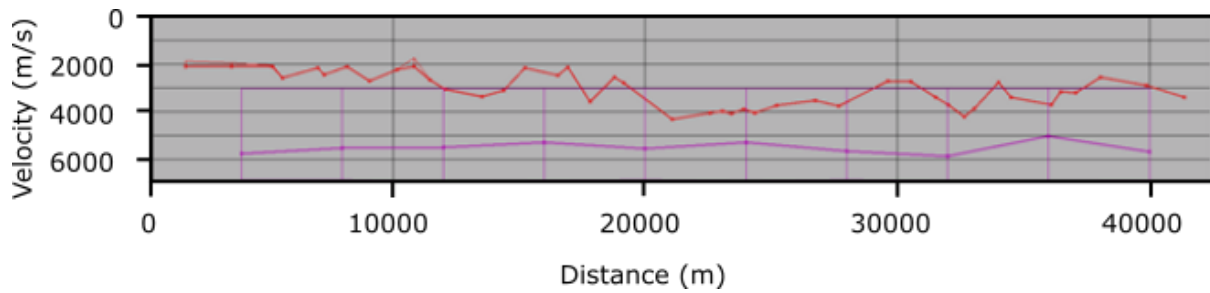


*Figure (5.16) Apparent velocity model of line 01 developed from Figure 5.15 where several distinct horizontal and vertical clusters can be seen. The arrows indicate different velocity clusters to choose to represent  $V_0$ .*

Despite the overwhelming chaotic view of Figure 5.16, clear horizontal alignments can be seen as indicated by the different coloured arrows. These clusters are representative of the velocities  $V_0$ ,  $V_1$  etc. However, it is noted that some of these could also be artefacts created by Claritas as an after-effect called division of multiples. To choose the appropriate velocity, I inspected the shot gathers in SV and used the velocity values from the first breaks as a rough indicator of which cluster to select. For line one, the line indicated by the black arrow is chosen since it represents a velocity of 3000 m/s, similar to the velocity measured in SV of 2949 m/s.

The “Current Velocities Model” was then derived from the picks and shown below in Figure 5.17. The red line represents the  $V_0$  layer while the purple line is the  $V_1$  layer. The two thinner purple lines found above and below the thicker, centred purple line represent the boundaries which specify how much variation  $V_1$  is allowed. Because  $V_0$  is fixed, it does not have those restrictive lines.

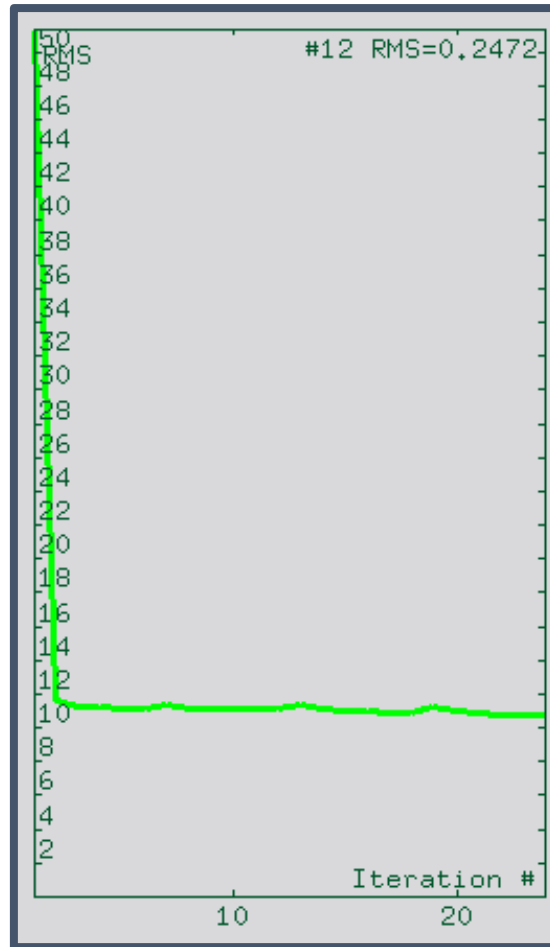




*Figure 5.17 A current velocity model of line 01, with the  $V_0$  (the red line) being fixed and  $V_1$  (the purple line) being malleable.*

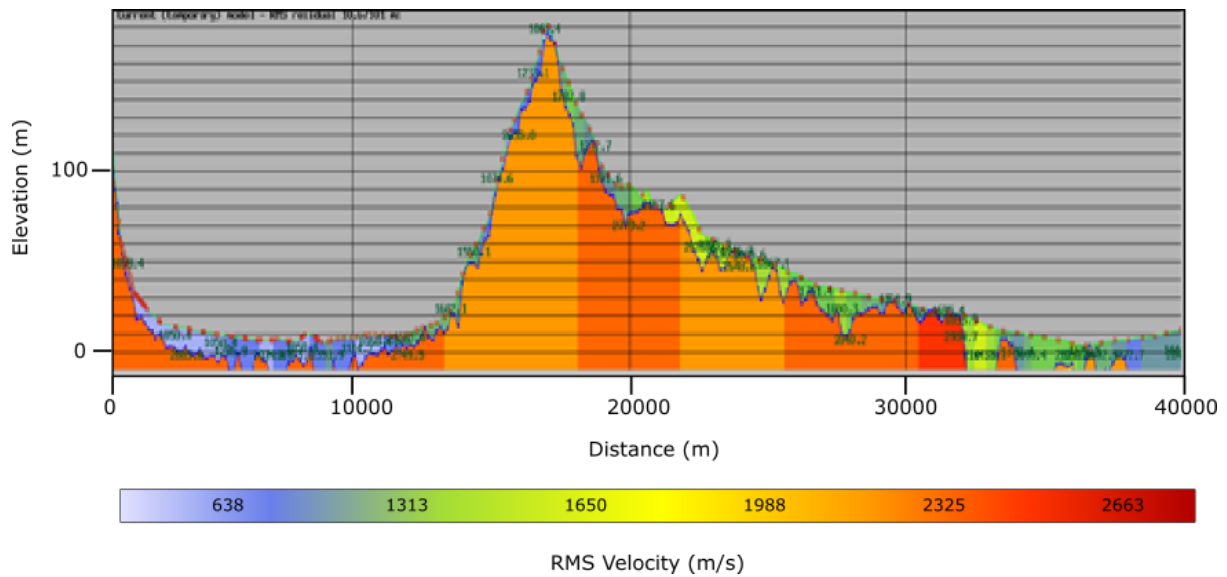
The refraction inversion procedure begins to calculate the statics error and correction. The Claritas program uses the first break picks made earlier and the secondary first breaks model made from the “Apparent Vels” window to produce two sets of data.

The first break picks are used because they are the first part of the signal to reach the receivers and hence are the easiest ones to distinguish in a seismic shot gather. This attribute allows them to reflect the velocities of the boundary layers well. The two are then compared to determine the amount of error between. The model is then adjusted to minimize the error between the first break picks and the model, in a least-square sense in order to produce a final near surface velocity model. The inversion process is then repeated several times (often to 10 - 20 times). To obtain a stable RMS value. For line 01, the RMS error value stagnates at about 11 ms (Figure 5.18).



*Figure 5.18* RMS history of the velocity picks. The higher the RMS the more erroneous the statics are. In this case, the Figure stagnates at approximately 11 ms. The vertical scale is in m/s while the horizontal scale is the iteration number.

In the velocity model for line 01 (Figure 5.19), the red dots represent the source statics whereas the blue dots represent the receiver statics. To improve the RMS value, the receiver static points for  $V_1$  were doubled. This was an attempt to relax the lower limit to allow more variation and potentially allow the velocity model to fit better. Too much relaxing of the limits as well as point doubling, however, can cause errors in the algorithm creating an unstable, fictitious model.



*Figure 5.19 Velocity model of line 01. The colour bar found at the bottom of the image represents the RMS velocities. X- and y-axes are the distance along the seismic line and the elevation above the MSL respectively.*

The final solution is then written out as four output files (Figure 5.12):

1. A residual statics file which shows the least-squares surface-consistent set of source and receiver statics. This in turn, would help reduce the difference between the modelled arrival times and first breaks.
2. The static file which shows the time difference using  $V_1$  rather than  $V_0$  for the interface values.
3. A combined file for 1 and 2.
4. An interpolated file for missing shots and receivers that were not included in the final model based on file 3.

The final interpolated file will be used for initial static corrections, imperative in later stages of processing and determining noise filtering and deconvolution parameters.

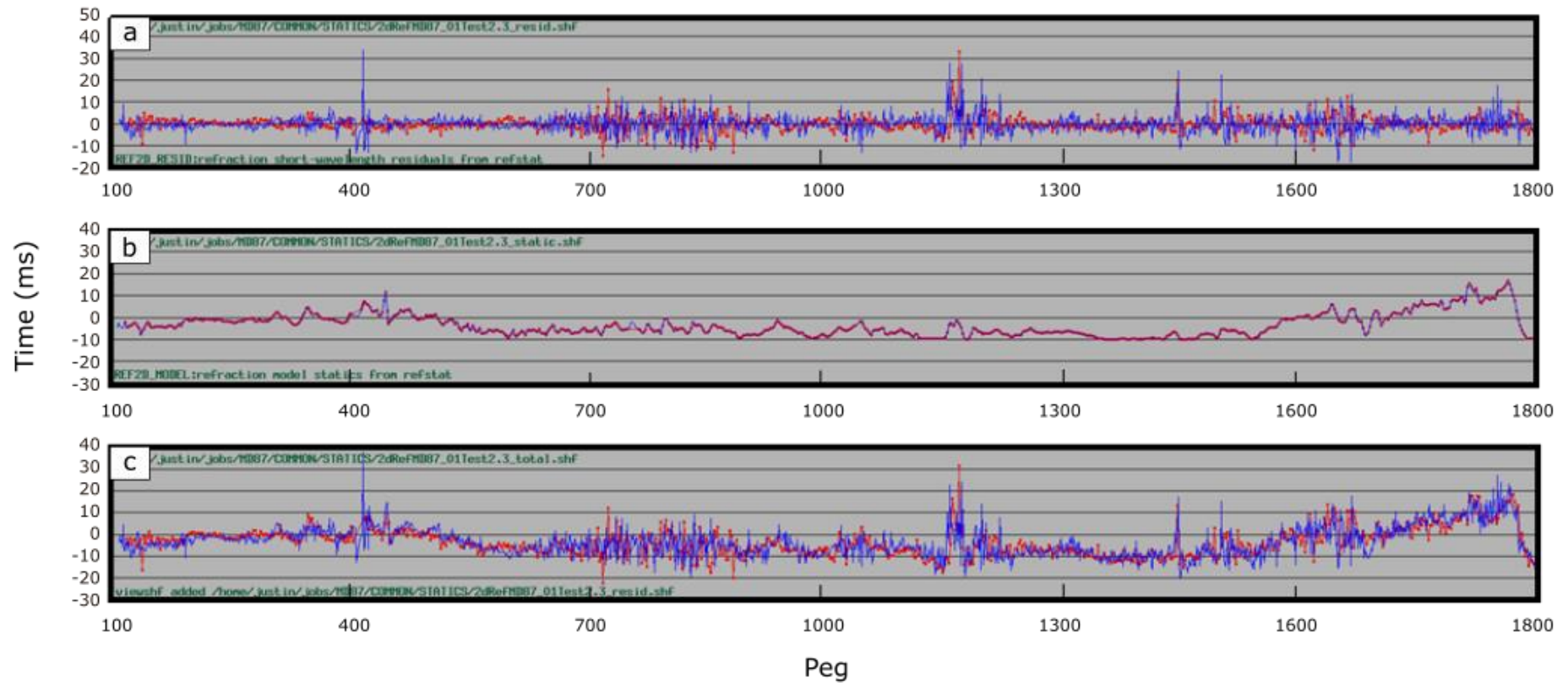


Figure 5.20 From top to bottom: a) Short-wavelength residuals, b) overall refraction model statics and c) the combined residual static model with interpolated missing shots and pegs using the first two panels. The overall refraction model statics indicate the difference between using  $V_1$  and  $V_0$ . The red line is the receiver statics while the blue line represents the shot statics. Note: Only three of the four output files (1,2,4) described previously are displayed in this figure.

The first passes of the initial first two models were adequate. The residual statics show that the surface consistent solution is fairly similar along the line, although with several spikes present in the model (Figure 5.20).

---

## 5.9 Gain

Gain is a process that is applied to seismic traces to boost amplitudes in a controlled way which allows the processor to determine specific characteristics within the seismic image with greater ease (Sheriff, 2002). Within the Globe Claritas program, the predominant gain functions that are used are trace balancing (BALANCE) and Automatic Gain Control (AGC).

The BALANCE module scales traces individually with no cross-referencing of adjacent traces. Each trace is scaled by a constant value and function that is relative to a given time window. This module adjusts each trace so that the output of every trace is modulated to the same average amplitude. The BALANCE module operates on a spatial dimension as opposed to a vertical component of a trace as occurs with Spherical Divergence, and AGC modules.

BALANCE is used more often at an early stage of processing and seismic trace quality control (Globe Claritas, 2010). The main reason for this is because AGC is “unrecoverable”; it is a non-linear process which changes the frequency content of the trace and hence in turn can change the reliability of the amplitude. The trace is then scaled by the absolute amplitude or power of the wave. Claritas provides methods of scaling depending on the number of windows. For a single window the scaling factor is derived from the average amplitude of a single trace. For variable and multiple windows, the program obtains the average amplitude of multiple windows with a degree of overlapping. For general picking of velocities and initial analysis we would use the BALANCE module.

The AGC balances out amplitudes within a trace by utilizing a sliding window. The average amplitude is calculated inside the windows and then a scale factor is calculated to normalise this to a fixed value. The process is then repeated down the window of length 250 - 500 ms. The shorter the window length, the greater the gain effect will be. Short window length AGC is often used on hard-copy wiggle trace plots where correct scaling is difficult (Yilmaz, 2001).

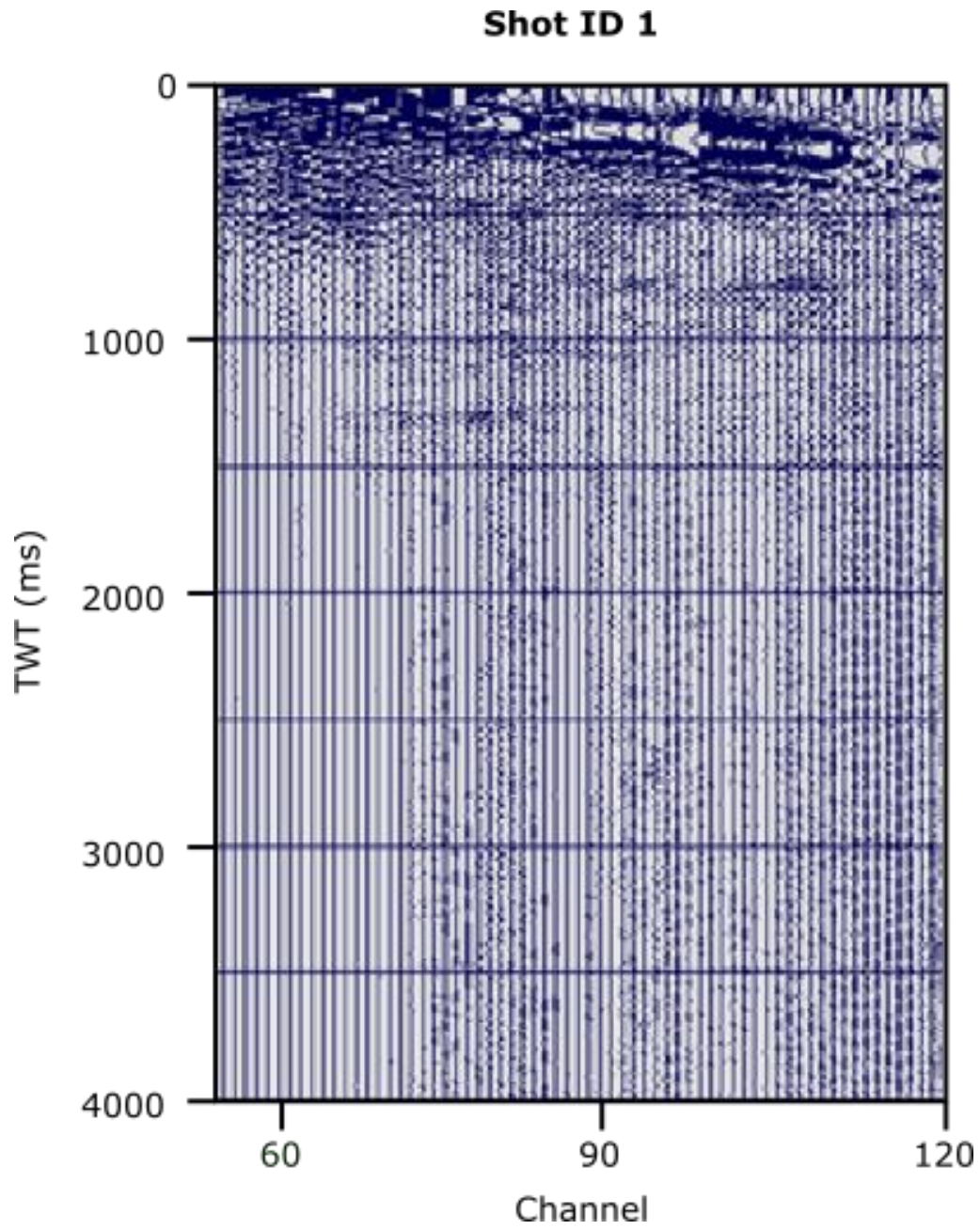
To determine the best gain for the line a “gain control” job flow is set up (Table 5.3).

Table 5.3 Job flow set up to test for gain parameters.

Gain Testing Job Flow		
Order	Claritas Module	Purpose
1	DISCREAD	Reads *.csgy file with the geometry file applied
2	STATIC	Applies static corrections for time distortions caused by topography
3	NMO	Applies *.nmo file to correct travel times
4	REPEAT	Reads the file four times to output four identical separate files
5	IF	Reads in second iteration of the file
6	AGC	Applies 250 ms normal AGC
7	ENDIF	
8	IF	Reads in third iteration of the file
9	AGC	Applies 500 ms normal AGC
10	ENDIF	
11	IF	Reads in fourth iteration of the file
12	AGC	Applies 1000 ms normal AGC
13	ENDIF	
14	PANELTEXT	Creates titles for each file
15	XVIEW	Interactive module used to view each of the output files

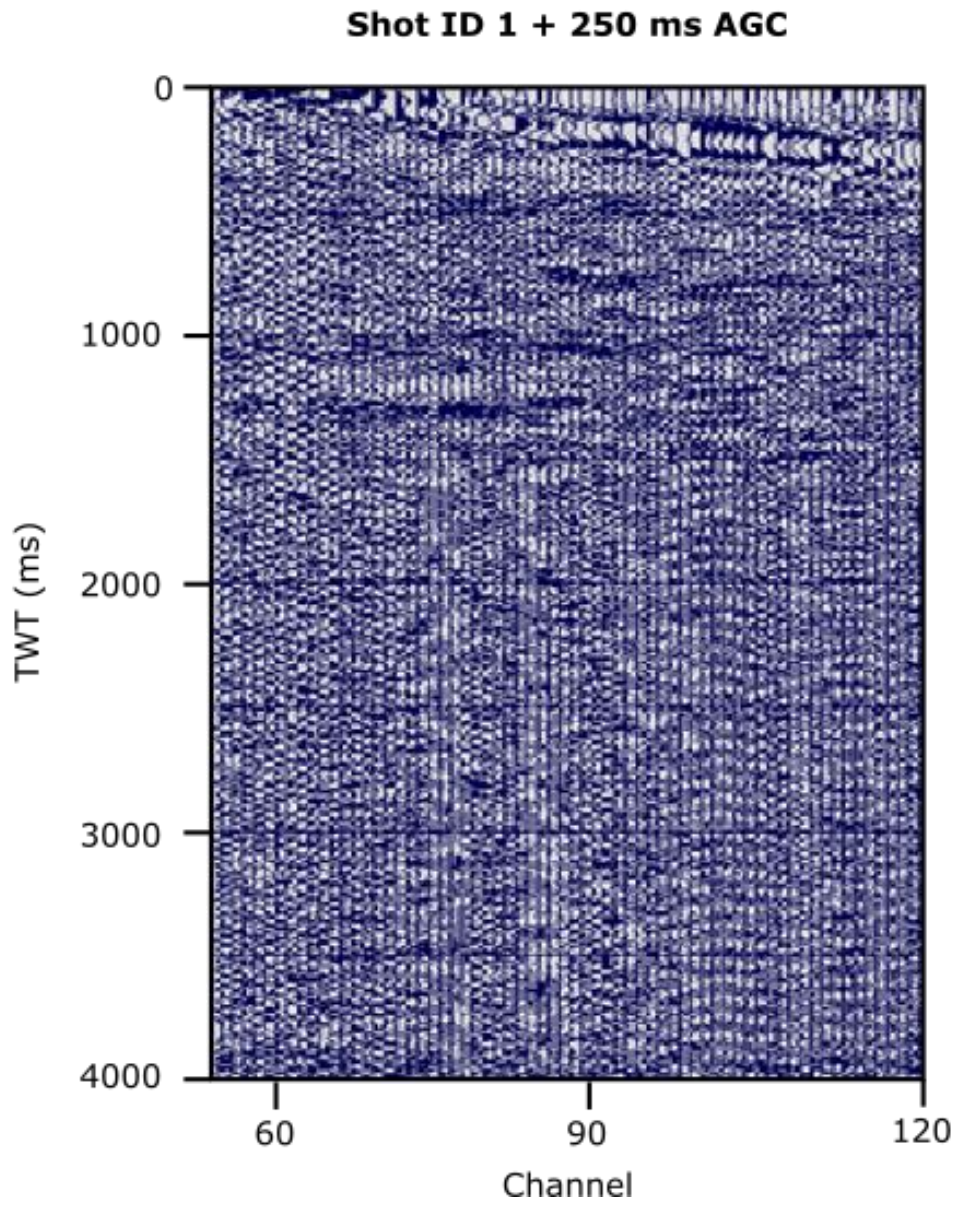
The input data were read in with statics and normal move out applied. The data were repeatedly read in five times where each time, a different value of AGC is applied. This is carried out by a series of “IF” loops. The first three AGC have lengths of 250, 500 and 1000 ms respectively in *normal* mode, while the fourth value has a value of 500 ms but in *median* mode. Median mode was tested in case for scenarios where a normal AGC would fail, e.g. data sets with anomalously high values which may skew results.

For line 01 data set, the “normal” mode is preferred because there were no significant outliers. In the following figures (Figures 5.21 – 23), the different panels represent different values of AGC that were applied to shot 01. Shot 01 is a short shot that abruptly ends at 4000 ms and contains distortions in the shallow regions of the gather. These distortions shown at times 0 - 500 ms just above the first break are artefacts caused by the application of NMO without a mute, however this can be applied and removed in later stages.



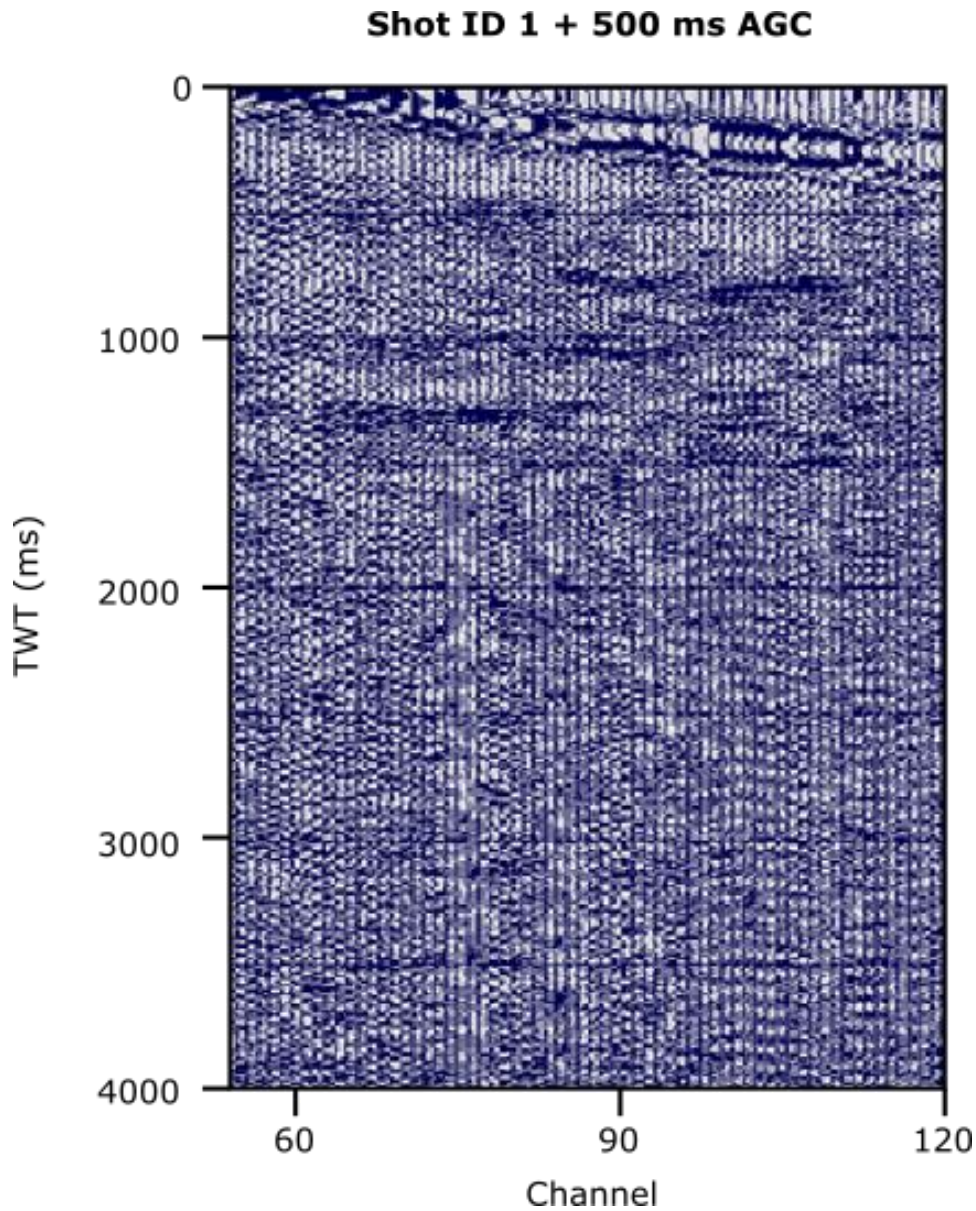
*Figure 5.21 Shot 1, line 01 with static, and NMO applied but no AGC.*





*Figure 5.22 Shot 1, line 01 with static, NMO and a 250 ms normal AGC applied.*





*Figure 5.23 Shot 1, line 01 with static, NMO and a 500 ms normal AGC applied.*

A job was then set up to view the effects of the surface corrections when applied to the shot. The first is with the application of the AGC (Figure 5.24), then AGC with the datum float adjustment (Figure 5.25) and finally a combination of the two with the addition of the refraction static (Figure 5.26). It can be seen that the seismic data slowly shifts higher to zero and the reflections become slightly more prominent with each process.

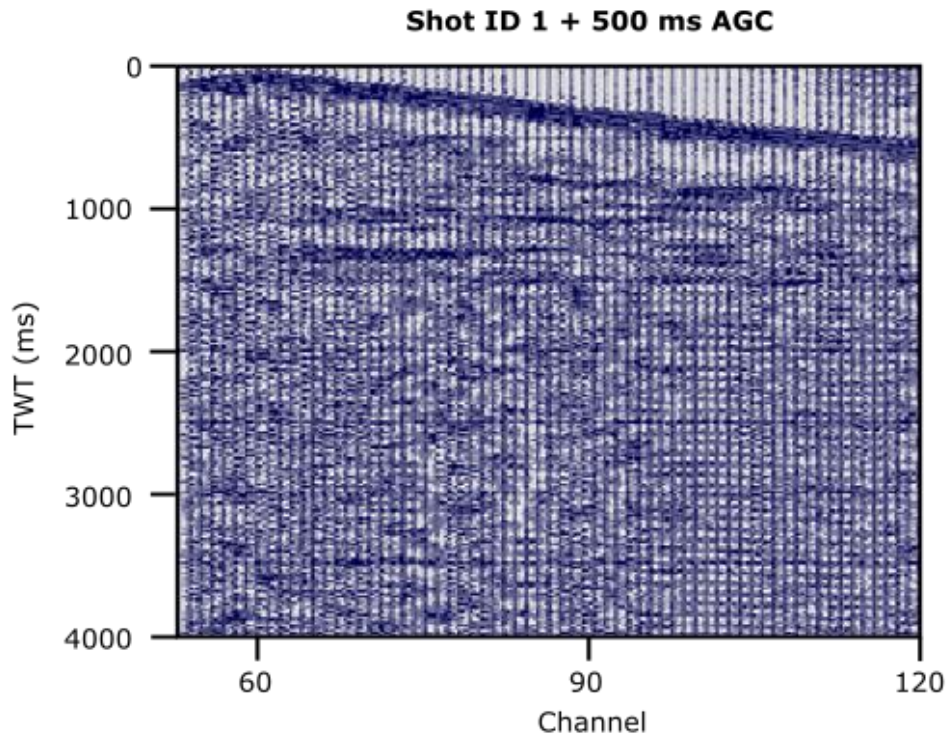


Figure 5.24 Shot 01, line 01 with a 500 ms normal AGC applied.

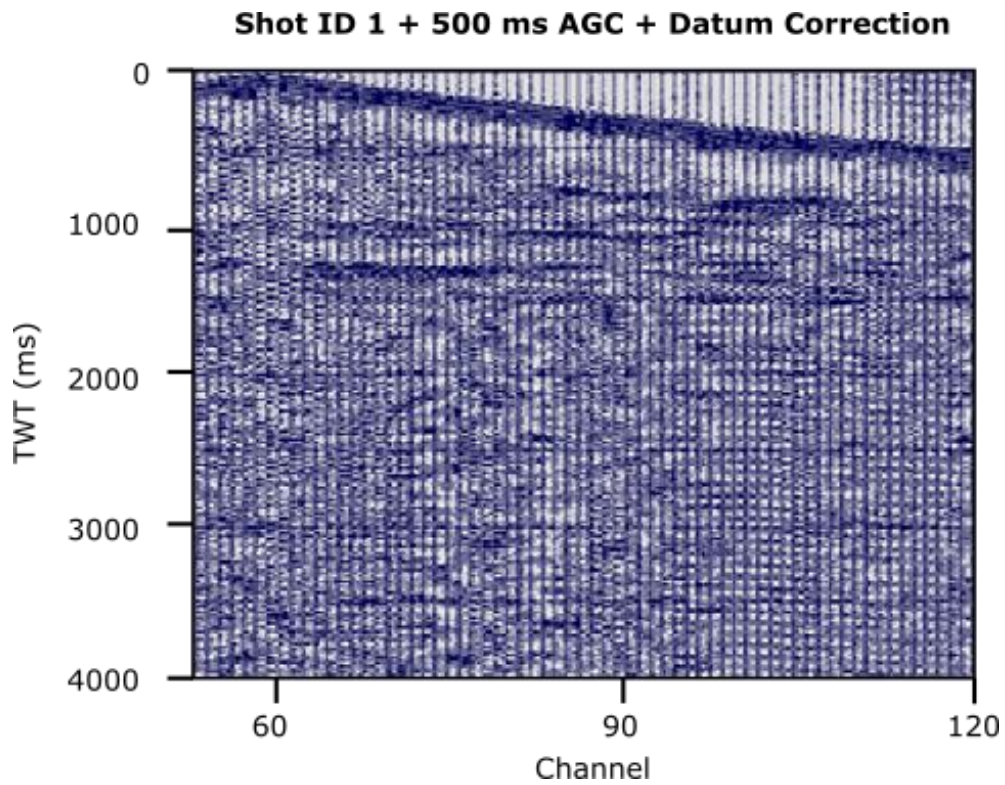
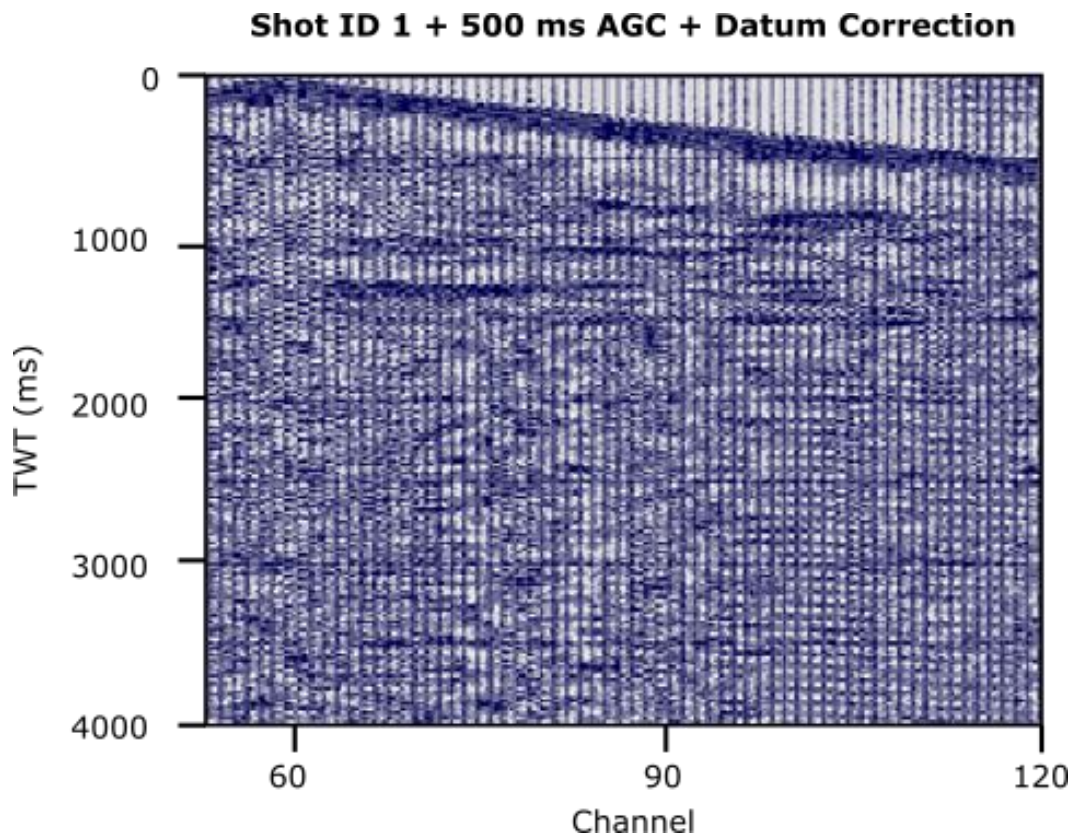


Figure 5.25 Shot 01, line 01 with a 500 ms normal AGC and floating datum correction applied.





*Figure 5.26 Shot 01, line 01 with a 500 ms normal AGC, floating datum and refraction statics applied.*

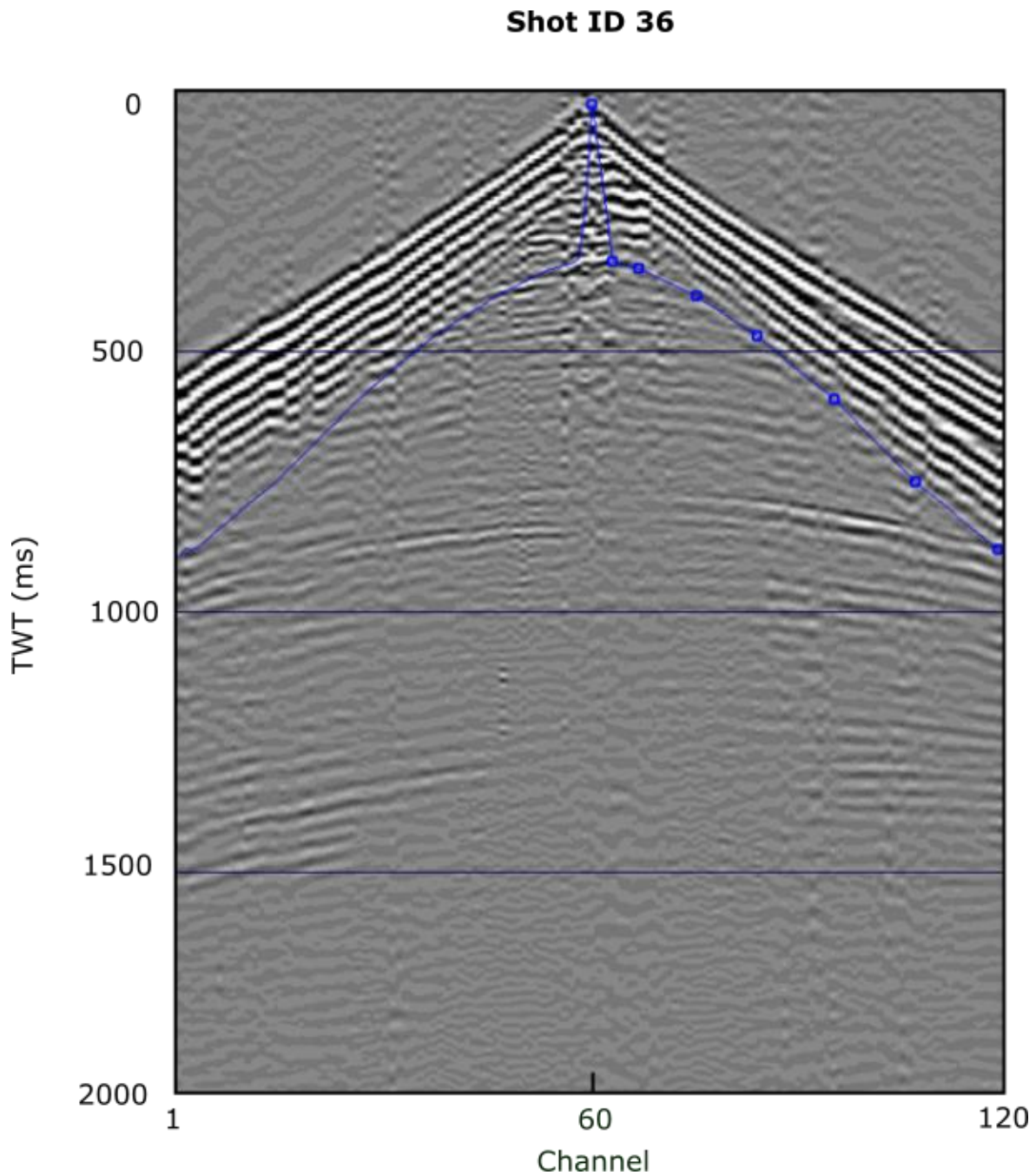
---

### 5.10 Initial refraction mute

An initial refraction mute was then performed on the seismic data prior to stacking. This initial muting process is set up using the SV application in Claritas. The aim was to zero the refracted energy since first break energies are significantly stronger compared with the rest of the shot (Sheriff and Geldart, 1983). Therefore, they should be removed to prevent degradation of the image and improve the reflections in shallow sections.

The input data was first prepared by correcting to a floating datum with statics and AGC applied. The "Front Mute" format was selected, and the extrapolation parameters "OFFSET" and "SLOPED" were used. This meant that the program would show that the picks are based on offset and interpolated and extrapolated with a defined slope.

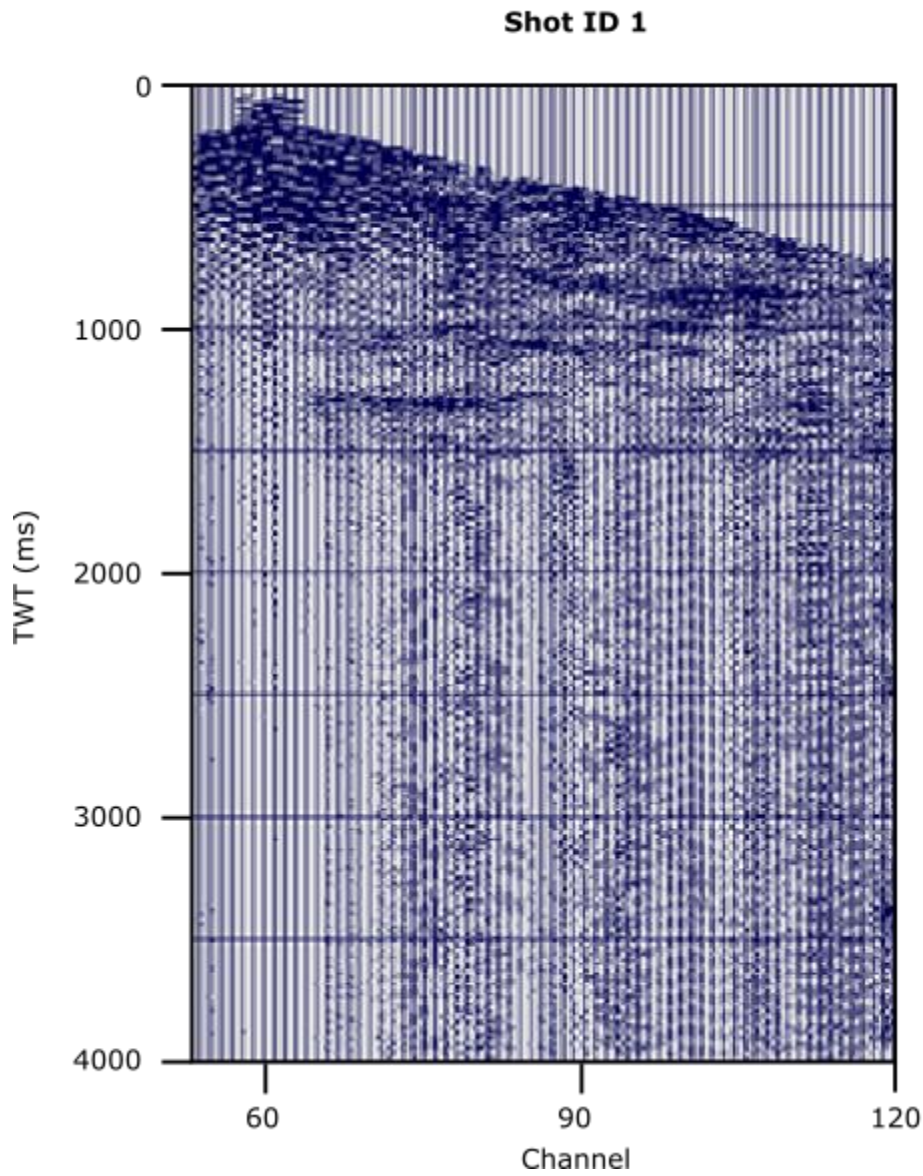
The picks selected were to be just below the refracted arrival with the mute beginning at 0 ms at zero-offset. Because of symmetry, when picks were selected on one side of the shot, they would also be selected at the corresponding offset on the other side automatically (Figure 5.27).



*Figure 5.27 Shot gather 36 of line 01. The blue line represents the front mute where everything above this line will be muted.*

The image below shows the effect of the initial refraction mute applied on to shot 01 (Figure 5.28). The unique shape found around the zero-offset reflects the type of mute that was

selected. The distortions seen in Figure 5.21 -23 were removed creating a cleaner shot gather.



*Figure 5.28 Shot 01 of seismic line 01 with a refraction mute applied. It can be seen there is a feature along the centre. This is to compensate for the zero offset.*

---

## 5.11 Noise Suppression Testing

Several pre-stack processes were assessed to strengthen the input signals by removing or mitigating random and coherent noise. Additionally, static corrections were applied prior to frequency filtering to reduce errors. Jitters from trace to trace due to static shifts can be suppressed by horizontal filters which favour low-dip signals. This is because jitter tends to increase proportionally with higher frequencies. They also help with NMO to flatten events. This can be shown by the standard sine wave equation of an input signal (Brannon and Barlow, 2006):

$$y = A \sin \frac{2\pi}{\lambda} (x - vt)$$

$$y' = \omega A \cos \frac{2\pi}{\lambda} (x - vt)$$

$$y'' = -\omega^2 A \sin \frac{2\pi}{\lambda} (x - vt)$$

with  $A$ ,  $\omega$ ,  $\lambda$ ,  $x$ ,  $v$  and  $t$  being maximum amplitude, angular frequency, wavelength, distance, velocity, and time respectively. The variable  $y$  refers to the amplitude. It can be seen that  $y'$  and  $y''$  are susceptible to frequency, especially if we suppose  $2\pi(x-vt)/\lambda$  equals zero. The equation would now be:

$$y' = \omega A$$

where  $\omega = 2\pi f$ ,  $y'$  would then represent the maximum sampling amplitude error and  $y''$  would be the rate of change for the sampling.

The Quick Frequency-Wavenumber filter (QFK) process module was applied in this project's processing sequence as a simple dip/coherency filter for noise suppression (Table 5.4). The QFK process module is a multichannel process in Globe Claritas that uses a 2D Fast Fourier Transform on the seismic data. This transform involves the conversion of the signal into the frequency domain. The module is a frequency filter which inverts and mutes part of data set. The muting is enacted on the frequency column rather than the wavenumber (K) and is defined as the dip cut-off.



The dip value is calculated by the following equation (Globe Claritas, 2010):

$$dip = 500 \times \frac{k}{f}$$

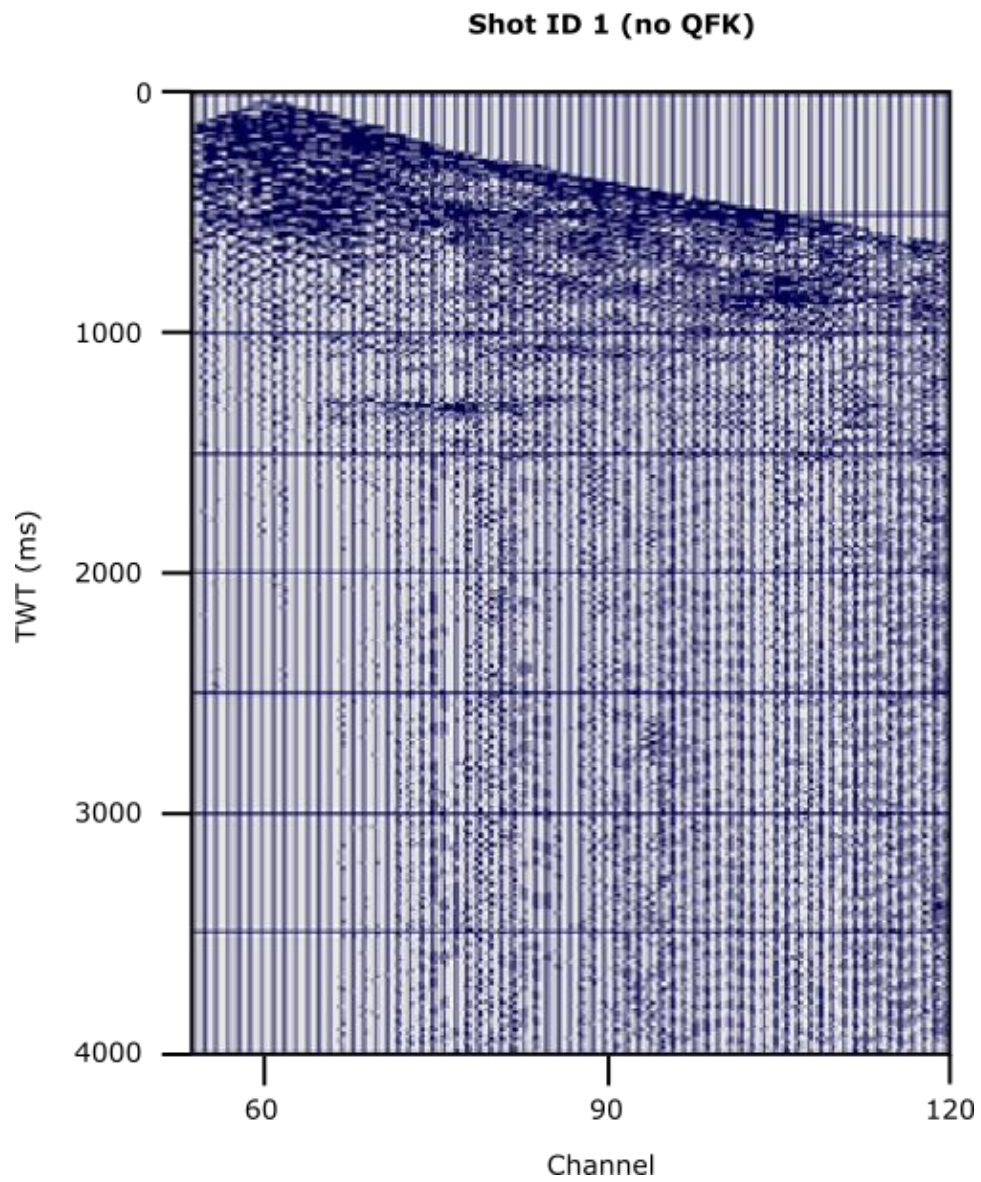
where  $k$  is the wave number and  $f$  is the frequency in Hz.

This cut-off can be specified as the frequency intercept along the  $k=1.0$  axis and the cosine taper length that is centred along  $k=0$ . This will produce a V shaped symmetrical filter. The QFK processor was used in preference to another similar frequency-wavenumber filter in Claritas (FK\_FILT) because QFK is faster and avoids affecting data along the  $K=0$  axis.

*Table 5.4 General job flow used for noise suppression testing.*

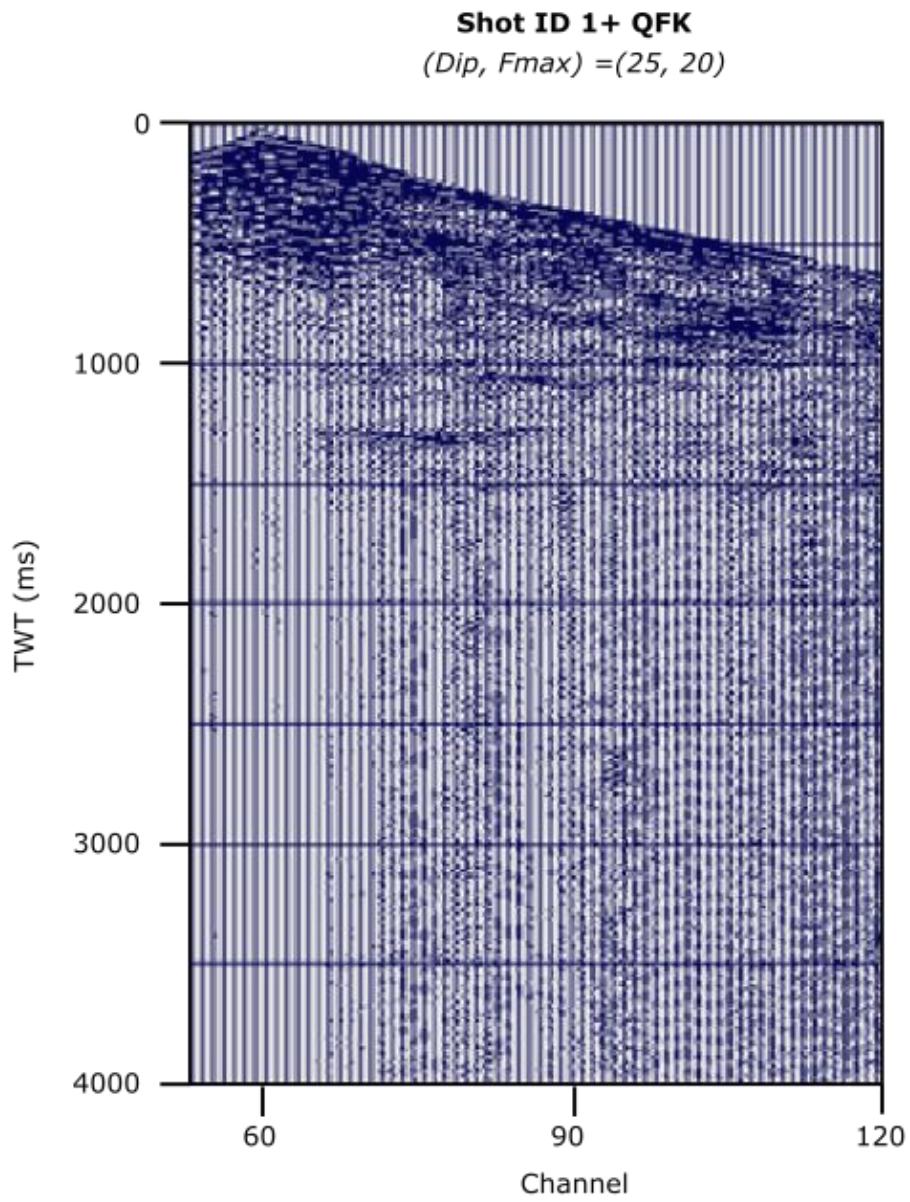
<b>Noise Suppression Testing Job Flow</b>		
<b>Order</b>	<b>Claritas Module</b>	<b>Purpose</b>
<b>1</b>	DISCREAD	Reads *.csgy file with the geometry file applied
<b>2</b>	DATUM_FLT	Corrects to floating datum
<b>3</b>	STATIC	Applies static corrections
<b>4</b>	AGC	Creates an AGC wrap to control extreme anomalous values
<b>5</b>	NMO	Applies *.nmo file to correct travel times
<b>6</b>	REPEAT	Reads the file four times to output four identical separate files
<b>7</b>	QFK	Applies f-k filters with various cut-off dips for each file
<b>8</b>	UNAGC	Removes the effects of the initial AGC
<b>9</b>	NMO	Undoes the effects of initial NMO module
<b>10</b>	PANELTEXT	Creates titles for each file
<b>11</b>	XVIEW	Interactive module used to view each of the output files

The cosine taper length was selected at 12 Hz, from options of out of 12, 20, 50, 60 and 80 Hz. I then set the QFK module to repeat the process five times with the dip parameters 25, 20, 15, 10 ms/trace with their corresponding  $F_{max}$  then calculated through the Claritas algorithm. The following images are of the five repeated processes respectively (Figures 5.29 – 33). The first image produced would be one with no QFK applied (Figures 5.29).

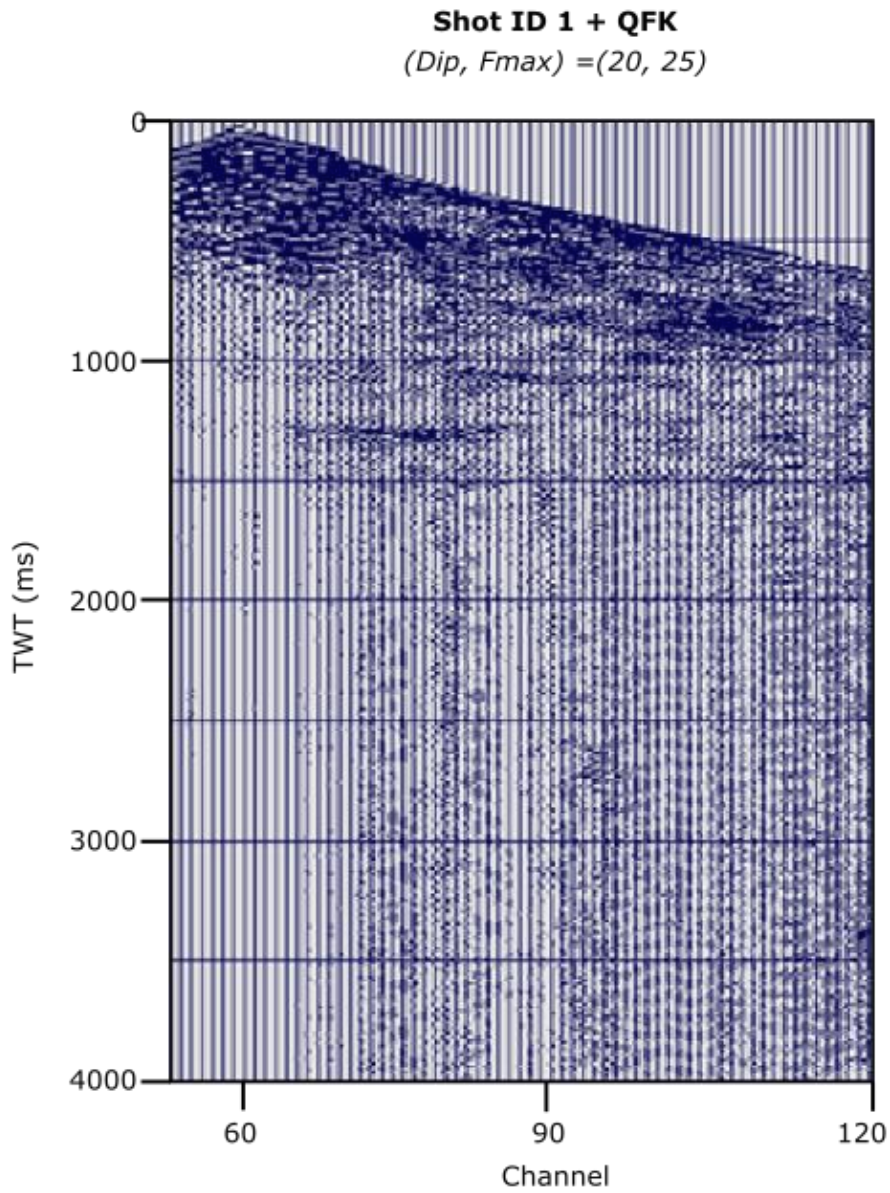


*Figure 5.29 Shot 01 line 01 with no QFK applied.*

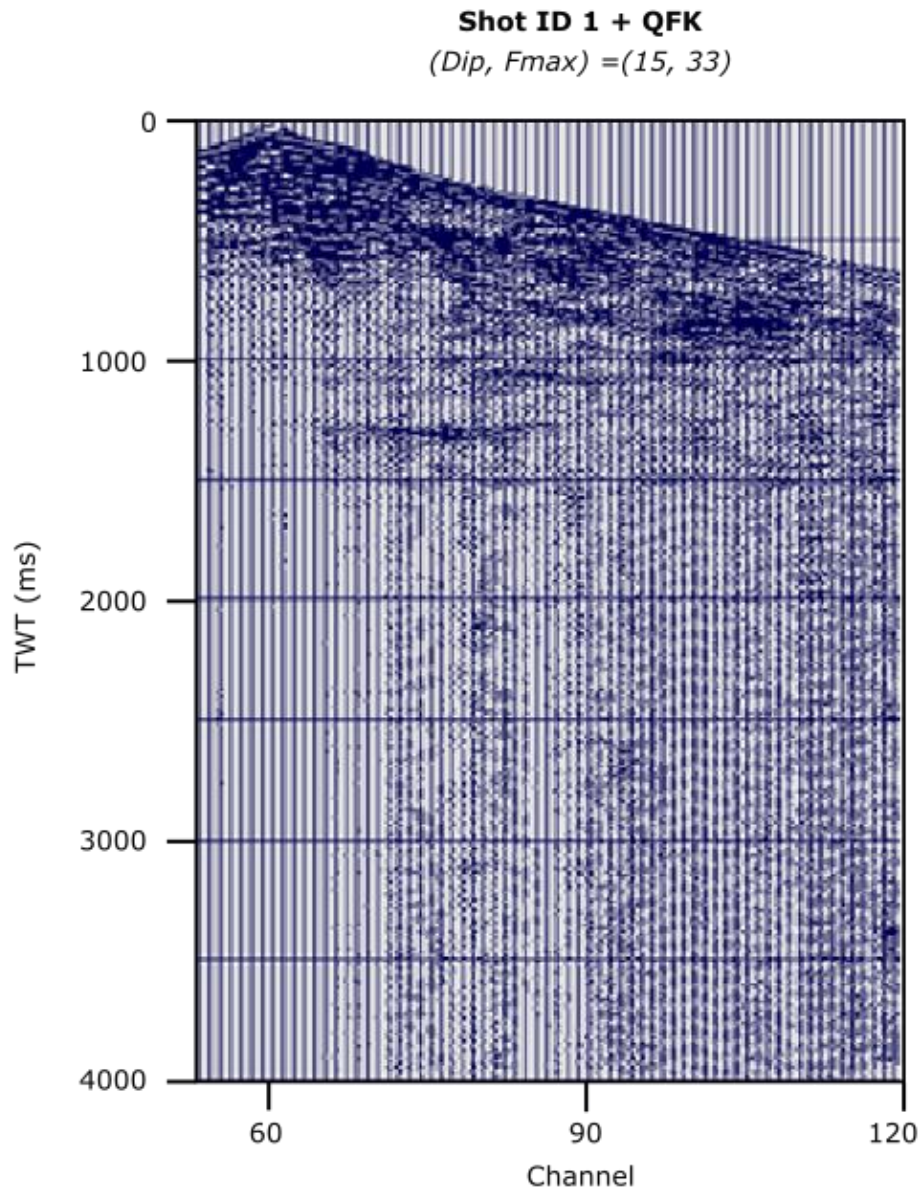




*Figure 5.30 Shot 01 line 01 with QFK applied with a cosine taper length of 12 Hz, and dip of 25 ms/trace.*

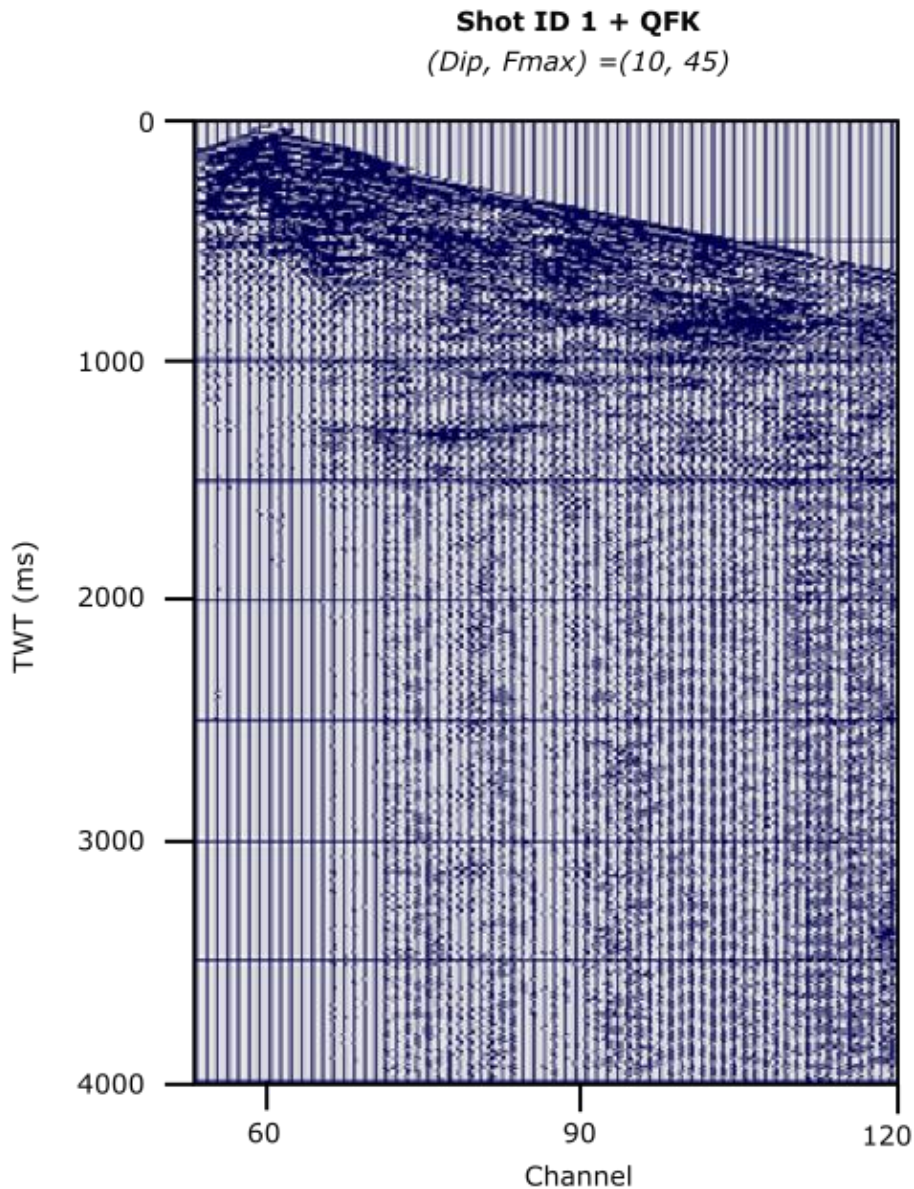


*Figure 5.31* Shot 1 line 01 with QFK applied with a cosine taper length of 12 Hz, and dip of 20 ms/trace.



*Figure 5.32 Shot 01 line 01 with QFK applied with a cosine taper length of 12 Hz, and dip of 15 ms/trace.*





*Figure 5.33 Shot 1 line 01 with QFK applied with a cosine taper length of 12 Hz, and dip of 10ms/trace.*

The results were all fairly synonymous; however, a dip of 25 ms/trace seemed to provide a slightly better image compared to the rest with a gentler filter. The final parameters used for line 01 would be cosine length of 12 Hz, dip of 25 ms/trace and maximum frequency of 20 Hz.

The effect of removing QFK of noise can be further observed in the following images (Figure 5.34 – 36). Each of the images shows the amount of subtracted signal through the use of QFK. The smaller the cut-off dip value, the more aggressive the noise removal becomes.

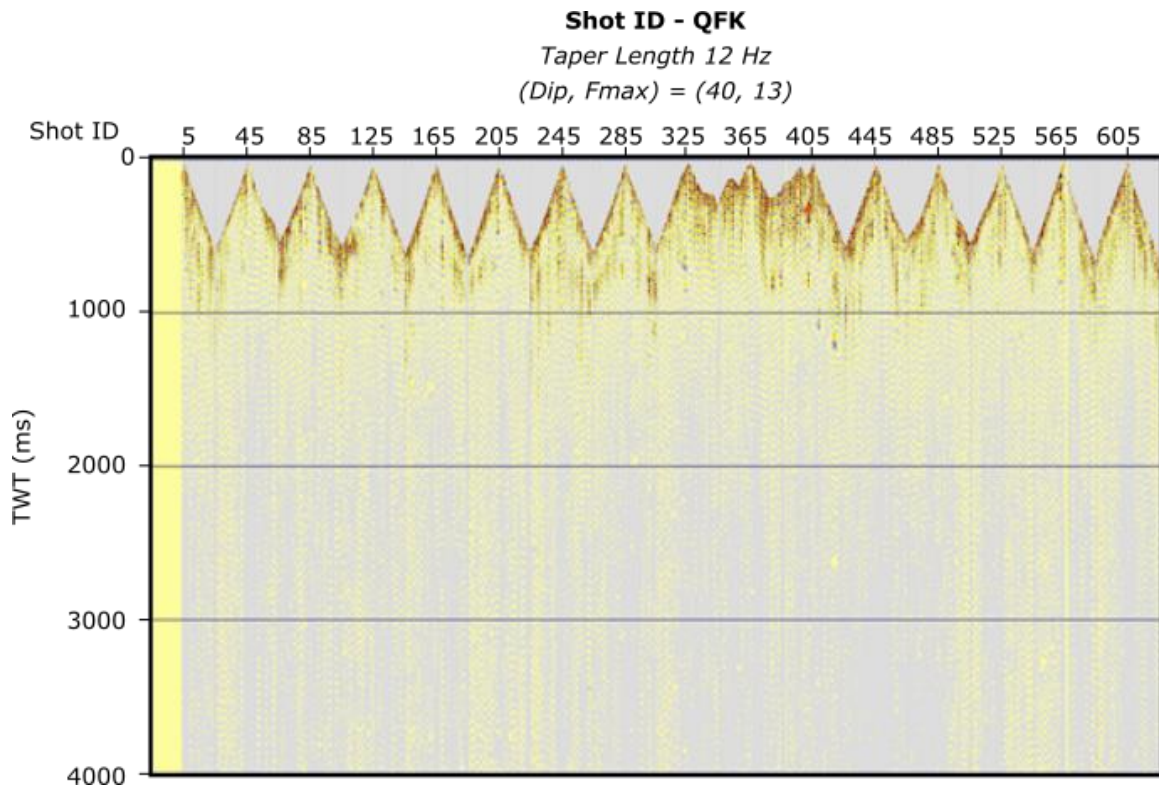


Figure 5.34 The above image is a series of shot gathers showing the subtracted signal from the use of QFK with a cut-off dip of 40 ms/trace.

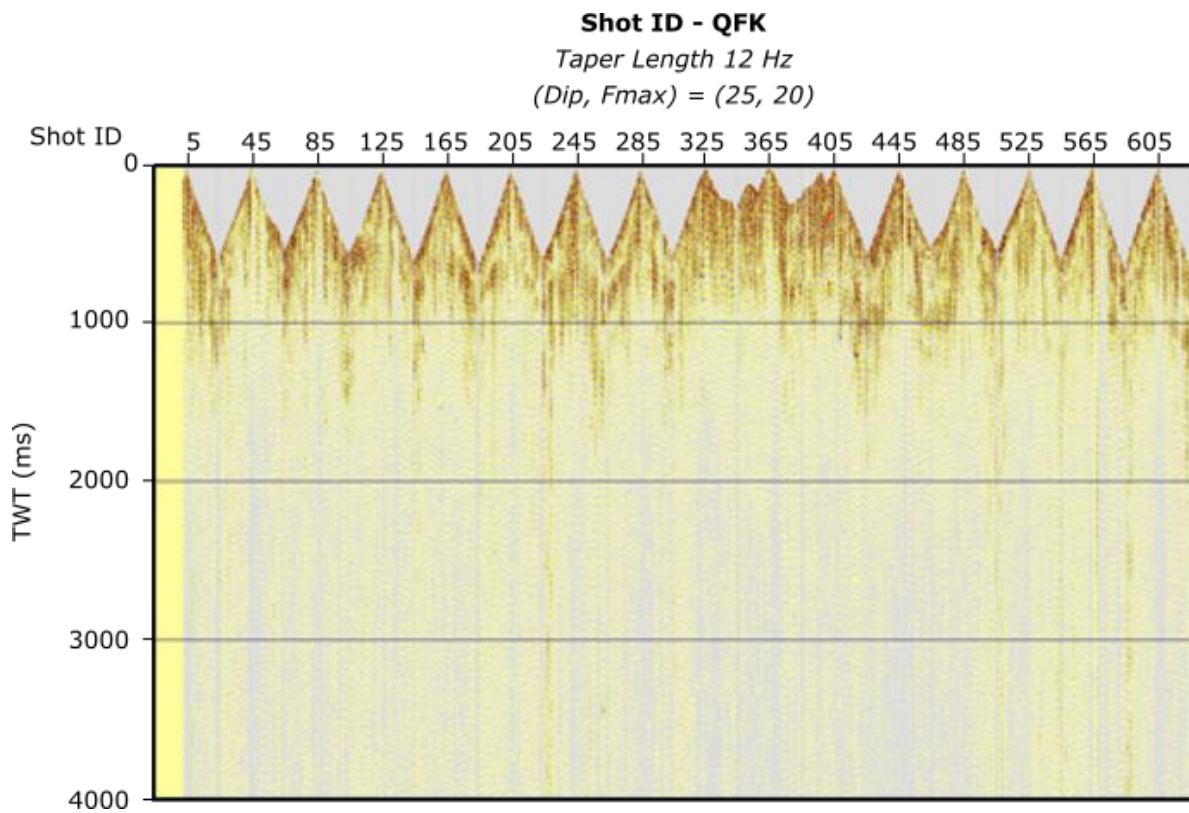
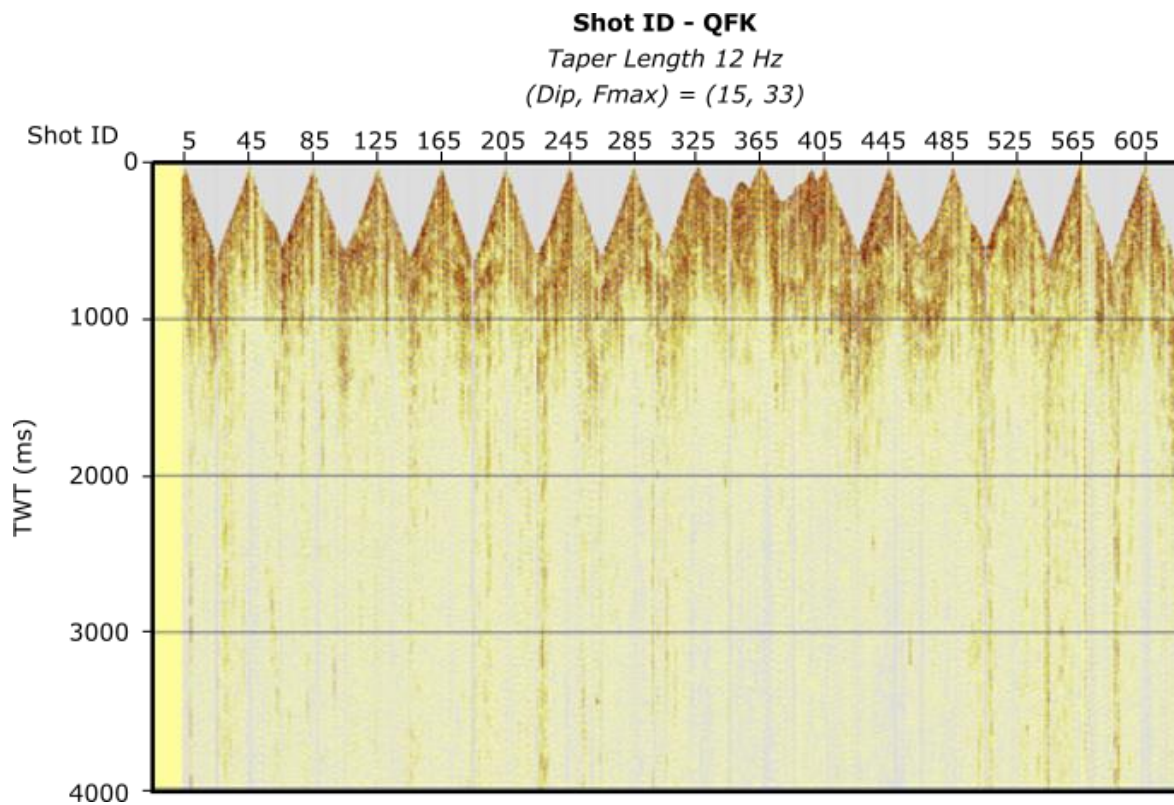


Figure 5.35 The above image is a series of shot gathers showing the subtracted signal from the use of QFK with a cut-off dip of 25 ms/trace.



*Figure 5.36 The above image is a series of shot gathers showing the subtracted signal from the use of QFK with a cut-off dip of 15 ms/trace.*

---

## 5.12 Comparisons

A comparison job was then set up to see the effects with other filters compared with QFK. Claritas native lateral resolution filters such as FXDECON and SEMBSMOOTH were added to the job flow (Table 5.5).

*Table 5.5 Job flow to show the view of different noise reduction filters.*

<b>Noise Filter Comparison Job Flow</b>		
<b>Order</b>	<b>Claritas Module</b>	<b>Purpose</b>
1	DISCREAD	Reads *.csgy file with the geometry file applied
2	DATUM_FLT	Corrects to floating datum
3	STATIC	Applies static corrections
4	SMUTE	Applies refraction mutes on the shot gathers
5	AGC	Creates an AGC wrap to control extreme anomalous values
6	NMO	Applies *.nmo file to correct travel times
7	REPEAT	Reads the file four times to output four identical separate files
8	IF	Reads in second iteration of the file
9	QFK	Applies a f-k filter to the seismic data
10	ENDIF	
11	IF	Reads in third iteration of the file
12	FXDECON	Removes noise through deconvolution along the x-domain
13	ENDIF	
14	IF	Reads in fourth iteration of the file
15	SEMBSMOOTH	Noise reduction through a coherency filter
16	ENDIF	
17	NMO	Undoes the effects of the initial NMO process
18	UNAGC	Removes the effects of the initial AGC
19	PANELTEXT	Creates titles for each file
20	XVIEW	Interactive module used to view each of the output files

The FXDECON process module in Claritas applies a complex Wiener Deconvolution to the trace. Generally, this module is applied post-stack; however, has a pre-stack application as well. The traces are first converted to the frequency-offset domain via Fourier transform. Deconvolution is then applied to each frequency along the space and the random noise is removed. The deconvolution process is applied twice within this module due to the predictive nature of deconvolution where the data are shifted forward by half a phase and then backwards half a phase. The output of both is then averaged and used. Ultimately FXDECON helps to filter and attenuate random noise.

The SEMBSMOOTH process module is a coherency filter within Claritas, designed by Bernd Milkereit, which adds back a portion of the original signal. The filter will extract only the coherent data and input it another file. This is used to overcome the difficulties of identifying



coherent data within large seismic events with significant background noise (Milkereit and Spencer, 1984).

The module operates similarly to the Spatial Linear Signal Detector Module (SLSD). It detects coherent linear seismic events discarding everything else. A tau-p transform is applied to the seismic data, then a corresponding semblance map is produced and multiplied against the tau-p image. The image itself is developed from the stacking of the traces following the tau-p transform and then inverse transformed. The SEMBSMOOTH module, however, is faster and produces a cleaner signal which is why it is used.

The following images show the effects on SHOT 1, line 01 with QFK, FKDECON and SEMBSMOOTH applied (Figures 5.37 - 39). For the sake of producing examples, the taper length used was 25 Hz and dip of 20 ms/trace. The final actual image was different with the application of a 12 Hz taper. Figure 5.39 show the most significant difference, with signal in the time range of 500 - 1000 ms being more pronounced.



### Shot ID 1 + QFK

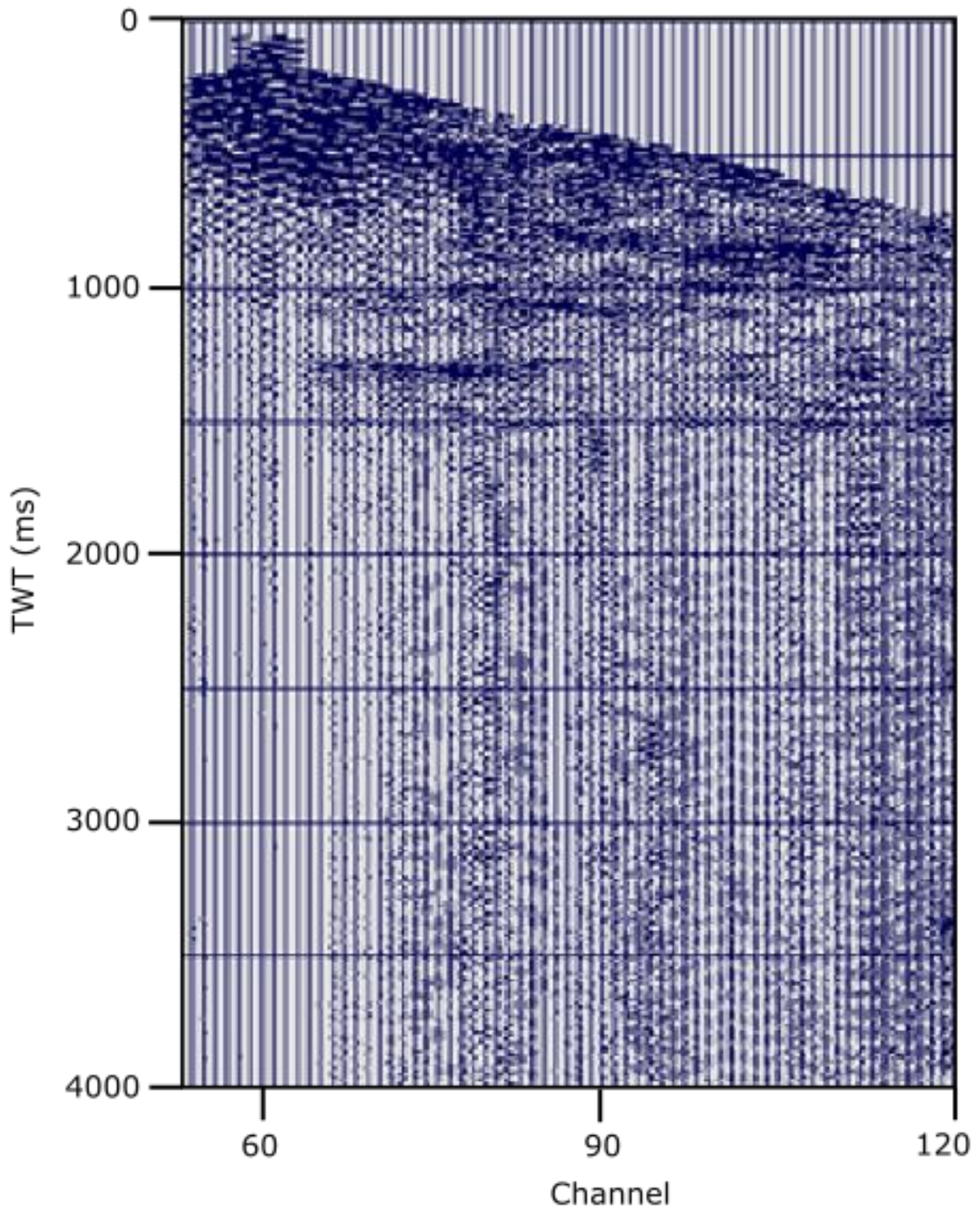
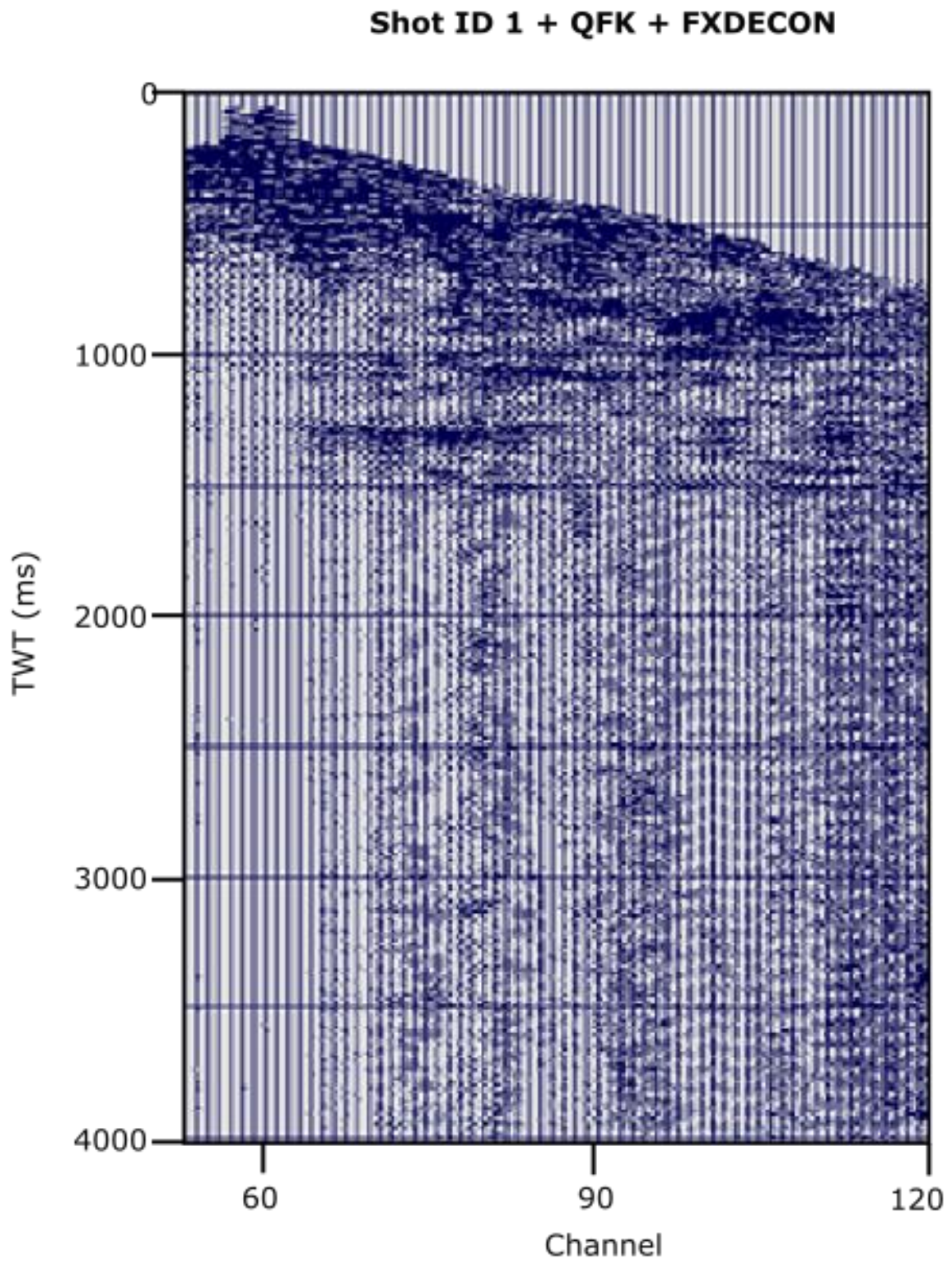
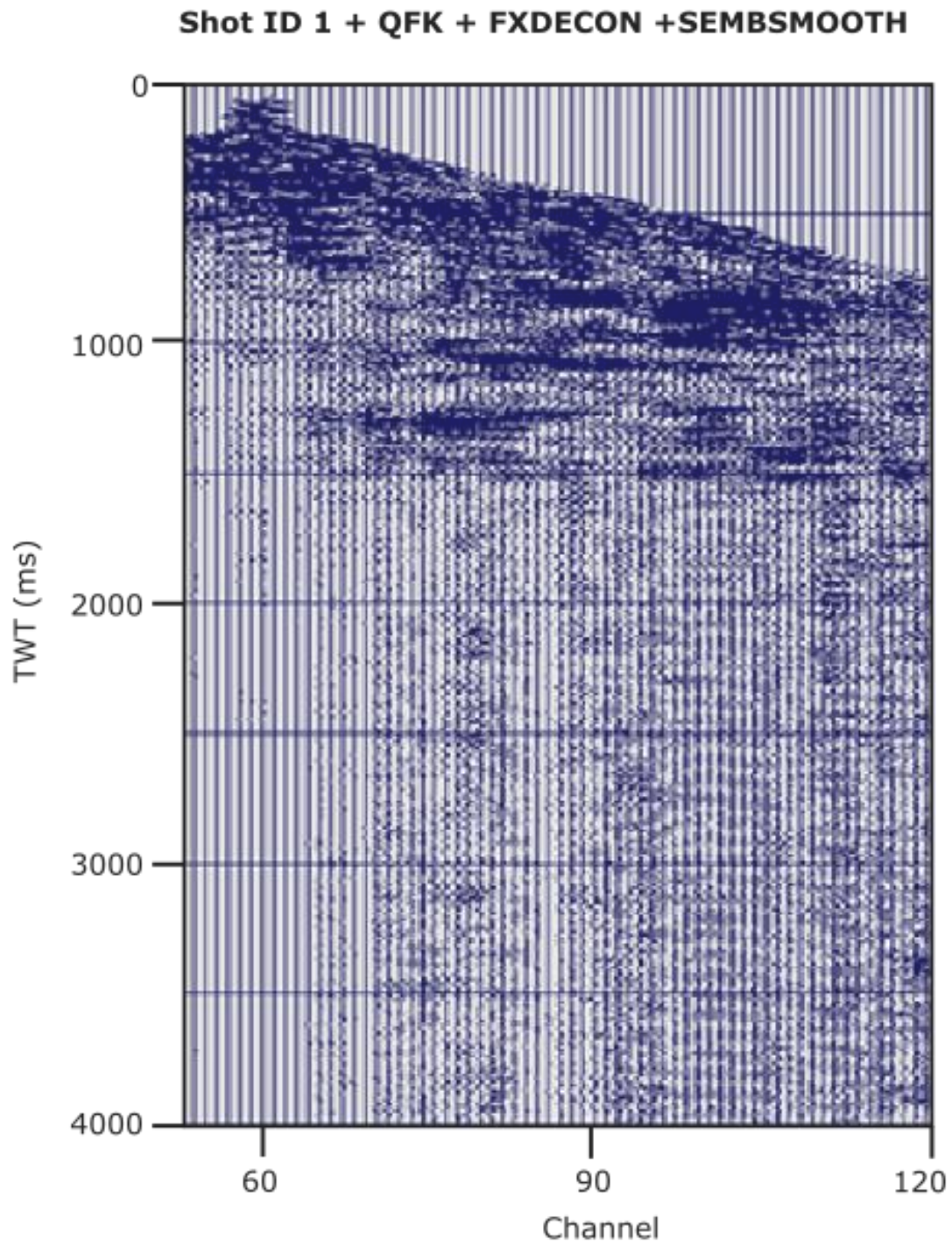


Figure 5.37 Shot 01 with no noise reduction processes applied.



*Figure 5.38 Shot 01 with only QFK (25 Hz taper and 20 ms/trace dip) and FXDECON applied.*





*Figure 5.39 Shot 01 with QFK (25 Hz taper and 20 ms/trace dip), FXDECON and SEMBSMOOTH applied.*

### 5.13 Deconvolution Parameter Testing

The time gates and other parameters for deconvolution were tested by setting up another job flow. Only every 50th shot was read in to save time whilst seeing the overall effects of the deconvolution. The job flow used is shown below (Table 5.6).

*Table 5.6 Job flow for Deconvolution testing.*

Deconvolution Testing Job Flow		
	Claritas Module	Purpose
1	DISCREAD	Reads in *.csgy file with geometry file applied
2	REPEAT	Reads the file six times to output six identical files
3	DECONW	Applies a standard Wiener deconvolution with varying parameters for each file
4	AGC	Gain control for viewing traces
5	PANELTEXT	Creates a title for each file
6	XVIEW	Interactive module used to view each of the output files

The tapered dimensions were first set as 650 -2000 ms as this window is the source of the most important seismic data for line 01. The entire length of the data was set from 0 - 6000 ms. For single window deconvolution (used for line 01, 02 and 06), the length and gap parameters were systematically tested in a trial-and-error fashion to see which worked the best. Initial DECONW gate parameters are shown in the figure below (Figure 5.40).

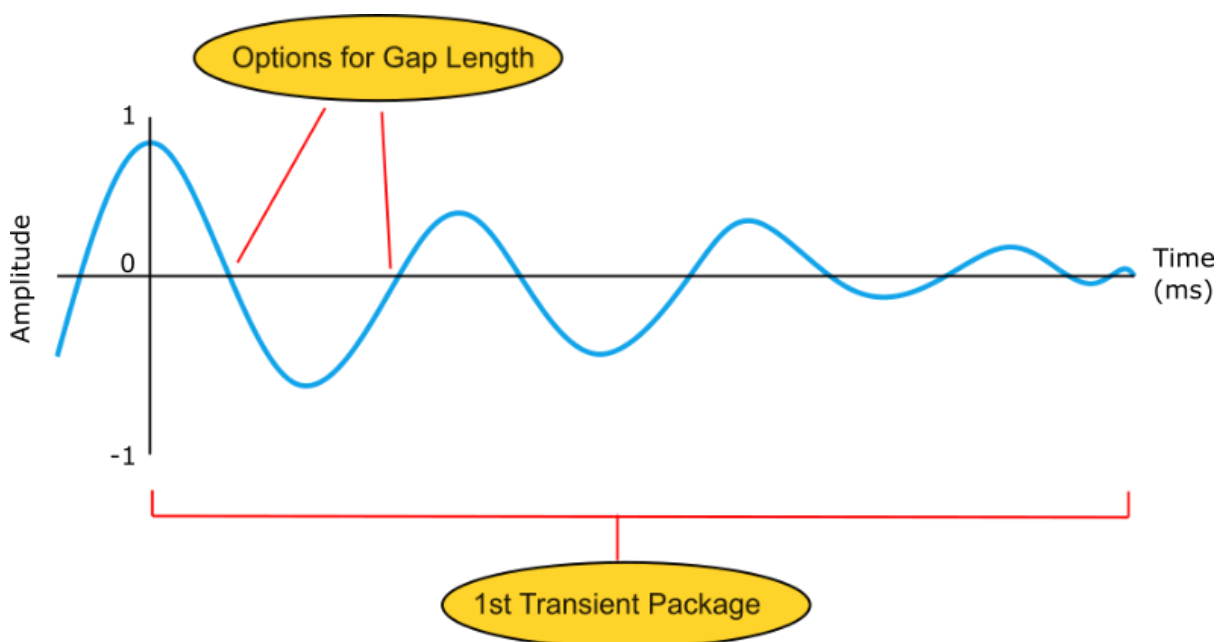
Process name	DECONW							Li
Primary key	REPEAT							Li
Secondary key	CHANNEL							Li
Qualifier	Exact/Noend							Li
Comment								
	P_key	S_key	TD_on	TD_off	TA_on	TA_off	[length]	[gap]
	2		650	2000	0	6000	150	32
	3		650	2000	0	6000	150	24
	4		650	2000	0	6000	150	16
	5		650	2000	0	6000	150	8
	6		650	2000	0	6000	150	0
	[EOF]							

*Figure 5.40 Testing deconvolution file used to test for the varying gap length.*

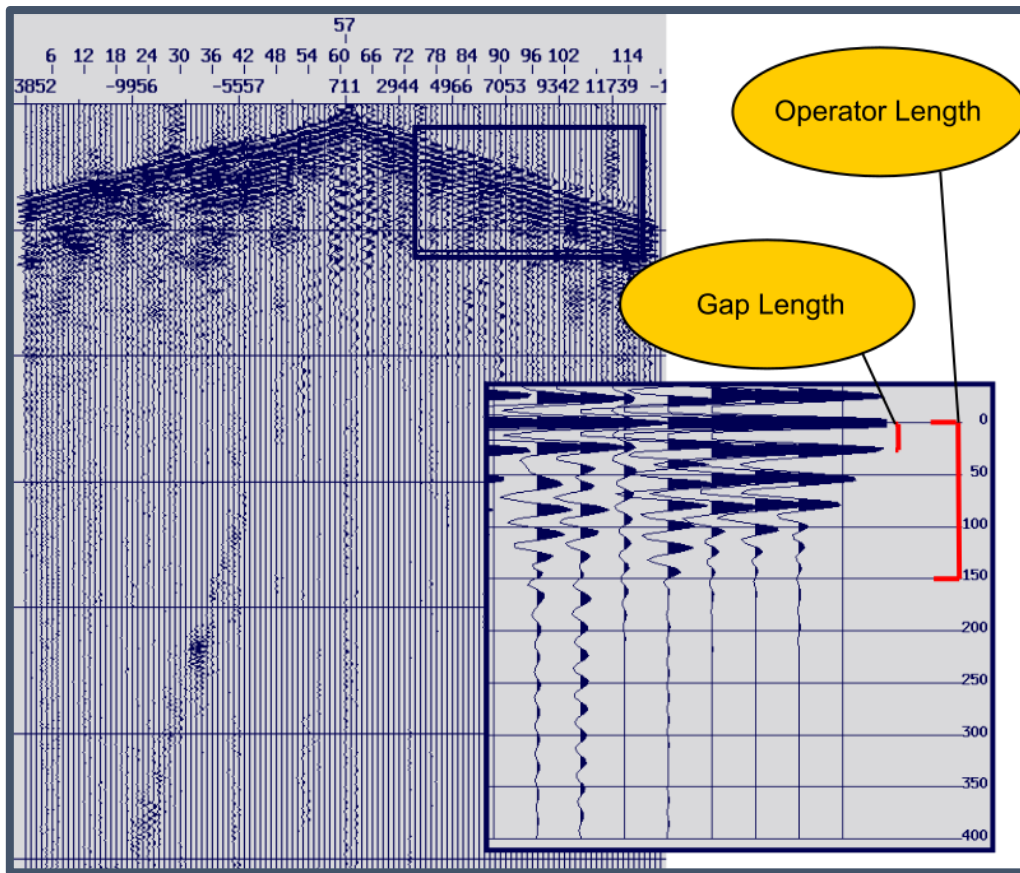
However, for multi-window deconvolution (used by the other lines), the design window, gap length and operator lengths were picked using the autocorrelation zoom function in Globe Claritas. The function is used as a tool to determine an estimate of the parameters.

The design window was selected to target reflections with the best signals where areas of high amplitude and noise were avoided. Larger windows allow greater analysis of the wavelets and determine the deconvolution operator of the trace (Dondurur 2018).

The gap length was selected between either the first or second point where the wave crosses the zero-amplitude line. The first transient package, also known as the operator length, is the part of the trace over which the wavelet approximately returns to zero. This region is then selected and is used to compare with the rest of the trace. This parameter has the greatest effect on multiple suppression where the larger the operator length the more significant the suppression will be. However, an operator length that is too long will deconvolve the geology (Dondurur, 2018). As an example, for line 03, a gap length and operator length of 16 ms and 150 ms were selected respectively. There were varying transient package lengths among the channels as seen in Figure 5.42; however, 150 ms seemed overall, an appropriate average. Figure 5.41 shows a rough illustration of the process.



*Figure 5.41 A rough illustration of a zero-phase wavelet and the characteristics relevant for determining deconvolution parameters.*



*Figure 5.42 Autocorrelation enlargement function in Seismic Viewer in Globe Claritas used on shot 57, line 03. The enlargement box focuses in on a portion of the shot, with its position shown by the smaller blue box in the shot gather. Vertical scale is the two-way time in milliseconds (ms) and horizontal scale in channels.*

DECONW is a process in Claritas which applies a time varying or spatially varying deconvolution to the seismic data. It incorporates the typical parameters for a standard Wiener filter (Globe Claritas, 2010), with the seismic trace being a combination of the source wavelet and the reflection coefficient and with the reflection coefficient being a product of a white noise sequence. The premise of applying deconvolution prior to stacking is to compress the source wavelet into a spike to improve the temporal resolution. The effects of various operator lengths in DECONW from 0 to 300 ms is shown in Figures 5.43 – 47.



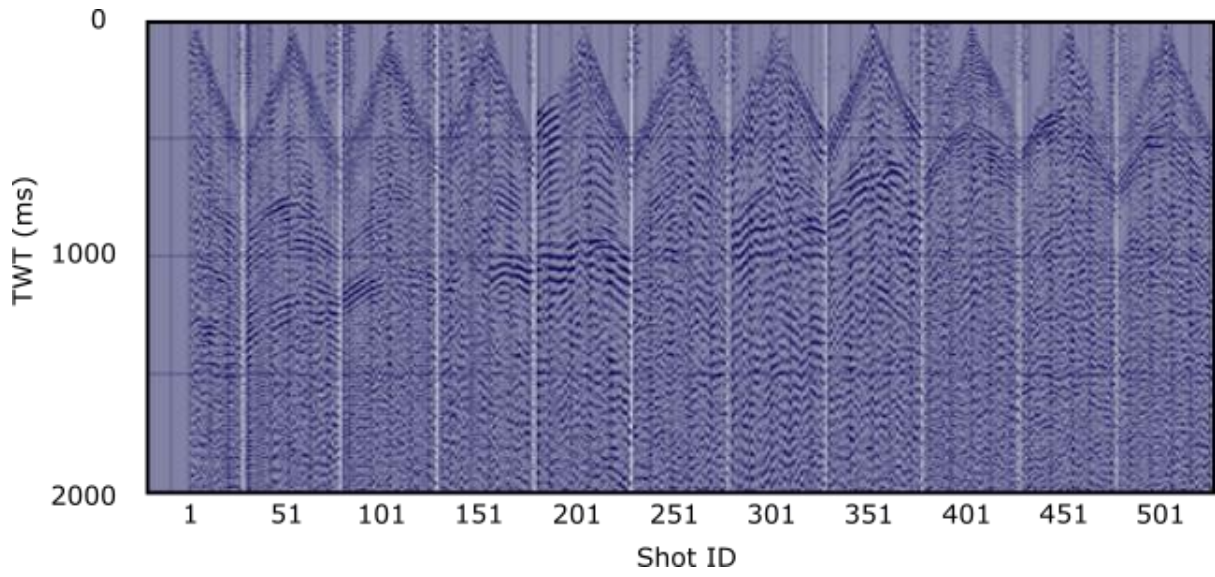


Figure 5.43 Raw shot files from line 01 prior to DECONW being applied.

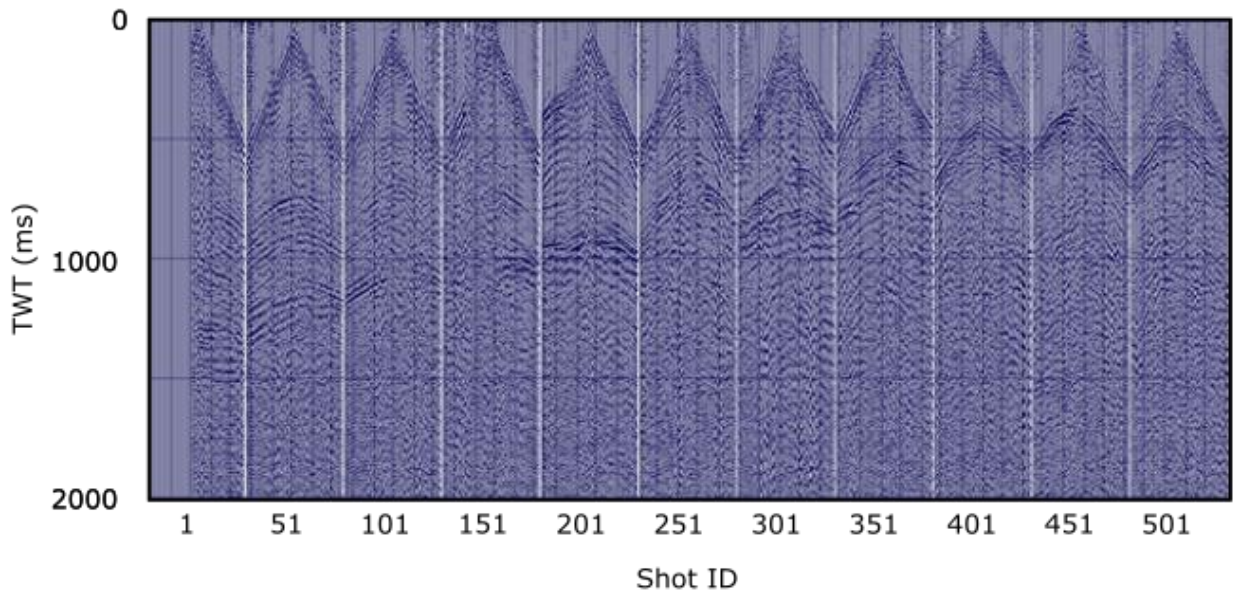


Figure 5.44 DECONW with 100ms length and 0 gap.

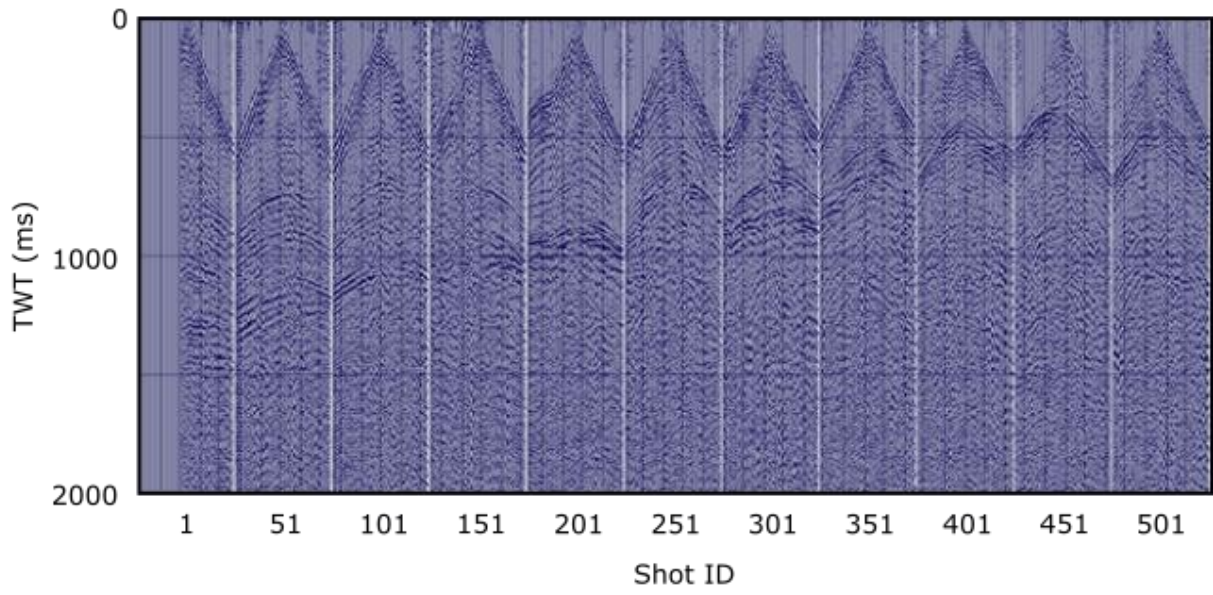


Figure 5.45 DECONW with 150 ms length and 0 gap.

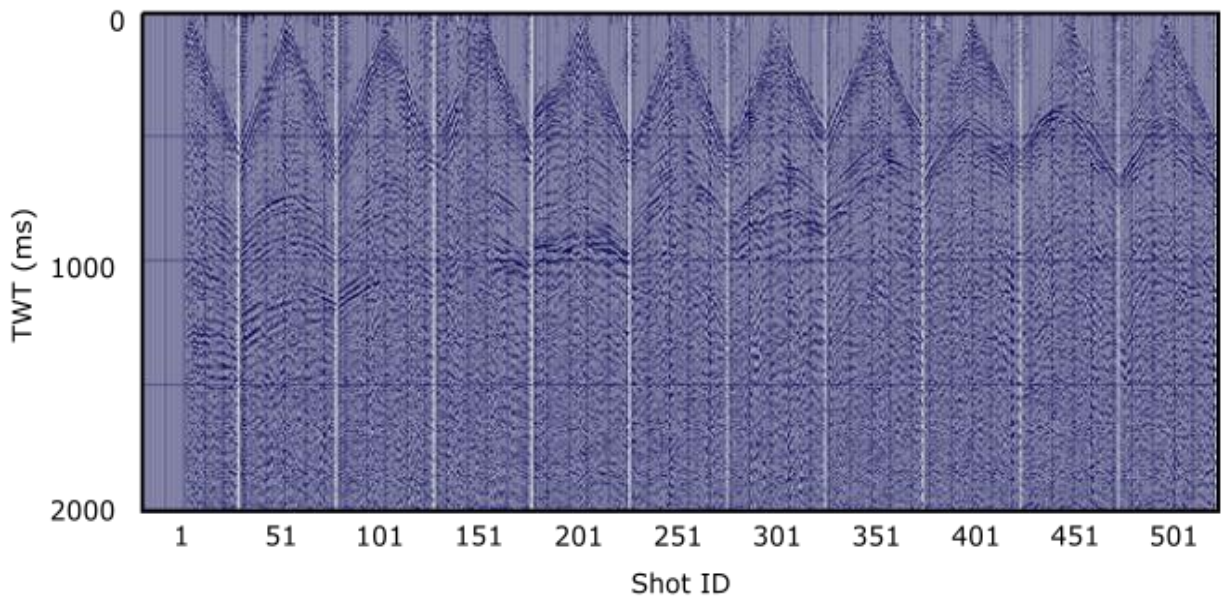
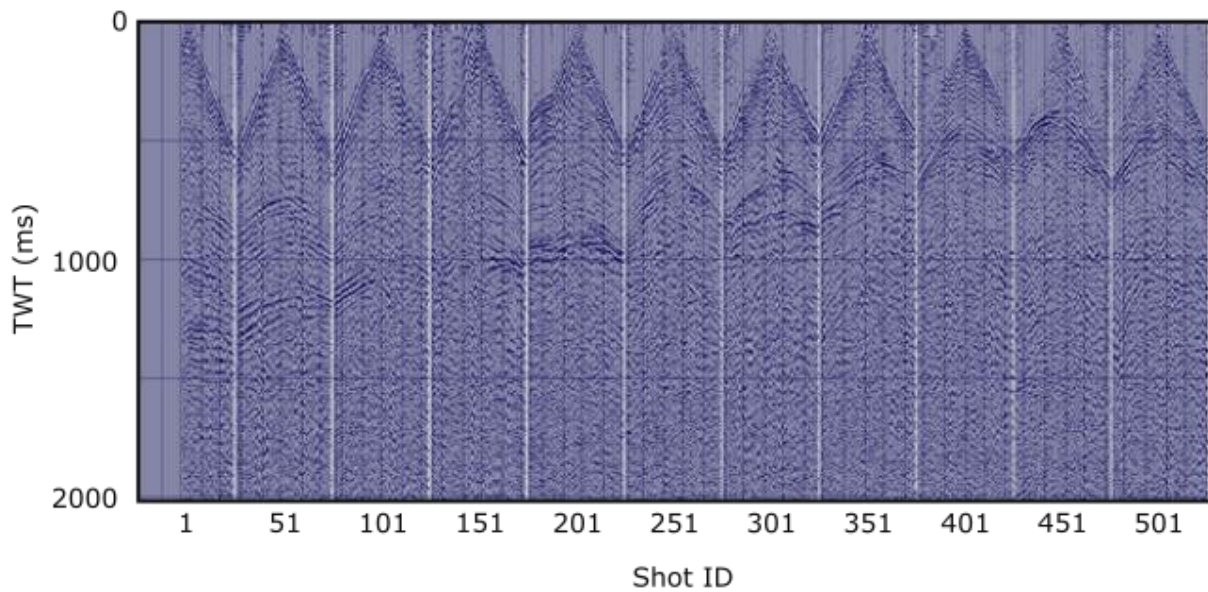


Figure 5.46 DECONW with 200 ms length and 0 gap.



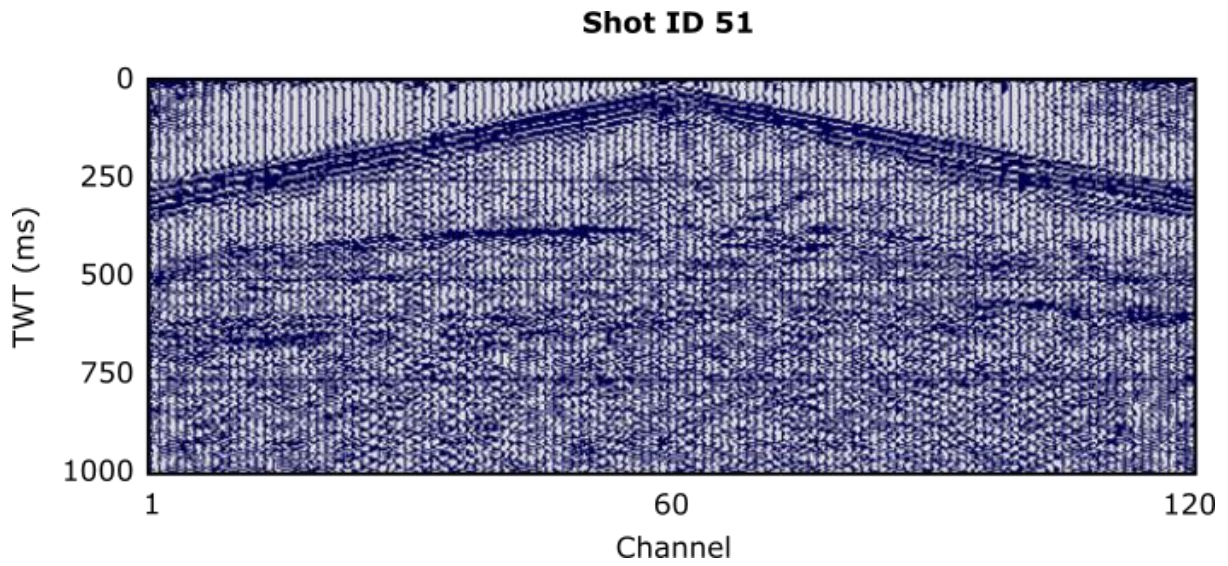


*Figure 5.47 DECONW with 300 ms length and 0 gap. Vertical scale is the two-way time in milliseconds (ms) and horizontal scale as labelled.*

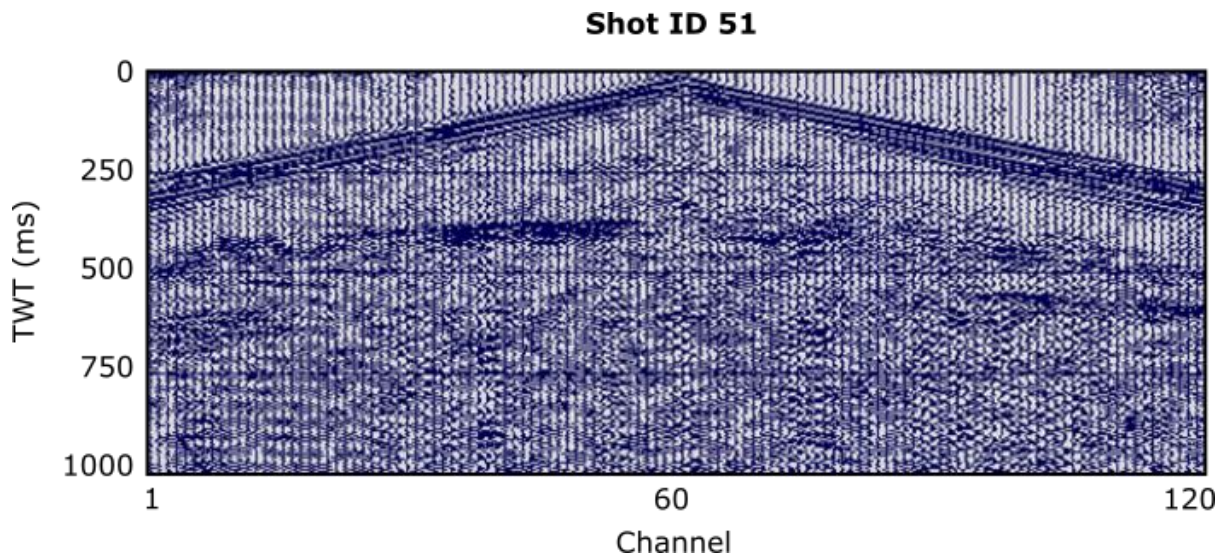
There is a significant improvement with DECONW applied. However, the various lengths with zero gap provided similar results, and image quality. A DECONW length of 150 ms was selected as subjectively, was possibly being the best visual result in these tests.

A zero-phase deconvolution filter (SPECQ) and a surface consistent (SCDECON) deconvolution filter were then tested as an alternative to DECONW. SPECQ was tested because of the zero-phase nature of Vibroseis, this form of deconvolution could potentially be more effective than the other two since it operates by the spectral equalization in the frequency domain. SCDECON was tested since it generally produces a better output because of the more stable operators. More specifically, the SCDECON module works by averaging the autocorrelation functions of all traces in each shot, and deriving and applying one operator per shot.

However, in line 01 in particular, DECONW was more effective than SCDECON with a clearer result with less smearing (Figures 5.48 – 5.49).



*Figure 5.48 Shot 51, line 01 with DECONW parameters of 150 ms length and 0 gap with a FDFILT of 8, 15, 80, 125 Hz.*



*Figure 5.49 Shot 51, line 01 with SCDECON parameters of 150 ms length and 0 gap and with a FDFILT of 8, 15, 80, 125 Hz.*

---

## 5.14 Bandpass Filter Parameter Testing

Thus far, the bandpass filter parameters used have been the values used by the original data processing team in 1987. With the preferred deconvolution process and parameters configured for the current processing sequence, it is now possible to better assess the low cut and high cut filters for the frequency filters.

Similar to the process of deconvolution testing, the job flow was then set up with a deconvolution process module with fixed parameters with FDFILT with varying corner frequencies. Refraction mutes are applied with a 500 ms normal AGC applied. The low-cut frequencies were then varied while keeping the high corner frequencies fixed (Figure 5.50) and then vice versa (Figure 5.53). The corner frequencies used for Figure 5.50 and 5.53 are found in Table 5.7 and 5.8 respectively.



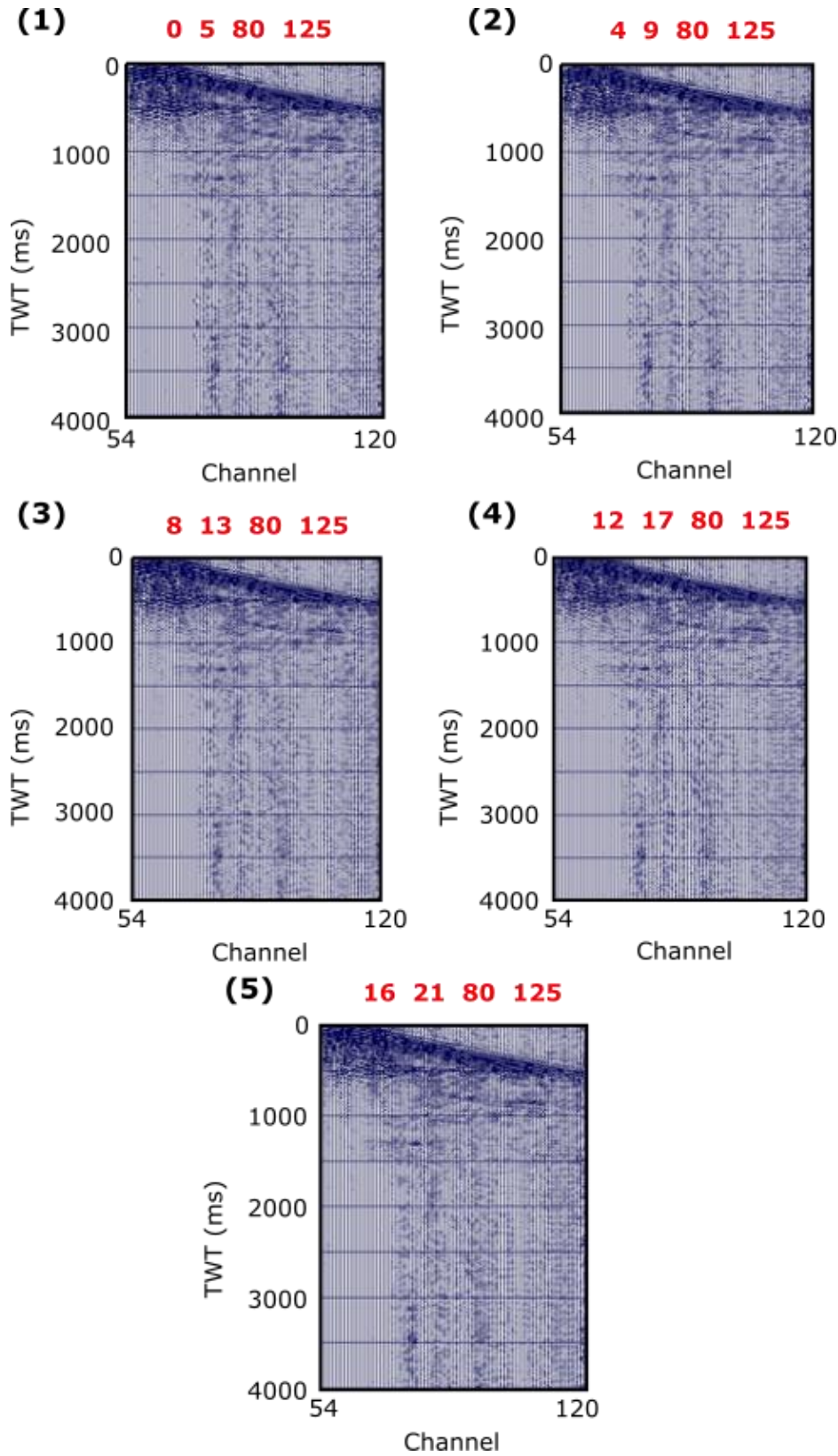


Figure 5.50 Low cut filters applied to shot 1 line 01. The corner frequencies (Hz) are labelled in red and the numbers in brackets correspond to the numbers in Table 5.7 .

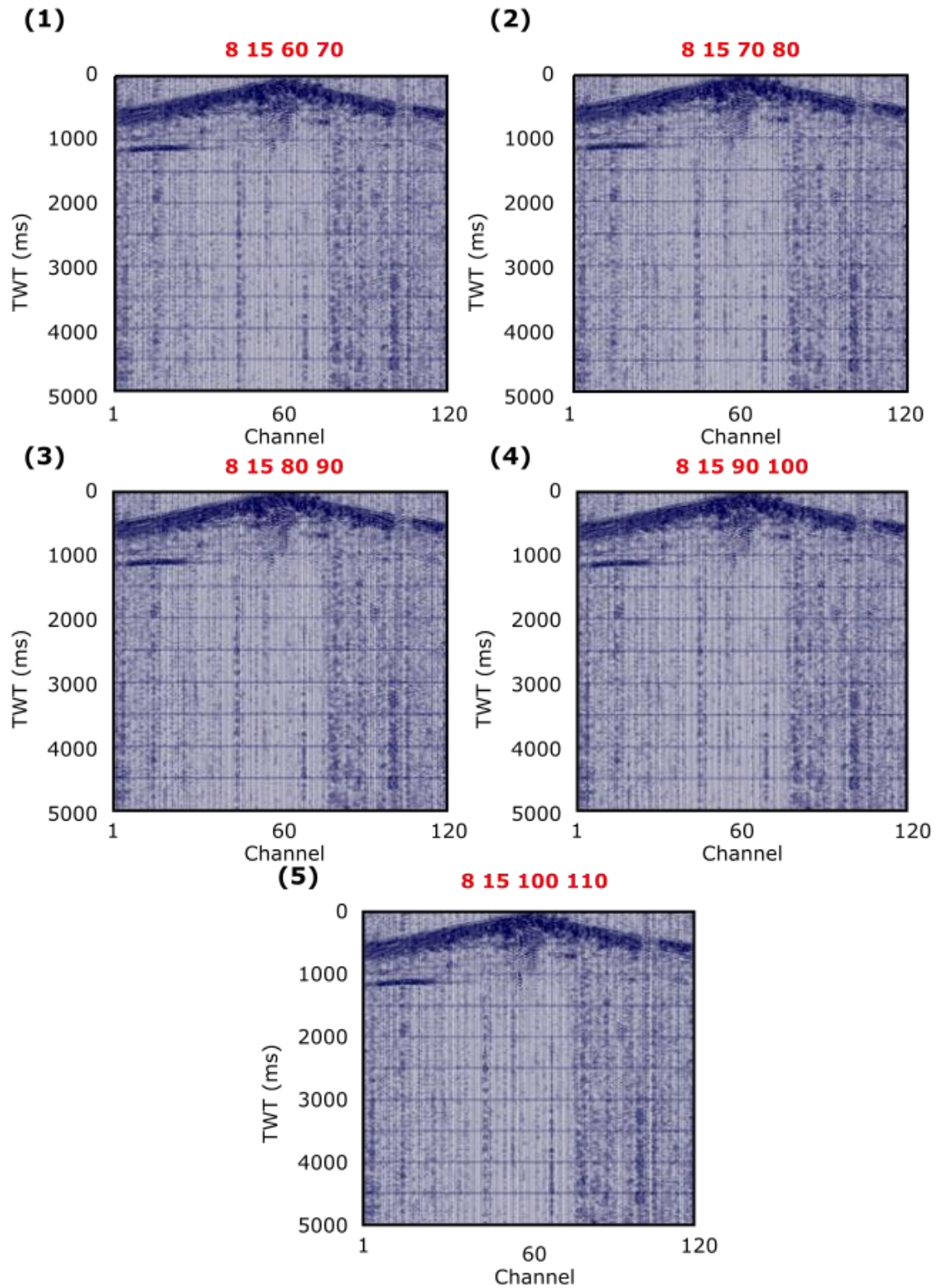
*Table 5.7 Parameters used for a low frequency filter testing.*

Low Frequency Filter Testing					
BP = Bandpass		Corner Frequencies (Hz)			
Number	Filter Type	F1	F2	F3	F4
1	BP	0	5	80	125
2	BP	4	9	80	125
3	BP	8	13	80	125
4	BP	12	17	80	125
5	BP	16	21	80	125

*Table 5.8 Parameters used for the high frequency filter testing*

High Frequency Filter Testing					
BP = Bandpass		Corner Frequencies (Hz)			
Number	Filter Type	F1	F2	F3	F4
1	BP	8	15	60	70
2	BP	8	15	70	80
3	BP	8	15	80	90
4	BP	8	15	90	100
5	BP	8	15	100	110

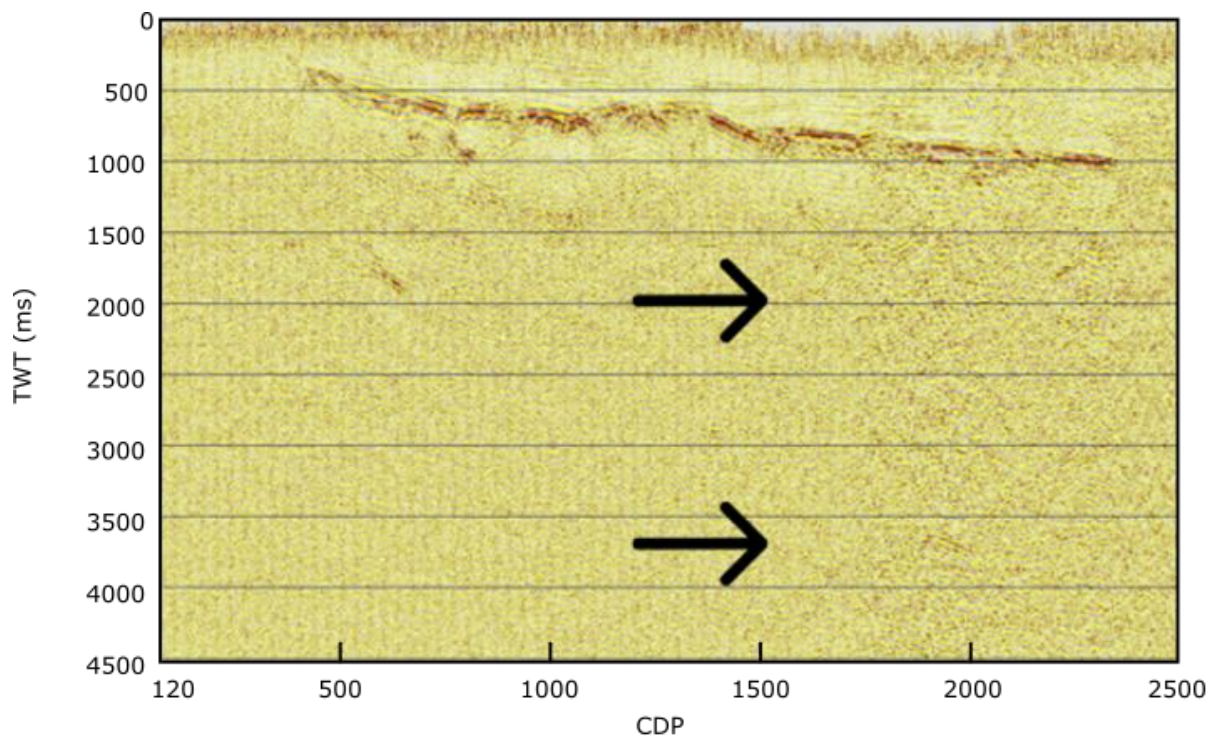
Frequencies 12 - 17 Hz appear to have a greater effect on times approximately 1550 ms and a smaller filter 8 - 13 Hz have a more significant effect on the lower portions of the data (Figure 5.50). These same low corner frequencies were used for all lines.



*Figures 5.51 High cut filters applied five different times to shot 101 of line 01. Low corner frequencies are kept the same while high corner frequencies  $f_3$ ,  $f_4$  of each shot are changed to match the values in previous Table 5.8.*

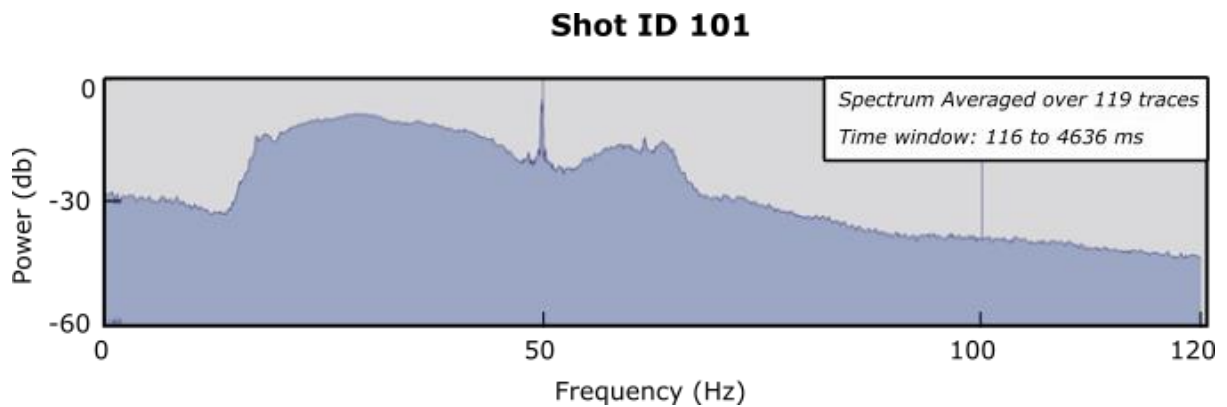
In general there is not a large amount of difference when the high-cut filters when applied. So the final parameters I will use will be the 74 - 104 Hz. The current study refrained from going above 125 Hz for the high frequency filter as it would exceed the Nyquist Frequency of 125 Hz.

Despite using regular bandpass filtering, “ringy-ness” can be seen in raw stacks of the lines (Figure 5.52). Using a frequency spectrum graph of the shots, spikes can be seen around frequencies 50 Hz and 62.5 Hz (Figure 5.53). These frequency spikes are seen in all lines. Using line 03 as an example, the effect of applying notch filters can be seen in the figures below (Figure 5.54 - 55).

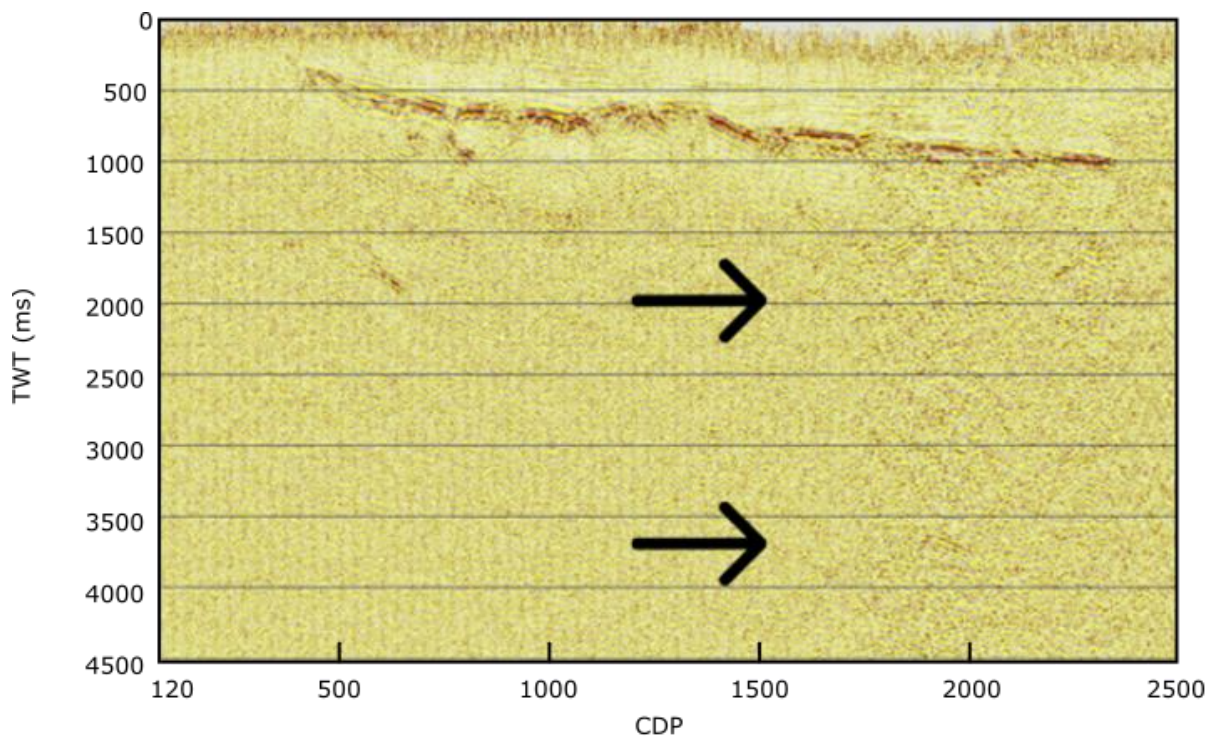


*Figure 5.52 Stacked image with FX\_Decon, FD\_Filt and DECONW of line 03, as well as a post-stack AGC for viewing purposes. However, the band-stop filter for frequencies 50 Hz and 62.5 Hz has not been added. The black arrows indicate region high environmental noise.*



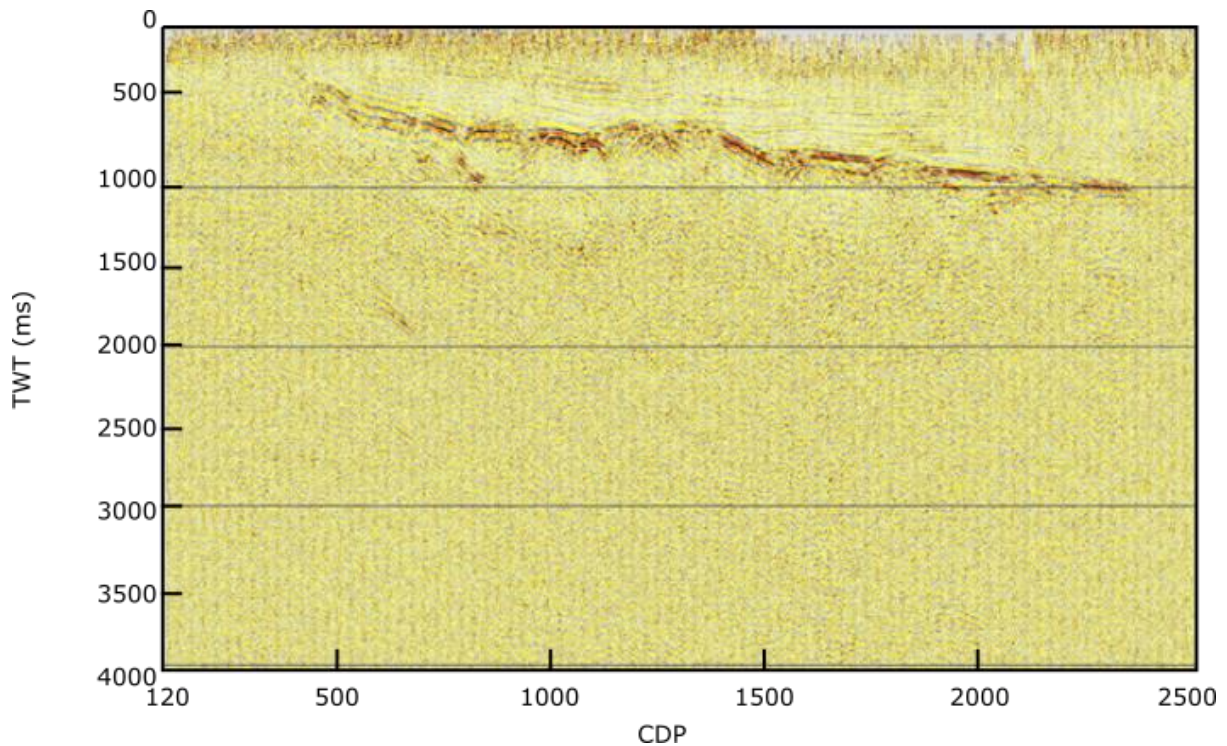


*Figure 5.53* A frequency spectrum for shot 101 with a trapezoidal frequency filter of 8-15-74-104 Hz. It can also be seen that there is a spike at about 50Hz. It is probable this is parasitic resonance from nearby power lines. A notch filter will be implemented to remove this spike.



*Figure 5.54* Stacked image with FX\_Decon, FD\_Filt and DECONW of line 03, as well as a post-stack AGC for viewing purposes. However, the band-stop filter for frequencies 50 Hz and 62.5 Hz has been added. The black arrows indicate the region where the filters are specifically trying to target.





*Figure 5.55 Stacked image with FX\_Decon, FD\_Filt and DECONW of line 03, as well as a post-stack AGC for viewing purposes. Compared with the previous Figure 5.59. There is a significant reduction of noise that was evident in CDPs 1600 - 2469 after applying a notch filter. Vertical scale is the two-way time in milliseconds (ms) and horizontal scale as labelled.*

The filtering effects of low frequency noise based on wavenumber and frequency (QFK) is greater than that of FD\_FILT. Although FD\_FILT makes it easier to target specific frequencies (such as powerline noise), the two are used in unison to provide a better overall image.

Figures 5.56 and 5.57 show the F-K spectrum of line 03 emphasising the filtering differences between QFK and FD\_FILT.

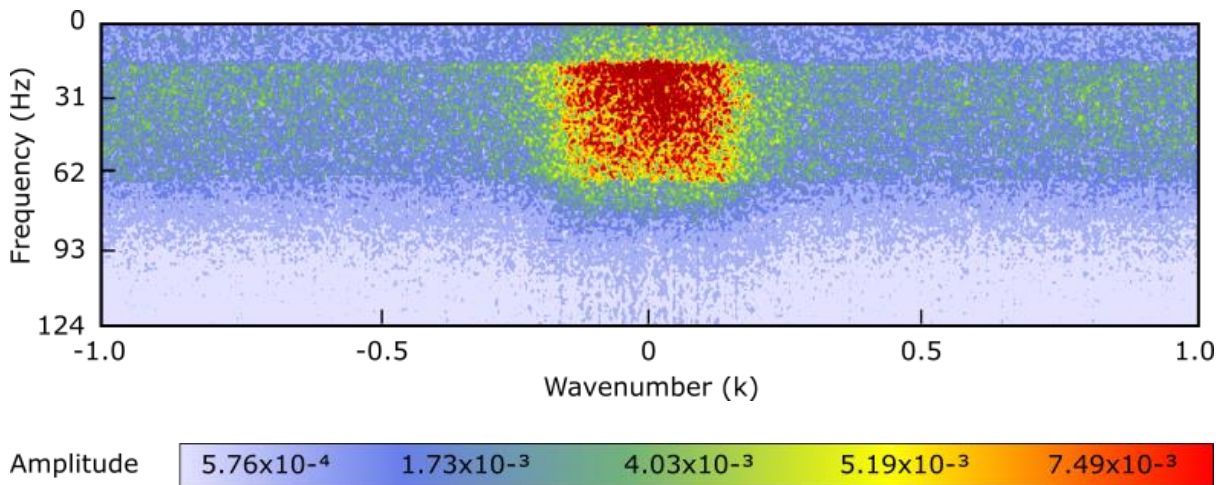


Figure 5.56 F-K spectrum of line 03 with the application of QFK.

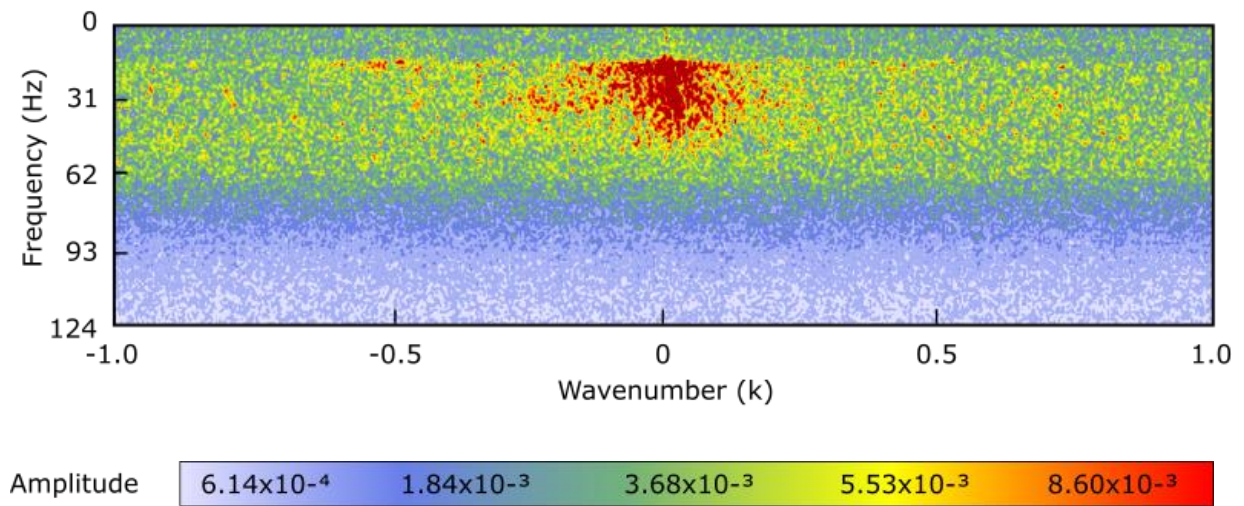


Figure 5.57 F-K spectrum of line 03 with no QFK but rather with FD\_Filt.

---

 5.15 Compilation

The shot records are then compiled together with QFK, FXDECON, DECONW, SMUTE, FDFILT and STATICS forming a single shot file with all of the desired pre-stack processing modules applied. The compilation into two separate jobs, one for noise suppression, i.e. QFK (Table 5.9), and another for deconvolution. (Table 5.10) Filtering was applied after deconvolution because the deconvolution process tends to increase the amount of low and high frequencies (Yilmaz, 2010).

*Table 5.9 Job flow for compiling the effects of noise filters to the shot records. Not all filtering effects are used for each line. These can be added in or taken off depending on the requirements of each seismic line. This particular job was previously called ADD\_FK\_FX.job.*

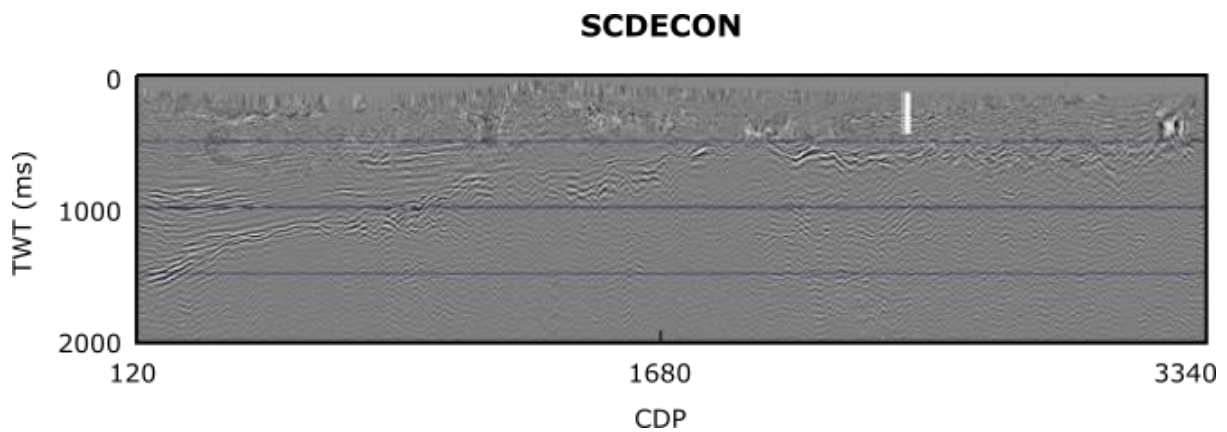
<b>Adding Noise Filters Job Flow</b>		
<b>Order</b>	<b>Claritas Module</b>	<b>Purpose</b>
<b>1</b>	DISCREAD	Reads *.csgy file with the geometry file applied
<b>2</b>	DATUM_FLT	Corrects to floating datum
<b>3</b>	STATIC	Applies static corrections
<b>4</b>	SMUTE	Applies refraction mutes on the shot gathers
<b>5</b>	AGC	Creates an AGC wrap to control extreme anomalous values
<b>6</b>	NMO	Applies *.nmo file to correct travel times
<b>7</b>	QFK	Applies an f-k filter to the seismic data
<b>8</b>	FXDECON	Removes noise through deconvolution along the x-domain
<b>9</b>	SEMBSMOOTH	Noise reduction through a coherency filter
<b>10</b>	NMO	Undoes the effects of the initial NMO process
<b>11</b>	DISCWRITE	Writes new output file

*Table 5.10 Job flow for introducing deconvolution to the shot records.*

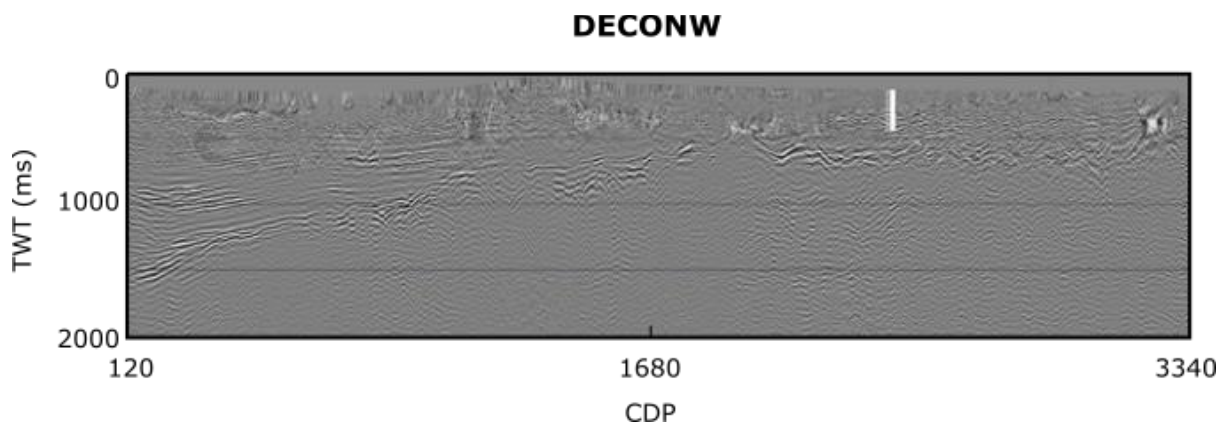
<b>Adding Deconvolution Job Flow</b>		
<b>Order</b>	<b>Claritas Module</b>	<b>Purpose</b>
<b>1</b>	DISCREAD	Reads in *.csgy file with geometry and filters applied
<b>2</b>	DECONW	Applies a standard Wiener deconvolution
	SCDECON	Applies a surface consistent Wiener deconvolution
	SPECQ	Applies a zero phase deconvolution filter
<b>3</b>	FDFILT	Applies a bandpass frequency filter
<b>4</b>	NOTCH	Applies a notch filter to target specific frequencies
<b>5</b>	SMUTE	Applies a refraction mute to the shots
<b>6</b>	DISCWRITE	Writes new output file

The shot file was then sorted to a CDP-ordered file in preparation for stacking, non-live traces are removed as well with the TREMOVE module. Due to the requirements of the version of Claritas used (version 6.8.1), CDP sorting and stacking were completed as two separate jobs.

For several lines such as lines 01 and 04, files with pre-stack processing applied produced Not-a-Number (NaN) values that gave empty spaces when the data was stacked (Figures 5.58 - 60). This occurred for all different types of deconvolution (i.e. spectral equalisation, Wiener deconvolution, and surface consistent deconvolution) but each stack was affected to varying degrees. For the following images, no AGC or BALANCE has been applied for viewing purposes (Figure 5.58 – 5.61).

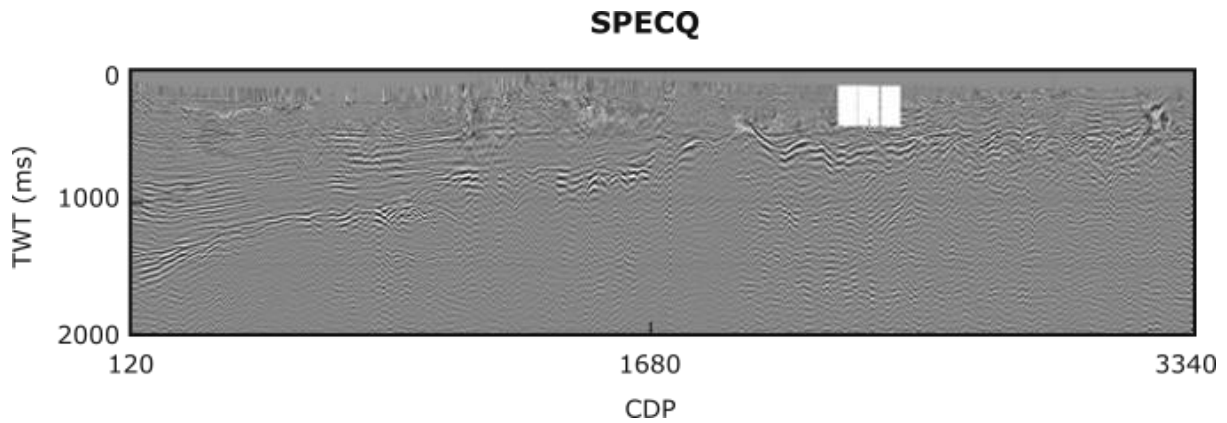


*Figure 5.58 NaN affected SDECON stack.*

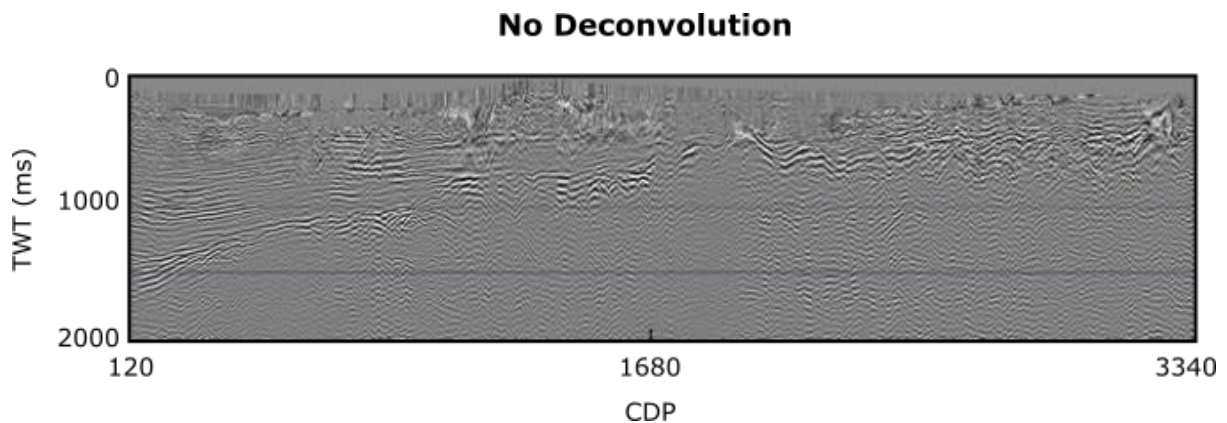


*Figure 5.59 NaN affected DECONW stack.*





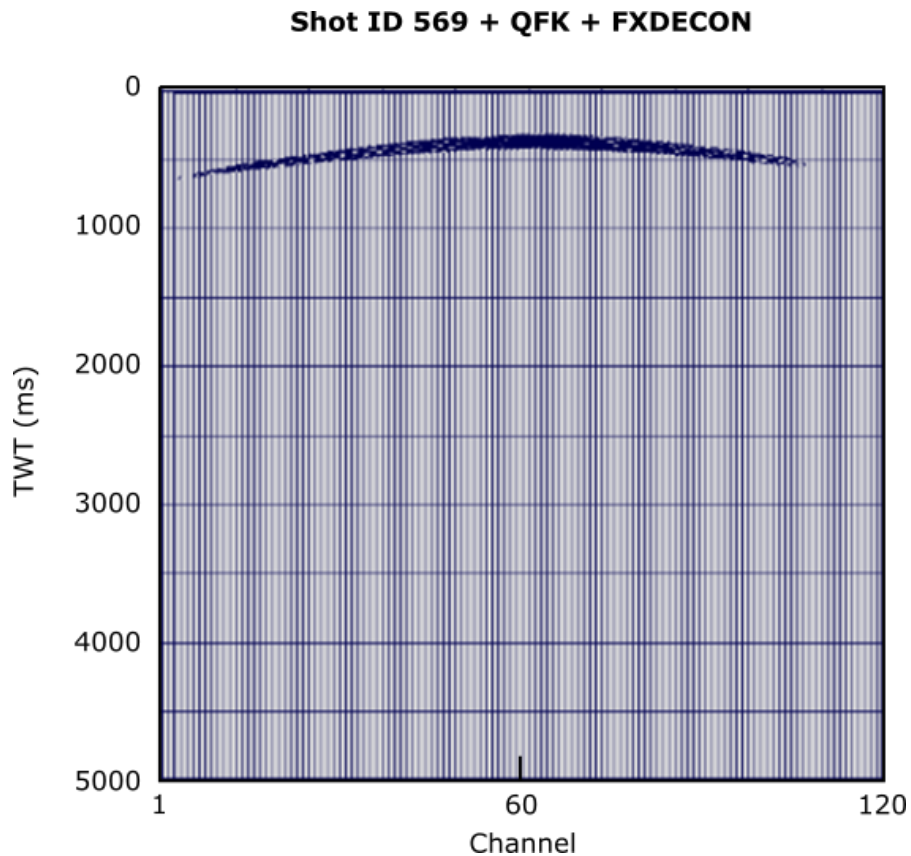
*Figure 5.60 SPECQ stack was affected the most by the NaN values.*



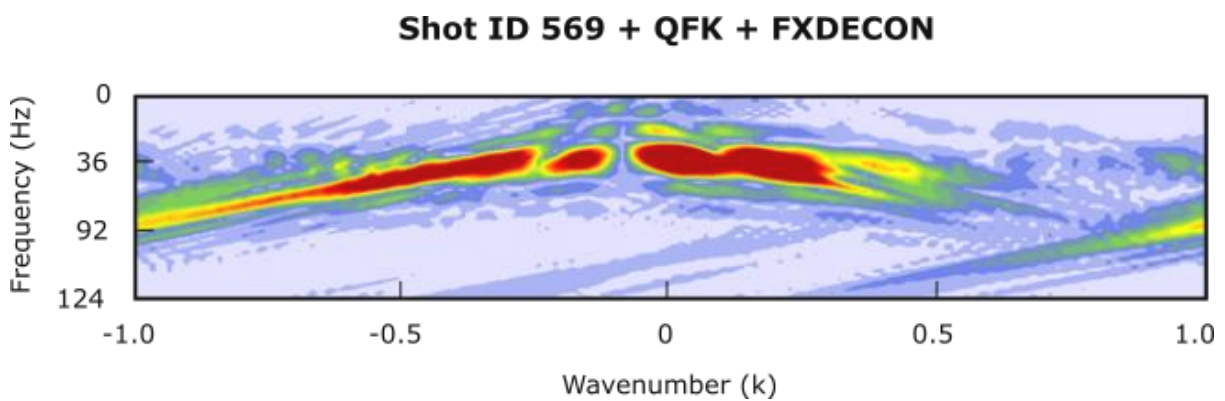
*Figure 5.61 Stack with no deconvolution applied.*

From the figures above, note that the spectral equalisation stack was affected the most by the NaN values. All deconvolution processes produced NaN values around shots 560 - 590 while the stack without deconvolution did not produce any. This means that there is a factor within the job flow prior to deconvolution that is causing this error.

The previous job flow was ADD\_FK\_FX.job (Table 5.9). This was where QFK and FXDECON was applied. As suspected, shots found around 560 - 590 had sections of anonymously high signal causing the surrounding traces to appear zero in comparison (Figure 5.62).



*Figure 5.62 Shot 569 with QFK and FXDECON applied. The reflection event can be seen clearly in this image and it seems that there is no signal present in the other areas of this image.*



Amplitude

$2.81 \times 10^{-4}$

$8.42 \times 10^{-4}$

$1.40 \times 10^{-3}$

$2.43 \times 10^{-2}$

$3.93 \times 10^{-2}$

*Figure 5.63 FK spectrum of Shot 569 with QFK+FXDECON. The spectrum shows the strong amplitudes appearing in the centre corresponding to the VAWG image. However, it also shows that the areas in pale blue (or appear as zero traces in the prior image) actually do have a non-zero amplitude.*

At first glance at Figure 5.62, it would appear the unusual shot gather had no signal in the deeper sections. However, this illusion is caused by the amplitudes in the upper section overpowering and dwarfing the other aspects of the trace (Figure 5.63). As a result, when FXDECON is applied it will remove a significant chunk of the image. When other deconvolution processes are then finally applied, it is unable to process this information thus breaking down producing NaN values seen in the previous figures. To overcome this, an AGC wrap was performed around the values to help balance the traces during deconvolution. The new ADD\_FK\_FX.job is shown below in Table 5.11.

*Table 5.11 Updated Table 5.9 with an AGC wrap to prevent NaN values from appearing.*

<b>Adding Noise Filters Job Flow (with AGC wrap)</b>		
<b>Order</b>	<b>Claritas Module</b>	<b>Purpose</b>
<b>1</b>	DISCREAD	Reads *.csgy file with the geometry file applied
<b>2</b>	DATUM_FLT	Corrects to floating datum
<b>3</b>	STATIC	Applies static corrections
<b>4</b>	SMUTE	Applies refraction mutes on the shot gathers
<b>5</b>	AGC	Creates an AGC wrap to control extreme anomalous values
<b>6</b>	NMO	Applies *.nmo file to correct travel times
<b>7</b>	QFK	Applies an f-k filter to the seismic data
<b>8</b>	FXDECON	Removes noise through deconvolution along the x-domain
<b>9</b>	SEMBSMOOTH	Noise reduction through a coherency filter
<b>10</b>	NMO	Undoes the effects of the initial NMO process
<b>11</b>	UNAGC	Removes the effects of the initial AGC
<b>12</b>	DISCWRITE	Writes new output file

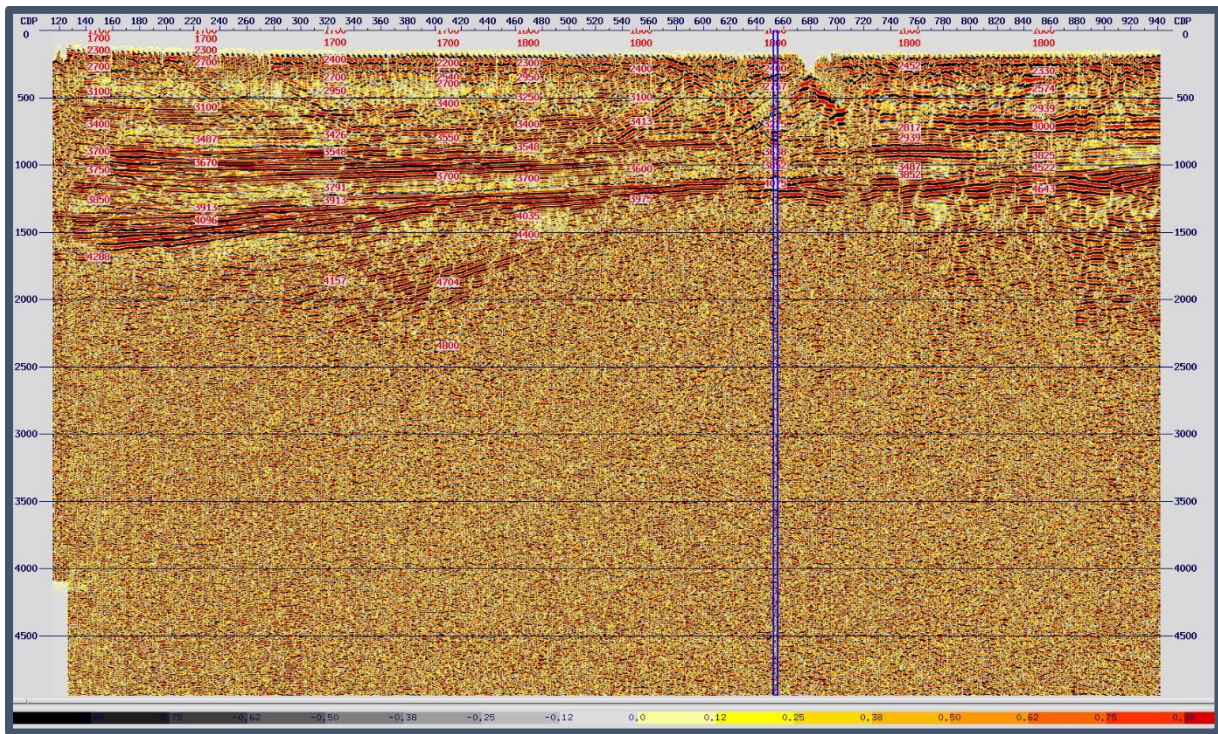
---

### 5.19 Velocity Analysis

Claritas Velocity Analysis (CVA) application in Claritas was used to begin the detailed stacking velocity analysis. The initial .nmo file was improved (Figure 5.6) by providing a stacked and an unstacked shot files with pre-stack processing applied. There are two modes available for picking in Claritas: constant and variable. The variable mode allows quicker calculations with the function using fewer scans to cover the velocity range. The constant mode uses a single velocity to analyse all the seismic data. Despite the disadvantage of taking longer, the constant mode provided a more solid result.



Claritas provides three main methods of velocity analysis: semblance, Constant Velocity Gather (CVG) and Constant Velocity Stacks (CVS). Semblance picking was used in areas with good clear data as a basis to start the analysis (Figure 5.66). However, for the rest, CVS was used.



*Figure 5.64 A stacked image of our initial NMO of line 01, minimal pre-stack processing applied. Vertical scale is the two-way time in milliseconds (ms) and horizontal scale as labelled.*

The new improved NMO (Figure 5.65) is then applied to our pre-processed shots and stacked to produce a better stacked image.

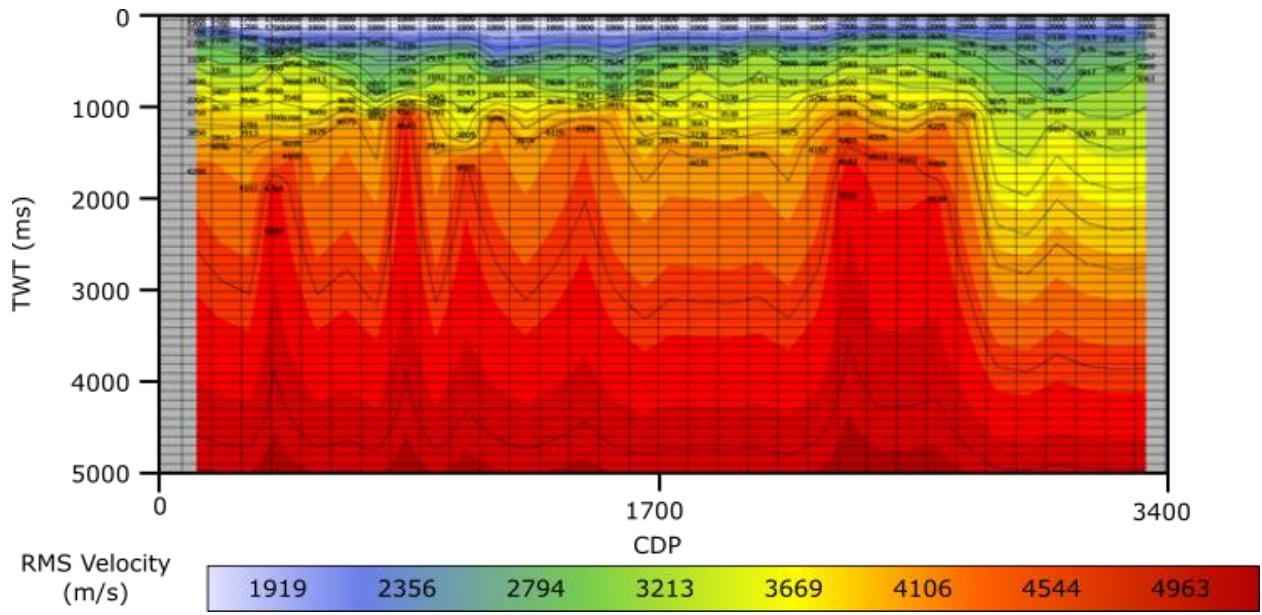


Figure 5.65  $V_{NMO}$  produced for line 01.

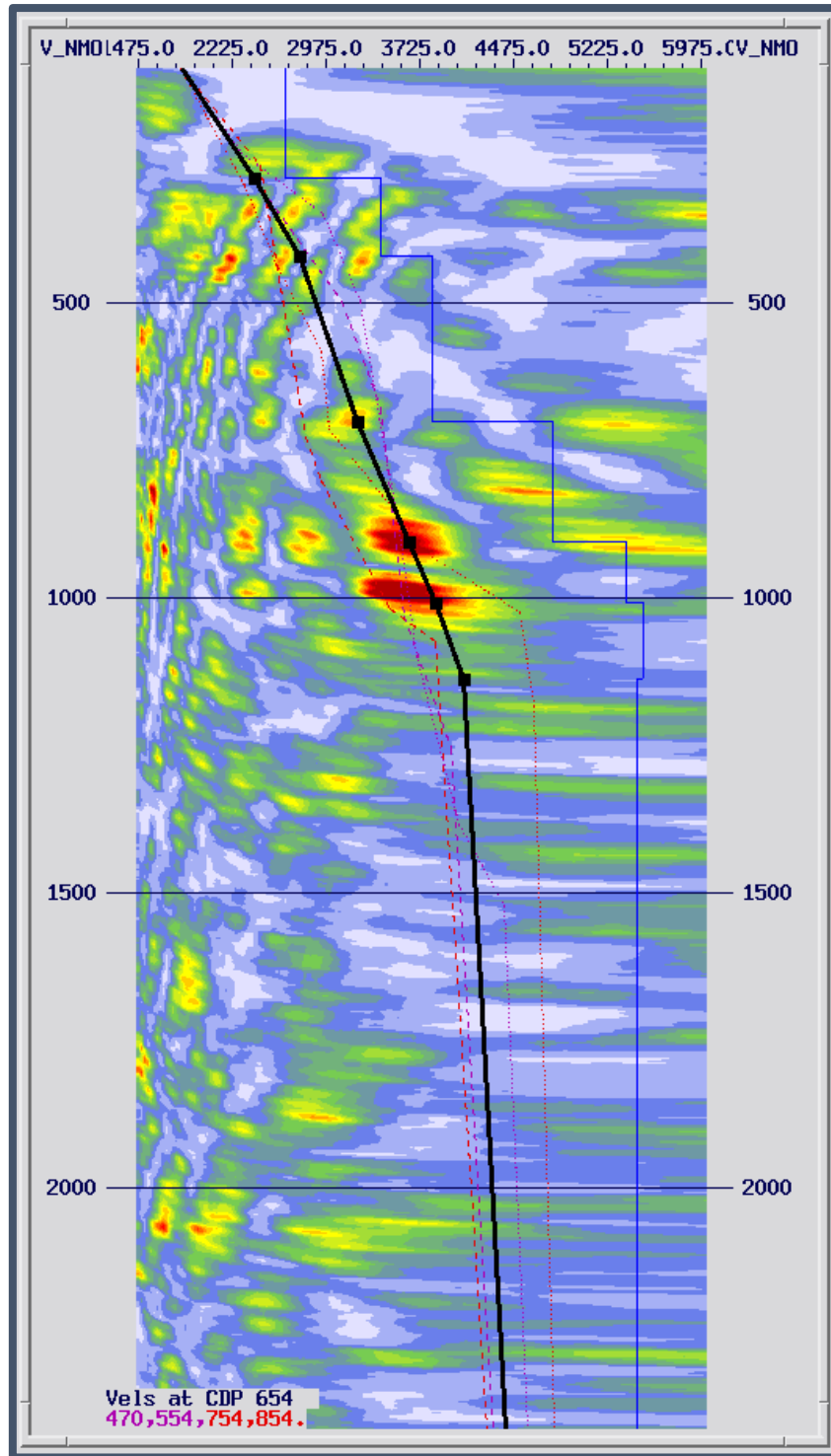


Figure 5.66 Semblance plot for CDP 654 from line 01. Vertical scale is the two-way time in milliseconds (ms) and horizontal scale is velocity (m/s)

---

## 5.20 Residual Static Analysis

High RMS amplitudes plague the land data as seen in previous sections. Upon closer viewing, vertical banding of high and low amplitude distortions can be seen littered across the shallower sections of the image (Figure 5.67). The banding is a symptom of scaling problems from residual and surface consistent scaling (Cary and Nagarajappa 2013). Due to this, the residual statics must be applied rigorously.

These scalars may be influenced by noise, which means that some of the current issues in the stack are caused by insufficient filtering. The high RMS values caused by noise will then mask the true signal. The algorithm, however, is unable to distinguish the difference between noise and signal and so applies a decreasing scaling factor to the entire shot file.

Static corrections are applied to combat this issue. SPSTAT and RESSTAT are the Claritas internal processing modules for residual statics. Both modules are tested and compared to see which can provide the best solutions. The effects of SPSTAT and RESSTAT can be seen in Figures 5.68 and 5.69.

---

### 5.20a Stack Power Residual Static

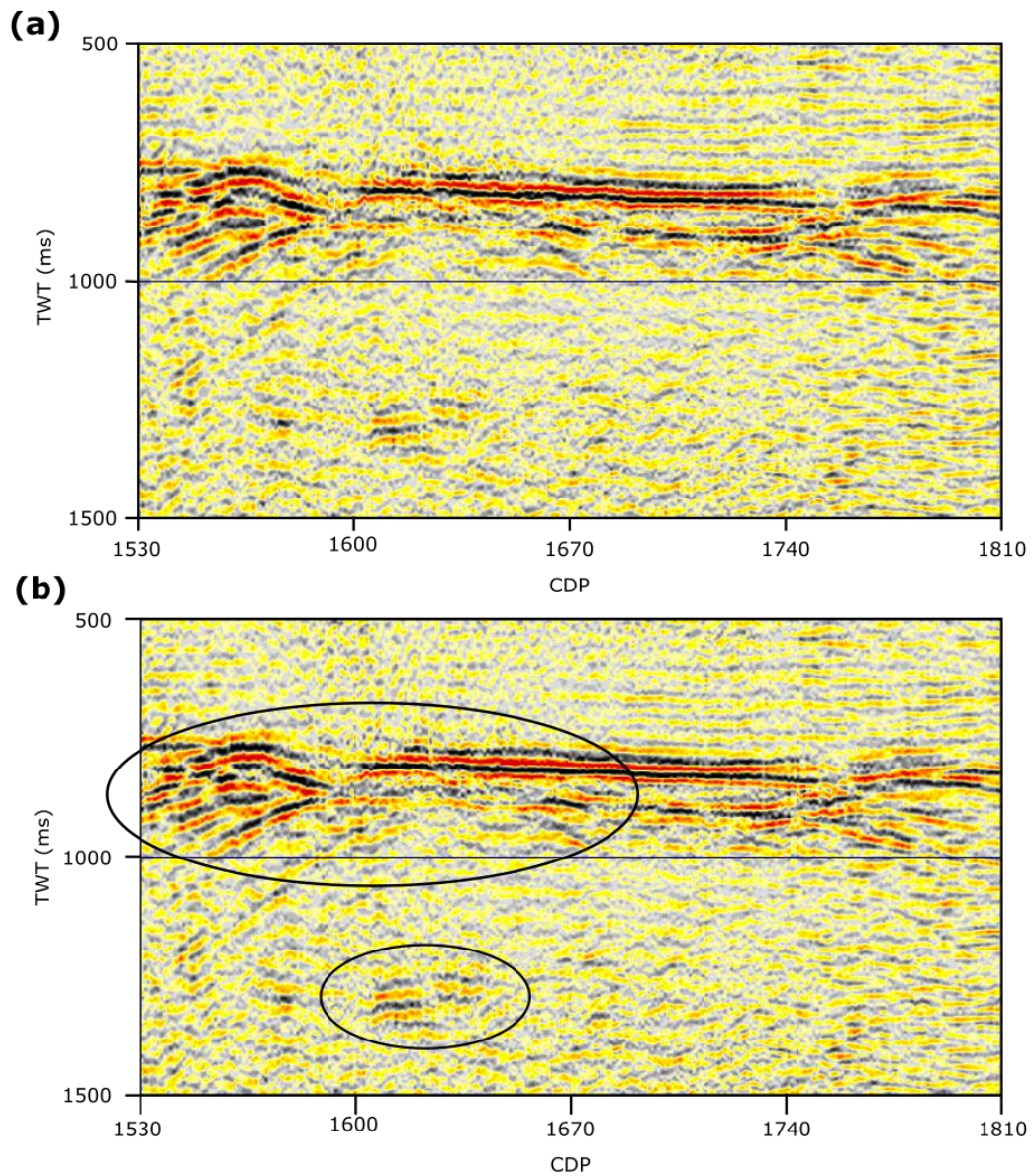
Claritas has a static process module called SPSTAT which allows for the calculation of stack power maximisation (SPM) for residual static corrections. Generally, the variable travel time is common in areas with large amount of noise hence producing erroneous shot and residual static shift calculations. SPM provides another method of determining the statics shifts.

SPM follows the overall arching theory of most residual static algorithms. This method works by cross correlating all traces for a particular shot with its corresponding stack to calculate the time shift required to optimally align the trace. This process is then repeated for all traces for a particular receiver.

The “maximum allowed time shift” is one of the parameters for SPSTAT with a self-explanatory name, it is the largest amount of time shift allowed for any shot or receiver within one iteration. A small value would produce an insufficient amount of improvement/quality to the seismic image. A large value would cause cycle skipping creating

strangely anomalous large time shifts. To test for this, the static analysis was repeated multiple times to view the final stacked image. As for the correlation window, one with the most signal was selected to improve the values and one that is large enough and outside the mute zone (refraction zone). The effects of SPSTAT on an image is shown in the image below (Figure 5.67).





*Figure 5.67 The above post-stack images are of the same area of line 03. Figure (a) is this image prior to the residual static corrections while (b) is the image after the application. The circles in (b) indicate the more noticeable improvements in the image. Reflections are more pronounced and aligned with the surrounding signal.*

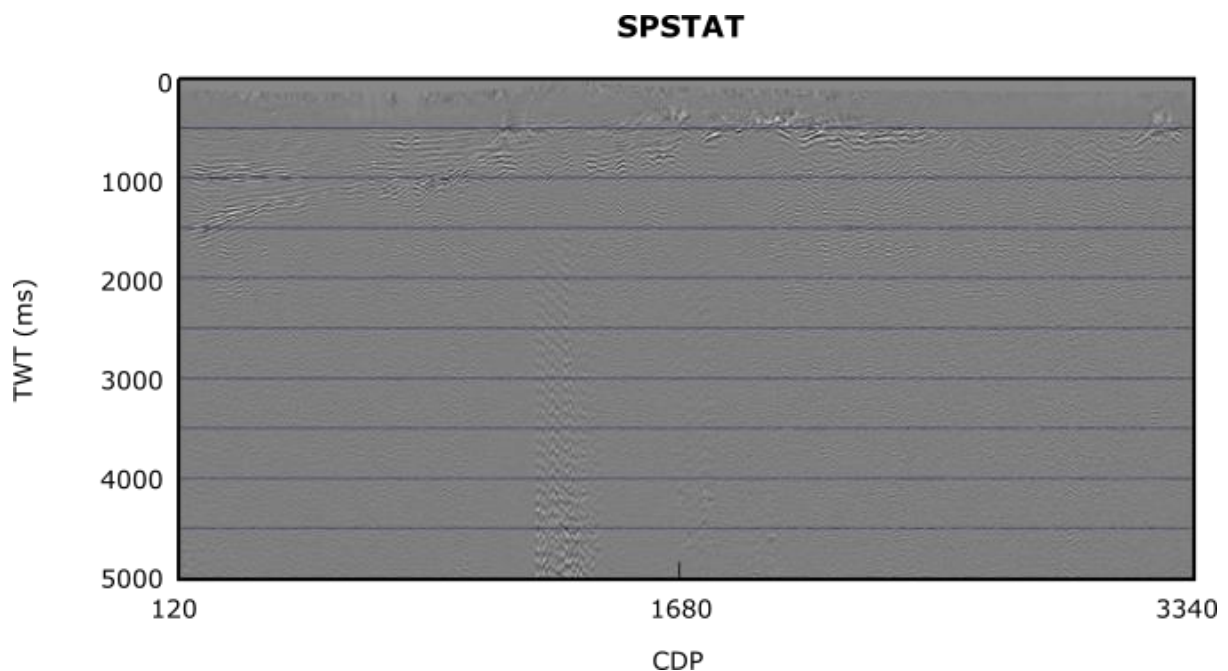
---

## 5.20b Residual Static Module

The Claritas residual static module, RESSTAT, was used for residual statics and was an alternative to SPSTAT. RESSTAT operates slightly faster than the SPSTAT module because it requires less sorting; however, it is generally slightly less accurate because the SPSTAT solution is a direct solution between the receiver and shot.

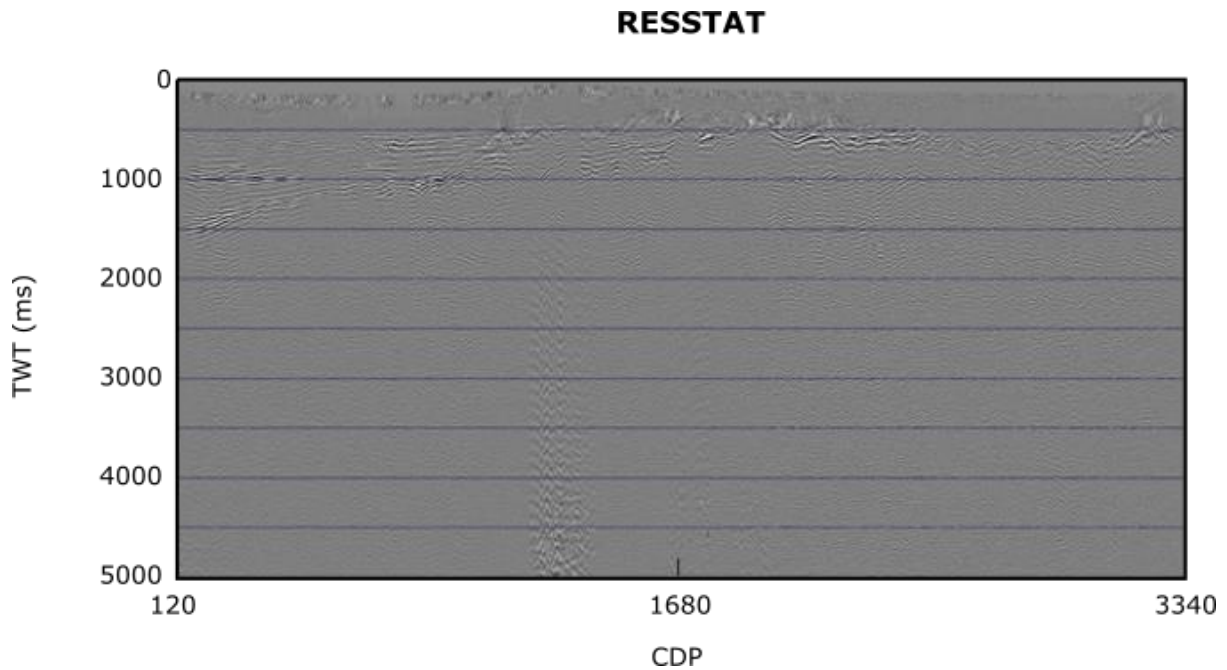
RESSTAT uses cross-correlation of pre-stack traces with a pilot CDP stack as a sort of running mix to create an input model and determine statics.

The SPSTAT and RESSTAT modules were carried out to 8 iterations. Cycle skipping began after the first cycle for the SPTAT module while cycle skipping occurred after the third iteration for RESSTAT. Both were applied to the stack modules as seen in the Figures 5.68 - 69 below. The result of both static shifts similar; however, the SPSTAT static file was used as a personal preference.



*Figure 5.68 Stacked section with Wiener deconvolution applied as well as the first iteration static file produced by the SPSTAT module.*





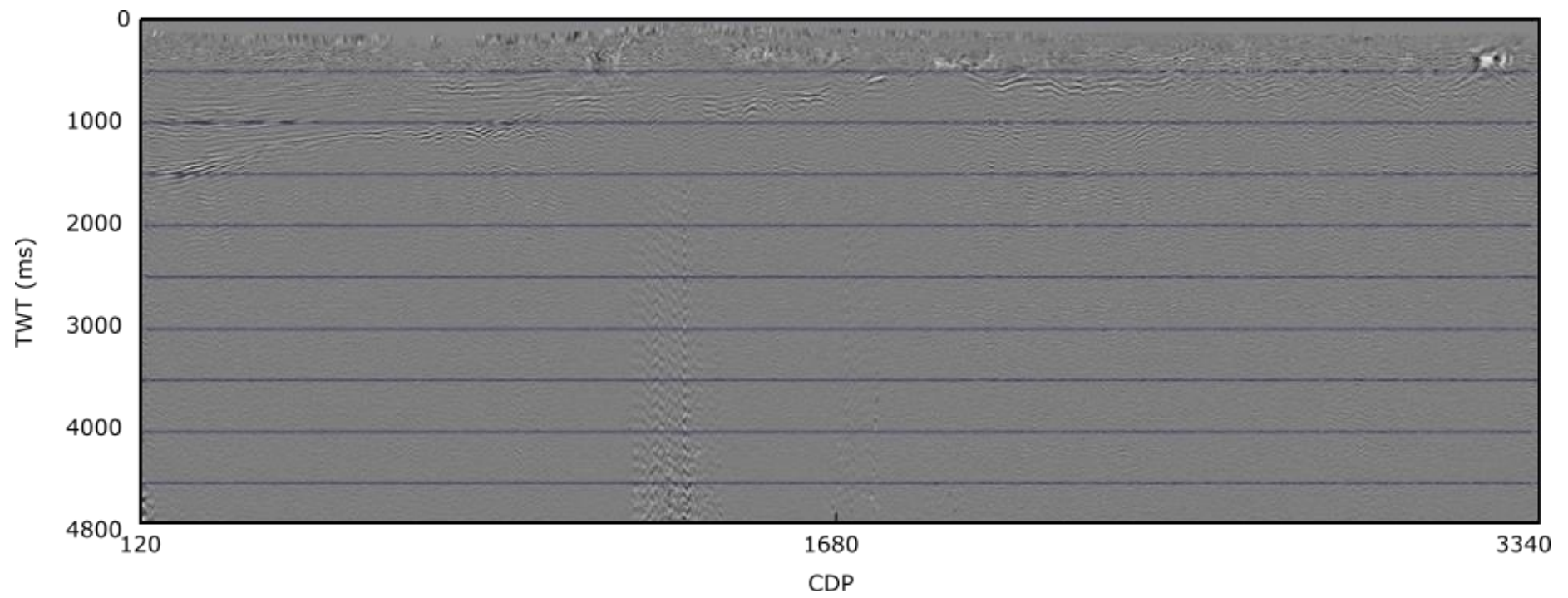
*Figure 5.69 Wiener deconvolution stacked file applied with the third iteration static file produced by RESSTAT module.*

---

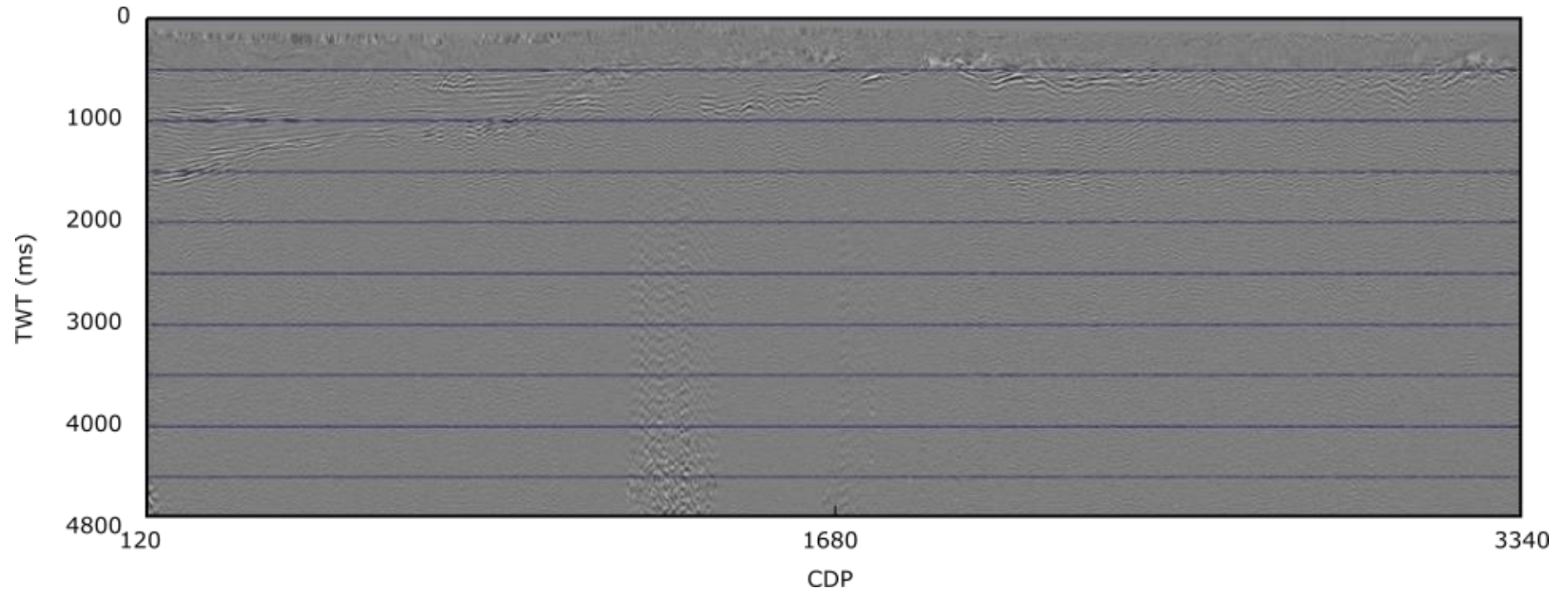
### 5.21 Second Pass Velocity Analysis

The static files were then applied to the original shot file. To produce a new CDP stack file, filtering processes were applied post-stack since large static errors can produce high-dip events which would cause further problems and perhaps create NaN values as seen earlier (Figures 5.58 – 60). The new static file has already improved the data quality significantly (Figures 5.70 - 71), particularly around CDPs 1170 - 1240 and 3200 - 3300.

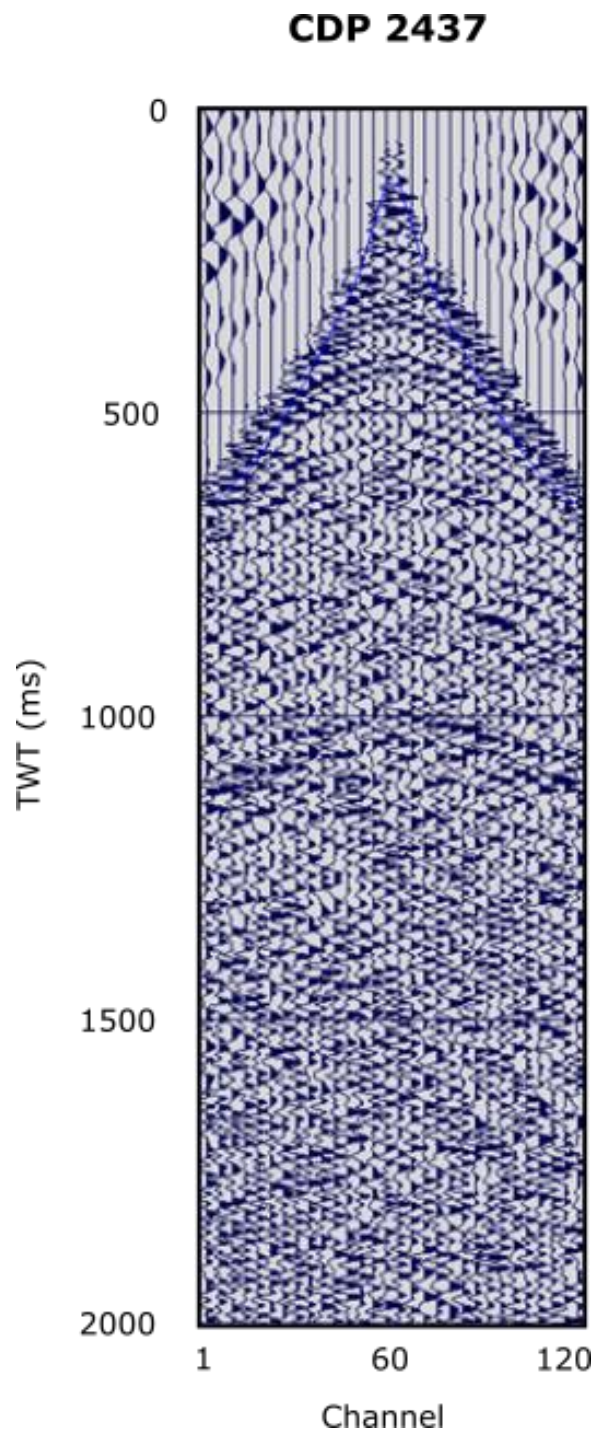
The new CDP, and stack file is then used together in combination to create a second NMO file. A second pass analysis is then carried out with the CVA application again with CVG and CVS. Using the “Gather” function, a mute file is also created for each CDP (Figure 5.72). The mute is used to null the distortions created in the shallow sections of the gathers after the application of NMO.



*Figure 5.70 Original file without the application of the SPSTAT static file.*



*Figure 5.71 New file with the static applied. Significant improvements can be seen in long the upper regions between 0 – 2000 ms.*



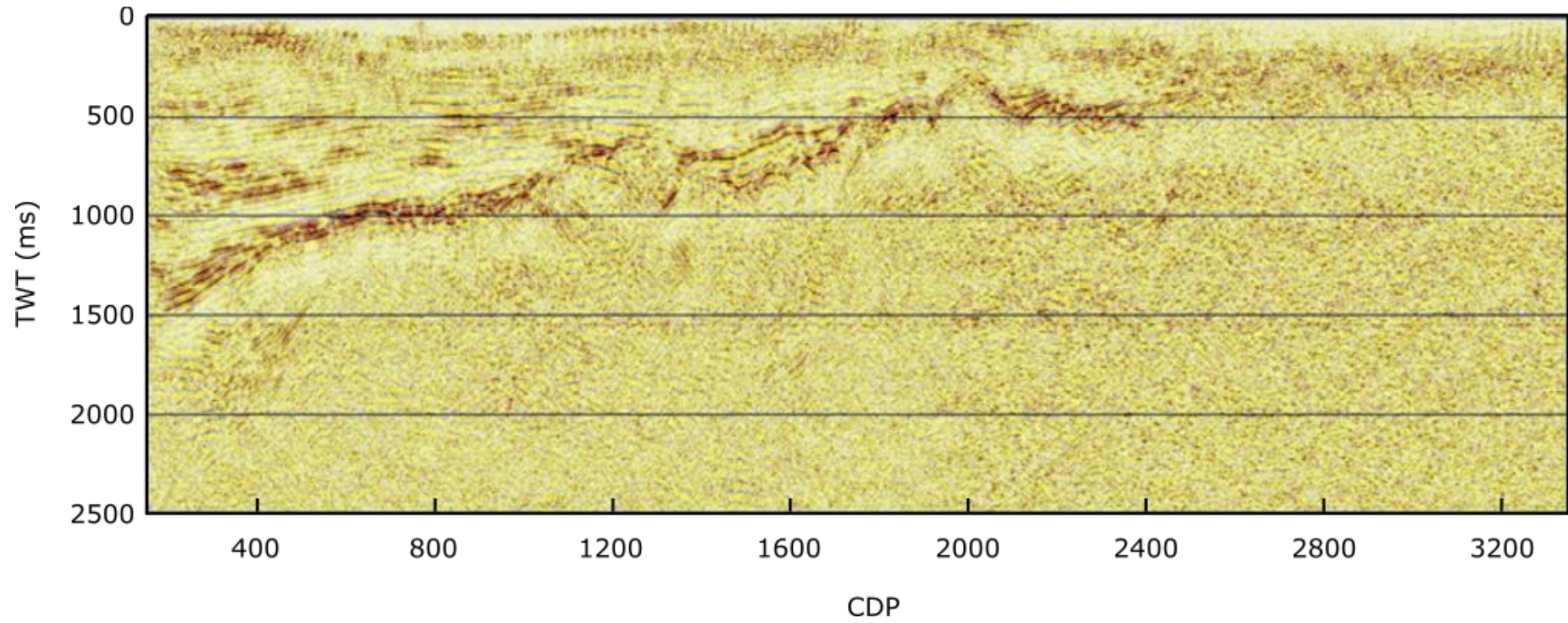
*Figure 5.72 Using the gather function in CVA we create a mute file from for CDP 2437. This mute line is seen in blue near the top of the gather.*

---

## 5.22 Post-Stack Deconvolution

After acquiring satisfactory normal move out velocities and statics, certain frequencies and remaining noise may be amplified and affect the image. At this stage, the stacked section goes through another round of testing for FXDECON, QFK, FDFILT and SEMBSMOOTH. However, depending on the individual seismic line this may not be necessary. For line 01, only FXDECON is used post-stack (Figure 5.73).





*Figure 5.73* Stacked seismic section of line 01 with post-stack FXDECON applied. The time axis ends at 2500 ms because no valuable signal could be seen below this point.



## 5.23 Migration

The stacked image was then migrated using finite difference migration (FDMIG) once the pre-stack processing has been applied. The finite-difference migration is a variation and application of the *downward continuation* method. This form of migration is more efficient than the Kirchhoff migration because of its ability to better account for lateral changes in velocity caused by dipping horizons using interval velocities and a smoothed NMO file (Figure 5.74). It is a recursive method that is applied at regular depth intervals so that the receivers are continually moved downwards until the energy diffraction hyperbola converges onto a single point (Berkhout 1980).

Frequency dependent errors and noise increase with depth from this method (Claerbout 1970). To combat this problem, the migration was applied to seismic data that was adjusted to the floating datum and only corrected back after migration. The line was then subjected to further frequency filter processes such as FKMUTE (another application similar to QFK), and a post-migration FXDECON. The final job flow is show below (Table 5.12).

*Table 5.12 Final migration job flow.*

Migration Job Flow		
Order	Claritas Module	Purpose
1	DISCREAD	Reads in *.csgy file with deconvolution, statics and all other filters applied
2	FDMIG	Applies a finite-difference migration
3	FDILT	Applies a bandpass filter
4	QFKPS	Applies the traditional QFK but post-stack
5	FXDECON	Applies post-stack FXDECON
6	DISCWRITE	Writes new output file

For the final migrated seismic section of line 01, a post stack QFK (QFKPS) with a cut off dip of 20 ms/trace was also applied (Figure 5.75).

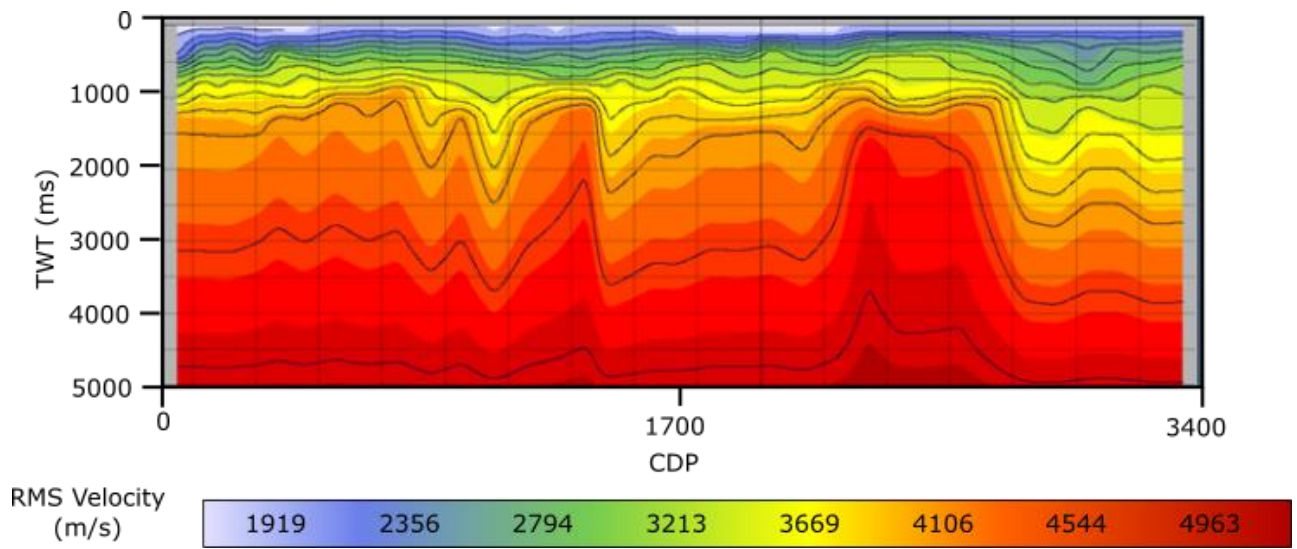
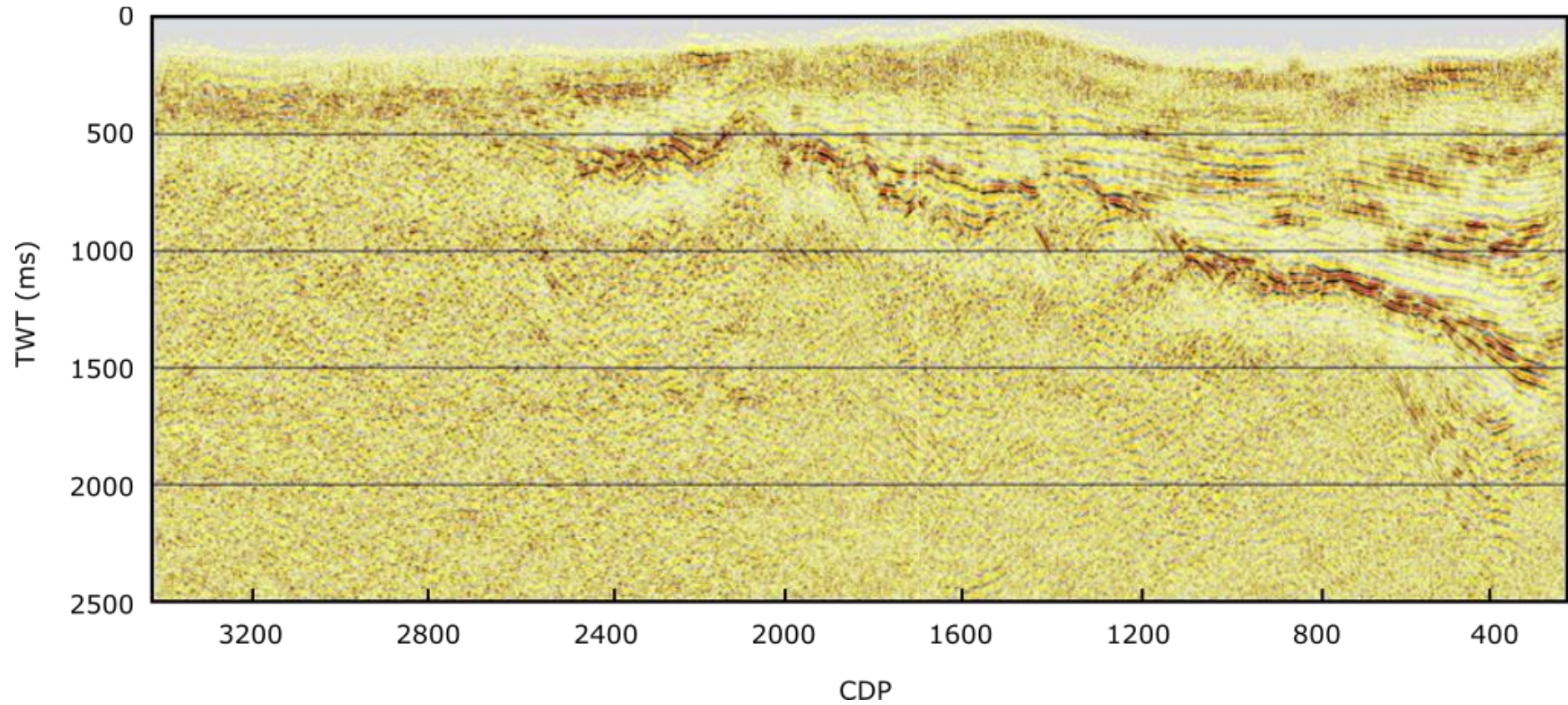


Figure 5.74 Smoothed  $V_{NMO}$  file of Figure 5.72. The isovel lines are smoother compared with the regular  $V_{NMO}$  file



*Figure 5.75 The final migrated section of line 01 with a post stack FK filter applying a 20 ms/trace cut off dip. This image has been flipped from right to left to match the west-east orientation of the seismic line.*

## 6.0 Processing Results (Line 02 – 08)

In this section, the final migrated results for each line are shown.

First, the vertical and horizontal resolutions for the seismic images are discussed Section 6.1. Then, the parameters used for processing are described in Section 6.2. Towards the end of the chapter, the modelling procedures utilised, and their resulting 3D outputs are found in Section 6.10.

---

### 6.1 Resolution Considerations

Using the equations in Section 3.2, the strongest reflector (the basement layer in this case) was used as the general target area to calculate the vertical and horizontal resolutions (Fresnel zone) for each seismic image. Since Vibroseis trucks emit a sweep of different frequencies, the dominant frequency and average velocity that occurs at the main reflector will be used to calculate the horizontal and vertical resolutions (Table 6.1). The wavelength used is calculated by its relation to frequency shown by the equation:

$$\lambda = \frac{v}{f}$$

where  $\lambda$ ,  $v$ , and  $f$  is the wavelength, velocity, and frequency, respectively.

*Table 6.1 The vertical and lateral resolutions for each seismic line is calculated with reference to the basement layer.*

Line	Dominant Frequency (Hz)	Time (ms)	Velocity (m/s)	Wavelength (ms)	Vertical Resolution (m)	Horizontal Resolution(m)
1	40	750	3400	85	21	233
2	30	660	3400	113	28	252
3	30	900	3200	107	27	277
4	36	860	3600	100	25	278
5	35	800	3600	103	26	272
6	36	750	3400	94	24	245
7	40	950	3600	90	23	277
8C	36	600	3500	97	24	226
8D	36	650	3350	93	23	225

The poor resolution observed in the seismic sections is in agreement with the large calculated horizontal resolution values (Table 6.1). The Fresnel zone will increase in size in deeper sections due to its proportional relationship with depth. Vertical resolution on the other hand, will not vary because it is not dependent on depth. These large resolution values could be improved if a broader sweep was used (e.g. 5 - 105 Hz). Such a frequency range was not available at the time of the 1987 acquisition thus a better resolution could be obtained if the survey was carried out today, i.e. finer stratigraphy can be captured (K. Driml, et al. 2004).

---

## 6.2 Processing Summary

The seismic processing job flows described in Chapter 5 has been applied to the other seven lines of the MD87 project. Through rigorous testing, the necessity and parameters of each module unique to each seismic line were determined. The specific parameters and modules used for each line are presented in the Tables 6.2 - 4. Subsequent sections in this chapter present the details of processing for each line.

*Table 6.2 Processing parameters used for first breaks and refraction static RMS values.*

Line	First Breaks			Refraction Static RMS
	LMO (m/s)	Envelope Threshold (Hi)	Acceptance (Amp) Ratio	RMS
1	2984	0.539	0.320	10.31
2	2849	1.067	0.349	7.37
3	3714	0.633	0.226	8.61
4	3000	0.822	0.320	10.44
5	3246	0.896	0.269	8.704
6	2800	0.58	0.134	10.86
7	2955	1.067	0.269	7.702
8C	3088	1.067	0.293	7.267
8D	2921	0.896	0.320	7.46

*Table 6.3 Pre-stack processing parameters used for F-K filters, deconvolution and gain. Preferred QFK values were tested for each line; however, QFK was not applied to lines where a regular bandpass filter proved sufficient, i.e. line 03.*

Line	QFK		Deconvolution	Gain		Pre-stack FK FX		
	Cut-off Dip	Cosine Taper Length	Type	Window	Type	QFK	FXDECON	SEMBSMOOTH
1	25	12	Deconw	500	Normal	Y	Y	
2	20	12	Scdecon	500	Median	Y		
3	15	12	Scdecon	1000	Normal		Y	Y
4	18	12	Deconw	500	Normal	Y	Y	
5	15	12	Deconw	500	Median	Y	Y	
6	20	12	Specq	750	Median	Y	Y	
7	18	12	Scdecon	500	Normal	y	y	
8C	25	12	Scdecon	500	Median		Y	
8D	15	12	Scdecon	750	Normal	Y	Y	



*Table 6.4 Post-stack processing parameters used for each seismic line.*

Line	Static Module Used		Post Stack FX			Migration		Scalar
	SPSTAT	REFSTAT	QFK	FXDECON	SEMBSMOOTH	Step size	Theta	
1	Y		Y			25	0.707	1.2
2	y		y			16	0.800	1.6
3	Y			y		30	0.707	1.2
4	Y		y			15	0.707	1.2
5		Y		y		25	0.500	1.3
6	y		y			25	0.800	1.4
7	y			Y		16	0.600	1.6
8C		Y	Y	Y		28	0.600	1.4
8D		Y	Y	Y	Y	14	0.707	1.8

---

### 6.3 Line 02

Line 02 is a shorter line with 898 CDPs compared with line 01 with over 3300 CDPs making data processing for this line quicker. Line 02 begins at peg 1096 of line 01. This line is a relatively straight line with few curves resulting in fewer issues with statics (Figure 6.1).

With line 02 SCDECON was used as the main type of deconvolution with an addition of the SEMBSMOOTH module in unison with QFK for the pre-stack processing. The effectiveness of QFK for the removal of ground roll is emphasised in Figure 6.2.

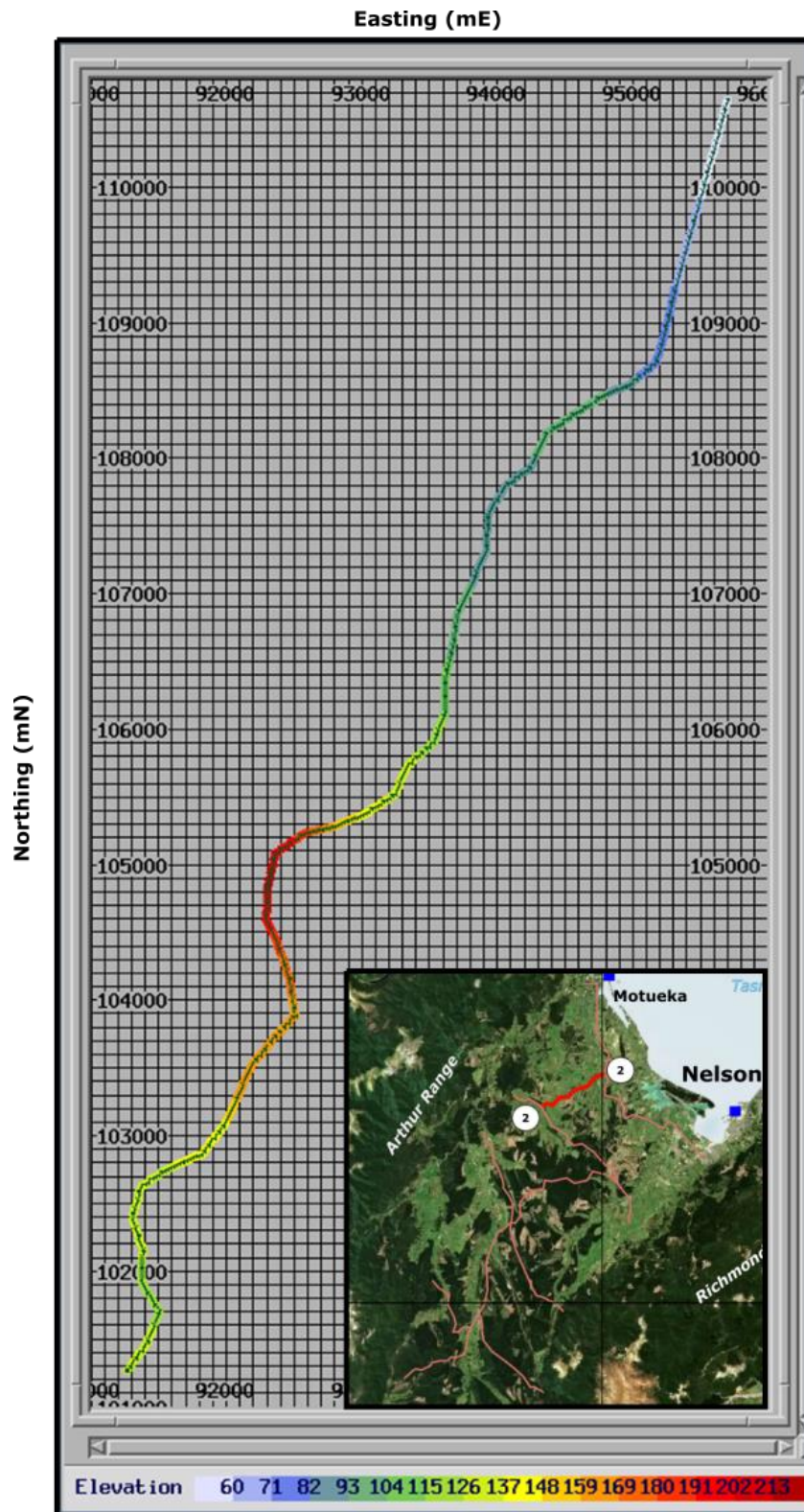
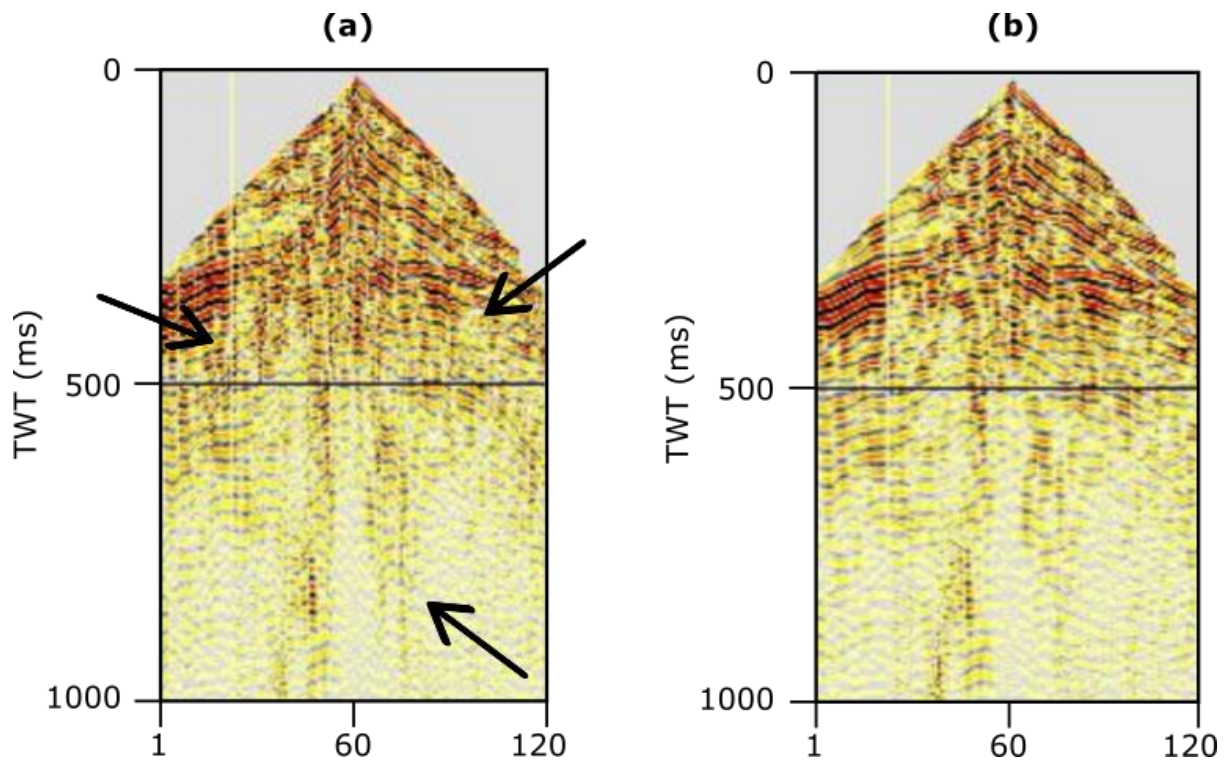
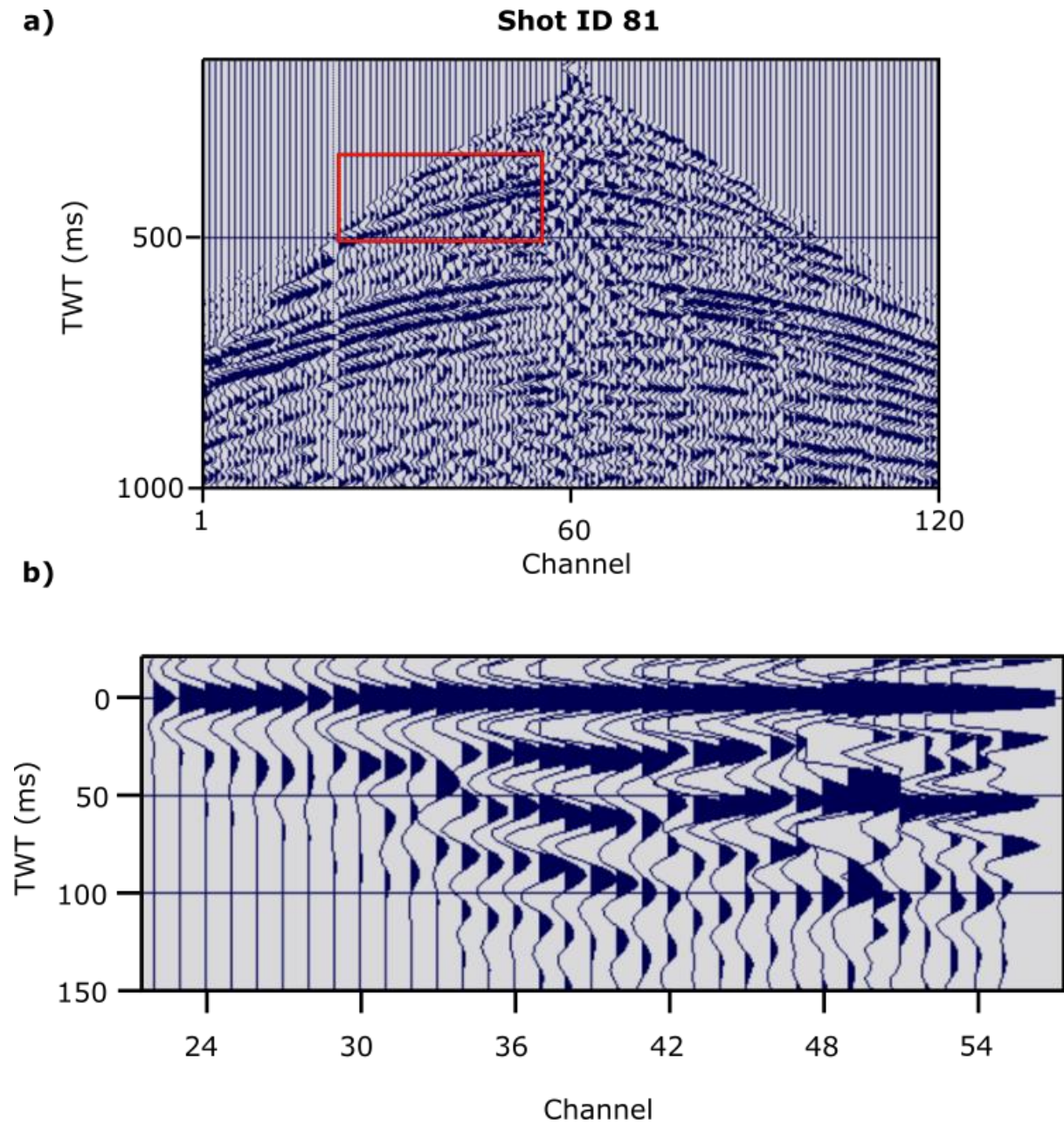


Figure 6.1 Geometry file of line 02. A cropped topographical map of Figure 1.1 has been added to provide a reference to the rest of the survey. Grid scales of the geometry are northings and eastings (mN, mE) in the NZMG coordinate system. Elevation is metres above MSL (m).



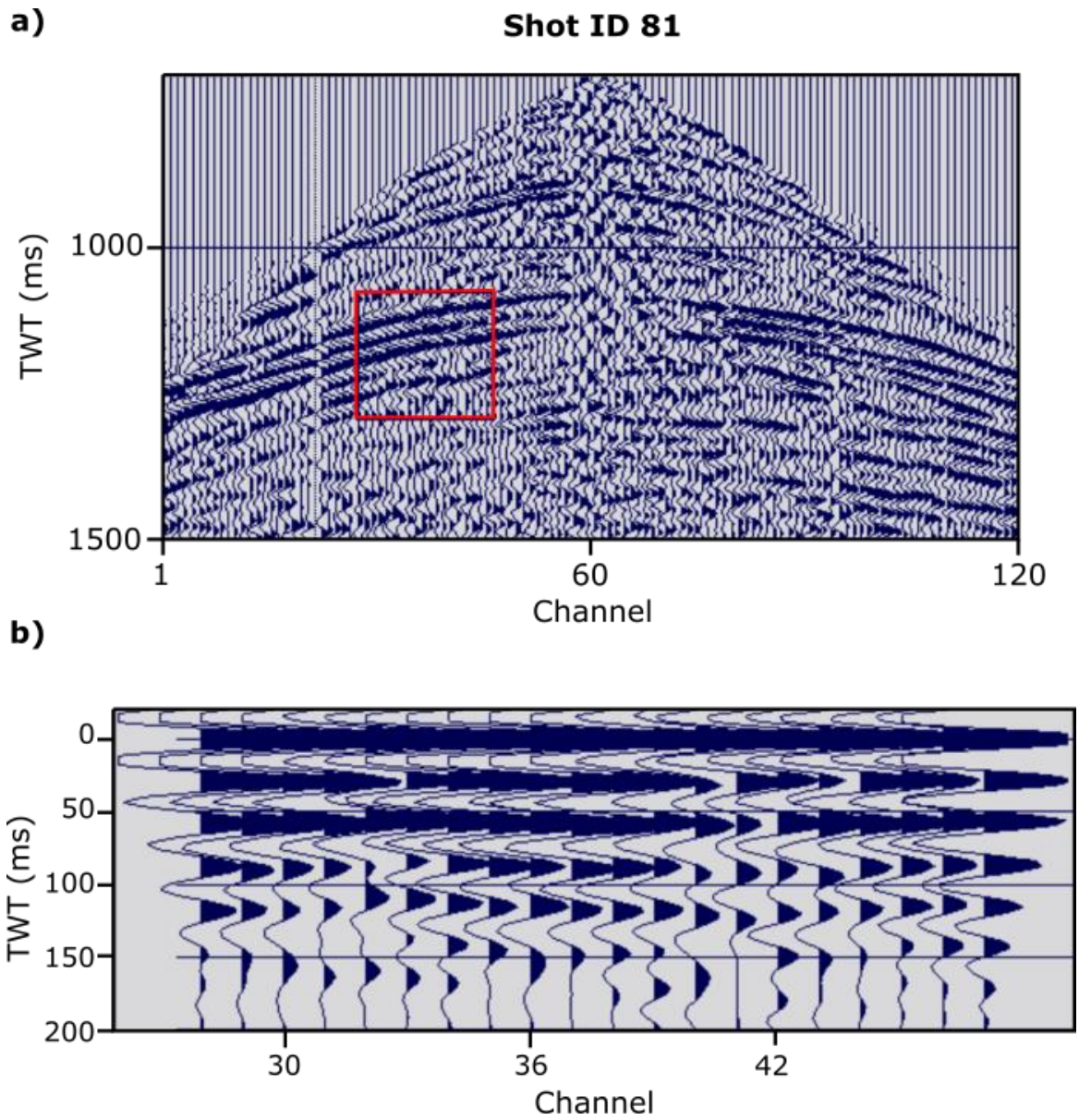
*Figure 6.2 Comparing the QFK for removing ground roll on shot 50 of line 02. Image (a) shows the effect without QFK, where the arrows indicate the areas of low frequency noise. Image (b) shows ground-roll being effectively removed after the application of QFK.*

The various types of deconvolution produced similar results and therefore the final selection of SCDECON was purely subjective. A two-window deconvolution was applied based on the two distinctive reflectors being identified in the shot gathers (Figures 6.4 and 6.5). Another reflector was spotted in the shallow section of 500 ms, however this was not included in the design window because the difference in value between gap length and operator length was not significant enough to warrant three deconvolution windows. The other deconvolution parameters were deduced using an autocorrelation zoom (Figure 6.3).



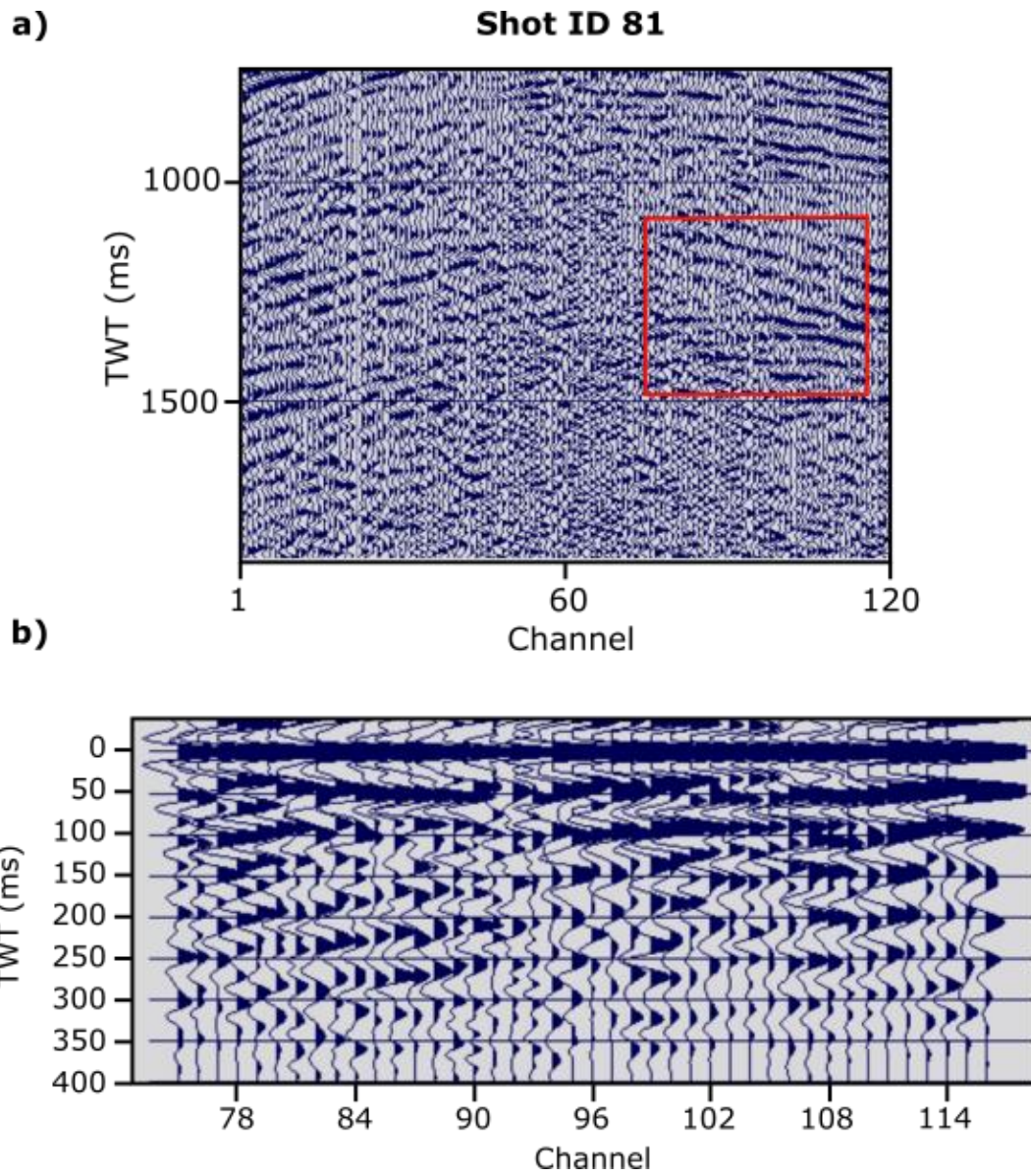
*Figure 6.3. Figure b) is the autocorrelation zoom of the boxed section of a strong upper reflector in a). The initial chosen operator length of 150 ms and gap length of 24 ms was chosen. However, because the operator value was less than 10x the gap length, the inclusion of this boxed area as a separate design window would have little improvement to the overall deconvolution of the seismic line.*



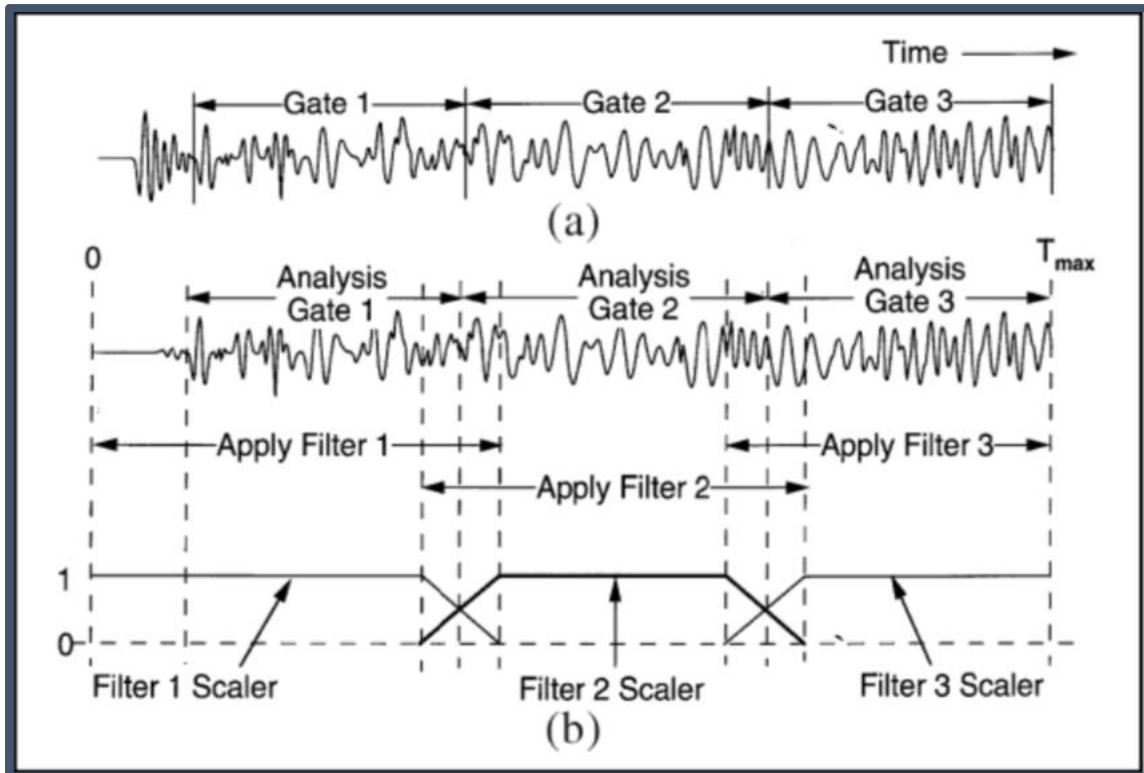


*Figure 6.4 Figure b) is the autocorrelation zoom of the boxed section of the middle reflector in a). An operator length of 250 ms and gap value of 24 ms was selected.*





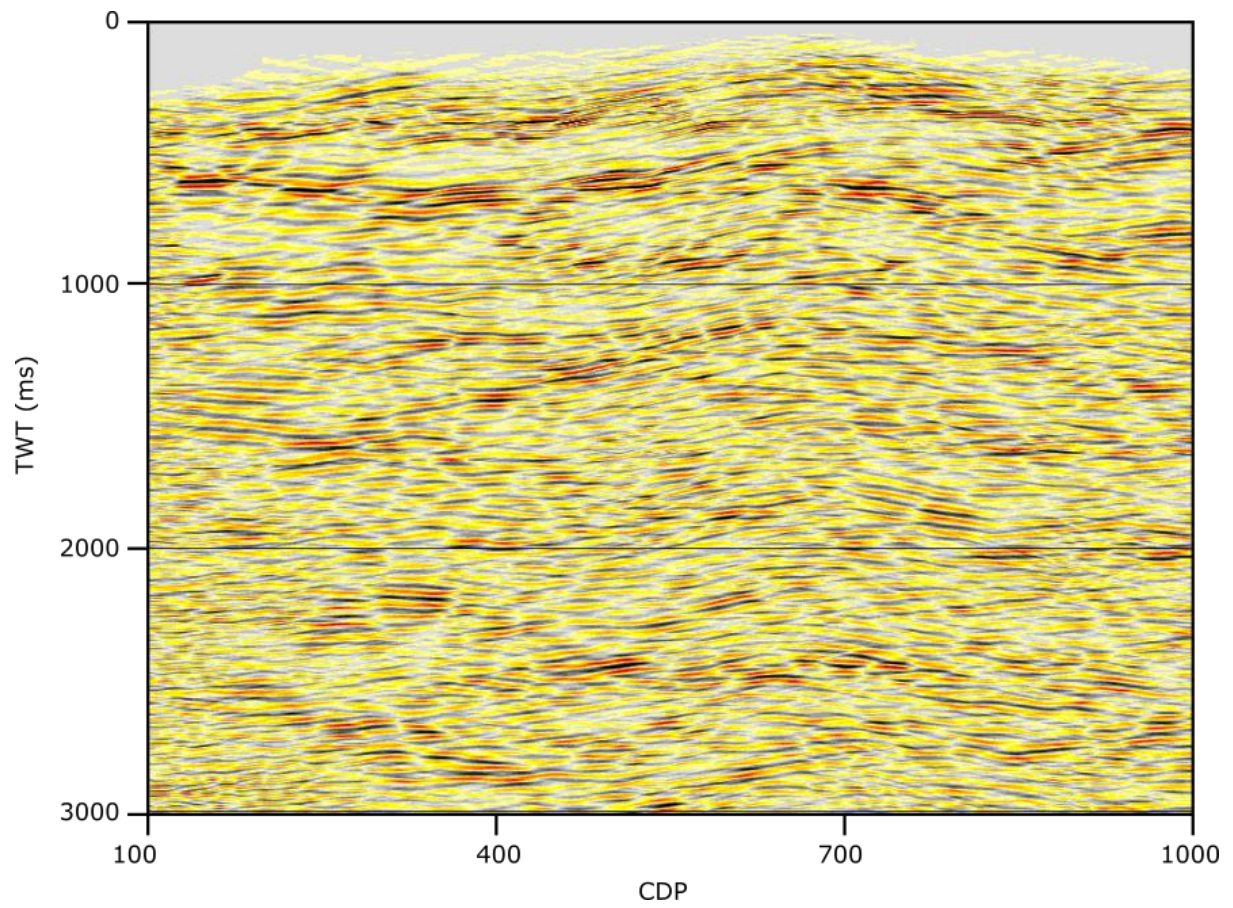
*Figure 6.5 Figure b) is the autocorrelation zoom of the boxed section of the lower reflector in a). An operator length of 350 ms and gap value of 32 ms was chosen.*



*Figure 6.6 Example of designing time-variant deconvolution gates. Image (a) shows a trace with three design windows for three areas of signal. (b) shows the area which the filter is then applied to with scaling functions overlapping each section of the trace to create a smoother amplitude change (after Gadallah and Fisher, 2005).*

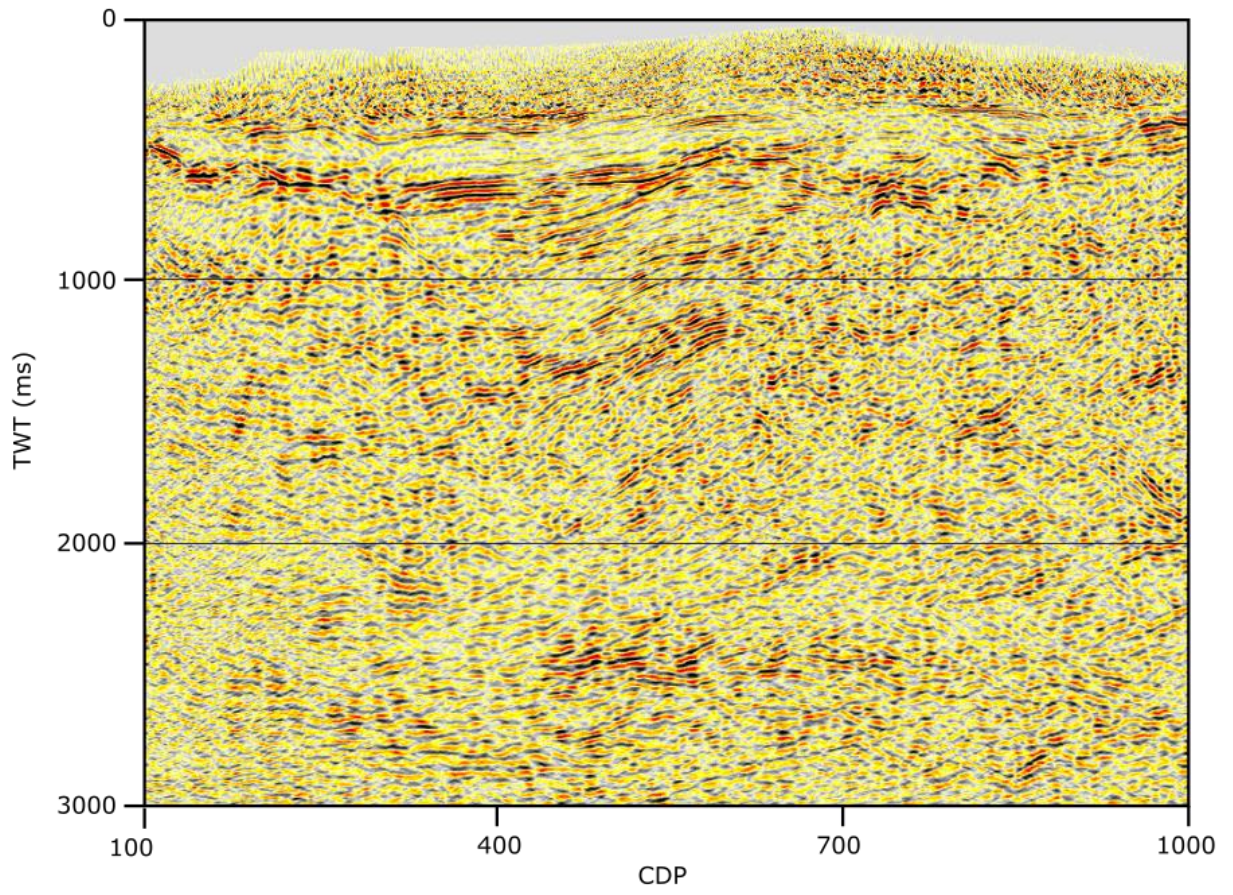
The multiple deconvolution operators were applied to noisy sections between design windows. Overlapping two operators over a noisier section allowed the image to appear less blocky and create smoother transitions between filters (Figure 6.6).

The processing for this line was straight forward with this line being relatively flat and linear. The use of mutes based on  $f$ - $k$  variables for noise reduction was rebuffed because it seemed to produce a more artificial result as seen in Figure 6.7 compared with Figure 6.8.



*Figure 6.7 A migrated stack of line 02 with a f-k mute applied.*





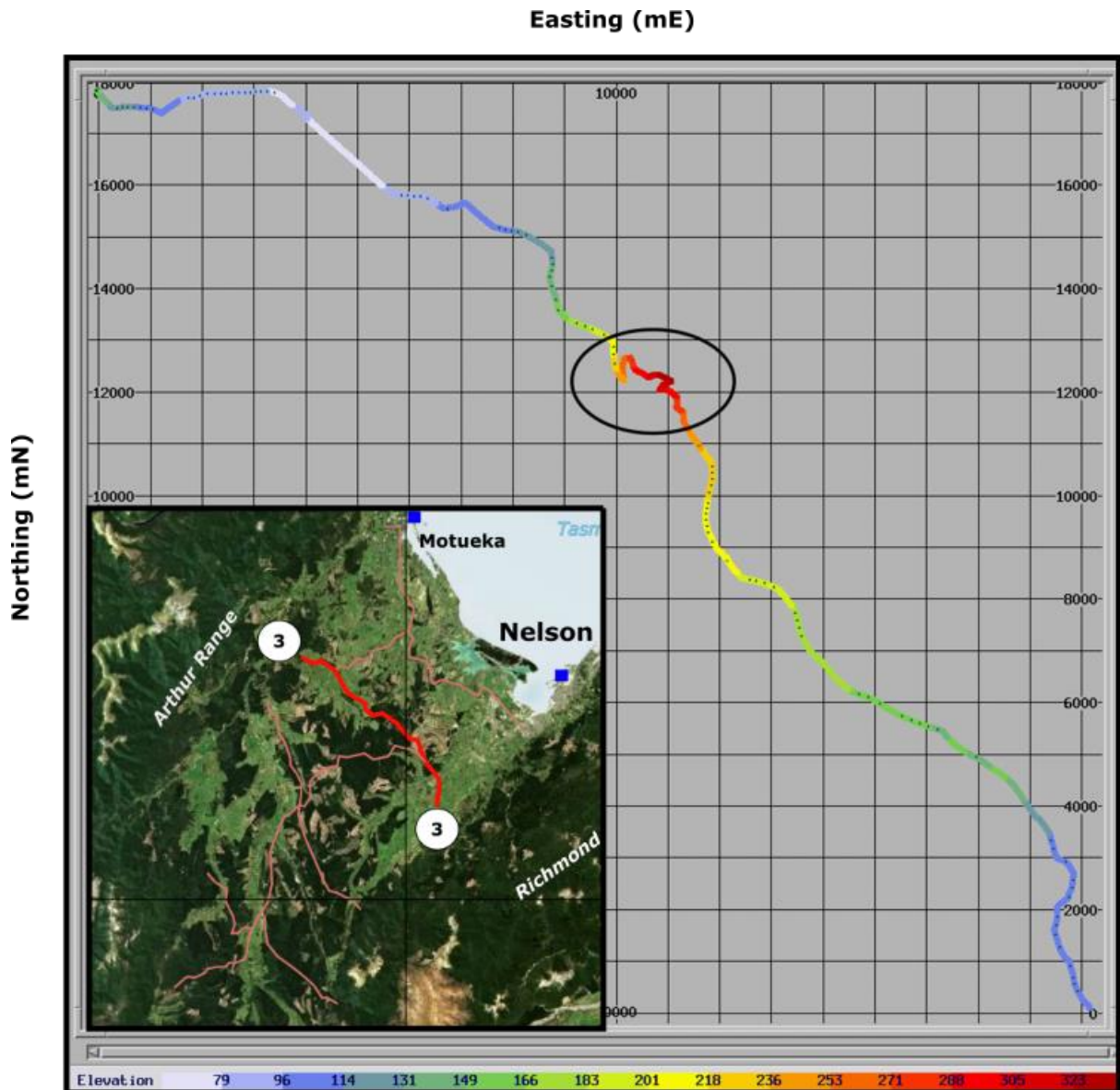
*Figure 6.8 Final migrated stack of line 02.*

---

## 6.4 Line 03

Line 03 of the MD87 project was carried out on a very windy road especially near the centre. This line contained 2418 CDPs and 674 shots and was significantly longer than line 02.

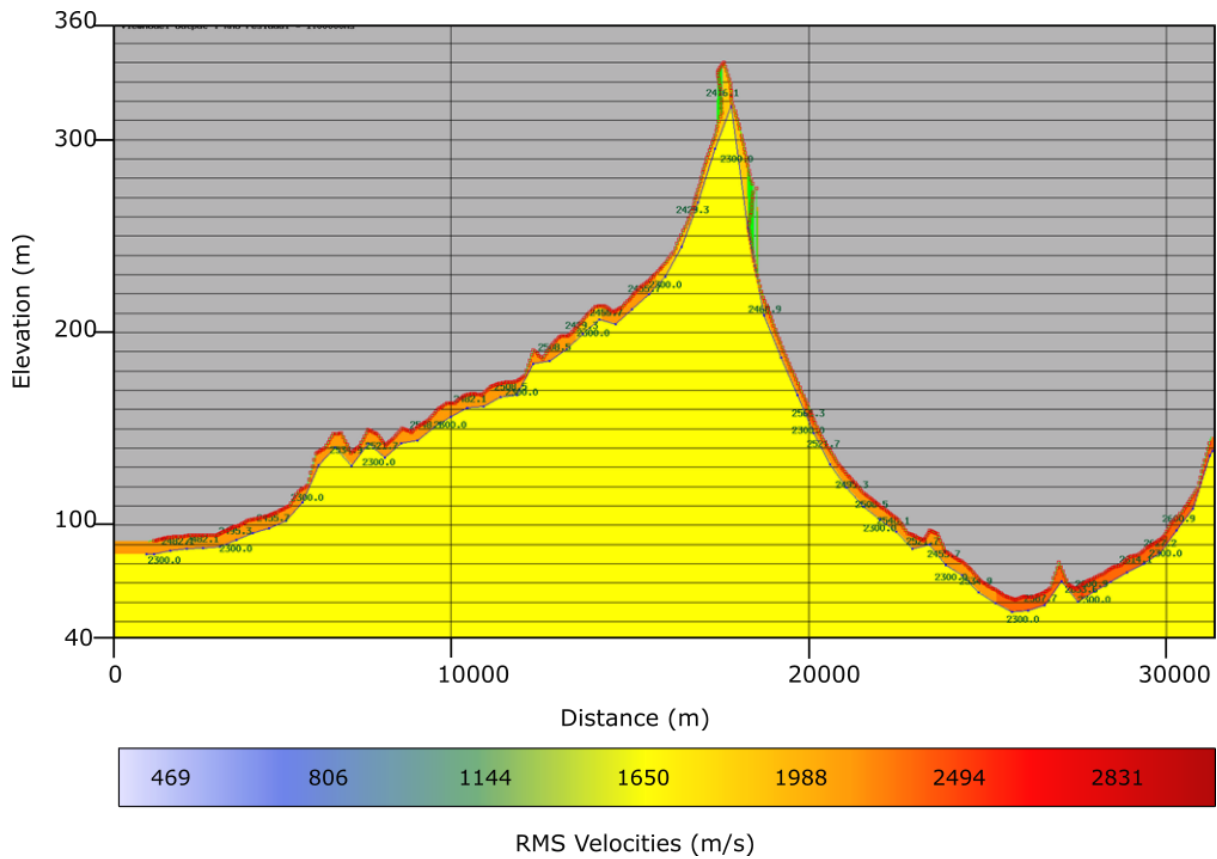
The extremely crooked shape of line 03 can be seen in the geometry image of Figure 6.9. This created several problems with binning, where the maximum fold was significantly larger than the normal fold of 120. This meant that despite careful picking of hit points and selection of bins, several traces were excluded. Due to the extreme folds, certain deconvolution methods such as surface consistent deconvolution (SCDECON) and Spectral Equalisation (SCPEQ) could not be used.



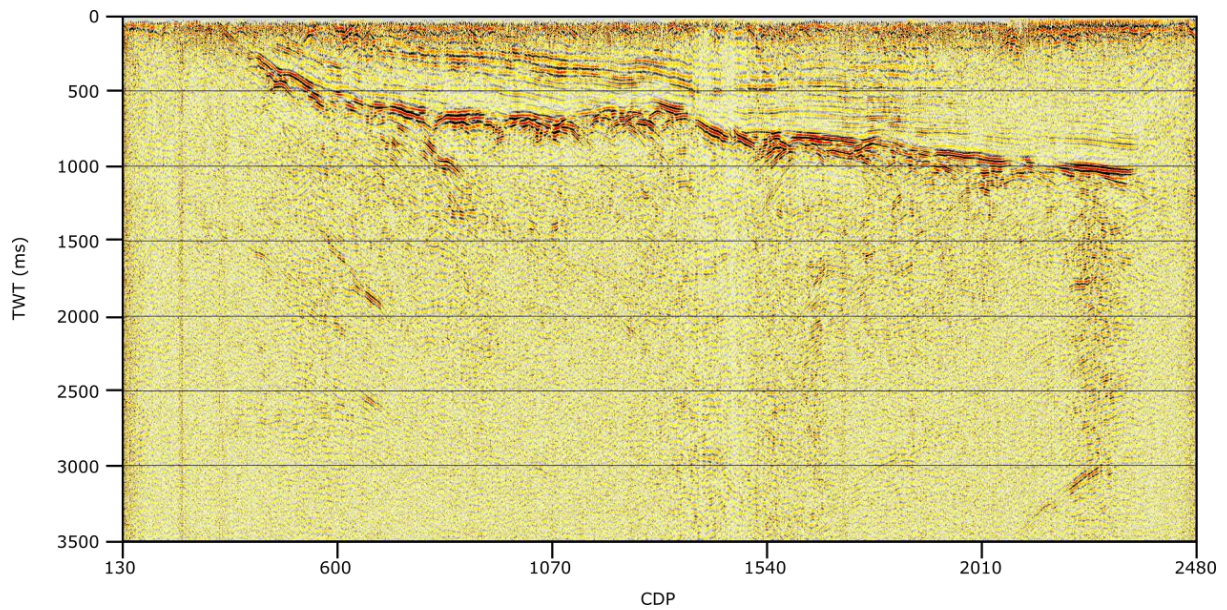
*Figure 6.9 Geometry file of line 03. The black circle marks the areas of extreme bending which causes major binning issues. Additionally, the higher elevation of this line would also aggravate this binning plight. A cropped topographical map of Figure 1.1 has been added to provide a reference to the rest of the survey. Grid scales of the geometry are northings and eastings (mN, mE) in the NZMG coordinate system. Elevation is metres above MSL (m).*

The extreme “wiggly-ness” of the line also creates problems with static corrections which could be seen in the static file for line 03 (Figure 6.10). Caution had to be taken when performing static corrections for this line.



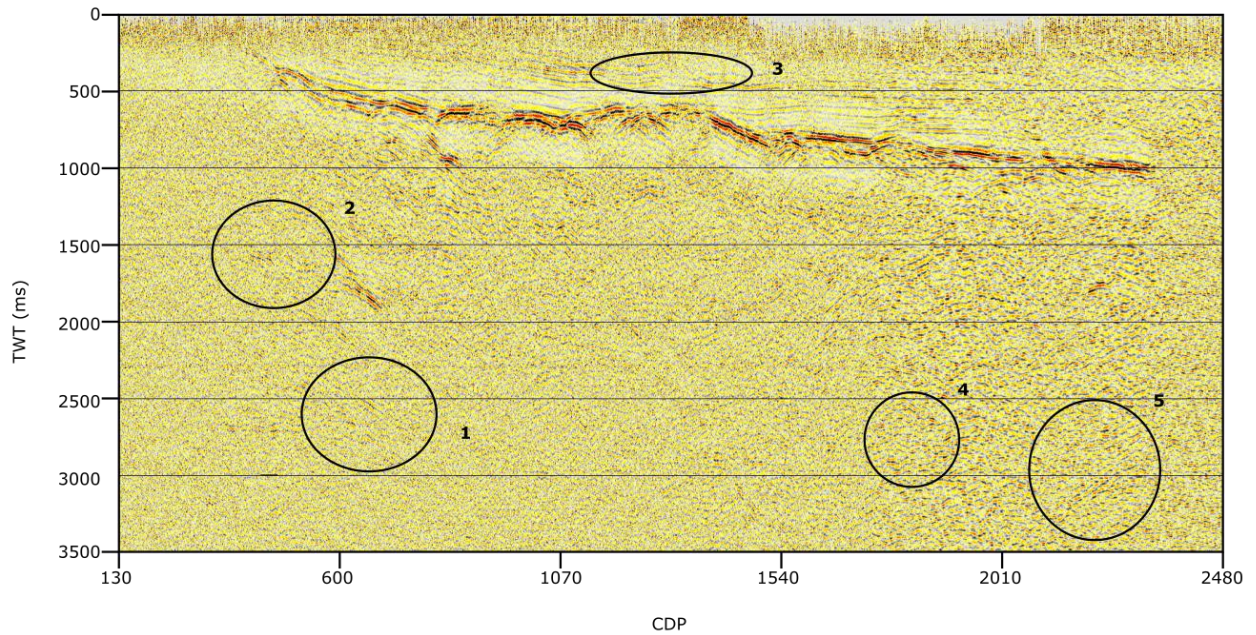


*Figure 6.10 A static test model for line 03. It can be seen there are some discrepancies around distance 18,000 m due to the extreme curvature of the line. X- and y-axis are the distance along the seismic line and the elevation above MSL respectively.*



*Figure 6.11 Raw stack of line 03 with no pre-processing applied. A 500 ms AGC has been applied.*

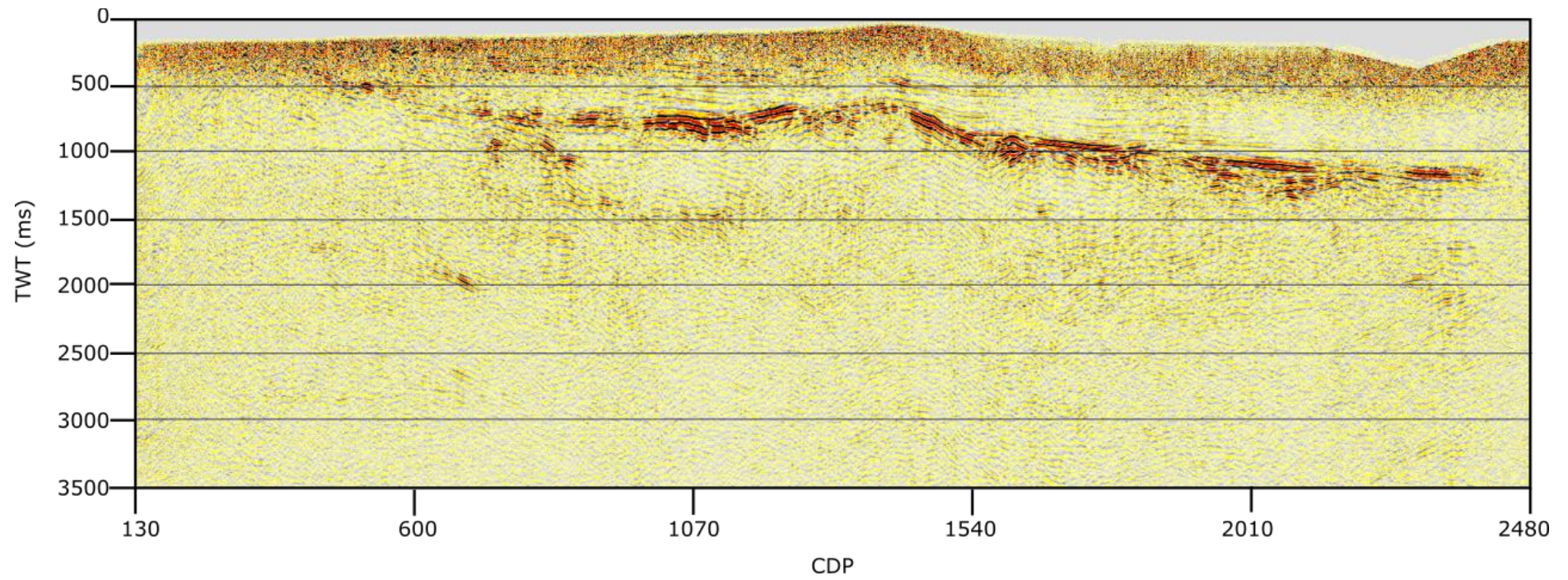
Line 03 presented more issues compared with line 01 and 02. There was more obvious loss of resolution in the lower areas in for CDPS greater than 1900. Two distinct layers and reflection events were able to be captured however missed a third event that GECO Ltd was able to achieve in their seismic image. The third event can be seen in the brute stack image (Figure 6.11) but failed to show properly in the deconvolved image (Figure 6.12). As in, the image did show but is almost impossible to distinguish from the neighbouring noise.



*Figure 6.12 Seismic stack of line 03. QFK,FX\_Decon DECONW and a FDFILT has been applied to this line. This stacked image has not been migrated yet. The circles show areas of observable major differences with a deconvolution.*

The circled areas in Figure 6.12 represent major areas where the deconvolution has affected the seismic image. The automatic gain control also proposes an issue where it can destroy signal by inappropriate scaling effect where it makes the signal indistinguishable to background noise. The effect of this can be seen in circles 4 and 5. In circle 5 there are remnants of a reflection event that can be seen in raw stack image in Figure 6.11. The event is very weak and is difficult to distinguish from background noise if not for the raw stack section. This suggests that a different gain control should be used to show the event. This is evident as well for circles 1 and 2. The adverse effects of deconvolution can be seen along the main reflection event and for circle 3, where the layer has flattened. The “frown” artefacts will be removed post-migration (Figure 6.13).





*Figure 6.13 Fully migrated seismic section of line 03.*

## 6.4 Line 05

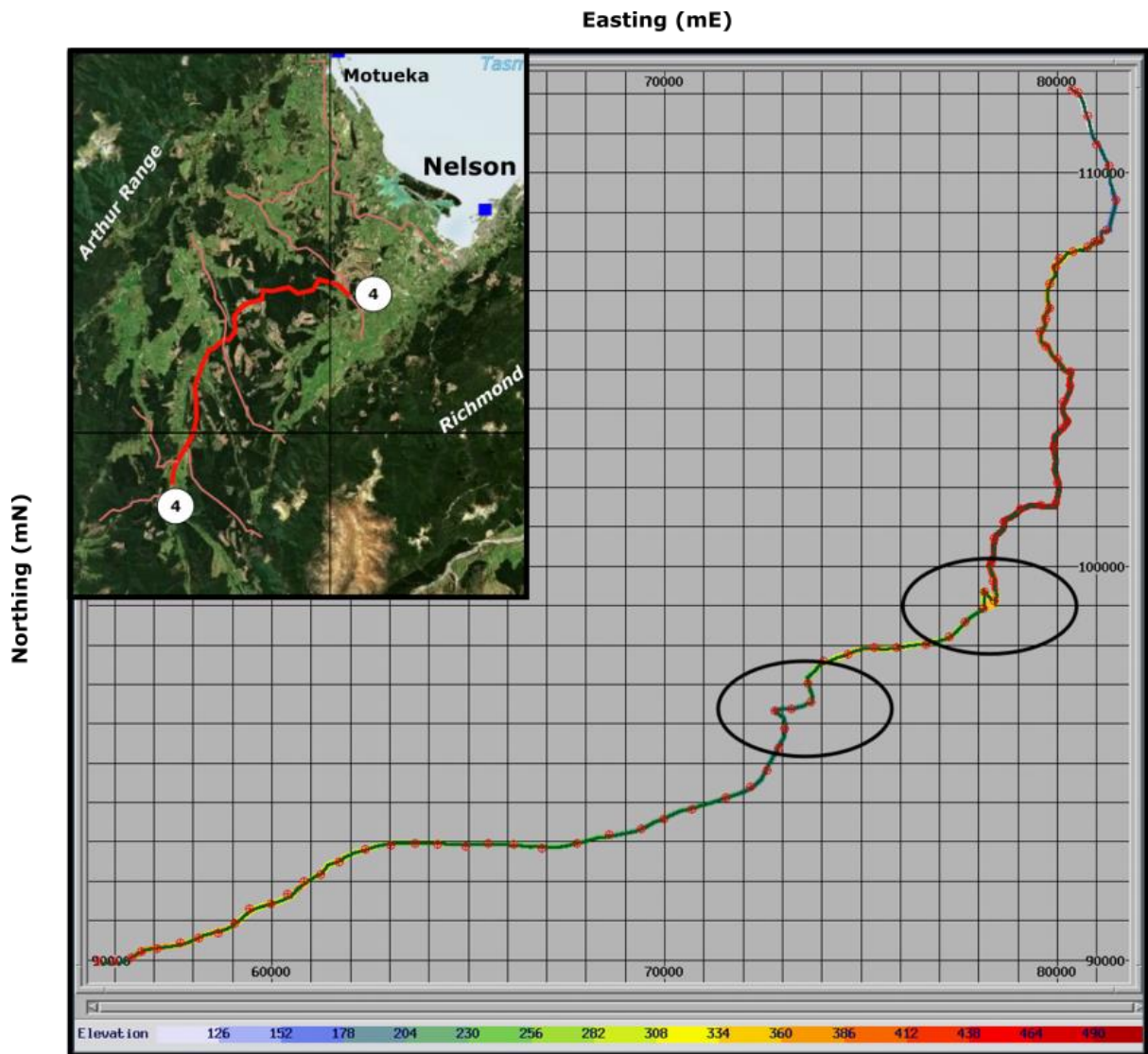
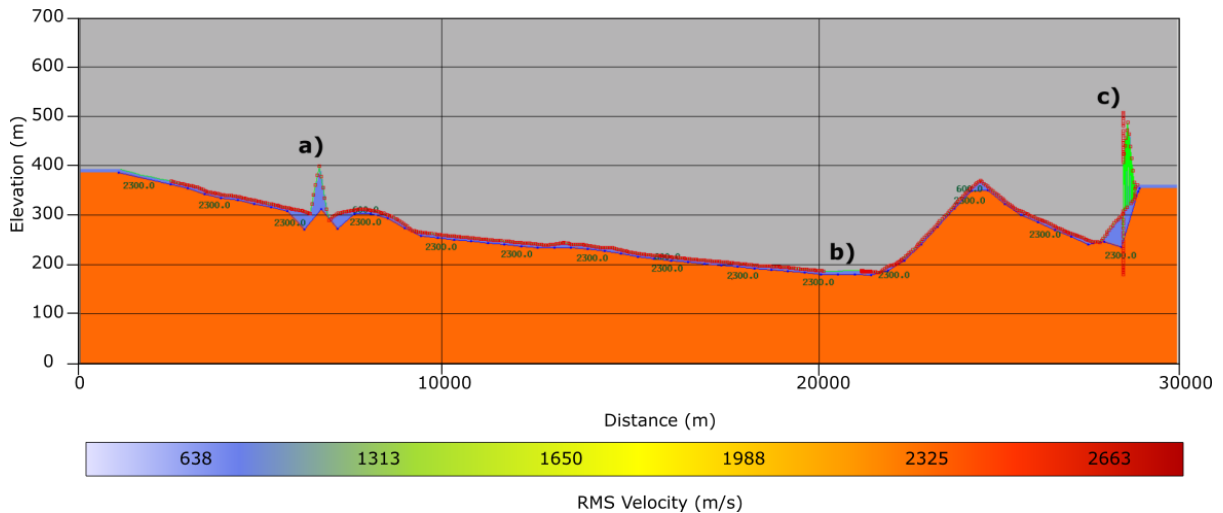


Figure 6.14 Geometry file of line 04. The red circles represent the hit points selected while the black circled regions are areas that may present issues with statics due to the extreme curvature. A cropped topographical map of Figure 1.1 has been added to provide a reference to the rest of the survey. Grid scales of the geometry are northings and eastings (mN, mE) in the NZMG coordinate system. Elevation is metres above MSL (m).

MD87 line 04 was a problematic line that shared characteristics with line 03 with extreme curvature or “wiggly-ness” throughout certain locations (Figure 6.14). There were initial qualms with the shot, survey and observation logs mismatching. The logs were previously

digitized by an Honours student in 2016, where the majority of the MD87 data was recorded adequately. However for this line, there was no agreeable number of shots between the \*.obl and \*.sur files. This made it difficult to produce an accurate geometry file, subsequently affecting the refraction statics (Figure 6.15). The cause of this bizarre predicament was the original surveyors with their unusual procedure detailed in their poorly recorded observation logs (Figure 6.16).



*Figure 6.15 Initial refraction statics for line 04. The spike a) is caused by a series of noise filled shots while b) is a series of noisy traces that were previously removed. Point c) represents the extremely curved section of the line that was circled in Figure 6.5.1. X- and y-axis are the distance along the seismic line and the elevation above MSL respectively.*

Line 04 also coincided with line 06 at the end of the line, where the last peg 1154 of line 04 is synonymous to peg 100 of line 06 and the last few shots of line 04 were found in the line 06 observation log (Figure 6.16a). They performed this way because the Vibroseis truck continued to line 06 immediately after shot 1154 and did not swap over the reels to signify a new seismic line.

GECO Ltd continued their seismic survey to peg 896 of line 06 before they realised their mistake and specified that the peg numbers should be amended. 1054 added to it to obtain the correct positions (so peg 896 is actually peg 1950) as shown in Figure 6.16b. It was because of this confusion, the raw shot file of line 04 contained 896 shots instead of planned 673 while the survey files only had source positions of 100 - 1150.



To solve this dilemma, line 04 was extended to encompass values of MD87\_06. Additional source positions were added into the survey files. This was done since the shot files of line 4 and line 6 have already been created and it was much easier to edit the survey files than the shot files. As a consequence, line 04 in this report will be significantly longer while line 06 will be shorter than the original PR1447 report.

a)

1154		N.B LINE MD-87-09, LAST STN = 1154 WHICH
1156		IS COINCIDENT WITH STN 100 ON LINE MD-87-06.
1158		THEREFORE FOR SURVEY NUMBERS $\geq$ 1154 (LINE 09)
1160		DEDUCT 1054 TO FIND EQUIVALENT SURVEY
1162		NUMBER FOR LINE MD-87-06.
1164		
1166		DELAY 15:35 VIB FAILING TO START, ALSO WAITING
1168		FOR STATIONS - 16:00
1170		VPC
1172		

b)

Reel No.	Shot ID	Source Position	No. Vib	Sweeps	Channel	Station	Channel	Station	Channel	Station	Channel	Station
138	S12	1122				1058	117	1125	1184			
139	S13	1124				1060	119	1127	1186			
140	S14	1126				1062	121	1129	1188			
141	S15	1128				1064	123	1131	1190			
142	S16	1130				1066	125	1133	1192			
143	S17	1132				1068	127	1135	1194			
144	S18	1134				1070	129	1137	1196			
145	S19	1136				1072	131	1139	1198			
146	S20	1138				1074	133	1141	1200			
147	S21	1140				1076	135	1143	1202			
148	S22	1142				1078	137	1145	1204			
149	S23	1144				1080	139	1147	1206			
150	S24	1146				1082	141	1149	1208			
151	S25	1148				1084	143	1151	1210			

↓  
cont. to line-06

c)

Record No.	Reel No.	Shot ID	Source Position	No. Vib	Sweeps	Channel	Station	Channel	Station	Channel	Station	Channel	Station
1	020	S26	1150	3	4	1	1086	60	1145	61	1153	120	1212
2		S27	1152				1088		1147		1155		1214
3		S28	1154				1090		1149		1157		1216
4	1	S29	102				038	097			105		164
5	2	S30	104				040	099			107		166
6	2	S31	105				042	100			108		167
7	4	S32	106				042	101			109		168
8	5	S33	107				043	102			110		169
9	5	S34	108				044	103			111		170

Figure 6.16 The survey of line 06 continued from line 04 as shown by the snippets taken from the observation logs. Figures a) and b) were both images taken from the line 04 observation logs and c) from the line 06 observation log. The note made on the comment section in a) details the numbering system for the pegs of the reports for lines 04 and 06 while the lower section in b) a comment is made saying the survey of line 04 continues onto line 06. The arrows in c) show the numbering of the source positions changing as noted in a).

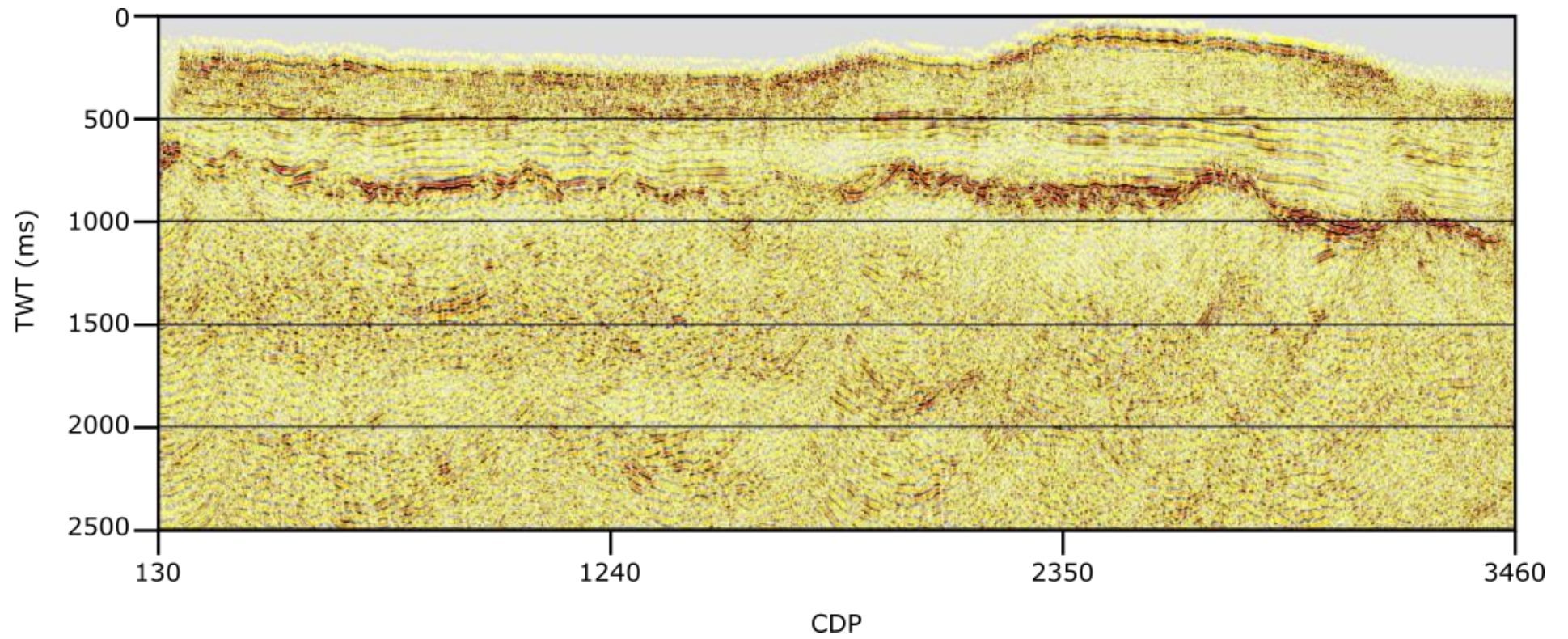
Numerous shots and traces (up to 26) were removed for reasons such as noise. An entire shot was removed (shot 532) since the shot was contaminated with severe electrical noise (Figure 5.3a). The shot removal caused an issue with a section of the refraction statics stage where there is a gap where shot 532 would have been positioned. Shot 894 was also labelled incorrectly as shot 4 with its line and reel number correct but record and shot number not so (Figure 6.17), so this was revised as well. The final migrated section is presented in Figure 6.18.

Bytes	Name	SEGY Value
1: 4 (4)	LINE	376
5: 8 (4)	REEL	376
9: 12 (4)	RECORDNUM	4
13: 16 (4)	FTRACE	1

Bytes	Name	SEGY Value
1: 4 (4)	LINE	113751
5: 8 (4)	REEL	113751
9: 12 (4)	RECORDNUM	4
13: 16 (4)	FTRACE	1

*Figure 6.17 Headers information taken from shot 4 and shot 894. In both images, the record number is identical. Using the line and reel number, it was possible to distinguish the difference between the two shots and correct them accordingly with line 376 being the “real” shot 4 and line 113751 being shot 894.*



*Figure 6. 18 Final migrated section of line 04.*

## 6.5 Line 05

Line 05 is a line of moderate length with 2680 CDP and presented very few issues making it easy for swift processing (Figure 6.20). The line was relatively flat until near the end when it reached the Western Province of Nelson and contained no extreme curves like the previous lines (Figure 6.19). DESPIKEV was applied to remove small spikes in electrical noise and a Weiner deconvolution was used.

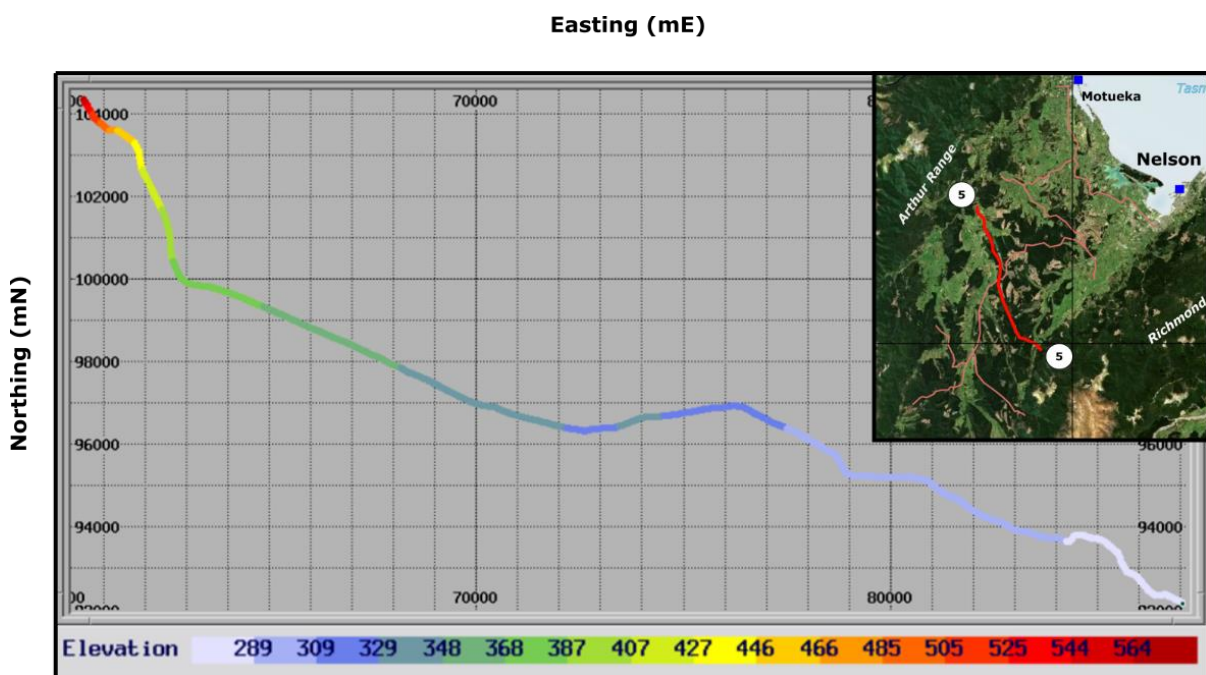
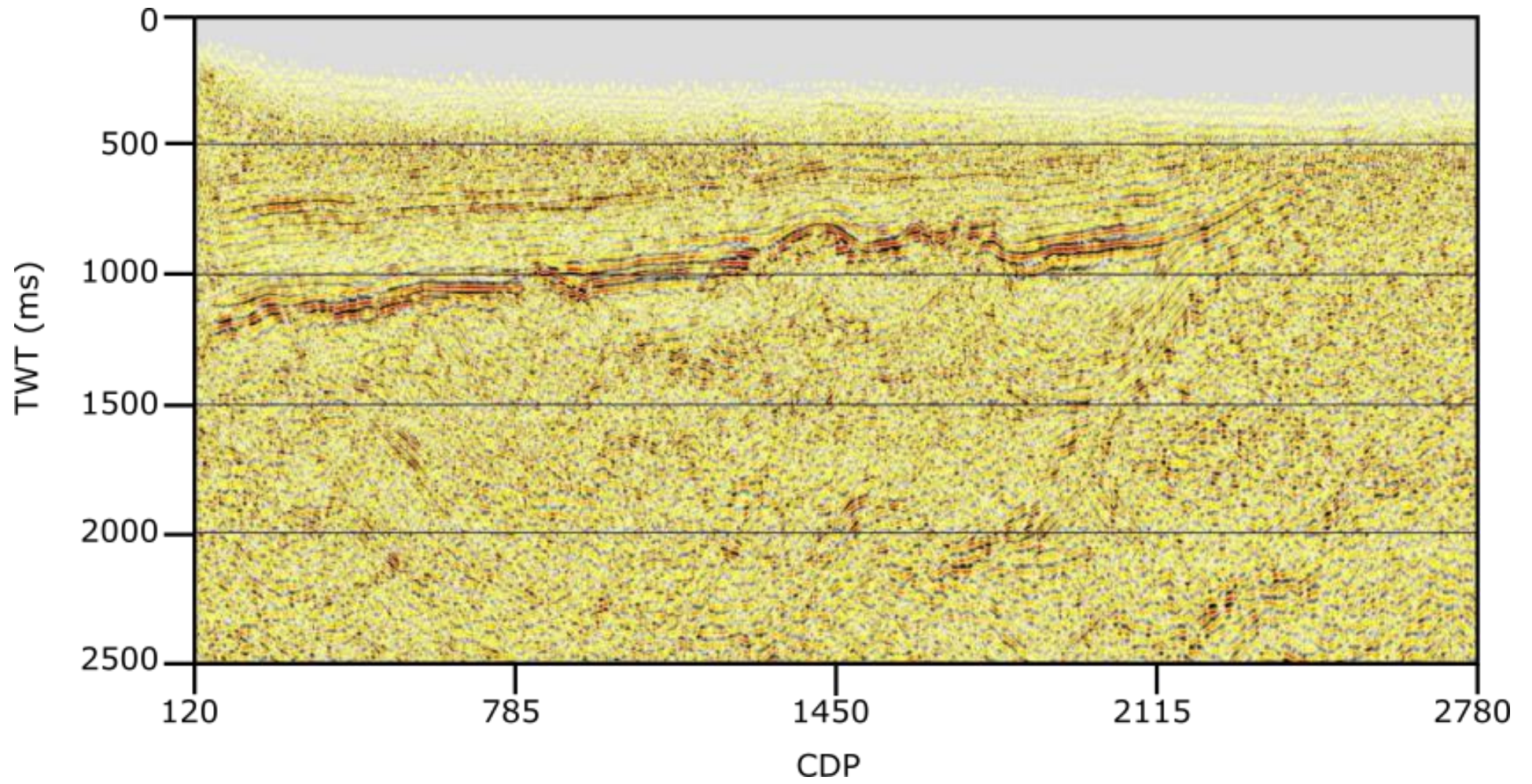


Figure 6.19 Geometry of line 05. A cropped topographical map of Figure 1.1 has been added to provide a reference to the rest of the survey. Grid scales of the geometry are northings and eastings (mN, mE) in the NZMG coordinate system. Elevation is metres above MSL (m).





*Figure 6.20 Final migrated seismic section of line 05.*



## 6.6 Line 06

Line 06 was a shorter line with few curves since many of its CDPs were transferred to line 04 (Figure 6.21). The final migrated seismic line however did suffer from statics and shallow sourced noise since the basement was so thin (Figure 6.22).

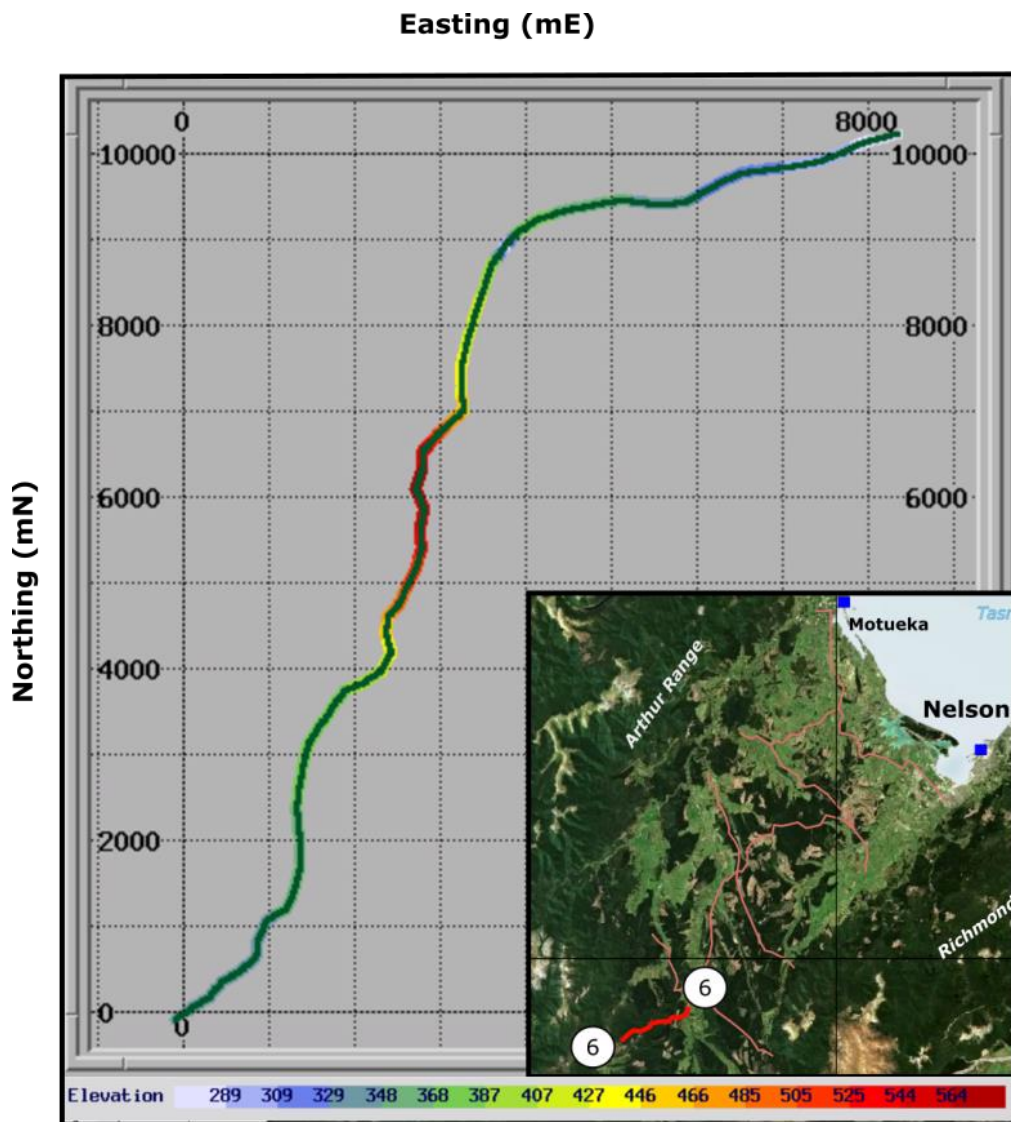
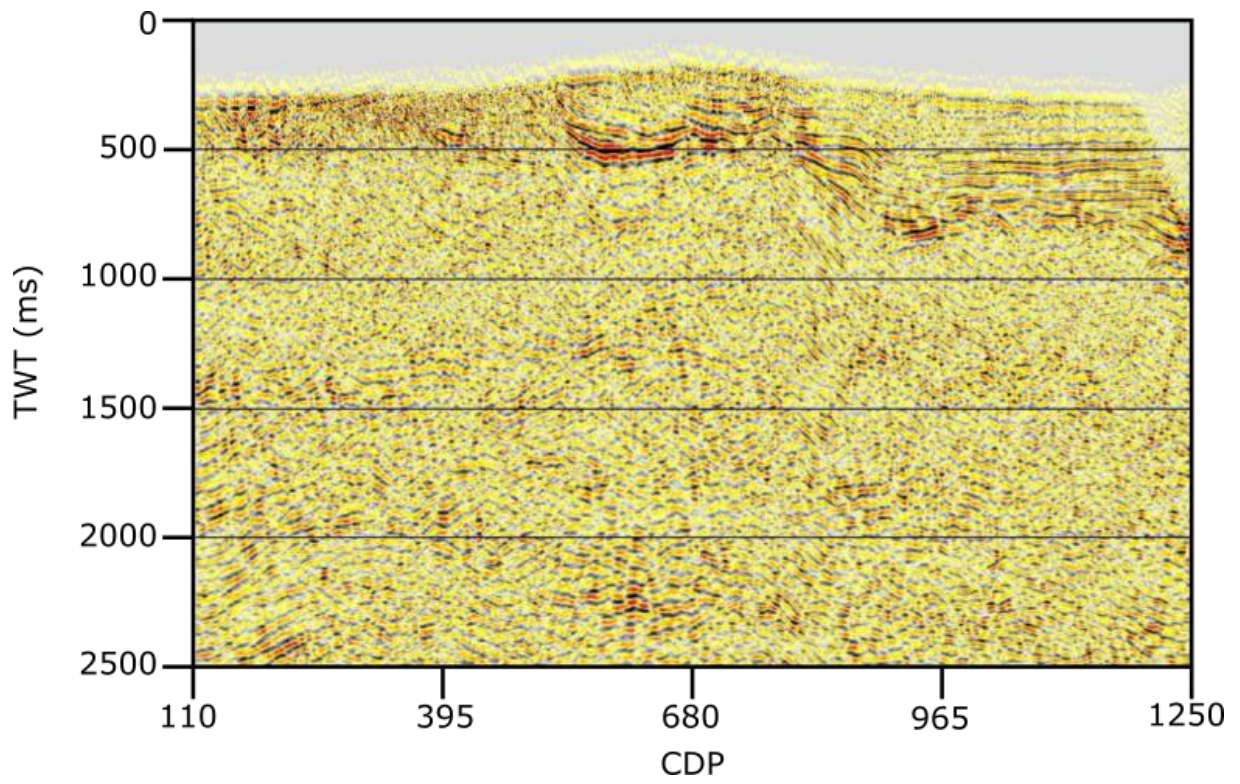


Figure 6.21 Geometry of line 06. The line is relatively straight compared to other lines. Grid scales of the geometry are northings and eastings (mN, mE) in the NZMG coordinate system. Line 06 northings and eastings were recorded reversed hence its inverted shape compared to the cropped topographical image of Figure 1.1. The coordinates of this line will be amended in later stages as elaborated in Section 6.10. Elevation is metres above



*Figure 6.22 Final migrated line 06.*

## 6.7 Line 07

Line 07 was a line that cut through the Moutere Basin, similar to line 05. However, it began in the eastern province rather than the west and ended in line 04. The line possessed a severe kink (Figure 6.23) and elevation changes near the beginning of the survey which caused issues with refraction statics as seen in the shot gathers (Figure 6.25) and refraction statics model (Figure 6.24).

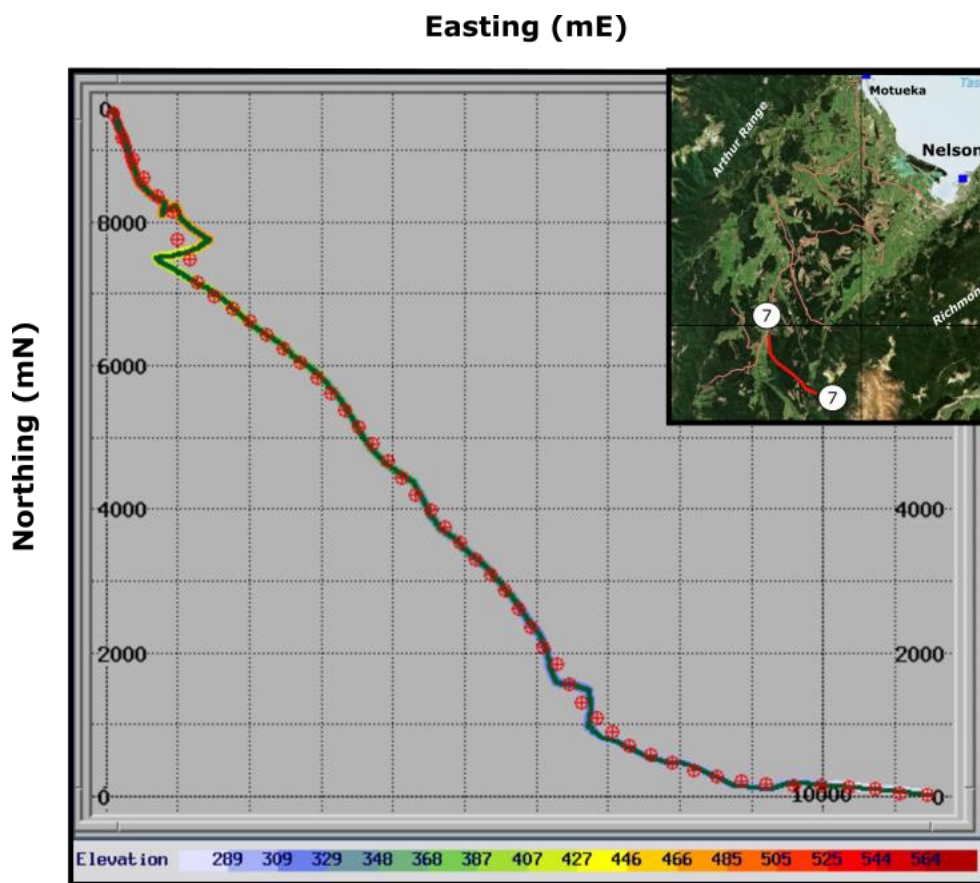
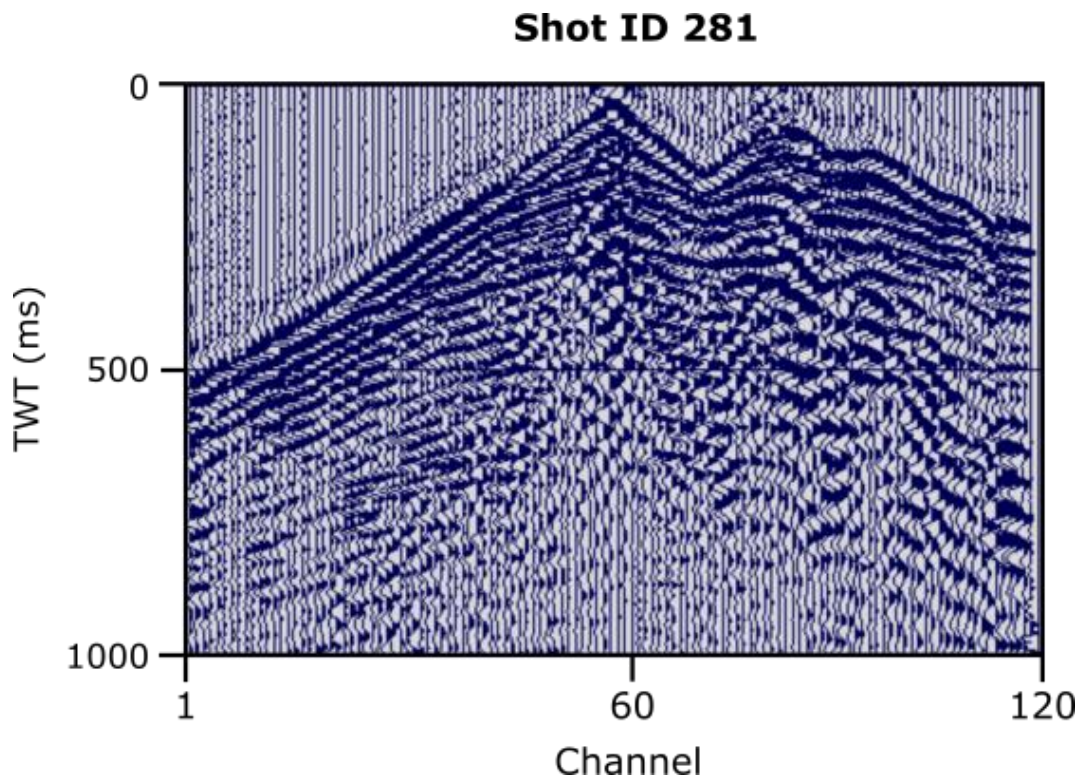
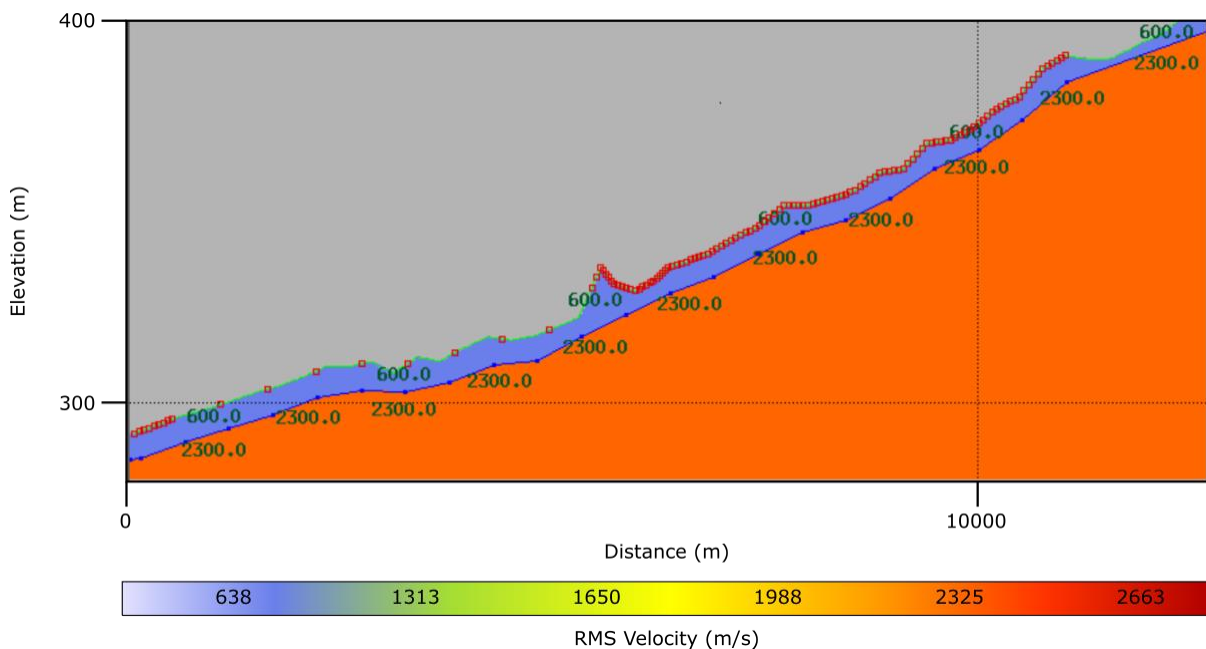


Figure 6.23 Geometry of line 07. There are several sharp curves seen in the area around (1000, 7500). The curvature was so extreme Claritas could not compute it as a wiggly-line and had to be calculated as a straight-line gather. Grid scales of the geometry are northings and eastings (mN, mE) in the NZMG coordinate system. Much like line 06, the geometry coordinates of line 07 were recorded with northings and eastings reversed; hence its mirrored image compared to the cropped topographical image of Figure 1.1. The coordinates of this line will be amended in later stages as elaborated in Section 6.10. Elevation in metres above MSL.





*Figure 6.24 Shot gather of 281. The undulated position of the first breaks in the shallow section of the gather is indicative of rapidly changing elevations and curvature of the lines.*



*Figure 6.25 Refraction statics model for line 07. Sharp elevation changes can be seen about 6000 m. These changes are reflected upon the shot gather (Figure 6.24). X- and y-axis are the distance along the seismic line and the elevation above MSL respectively.*

The number shot pegs and receivers were incorrect for shots 121 and 126 in the shot files and were noted in observation logs. These had to be individually adjusted in the files otherwise they caused a mis-stack (Figure 6.26). The final migration stack is presented in Figure 6.27.

LINE NODE (LINE)													
911		4	1	117	337	120	340			UNCORRELATED VIB SIM (10 f			
912										CORRELATED VIB SIM (5 f			
										#117 VIB 4, #118 VIB 1, #119 VIB 1			
121	340	3	4	1	273	60	338	61	340	120	404	1	} NEW SWEEP PARAMETERS FROM FILES 121-126 MISSTACK X
122	342				275		337		342		403	2	
123	344				277		336		344		405	3	
124	346				279		338		346		407	4	
125	348				281		340		348		409	5	
126	350				283		342		350		411	6	
127	352				285		347		355		414	7	VPC
128	354				290		349		357		416	8	STACKING CORRECTED.
129	356				292		351		359		418	9	
130	358				294		353		361		420	10	

**.make\_geometry\_errors**

Please see the summary at the end of the file for a list of any missing receivers or shot-pegs.

```

Shot 121 : 60 channels (61:120) and 62 receivers (340:401) is inconsistent
Shot 122 : 60 channels (61:120) and 62 receivers (342:403) is inconsistent
Shot 123 : 60 channels (61:120) and 62 receivers (344:405) is inconsistent
Shot 124 : 60 channels (61:120) and 62 receivers (346:407) is inconsistent
Shot 125 : 60 channels (61:120) and 62 receivers (348:409) is inconsistent
Shot 126 : 60 channels (61:120) and 62 receivers (350:411) is inconsistent

```

Figure 6.26 The misnumbering of channels between the shot and survey files caused an error whilst creating the geometry file for line 07. The cause of the error was mentioned in the observation log. Manual adjustments had to be made to correct this

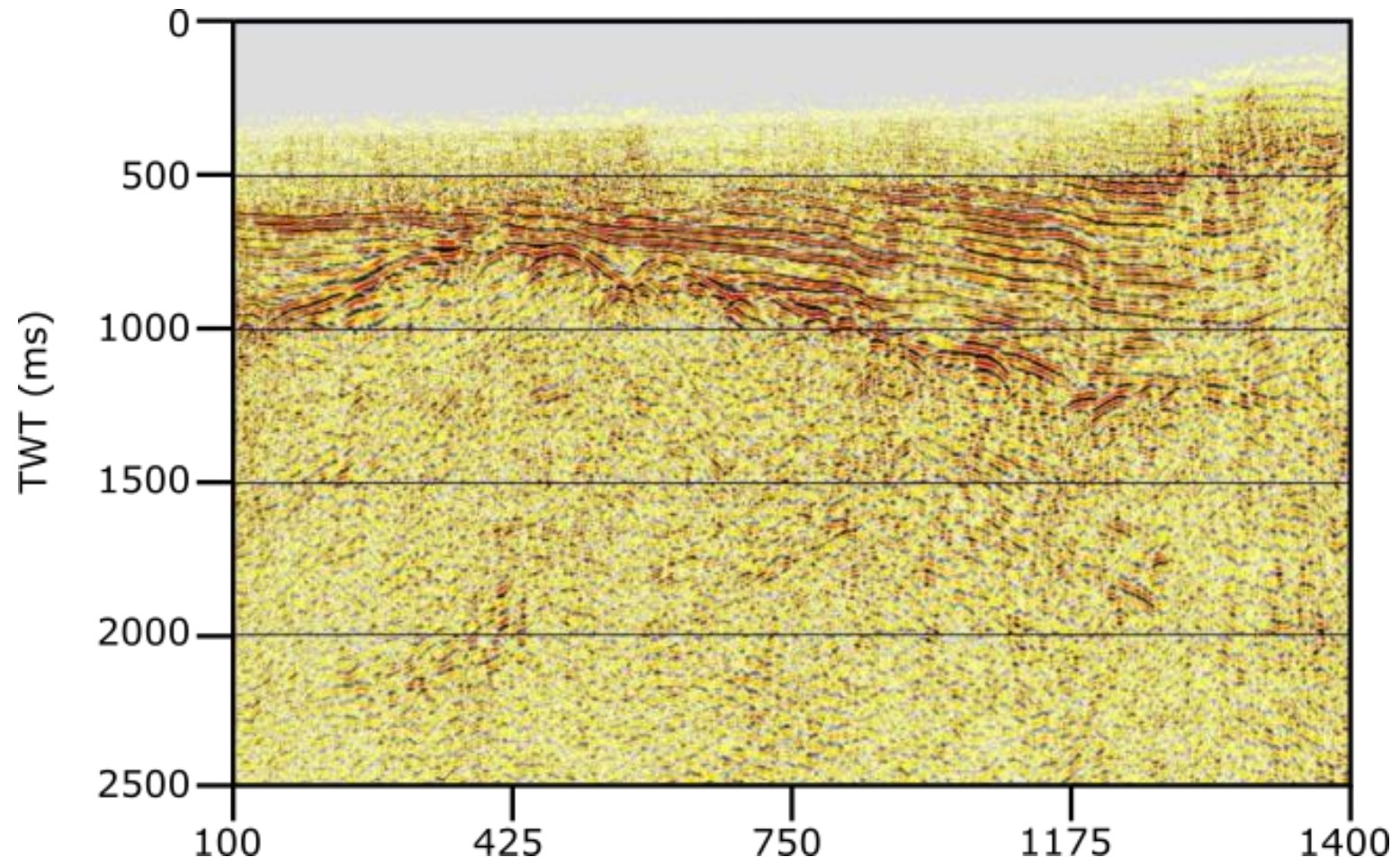


Figure 6.27 The final migrated section of line 07.



## 6.9 Line 08

Line 08 was extremely wiggly, particularly around the end of the of line (Figure 6.28). To overcome this, the line was divided into two smaller sections separated about that area and labelled “Line 08C” and “Line 08D” (Figure 6.29 to Figure 6.30). With line 08D being straighter than it was previously, it allowed seismic processing to be run more smoothly. In light of this, 08C was still difficult with the line still being very crooked. So, in a similar method to line 07, the file was processed as a straight line gather since it was too curvy and too many traces would be lost.

In comparison to the other lines, line 08C suffered more shallow noise shown by the areal file (Figure 6.31). This was also due to the hilly terrain that effect many of the shots also increasing the difficulty for making first break picks (Figure 6.32 to Figure 3.33).

Final migrated sections of line 08C and 08D are shown in Figures 6.33 and 6.34, respectively.

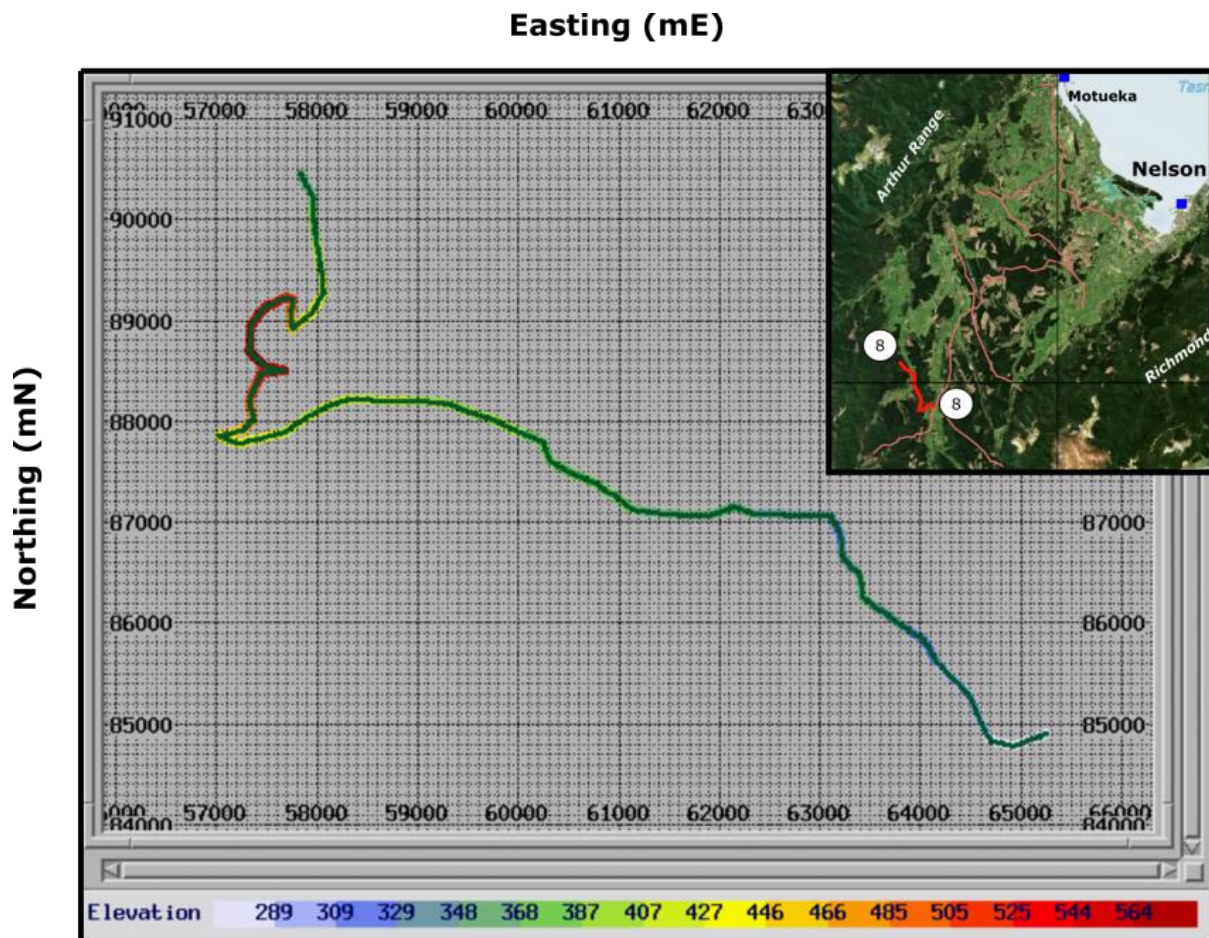
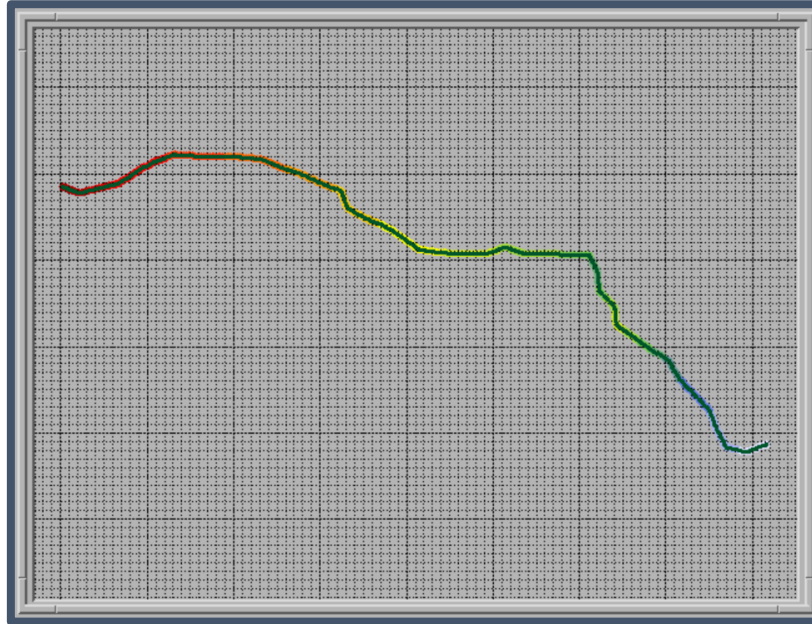
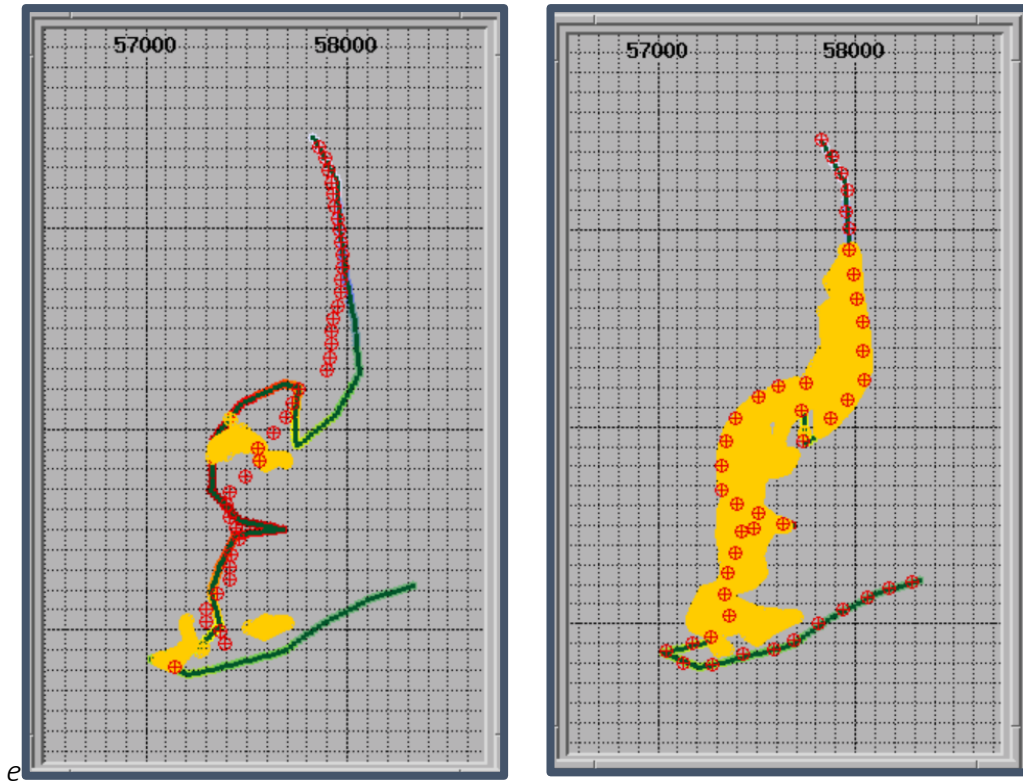


Figure 6.28 Original complete line of 08. Grid scales of the geometry are northings and

*eastings (mN, mE) in the NZMG coordinate system. Much like line 06 and 07, line 08 is part of the group of lines with their northings and eastings reversed. This can be seen by comparing the geometry to the cropped topographic image of Figure 1.1.*

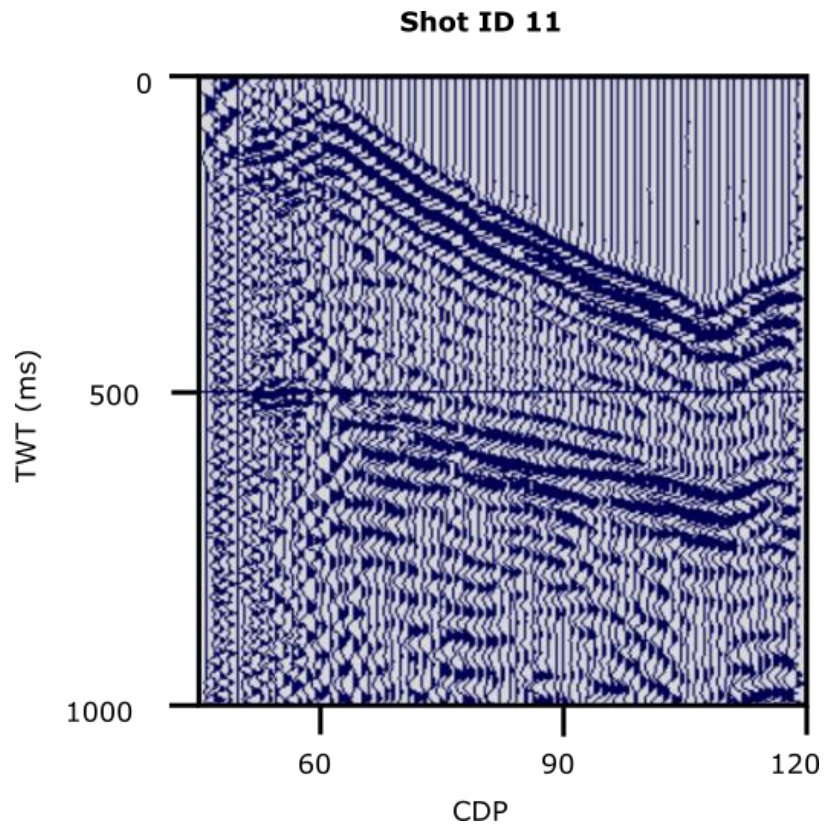


*Figure 6.29 New sub-geometry file line 08D.*

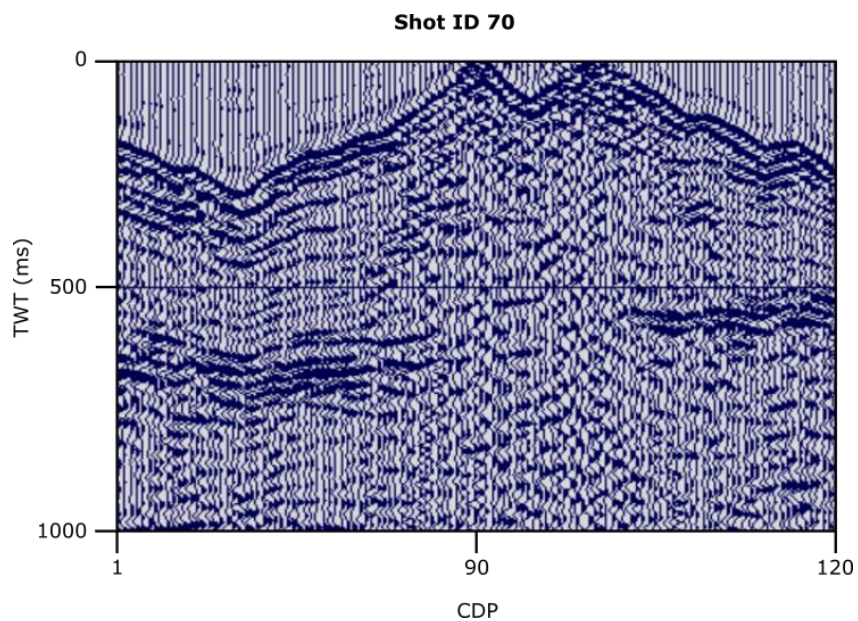


*Figure 6.30 Comparison of lost traces between automatic and manual hit-point selection for the geometry file of line 08C. Image on the left is the automatic option while the image on the right is manual. The bin parameters of both are the same. It is evident that manual picking is not appropriate for this line. The yellowed areas are the positions of 'lost' traces'.*





*Figure 6.31* A raw shot gather of shot 11 of line 08C. The hilly terrain is noticeable in the section 0 - 500 ms where the signal comes back to the receiver earlier. Numerous faulty and noisy geophones can be seen between channels 40 - 60. The effects of ground-roll is evident in this line.



*Figure 6.32* A raw shot gather of shot 70 of line 08C illustrating the rolling terrain of the seismic line.

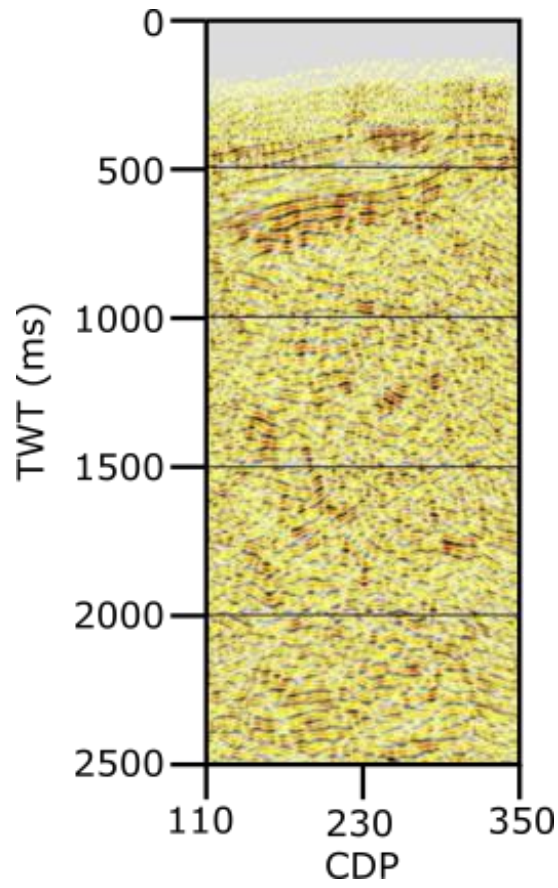


Figure 6.33 Final migrated line of 8C.

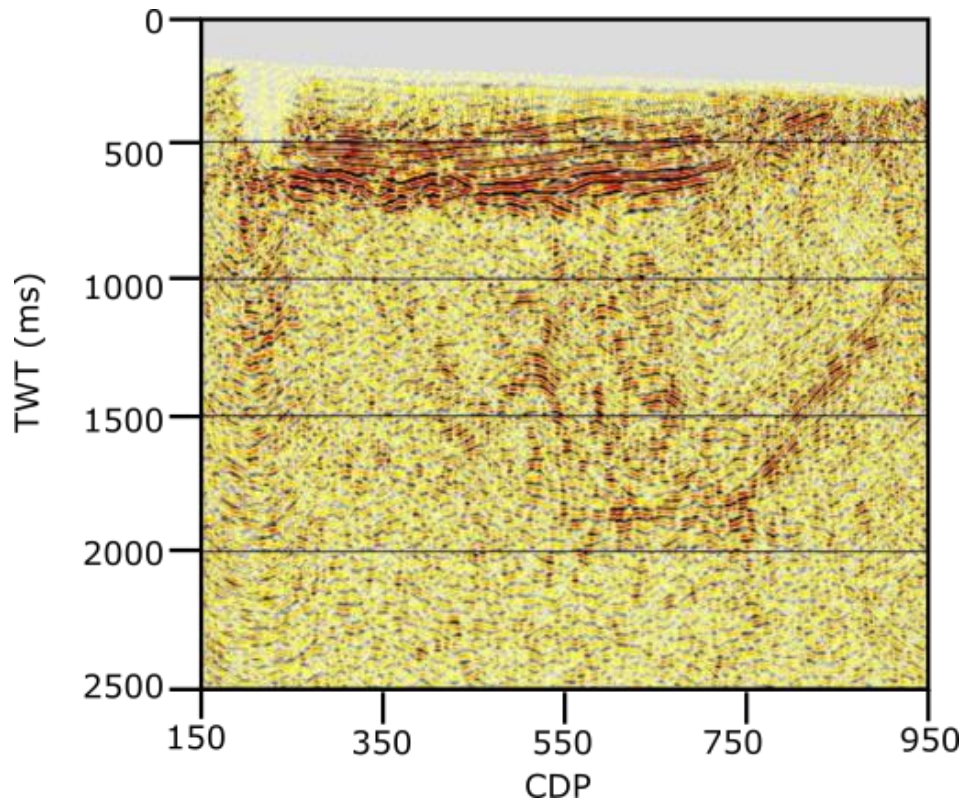


Figure 6.34 Final migrated line of 8D.

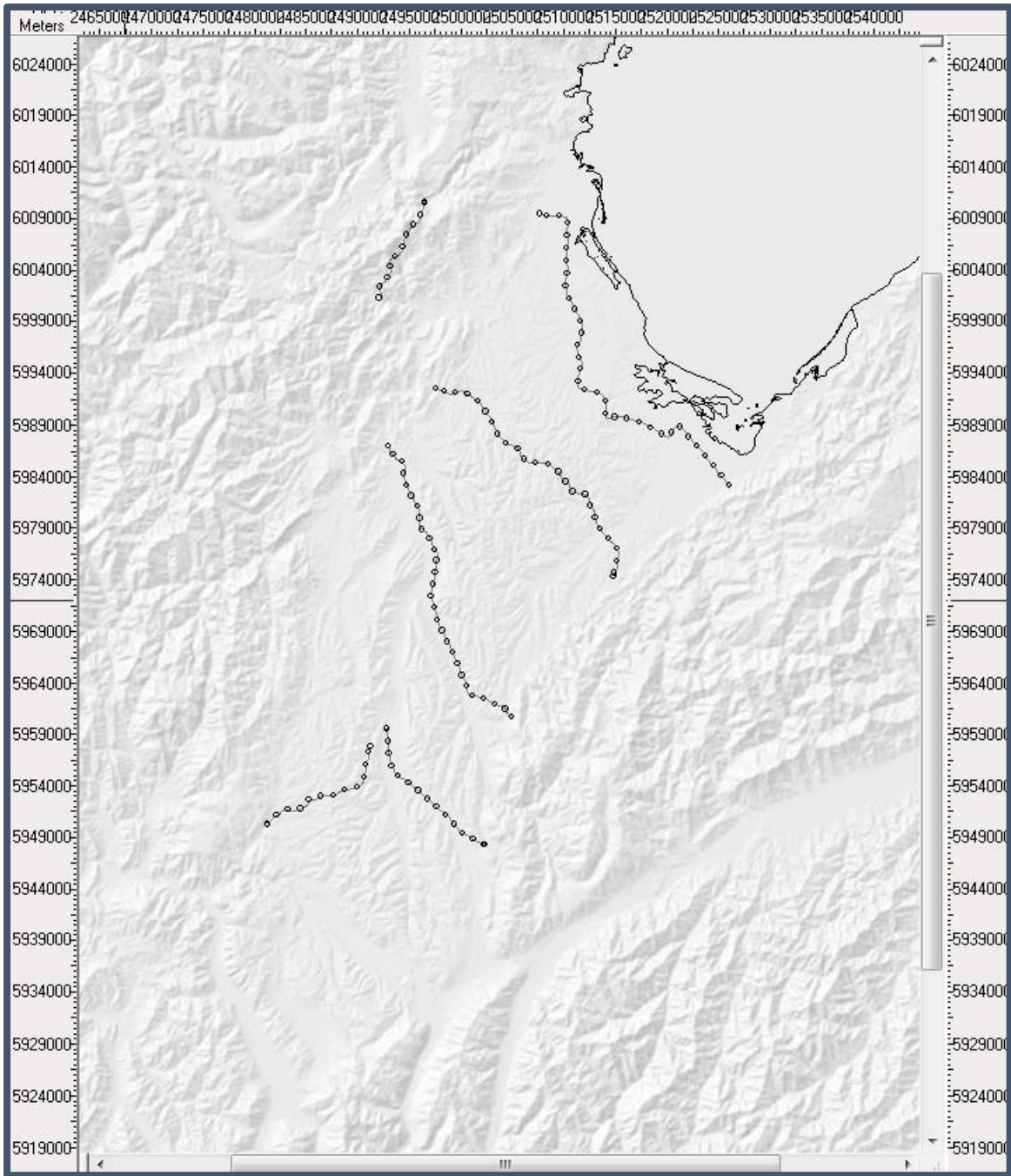
---

## 6.10 3D modelling

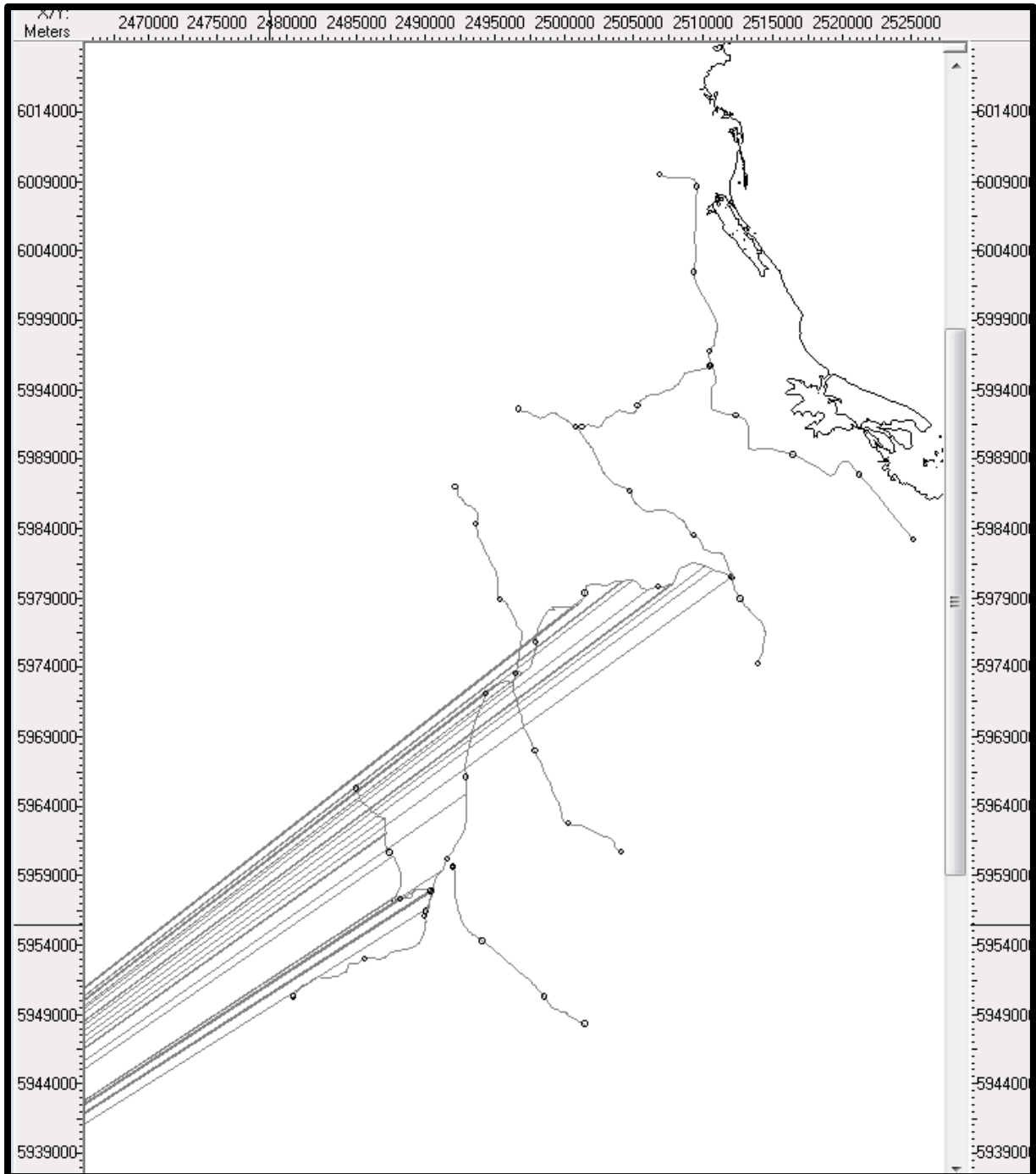
All processed seismic lines and their survey locations were then imported into IHS Kingdom to view the data in 3D, thereby providing a novel perspective of the Moutere Depression.

Eastings and Northings of most peg locations were adjusted because the recorded grid coordinates of some lines were inverted and needed to be modified to the relevant grid reference, NZGD64 (Figure 6.35). A total of up to 20 pegs had no positions and defaulted to a (0,0) origin (Figure 6.36). Despite this, traces corresponding to these pegs were “lost” and did not fall into any CDP bins. The absence of these traces did not severely affect the seismic stacks. These missing positions were eventually interpolated to produce an interpretable locality map (Figure 6.37).





*Figure 6.35 Base map of MD87 in IHS Kingdom. Note the misalignment of line 02 and how line 04, 08C and 08D do not show up on the map. The map is part of the NZGD64 coordinate system with grid scales being the northings and eastings (mN, mE).*



*Figure 6.36 The lines strewn to the corner to the map are caused by pegs with no coordinate points in the survey file and are automatically assigned a (0,0) position. The map is part of the NZGD49 coordinate system with grid scales being the northings and eastings (mN, mE).*

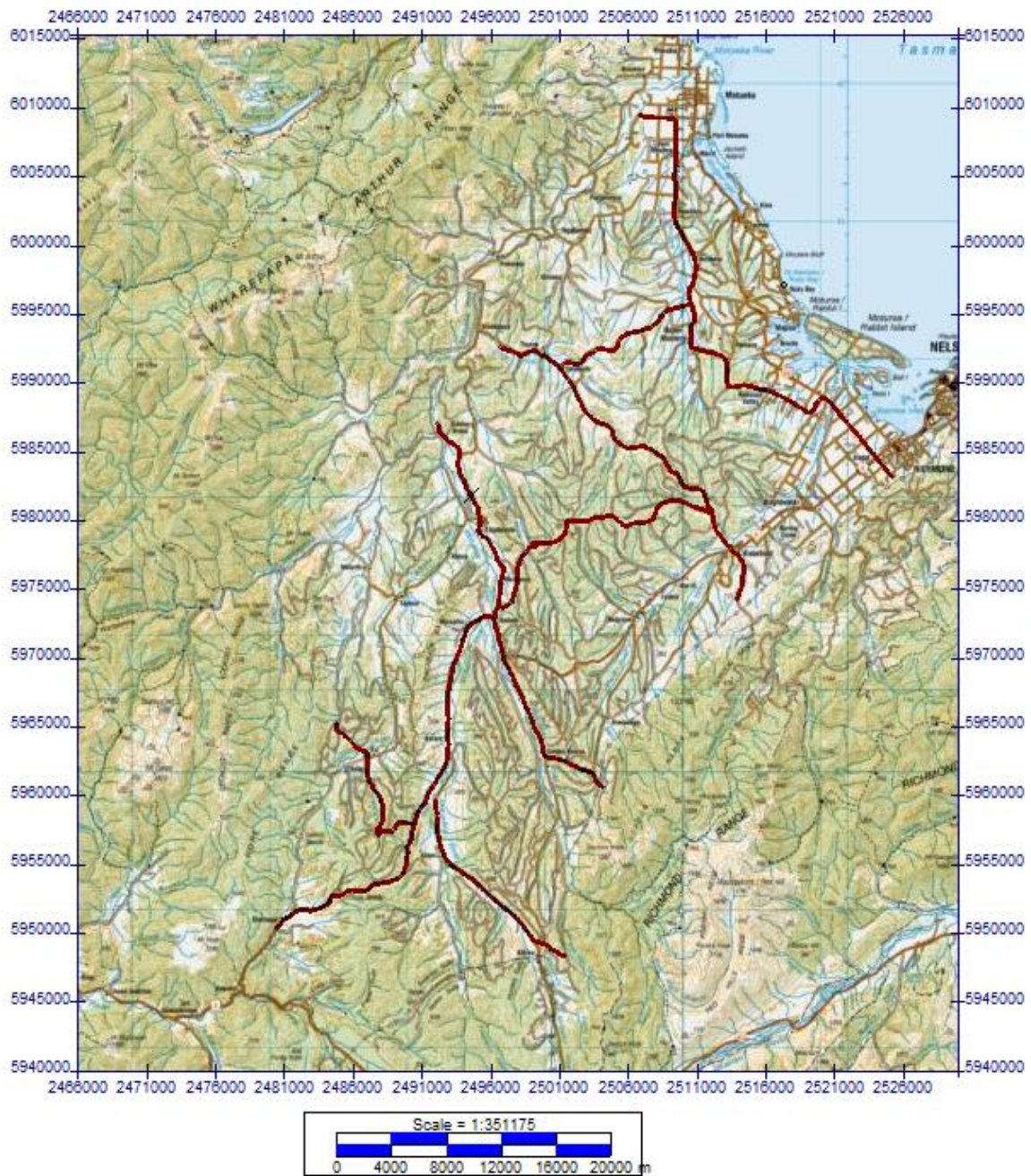
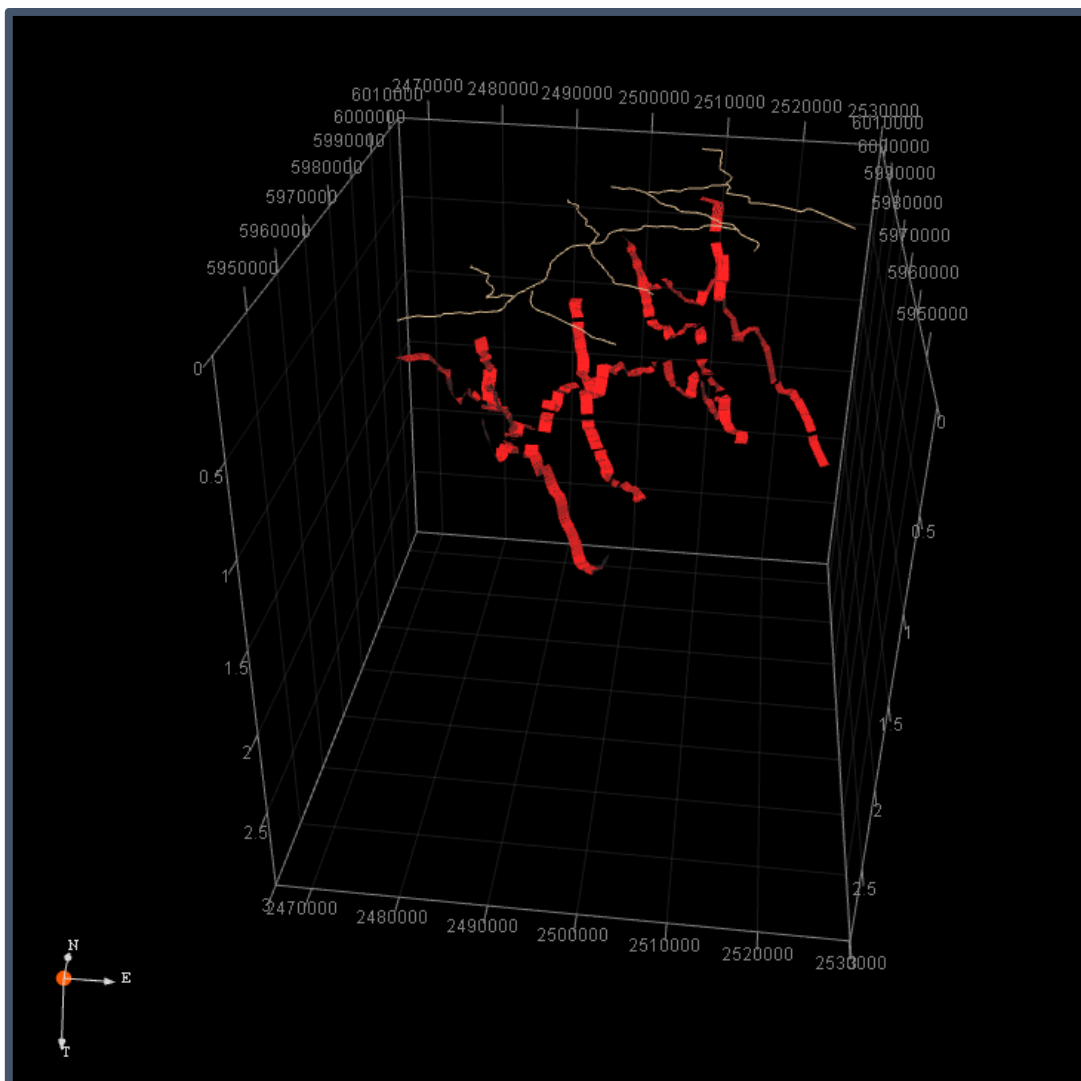


Figure 6.37 Final base map in IHS Kingdom. The dark red lines are the MD87 seismic lines. The map is part of the NZGD49 coordinate system with grid scales being the northings and eastings (mN, mE).

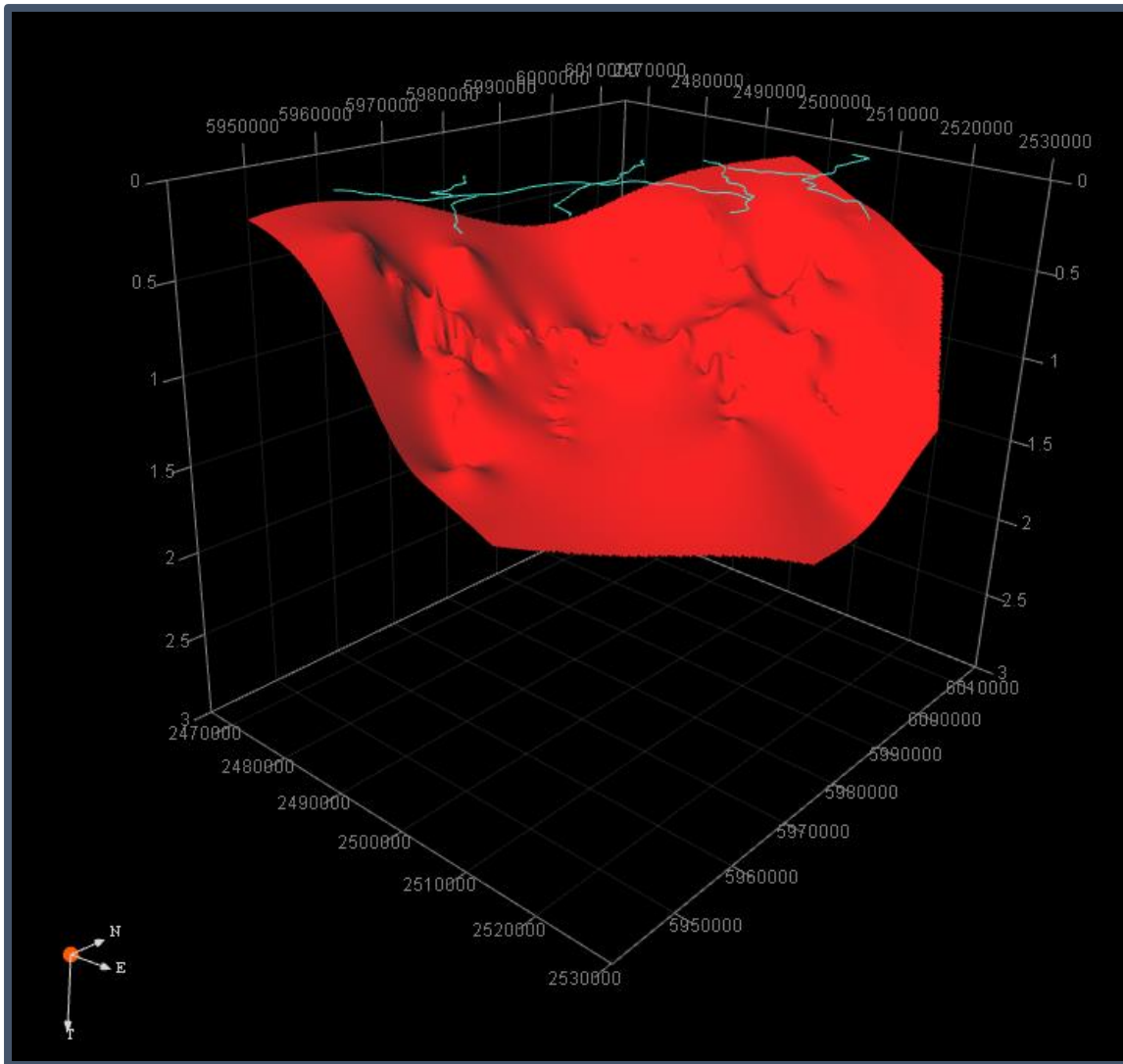


## Horizons

The basin was subdivided by into four main identifiable horizons with two sub-horizons. The upper horizons were difficult to constrain because of the poor resolution in the shallower areas of the seismic sections while horizon two (Figures 6.38 and 6.39) and three were picked with a higher degree of confidence. These horizons were categorized mainly based on their varying seismic facies attributes.



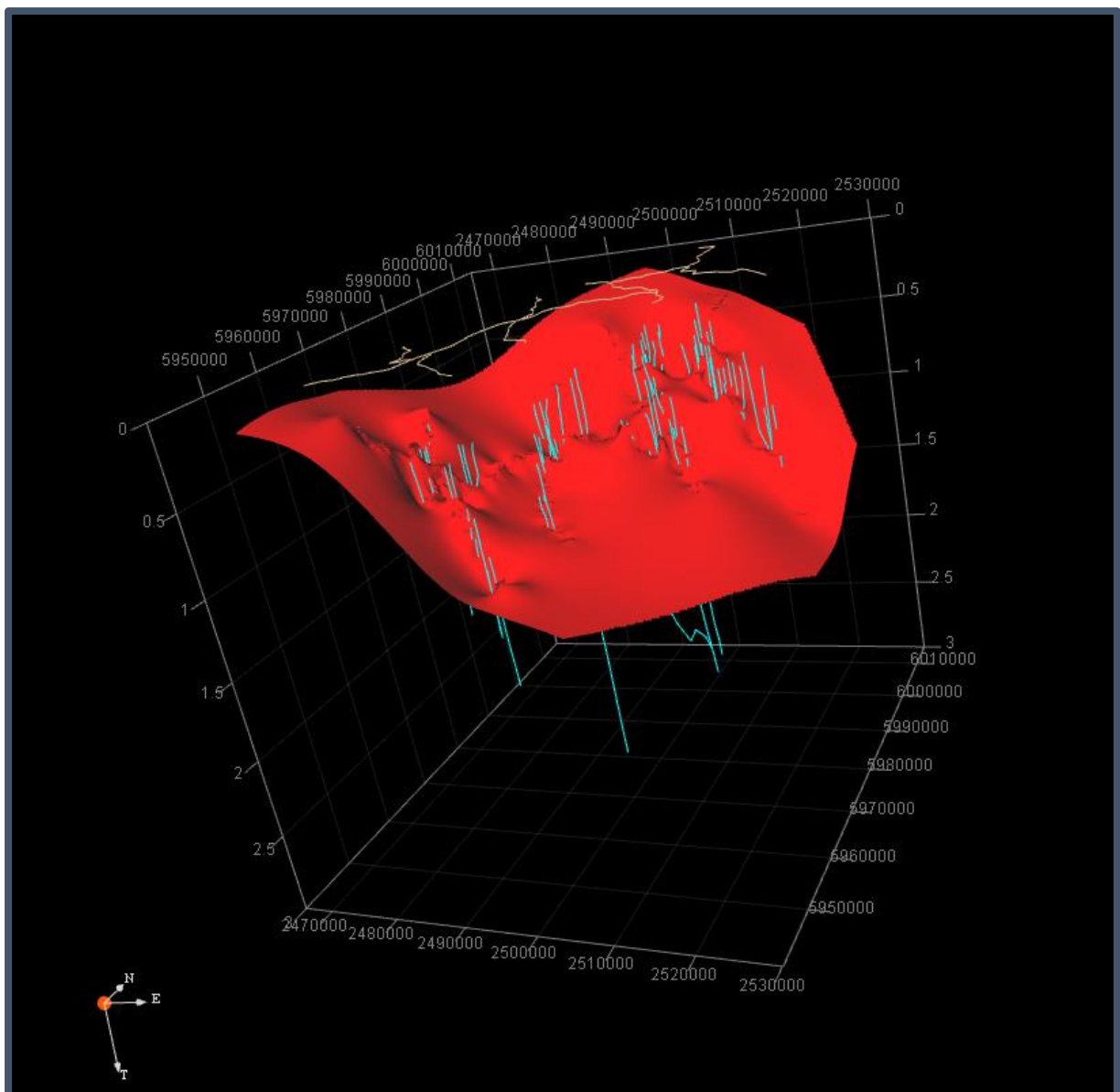
*Figure 6.38 A 3-D view of picks made of horizon 2 in the basin. This is the horizon with the strongest reflections. These picks are made from 2D seismic lines. The tan coloured lines represent the NZGD49 grid positions of the MD87 seismic lines. Z-axis is the depth in TWT (s).*



*Figure 6.39* Horizon 2 of 6 in the Moutere Depression. This is the horizon with the strongest and distinct reflection in all lines. The surface of the horizon is interpolated using the picks made for each line. The light blue lines located at the top of the image indicate the NZGD49 grid positions of the 2D seismic lines. Z-axis is the depth in TWT (s).

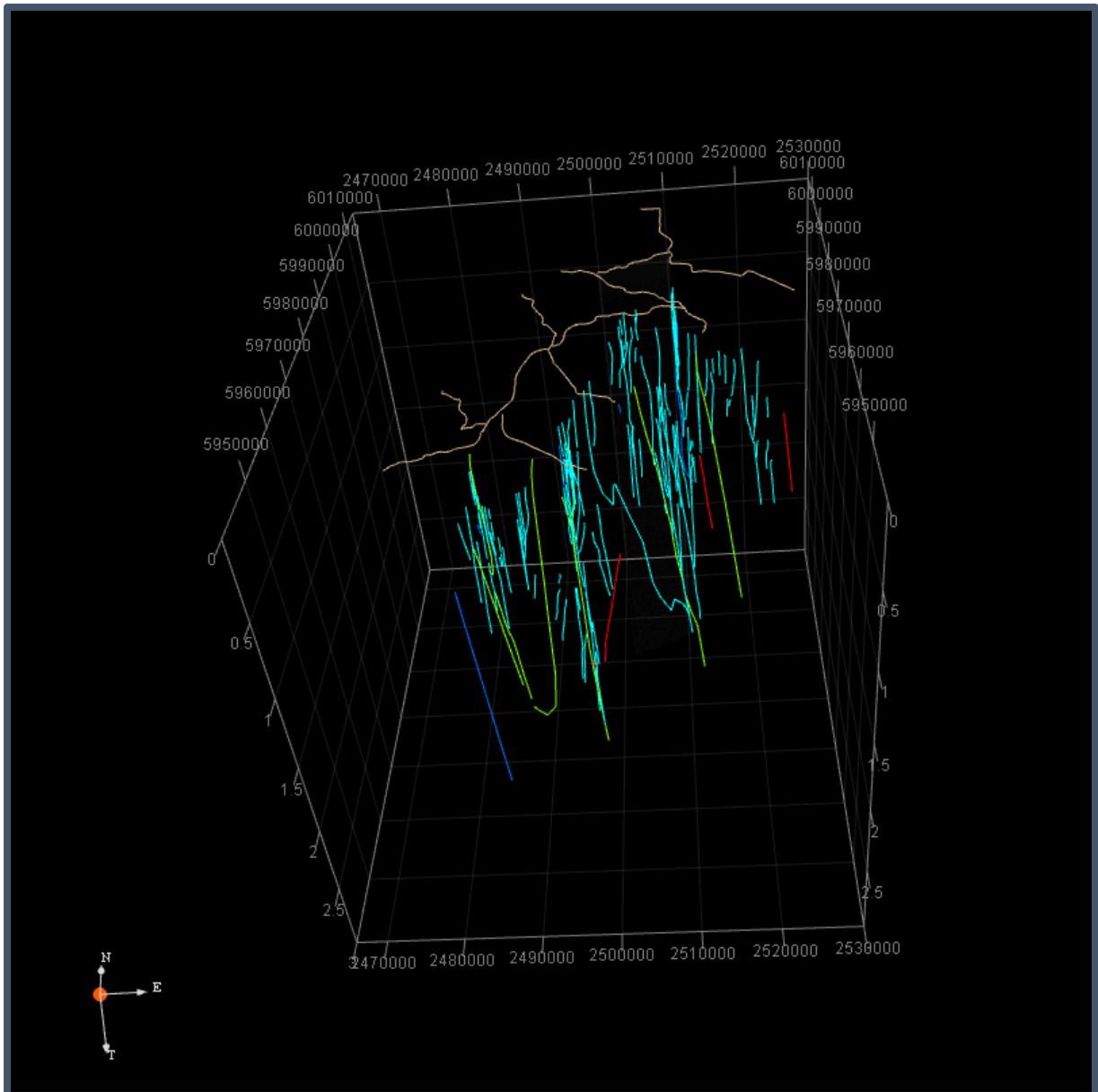
## Faults

Distinct breaks in continuity identified in 2D seismic sections are labelled in Kingdom. Major faults that can be correlated between the sections are assigned distinct colours while other faults are given a light blue colour (Figure 6.41). Due to the decrease in resolution in the shallow and deeper segments of the seismic sections it has been difficult to follow the breaks along faults in these areas. The faults were mainly identifiable when they intersect Horizon 2 (Figure 6.40).



*Figure 6.40* Faults (light blue) intersecting Horizon 2 (red). The tan coloured lines represent the NZGD49 grid positions of the MD87 seismic lines. Z-axis is the depth in TWT (s).





*Figure 6.41 Unassigned faults are labelled light blue. The tan lines are the NZGD49 grid positions of the survey lines. Other coloured lines are distinct faults that can be correlated between seismic sections. Red: Waimea-Flaxmore Fault System (W-FF); Blue: Unnamed Normal fault (UNF); Green; Ruby Bay-Moutere Fault System (RB-MF). The depth is the TWT recorded in seconds.*

---

## 6.11 Processing Results Summary

The eight Vibroseis seismic lines acquired in the Moutere Depression in 1987, extended over a total distance of 213 km. All eight datasets underwent the same general processing flow outlined in Chapter 5 with all the lines mostly using the same noise filtering modules. Pre-stack noise suppression modules QFK and FXDECON were consistently applied, with the exception of line 03 where a regular bandpass filter sufficed and QFK was not required. Unlike the parameters set for noise filtering, the gain control and deconvolution types employed to individual lines varied greatly. The AGC type fluctuated evenly between *normal* and *median* types while deconvolution type mirrored this trend with DECONW and SCDECON used equally between the lines.

In appearance, the final migrated lines of the echoed the results attained by GECO Ltd. The seismic sections had poor average horizontal and vertical resolutions of 254 and 25 m respectively. Achieving a low average refraction static RMS value of 8.747 ms made little improvement, resolution continued to worsen with depth, particularly after 3 s where valuable information was scarce. The area with the best resolution was found at 0.8 – 1.5 s where the undulating surface of the strongest horizon (out of four) and the overlying layered stratigraphy could be seen with great clarity.

Nevertheless, numerous faults were distinguishable and were picked through the 2D seismic sections in IHS Kingdom with confidence. Difficulty with picking due to resolution only occurred in segments shallower than 0.3 s and greater than 3.0 s as previously mentioned. Three main faults, the Waimea-Flaxmore Fault (W-FF), Ruby Bay-Moutere Fault (RB-MF) and an Unnamed Normal Fault (UNF), were recognised and correlated between the sections to reproduce the fault system in the Moutere Basin.

The identification of the main subsurface geological features, such as faults and horizons, provided an adequate foundation for interpretation.

---

---

## 7.0 Interpretations

The construction of a 3D model consisting of eight seismic sections extending from the surface to basement, has made it possible to visualise the Moutere Depression with a new perspective. Main geological features such as horizons and faults were able to be mapped out clearly in Kingdom. The four main horizons were mapped by their sedimentary facies while faults were distinguished based on their correlation between seismic sections (Figures 7.3 – 5).

---

### 7.1 Faults

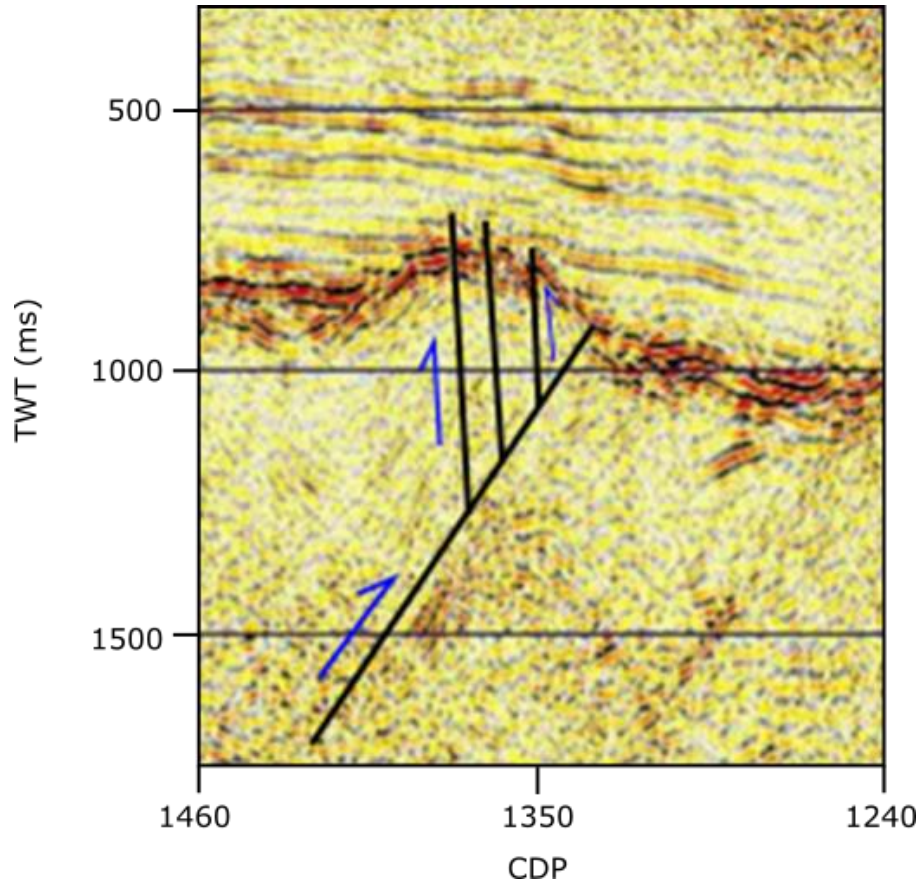
Each fault was mapped out in Kingdom and categorised into one of four groups as introduced in Section 6.10: Ruby Bay- Moutere Reverse fault (RB-MF), Waimea-Flaxmore Fault (W-FF), an Unnamed Normal Fault (UNF) and the rest were unspecified. The first three mapped fault groups have a similar shape: steeply dipping and with an angular curve away from the Eastern Province (Figure 7.2).

The shallower ends of the faults reaching the surface were difficult to map since the resolution decreased significantly in the shallower regions. Because of this, I was unable to conclusively determine whether these faults were open. However, based on the studies by Ghisetti (2018) and Li (1998), the majority of these faults are assumed to be blind.

The Ruby Bay-Moutere Fault is a reverse fault that stretches across the Depression and connects the Tutaki Fault in the south and the offshore Surville Fault in the north (Mortimer et al, 2001). The Ruby Bay-Moutere Fault created a related fold system with a low angle bounding fault and numerous antithetic splays (Figure 7.1). These fold systems are evident in Horizon 3, giving it a hummocky structure.

The Waimea-Flaxmore Fault is a reverse fault found in the east, bounded by the Eastern Province and the Median Batholith. The fault is mapped as a set of reactivated east-dipping reverse faults with a normal fault origin (Johnston and Nicol 2013).

The Unknown Normal Fault (UNF) is found in the western side of the Moutere Depression. It intersects most of the horizon and is bounded by the top of the Western Province and Median Batholith.



*Figure 7.1 Annotated figure taken from line 05, illustrating antithetic splays that are prevalent in the Moutere Depression.*

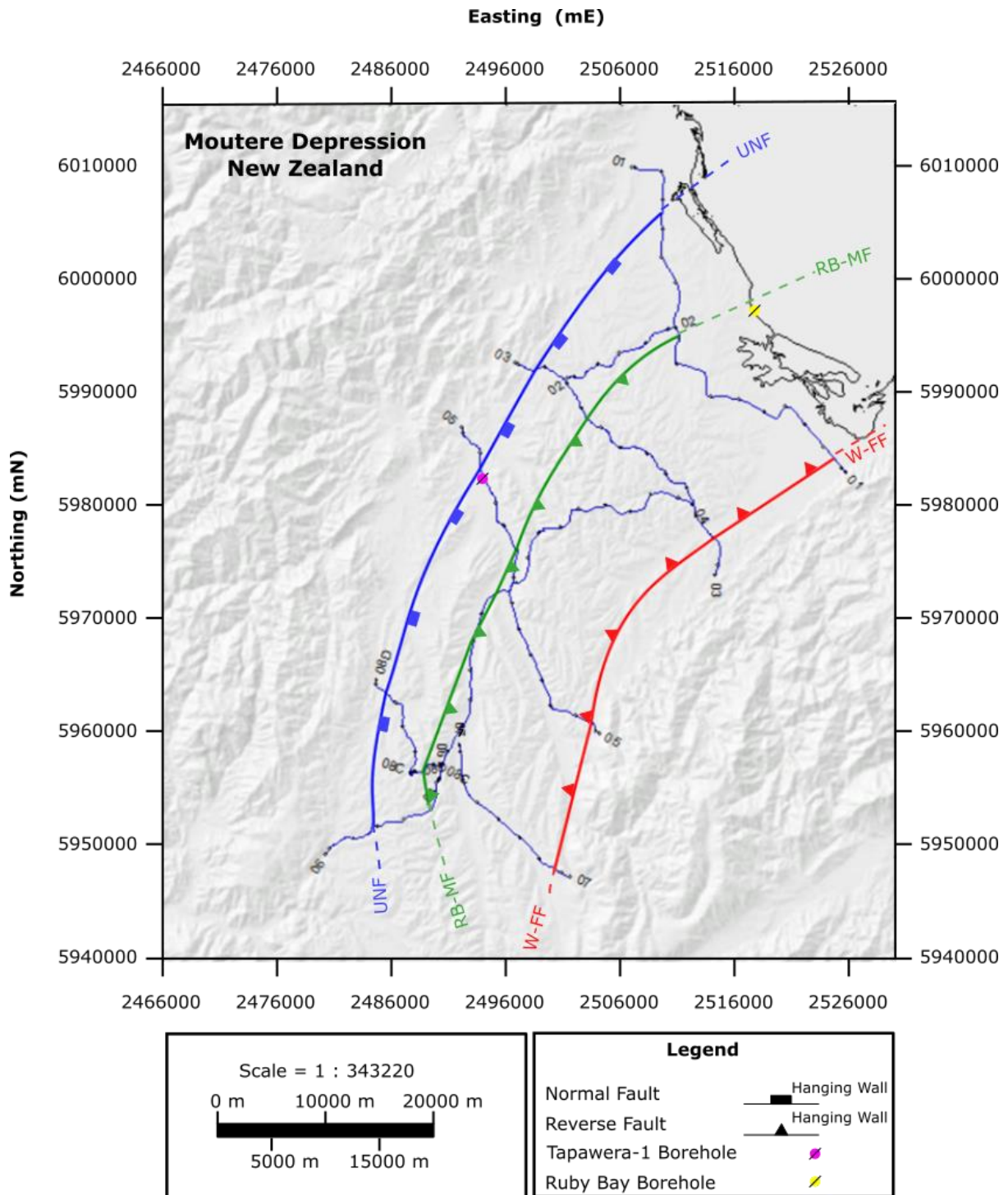



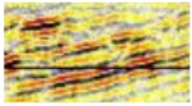



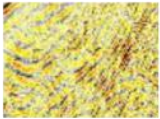
Figure 7.2 A map view of the MD87 survey with a topographical background applied. Thin blue lines represent the seismic survey lines. Up dip tips of the interpreted faults in the seismic data are shown. Northings and eastings are set to the NZGD64 coordinate system.



## 7.2 Stratigraphy

The six horizons were mapped out based on their seismic facies attributes. Four of the main horizons are displayed in 3-D. The boundaries of seismic facies 1 were difficult to constrain so the horizon was not mapped. The other upper horizons (e.g. seismic facies 2) were also tricky to distinguish due to the poor resolution, when these horizons reach shallower sections its position is determined by my own interpretation. Each of the main seismic facies are categorised below in Table 7.1.

*Table 7.1 Seismic facies of the horizons.*

<b>Seismic Facies</b>	<b>Amplitude</b>	<b>Continuity</b>	<b>Vertical Extent</b>	<b>Other</b>	<b>Seismic Character</b>
1	Low to High	-Parallel -Horizontal -Low Frequency -Weakly Stratified	Upper 200ms	-Incoherent	
2	Moderate to High	-Parallel to sub-parallel -Horizontal -High Frequency -Continuous	200~1200ms	-Onlap to SF3 -Semi-transparent	
3	High	-Parallel/wavy -Discontinuous -High Frequencies	1200~2500ms	-Mounded	
4	Low to Moderate	-Low Frequencies -Discontinuous -Wavy	2000~3000ms		
5	Low	-Low Frequencies -Chaotic	25000~5000ms	-Incoherent	
6	Low	-Sub-parallel -Low to High Frequency -Stratified	1500~2500ms	-Only present in line 01	

## Seismic Facies 1

Seismic facies 1 has a low frequency and low to high amplitude. This facies occurs intermittently in the upper sections of all lines in the Moutere Depression. It is distinguishable by its their parallel and stratified nature. The facies is draped on and differs from the facies below with its internal reflectivity orientation being horizontal as opposed to sub-horizontal. This indicates it has not been affected by the faulting that occurs below and is deposited a significant period after facies 2. The low frequency suggests a calm depositional period with low relief. Breaks in sedimentation possibly will have occurred during interglacial periods (Lihou 1992). It is difficult to trace the facies continuously in all lines because of the effects of near surface noise. This leaves the shallowest regions void of useful information. Seismic facies 1 could represent the Pleistocene Moutere Gravels.

## Seismic Facies 2 - Horizon 1 (Gold)

Seismic facies 2 is a distinct layer that lies above and onlaps onto facies 3, particularly in the southwestern lines i.e. line 06, 8C and 8D. It is a stratified layer that is characterised by low to moderate amplitudes with high frequencies. Because of the continuous nature of the facies, it makes it easy to identify faults when the orientation changes from parallel to sub-parallel. The facies reflectivity suggests a gentle depositional environment, possibly a shallow marine environment transgressing from the Separation Point granite, as evidence by the presence of onlapping in lines 06 and 08. This facies could represent the Pliocene aged, calcareous Glenhope Formation in the west and Port Hills Gravels in the east. The lack of horizon 1 in the west onto Horizon 2 (Figure 7.4) suggests the formation was possibly removed by erosion since the formation can be found in the regions further south of the Moutere Basin.

### **Seismic Facies 3 – Horizon 2 (Red)**

Facies 3 is the most distinct facies of all six characterised with its high amplitudes and frequencies. It is a semi-continuous, wavy facies that is recognisable throughout all lines. Numerous mounds that form along folds are caused by reverse faulting with antithetic splays. The layer is highly undulating and fractured compared to the sub-parallel facies 2, indicating a significant difference in the duration of deposition and a more brittle composition. The facies could represent the transition between a deeper marine environment and a shallower state. I have interpreted the facies to consist of the Middle Miocene upper Sherry River Formation that is part of the West Haven Group.

### **Seismic Facies 4 – Horizon 3 (Grey)**

Facies 4 consists of low to high amplitudes and frequencies at depths corresponding around 2000 – 3000 ms. It is a highly chaotic facies; however, also includes numerous discontinuous, high-amplitude, sub-parallel reflections. The facies is difficult to see in lines that are closer to shore, but more distinguishable in seismic sections closer inland. I have interpreted the facies to be part of the Late Oligocene, lower Sherry River Formation. A hardened calcified lower section of the formation was reported in Tapawera-1 that could have influenced the sonic transition between this layer and the basement.

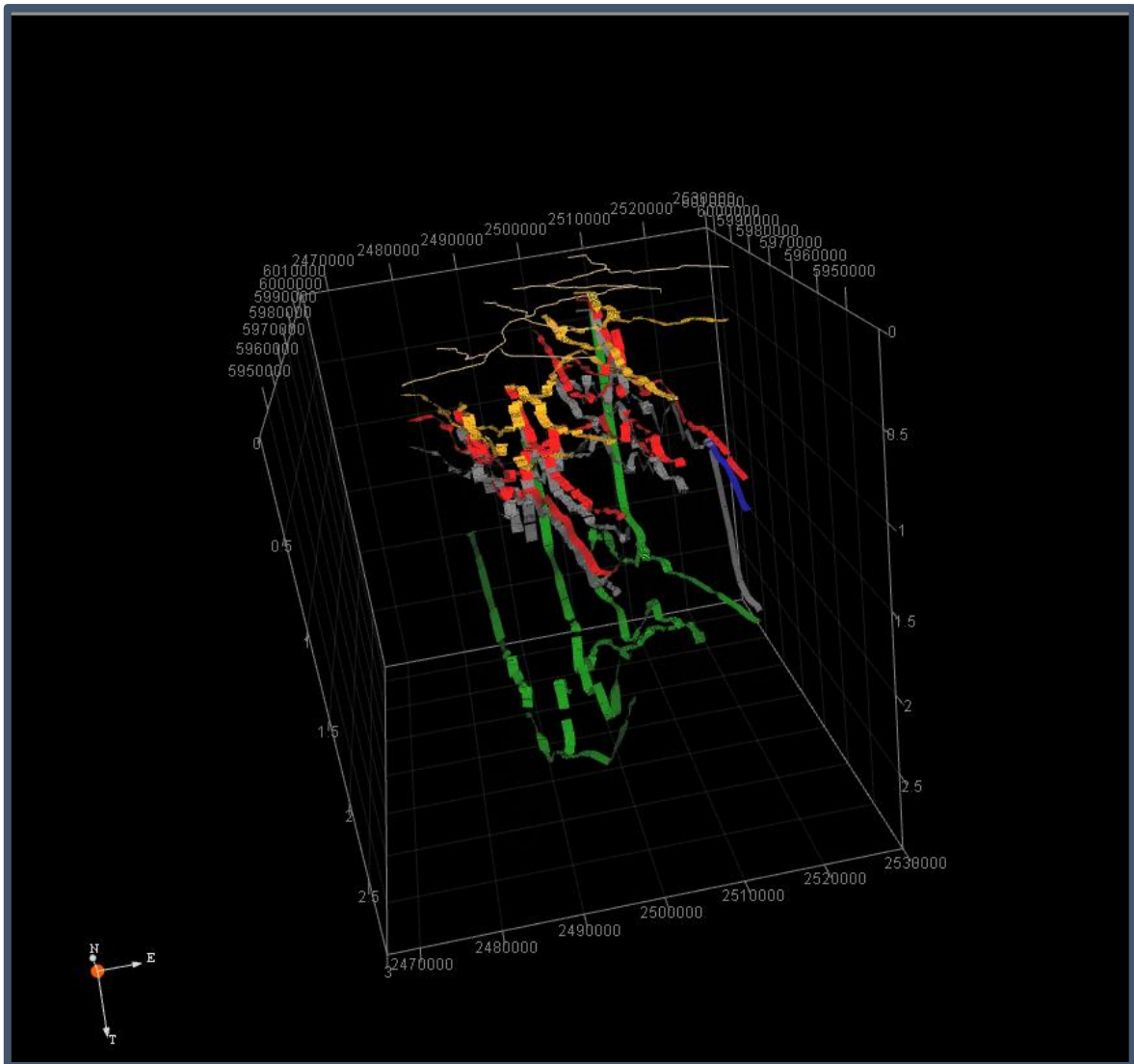
### **Seismic Facies 5 -Horizon 4 (Green)**

Facies 5 is deemed to be the basement and differs significantly from to the rest of the seismic facies. It is found in the deeper sections, usually greater than 1500 ms but can also be as shallow as 1000 ms further in land towards the West Coast. The facies is characterised by mainly chaotic reflections with varying low to moderate amplitudes. Amplitudes of this facies decrease with depth, as expected from spherical attenuation. I have interpreted the facies to

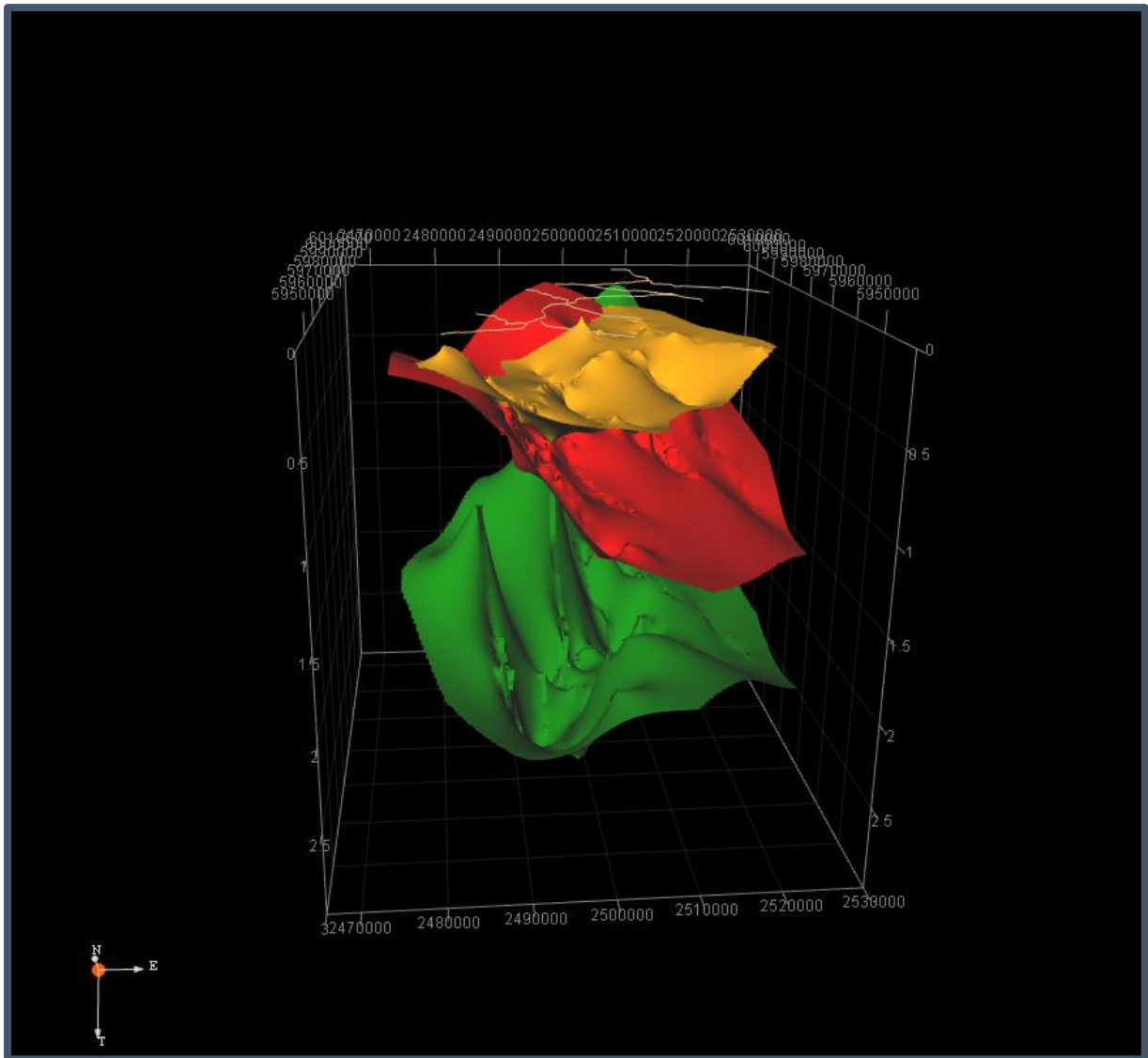
be the basement consisting of the Cretaceous Separation Point Granite, Permian Brook Stream Volcanics, and Median Batholith.

### **Seismic Facies 6 – Horizon 5 (Blue)**

Facies 6 is a stand-alone feature that can be seen in the north-eastern margin of line 01 below facies 3 at times 1000 - 2000 ms. It contains low amplitudes, high frequencies, and highly stratified layers. The layering verges on being divergent with it curving upwards towards facies 3. This could represent the volcanic assemblages present in the north-eastern areas of Nelson (Rainey and Waghorn 1989).

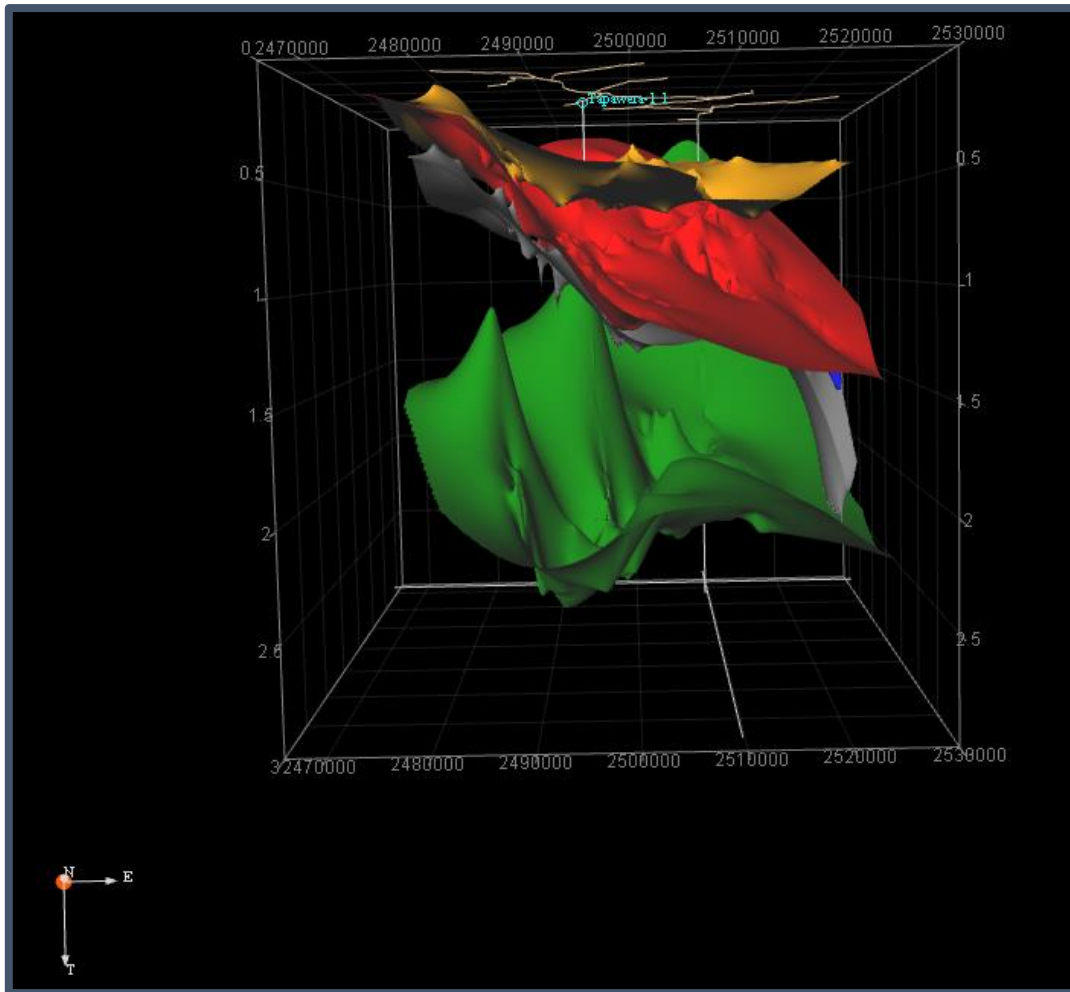


*Figure 7.3 3D perspective of the horizons. The tan lines at the top help illustrate the position of the survey lines. The tan coloured lines represent the NZGD64 grid positions of the MD87 seismic lines. Z-axis is the depth in TWT (s).*



*Figure 7.4 The three main horizons (1, 2 and 4) displayed with interpolated horizon surface. The tan coloured lines represent the NZGD64 grid positions of the MD87 seismic lines. Z-axis is the depth in TWT (s).*





*Figure 7.5 The six horizons displayed in a cross-sectional view with interpolated horizon surface. The 1989 Tapawera-1 exploration well is labelled as well. The tan coloured lines represent the NZGD64 grid positions of the MD87 seismic lines. Z-axis is the depth in TWT (s).*

---

## 8.0 Conclusions

Reprocessing of the 1987 vintage Vibroseis dataset from the Moutere Depression was a worthwhile and intriguing endeavour. This is in large part due to the additional techniques adopted in the current study. The use of noise filtering processes such as QFK and FXDECON resulted in considerable noise reduction in the seismic sections. The addition of colour and 3D modelling provided easier visualisation and identification of subsurface structures. This final chapter is divided into three concluding sections. The first concerns the overall geology and structure of the Moutere Depression based on my own seismic interpretations. The second section details project limitations and the challenges that the study faced due to the nature of the available data. The third section explores further work which may supplement this project and provide further insight to the tectonomorphology of the Moutere Basin.

---

### 8.1 Moutere Depression

The Moutere Depression is an NNE trending, elongated trough that is situated between the Cretaceous Separation Point Granite, Permian Brook Street Volcanics and Rotoroa Igneous Complex. In between the two Western and Eastern provinces, the Median Batholith is wedged. The 3D seismic model indicates that the basin is a trough infilling with sedimentary sequences that can be mapped by several different horizons. The Quaternary sediments (Moutere Gravel and Glenhope Formation) pinch out towards the western side and thicken to the east.

The basin is subject to WNW directed compressional regime that potentially was initiated in the mid-Miocene suggested by the extensive folding and fracturing in Facies 2 and 3. Such compression is ongoing (Townend, et al. 2012), reactivating and creating further faults within the basin, many of which remain blind, based on the seismic sections.

Three major faults were identified through the seismic section. The most identifiable fault was the Waimea-Flaxmore reverse fault. The WFF can be found curving around from N to NEE along fringe of the Eastern Province. This reverse thrust uplifted Permian mafic rocks and as a result caused the tilt observed in Seismic Facies 2 creating an overall dip to the east. The

Ruby Bay-Moutere Fault remains predominantly blind and follows the same pattern as WFF further inland. The steep angled reverse fault consists of numerous antithetic splays that cause abundant folding in Seismic Facies 3. A large normal fault is seen on the western side of the basin. The fault additionally penetrates the basement and has a similar appearance to the other two faults.

---

## 8.2 Data and technical limitations

Despite the merits of this study, there were challenges that hindered the progress of the seismic data processing. These included both external and internal factors regarding the raw data itself and the technical aspects regarding the data processing program.

In the university, there were a small select group of people that were familiar with the Globe Claritas program. Even fewer, with expertise in Vibroseis data. Combined with the Globe Claritas headquarters located in Wellington, it introduced additional difficulties in receiving technical support and advice.

The original data, as mentioned in previous chapters, was poorly recorded and plagued with noise. Many shots were positioned and incorrectly numbered, this significantly hindered data processing which resulted in many steps being repeated.

The seismic survey and the Moutere Depression were deprived of valuable borehole and geophone depth data. This in turn, affected refraction static calculations and shallow seismic interpretations. Only two wells were drilled in the vicinity of the Moutere Depression, the Taparwera-1 (spud date, 1989) and Ruby Bay (spud date 1966) wells, where only one of which had sonic log data. The absence of well data resulted in difficulties in constraining the NMO velocities and horizons to a high degree of confidence.

---

---

## 8.3 Future work

### Processing

Noise was a significant problem in the data set. Further filtering processes and migration tests could be attempted to help mitigate this issue. Only the main filters such as f-k and finite difference filters were used due to time constraints. Other filters and migration routines such as radon and tau-p transforms as well as phase migration could be attempted to increase clarity in the seismic sections. If non-Claritas based processing methods are applied, machine and dictionary learning methods advocated by Li et al. (2019) could also be advantageous on such noisy data with crooked-line geometries.

AGC was primarily used as a compensator for energy attenuation for this project. Since AGC is not a linear gain application, it can distort and ruin wavelet data. Spherical divergence and balance gain methods are preferable and were attempted to no avail. Further work into this area would improve seismic resolution.

### Seismic Hazard

With the number of faults running through the Moutere Basin and the active compressive regime, further work regarding seismic hazard and prediction is encouraged. The two most recent and only works, focusing on the seismic movement of faults within the Moutere Depression by Lihou (1992) and Ghisetti (2018) have varying opinions on the seismic activity. The more recent paper suggests that the Quaternary activity deduced from deformation of rivers and topography can reactivate the concealed fault system. Lihou on the other hand, suggests that the present-day stress field presents no significant issue for fault activation.

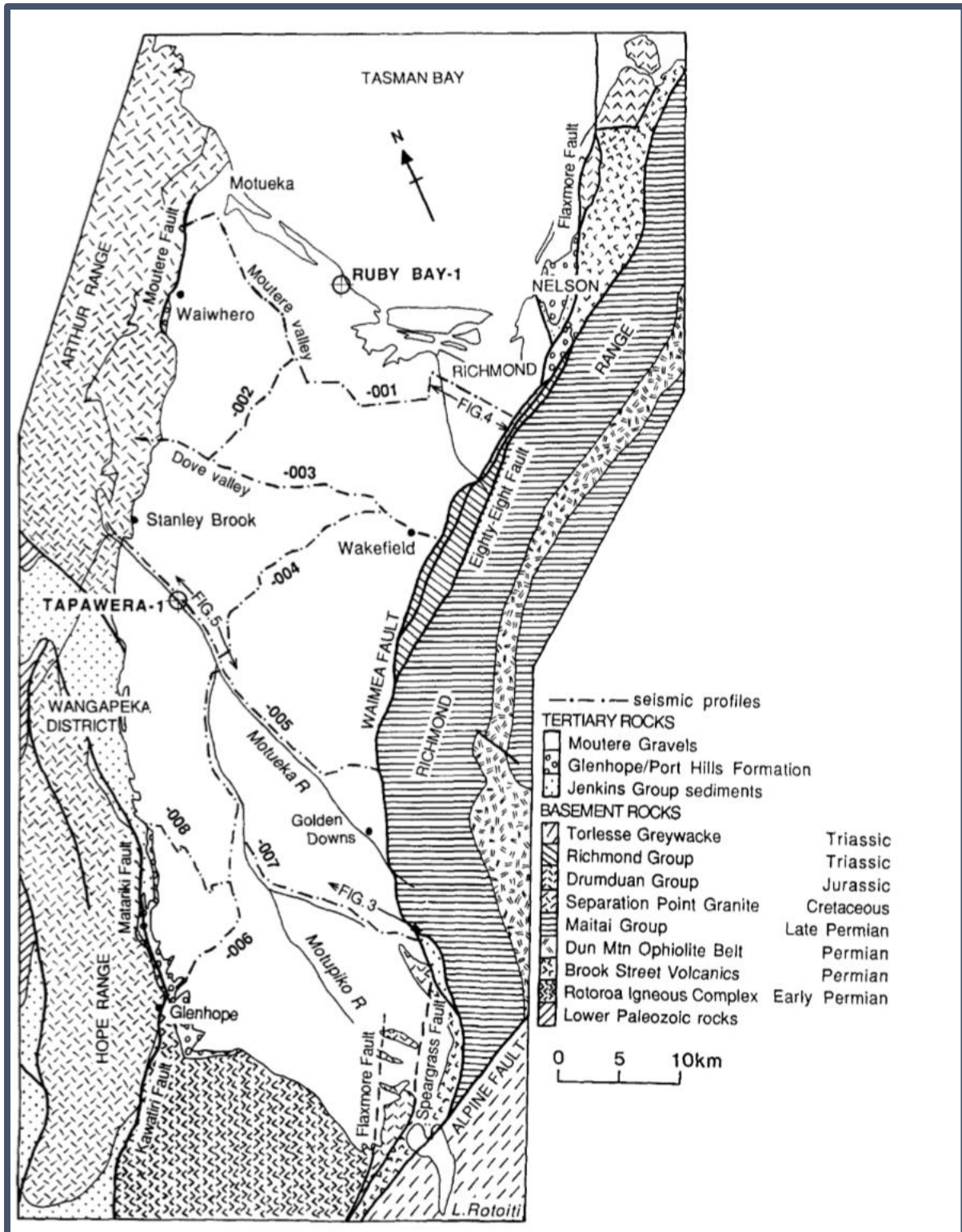
New seismic surveying in the area may well be useful. Using newer Vibroseis trucks that can produce sweeps up to 105 Hz (Driml, et al. 2004) compared to the previous 66 Hz would result in higher resolution images of the shallow depths of the subsurface, an area that had unfortunately poor resolution in the original survey. Chemical explosives as a source should

be considered as well, since they are able to produce a wider, range of frequencies. If the survey is carried out a second time, the addition of more inline/cross-line data will allow a more accurate fault identification through 2D time slices. Such methods were not available for the original survey.

The addition of more borehole data would also provide benefits for subsurface imaging, allowing better control of the interval and sub-weathering layer velocities. It additionally has the benefit of better constraining the final seismic velocity model and improve the accuracy of refraction statics.

---

Appendix



*Appendix i An adapted geological map showing the seismic lines in the Moutere Depression as well as the local geologies and faults. The map was sourced from Lihou (1992) with her reinterpretation of the seismic data. No data reprocessing was done in her study.*



## PROCESSING SEQUENCE

**PROCESSED BY** GECO NZ  
**DATE** OCTOBER - DECEMBER 1987  
**INITIAL PROCESSING** from field summed and correlated tapes  
     data length 5 s  
     sample rate 4 ms  
     demultiplex with gain recovery  
     trace edit  
     spherical divergence  
**CROOKED LINE ANALYSIS**  
**COMMON DEPTH POINT GATHER**  
**DECONVOLUTION**  
     type predictive  
     total operator length 200 ms  
     gap 12 ms  
     design start time near trace : 300 ms  
     far trace : 1600 ms  
     design window length 2000 ms  
**ELEVATION STATIC CORRECTION**  
     statics calculated to msl  
     elevation replacement velocity 2600 m/s  
     positive long wavelength correction to processing datum  
**DYNAMIC CORRECTION**  
     velocities derived from CVS analyses  
**PRE-STACK MUTE**  
**AMPLITUDE MODULATION**  
     time variant scaling 500 ms windows 50% overlap  
**CDP TRIM**  
**COMMON DEPTH POINT STACK** square root of fold compensation scaling  
**STATIC CORRECTION**  
     negative long wavelength static correction , time 0.0 s equals msl  
**TIME VARIANT BANDPASS FILTERING**

TIME (ms)	LOW CUT (Hz)		HIGH CUT (Hz)	
(below top section)	-3 dB	-30 dB	-3 dB	-30 dB
0	15	8.5	60	83
1000	15	8.5	60	83
1200	15	8.5	50	79
1400	15	8.5	50	79
1600	15	8.5	40	65
2300	15	8.5	40	65
2900	15	8.5	35	60
5200	15	8.5	35	60

  
**TIME VARIANT SCALING**  
     window 500 ms  
     overlap 50%  
**FINITE DIFFERENCE WAVE EQUATION MIGRATION**  
**ADAPTIVE K-F FILTERING**

Appendix ii *The processing sequence carried out by Geco Ltd (taken from PR1488).*

## References

- Aki, K. (1982); *"Scattering and Attenuation"*, Bulletin of the seismological society of America, 72:6, s319-s330.
- Ali, Hassan Z, and Hassan A Thabit (2018); *"The Effect of Spike and Gap Deconvolution on 2D Land Seismic Data."* Open Access Library Journal 1-11.
- Al-sadi, H.N.(2017); *"Seismic Hydrocarbon Exploration; Advances in Oil and Gas Exploration and Production"*, Springer International Publishing, Switzerland 2017,
- Ayres, A. and Theilen, F. (1999); *"Relationship between P- and S-wave velocities and geological properties of near-surface sediments of the continental slope of the Barents Sea"*, Geophys. Prospect., 47(04), 431–441.
- Bally, A.W., Roberts, D.G., (2012); *"Regional Geology and Tectonics: Principles of Geologic Analysis"*, Elsevier Science, <https://doi.org/10.1016/C2009-0-17259-8>
- Bancroft, J. C., (2007); *"A Practical understanding of pre- and poststack migrations"*, VOL 2 SEG, Tulsa, USA.
- Berkhout, A. J. (1980); *"Developments in Solid Earth Geophysics"*, Vol. 12. Netherlands: Elsevier Scientific Publishing Company.
- Bill Dragoset (2005); *"A historical reflection on reflections"* ;The Leading Edge, 24(s1), s46-s70.
- Boas, Daniel B V, and Milton J. Porsani. (2015); *"Comparison of FK and SVD filtering in the processing of land seismic data"*, 14th International Congress of the Brazilian Geophysical Society. Rio de Janeiro, Brazil: Sociedade Brasileira de Geofisica. 1-7.
- Boyce, J. F., (1986); *"Seismic processing and image analysis"* . J.Phys. D:Appl. Phys, 19, pp397-415.
- Brown, A.R. (1999); *"Interpretation of three-dimensional seismic data"*, 5th edition. AAPG Memoir 42, Tulsa, Oklahoma, pp. 514.
- Bull, S, M Hill, MJ Arnot, H Seebeck, K Kroeger, and H. Zhu. (2015); *"Depth Structure Maps, Isopach Maps and Regional Velocity Model from the Southern Taranaki Basin."* 4D Taranaki Project. Lower Hutt: GNS Science Data Series.

- Butler, P. (2012); *"White Noise Suppression in the Time Domain."* CSEG Recorder 38-44.
- Cary, P and Nirupama N. (2013); *"A New , Simple Approach to Surface-Consistent Scaling"* CSEG Recorder 38-44.
- Choi, Y., Stewart, J. P., Graves R. W. (2005); *"Empirical Model for Basin Effects Accounts for Basin Depth and Source Location"*, Bulletin of the seismological society of America, 95:4, 1412-1427,
- Claerbout, J.F. (1970); *"Coarse Grid Calculations of Waves in Inhomogeneous Media with Application to Delineation of Complicated Seismic Structure"*, Geophysics 35: 407-418.
- Claritas, GLOBE (2013) *"GLOBE Claritas Land 2D Tutorial Version 6.0."* GLOBE Claritas Software Documentation 6.0.1. Wellington, New Zealand, June.
- Craig, M. S., Genter, R. L. (2006); *"Geophone array formation and semblance evaluation; Geophysics"*, 71:1, doi: 10.1190/1.2159055
- D'Arnaud Gerkens, J. C., (1989); *"Foundation of Exploration Geophysics"*, Amsterdam: Elsevier Science.
- Dingus, Carolyn. (2010); *"Seismic Processing- Noise Attenuation Techniques for Relative Amplitude Processing."* Petroleum Africa 47-49.
- Dondurur, Derman. (2018); *"Acquisition and Processing of Marine Seismic Data"*. Elsevier.
- Driml, K, B Smith, J Saunders, and R Taylor. (2004); *"Vibroseis or Dynamite: investigating source characteristics."* ASEG Extended Abstracts 1-6.
- Driml, Karel, Barry Smith, John Saunders, and Randall Taylor. (2004); *"Vibroseis or Dynamite: Investigating Source Characteristics."* ASEG Extended Abstracts 1-6.
- Dziewonski, A. M. (2004); *"Global seismic tomography: What we really can say and what we make up"*, ([www.mantleplumes.org/ Penrose/PenPDFAbstracts/DziewonskiAdam\\_abs.pdf](http://www.mantleplumes.org/Penrose/PenPDFAbstracts/DziewonskiAdam_abs.pdf))
- Fortner, B. (2012); *"The Data Handbook"*, Springer science and business media.
- Gadallah, Mamdouh R, and Ray L Fisher. (2005); *"Applied Seismology: A comprehensive guide to seismic theory and application"* Tulsa, Oklahoma: PenWell Corporation.

- Gaiser, J.E. (1996); "*Multicomponent Vp/Vs correlation analysis*", *Geophysics*, 61(04), 1137–1149.
- Ghisetti, F C, M R Johnston, P Wopereis, and R H Sibson. (2018); "*Structural morpho-tectonic evidence of Quaternary faulting within the Moutere Depression, South Island, New Zealand.*" *New Zealand Journal of Geology and Geophysics* 461-479.
- Gupta JB (2009); "*Electronic Devices and Circuits*", Third Edition, New Delhi, India: SK Kataria and Sons.
- Hagelund, R., Levin, S.A. (2017); "*Seg-Y\_r2.0: SEG-Y revision 2.0 Data Exchange format*", Society of Exploration Geophysicists.
- Henry G (1997); "*Geophysics for Sedimentary Basins*", Editions Technip, Paris, France, Pp1 – 445.
- Henry, Steven G. (1997); "*Catch the (Seismic) Wavelet.*" *Geophysical Corner*, AAPG Explorer.
- Huang L, Fehler MC. (2001a); "*Advanced wave equation migration*". In Proc. Int. Symp. Recent Advances Exploration Geophysics, 5th, Kyoto, pp. 38–45. Kyoto, Jpn: Kyoto Univ.
- Huang, L., Fehler M.C.,(2002); "*Modern Imaging Using Seismic Reflection Data*", *Annu. Rev. Earth Planet. Sci.* ;30, pp259-284
- Jiao, H., Yuzhu, L., Jianhua, G., (2007); "*The study and Analysis of floating datum selection for rugged terrain*"; *Applied Geophysics*, 4:2, pp101-110.
- Johnston, M R, and A Nicol. (2013); "*Assessment of the location and paleoearthquake history of the Waimea-Flaxmore Fault system in the Nelson -Richmond area with recommendations to mitigate the hazard arising from fault rupture of the ground surface*". Wellington: GNS Science Consultancy Report.
- Johnston, M. R. (2013); "*Preliminary Assessment of the Liquefaction Hazard in Tasman and Nelson*", Nelson City Council, Open File, <http://www.nelson.govt.nz/environment/nelson-plan/natural-hazards/liquefaction>.
- Johnston, M. R. (1971); "*Pre-Hawera geology of the Kaka district, northwest Nelson*". *New Zealand journal of geology and geophysics*, 14: 82-108.
- Kaiser, A., Holden, C., Beavan, J., Beetham, D., Benites, R., Celentano, A., Collett, D., Cousins, J., Cubrinovski, M., Dellow, G., Denys, P., Fielding, E., Fry, B., Gerstenberger, B., Langridge, R.,

- Massey, C., Motagh, M., Pondard, N., McVerry, G., Ristau, J., Stirling, M., Thomas, J., Uma, SR., and Zhao, J., (2012); "*The Mw 6.2 Christchurch earthquake of February 2011: preliminary report*", New Zealand Journal of Geology and Geophysics, 55:1, 67-90,
- Kamei, R., Miyoshi, T., Pratt, R. G., Takanashi, M., Masaya, S. (2015); "*Case History: Application of Waveform Tomography to a crooked-line 2D land Seismic Data Set*"; Geophysics, 80:5, P. B115-B129.
- Kugler, S., Bohlen, T., Forbriger, T., Bussat, S., Klein, G., (2006); "*Scholte-wave tomography for shallow-water marine sediments*". Geophysics j.int. (2007) 168, 551-570. doi: 10.1111/j.1365-246X.2006.03233.
- Lay, T., Wallace, T.C., (1995); "*Modern Global Seismology*"; Vol 58, International Geophysics, Academic Press, California.
- Le Meur, D., Benjamin, N. , Cole, R., and Al Harthy, M., (2008); "*Adaptive Ground-Roll Filtering.*" 70th EAGE Conference and Exhibition . Rome, Italy: EAGE.
- Li, C, Y Zhang, and C Mosher( 2019); "*A hybrid learning -based framework for seismic denoising*", The Leading Edge.
- Lihou, J C. (1992);"*Reinterpretation of seismic reflection data from the Moutere Depression, Nelson region, South Island, New Zealand*", New Zealand Journal of Geology and Geophysics, 477-490.
- Lowrie, W. (2007); "*Fundamentals of Geophysics*", New York: Cambridge Press.
- Mashiniskii, E. I. (2008); "*Amplitude-frequency dependencies of wave attenuation in a single crystal quartz: Experimental Study*", J. geophys Res, 113,b11304, [doi.10.1029/2008JB005719](https://doi.org/10.1029/2008JB005719)
- Mendel, J M (1983); "*Optimal seismic deconvolution*". New York, New York: Academic Press Inc. LTD.
- Mortimer, N, A J Tulloch, R N Spark, N W Walker, E Ladley, A Allibone, and D L Kimbrough. (1999); "*Overview of the Median Batholith, New Zealand: a new interpretation of the geology of the Median Tectonic Zone and adjacent rocks*", Journal of African Earth Sciences 257-268.
- Mortimer, N, P Gans, A Calvert, and N Walker (1999) "*Geology and thermochronometry of the east edge of the Median Batholith (Median Tectonic Zone): a new perspective on the Permian to Cretaceous crustal growth of New Zealand.*" The Island Arc 404-425.

- Mortimer, N. (2004); "*New Zealand's Geological Foundations.*" *Gondwana Research* 261-272.
- Muller, T. M., Shapiro, S. A., (2001); "*Most Probable seismic pulses in single realizations of three-dimensional random media*", *Geophys. J. Int.*, 144, 83-95.
- Mullick, N., Buske, S., (2017); "*Fresnel Zone Imaging of Seismic Data*", *Geophys J. Int.*, 211:2, pp784:796, <https://doi.org/10.1093/gji/ggx320>
- Nazarchuk, Z., (2017); "*Acoustic Emission, Foundations of Engineering Mechanics*", Ch. 2, Springer Int. Publishing.
- Nedimovic, M. R., West, G. F., (2003); "*Crooked-line 2D Seismic Reflection Imaging in Crystalline Terrains: Part 2, migration*" *GEOPHYSICS* 68: 286 – 296.
- Officer, C.B., (2012); "*Introduction to Theoretical geophysics*", Springer Science and Business media.
- Onajite, E. (2014); "*Seismic Data Analysis Techniques in Hydrocarbon Exploration*", Elsevier Journal, Vol 160, 3-4.
- Oppong, I.A., Danour, S.K. (2014); "*Amplitude Simulation Technique for Seismic Amplitude Scaling*". *Int. Res. J. Geo. Min.* 4(5): 133-138
- Parasnis, D. S., (1979); "*Principles of Applied Geophysics*", London, Chapman and Hall.
- Rainey, S., and D. Waghorn. (1989); "*Tapawerea-1 Well Completion Report, PPL38500*". Well Report - Completion, Nelson: Ministry of Economic Development New Zealand.
- Rajput, S., Thakur, N. (2016); "*Geological Controls for Gas Hydrate Formations and Unconventionals*", Elsevier
- Rattenbury, M.S.; Cooper, R.A.; Johnston, M.R. (1998); "*Geology of the Nelson area : scale 1:250,000*", *Institute of Geological and Nuclear Sciences 1:250,000 geological map 9***
- Redshaw, T.C. (2012), "*Principles of Geologic Analysis*", Elsevier, pp296-309.
- Rehmer, D. (1997); "*Velocity Analysis, NMO, and Stacking: An example from the Northwestern Shelf of Australia*"  
<http://www.geol.lsu.edu/jlorenzo/ReflectSeismol97/cmfraticelli/WWW/velocity.html>.



- Riene, C., van der Baan, M., Clark, R., (2009); *"The robustness of seismic attenuation measurements using fixed- and variable-window time-frequency transforms"* Geophysics, 74:2, doi 10.1190/1.3043726.
- Rjasekaran, S., McMechan, (1995); *"A new approach to pre-stack seismic processing"*, Geophys. J. Int. 121, 255-266.
- Robert Burger, H., (1992); *"Exploration Geophysics of the Shallow Subsurface"*, New Jersey: Prentice Hall.
- Schroeder, D.V. (1999), *"An Introduction to Thermal Physics"*, Pearson Education United states.
- Seismograph Service Ltd/Petroleum Corporation of NZ Exploration Ltd (1987); *"Field area report on a seismic reflection survey conducted in Nelson Area, PPL38500"*. (MD87 lines). Ministry of Economic Development New Zealand. Unpublished Petroleum Report PR 1488.
- Shapiro, S. A., Kneib, G. (1993) *"Seismic Attenuation by Scattering: Theory and Numerical Results"*, Geophys. J. int., 114, 373-391
- Sheriff, R. E. (1996) *"Understanding the Fresnel Zone"*, AAPG Explorer, Oct, pp. 18-19.
- Sheriff, R. E., and L. P. Geldart. (1985). *"Exploration Seismology"*. Vol. 1. 2 vols. Cambridge: Cambridge University Press.
- Sheriff, R.E. (2001). *"Encyclopedic Dictionary of Exploration Geophysics"*, Society for Exploration Geophysicists, Tulsa, OK.
- Shuey, R.T., (1985) *"A simplification of the Zoeppritz equations"*, Geophysics, 50:4, 609-614.
- Stucchi, E., Mirabella, F., Ciaccio, M.G. (2006), *"Comparison between reprocessed seismic profiles: seismologic and geologic data – A case study of the Colfiorito earthquake area"*, Geophysics, 71:2, P.B29-b40.
- Tandon, K., Tuncay, K., Hubbard, K., Comer, J., Ortoleva, P. (2004) *"Estimating tectonic history through basin simulation-enhanced seismic inversion: geoinformatics for sedimentary basins"*. Geophys. J. Int, 156, pp129-139
- Taner, M.T., Koehler, F., (1969), *"Velocity spectra- digital computer derivation and applications of velocity functions"*. Geophysics, 34, 859-881

- Taylor, John R. (2005); *"Classical Mechanics"*. Sausalito, California: University Science Books.
- Telford WM, Geldart LP, Sheriff RE (1990); *"Applied Geophysics"*, Second Edition, Cambridge University Press, Cambridge, UK.
- Townend, J, S Sherburn, R Arnold, C Boese, and L Woods, (2012). *"Three-dimensional variations in present-day tectonic stress along the Australia-Pacific plate boundary in New Zealand."* Earth and Planetary Science Letters 353-354.
- Tuncay, K., Park, A. and Ortoleva, P., (2000). *"Sedimentary basin deformation: An incremental stress approach"*, Tectonophysics, 23, 77–104.
- Wiederhold, Helga and M. Krawczyk, C. (2007). *"Geophysical mapping of buried valley aquifer systems: the project BurVal"*, American Geophysical Union.
- Yilmaz, Oz. (2001). *"Seismic data analysis"*. Society of Exploration Geophysicists.
- Zhu, J., Lines, L., Gray, S., (1998) *"Smiles and frowns in migration/velocity analysis"*, Geophysics, 63:4, pp1200-1209.